



TÍTULO

FLUID AND MELT INCLUSION STUDY OF MAGMATIC-HYDROTHERMAL MINERALIZATION IN THE OSSA MORENA ZONE (SW SPAIN)

ESTUDIO DE INCLUSIONES FLUIDAS Y VÍTREAS EN MINERALIZACIONES HIDROTHERMALES DE LA ZONA DE OSSA MORENA (SO DE ESPAÑA)

AUTORA

Cristina Martínez Tomé

	Esta edición electrónica ha sido realizada en 2013
Director	Fernando Tornos Arroyo, Instituto Tecnológico Geominero de España (ITGME)
Institución	Universidad Internacional de Andalucía e Instituto Tecnológico Geominero de España (ITGME)
	Tesis Doctoral
ISBN	978-84-7993-935-9
©	Cristina Martínez Tomé
©	De esta edición: Universidad Internacional de Andalucía
Fecha Lectura	23/11/2012



Reconocimiento-No comercial-Sin obras derivadas

Usted es libre de:

- Copiar, distribuir y comunicar públicamente la obra.

Bajo las condiciones siguientes:

- **Reconocimiento.** Debe reconocer los créditos de la obra de la manera especificada por el autor o el licenciador (pero no de una manera que sugiera que tiene su apoyo o apoyan el uso que hace de su obra).
 - **No comercial.** No puede utilizar esta obra para fines comerciales.
 - **Sin obras derivadas.** No se puede alterar, transformar o generar una obra derivada a partir de esta obra.
-
- *Al reutilizar o distribuir la obra, tiene que dejar bien claro los términos de la licencia de esta obra.*
 - *Alguna de estas condiciones puede no aplicarse si se obtiene el permiso del titular de los derechos de autor.*
 - *Nada en esta licencia menoscaba o restringe los derechos morales del autor.*

Fluid and melt inclusion study of magmatic- hydrothermal mineralization in the Ossa Morena Zone (SW Spain)

**Estudio de inclusiones fluidas y vítreas en mineralizaciones hidrotermales de la
Zona de Ossa Morena (SO de España)**

Cristina Martínez Tomé

Tesis

Presentada en la **Universidad Internacional de Andalucía (UNIA)** y el
Instituto Geológico y Minero de España (IGME)

Dirigida por

Dr. Fernando Tornos Arroyo

2012

Contents

Resumen	iii
Summary.....	viii
Agradecimientos	xii
Introduction.....	1
Chapter I: Regional geology and metallogeny of the Ossa Morena Zone: a review.....	7
<i>I.1. Introduction.....</i>	<i>7</i>
<i>I.2. Tectonic evolution of the Ossa Morena Zone: from the Cadomian to the Variscan orogenies.....</i>	<i>8</i>
<i>I.3. The Olivenza-Monesterio belt and associated mineralization</i>	<i>18</i>
<i>I.4. The magnetite – (Cu-Au) mineralization of the OMZ: a controversial origin.....</i>	<i>27</i>
<i>I.5. The “Iberian Reflective Body”: a link between the Variscan magmatism and the mineralization.</i>	<i>29</i>
<i>I.6. Mining history.....</i>	<i>31</i>
Chapter II: Fluid inclusion evidence for magmatic-hydrothermal fluid evolution in the intrusion-related copper-gold Sultana vein deposit at Huelva, Spain	33
<i>Abstract.....</i>	<i>33</i>
<i>II.1. Introduction.....</i>	<i>34</i>
<i>II.2. Geological setting</i>	<i>36</i>
<i>II.3. Methods</i>	<i>42</i>
<i>II.3.1. Fluid inclusion petrography</i>	<i>43</i>
<i>II.4. Vein quartz textures from SEM-cathodoluminescence</i>	<i>48</i>
<i>II.5. Types and distribution of fluid inclusions.....</i>	<i>53</i>
<i>II.5.1. Fluid inclusion types</i>	<i>53</i>
<i>II.5.2. Distribution of the fluid inclusions: relative timing of fluid entrapment.....</i>	<i>57</i>
<i>II.6. Microthermometric data and Raman results.....</i>	<i>61</i>
<i>II.7. Density, molar volume calculations and minimum pressure – temperature estimations</i>	<i>65</i>
<i>II.8. LA-ICPMS microanalytical results: element concentrations in the fluids.....</i>	<i>69</i>
<i>II.9. Interpretation and discussion.....</i>	<i>75</i>
<i>II.9.1. Representativeness of the fluid inclusions and postentrapment modifications</i>	<i>75</i>
<i>II.9.2. Intermediate density deep fluid and phase separation</i>	<i>76</i>
<i>II.9.3. Did the sulfides and gold precipitated during the quartz dissolution?</i>	<i>81</i>
<i>II.9.4. Pressure and temperature formation conditions of the fluids.....</i>	<i>82</i>
<i>II.9.5. Fluid and metal source: magmatic vs. metamorphic origin.....</i>	<i>84</i>
<i>II.9.6. Fluid chemistry and ore deposition.....</i>	<i>90</i>

II.9.7. <i>Conclusions: Fluid evolution scenario with deep single phase fluid input, phase separation and ore deposition</i>	94
Chapter III: Albitite related to magnetite deposits: melt inclusion evidence for a magmatic origin and its role in the genesis of the hydrothermal mineralization	97
<i>Abstract</i>	97
III.1. <i>Introduction</i>	98
III.2. <i>Geological setting: the Valuengo area and the associated mineralization</i>	101
III.3. <i>Sampling and Methods</i>	120
III.4. <i>Results I: The albitite problem</i>	136
III.4.1. <i>Petrography of melt inclusions</i>	136
III.4.2. <i>Data evaluation: representativeness of the melt inclusions</i>	139
III.4.3. <i>Bulk rock and SMI compositions: a comparison</i>	143
III.4.4. <i>Heterogeneous entrapment of immiscible phases?</i>	153
III.4.5. <i>Preliminary Sr-Nd-Pb isotopic data</i>	157
III.5. <i>Results II: Fluid inclusion study in the La Berrona deposit</i>	159
III.5.1. <i>Fluid inclusion characteristics and SEM-Cathodoluminescence images</i>	159
III.5. 2. <i>LA-ICPMS analysis of the fluid inclusions</i>	165
III.6. <i>Discussion</i>	167
III.6.1. <i>Distinguishing albitites: a metasomatic vs. a magmatic origin</i>	167
III.6.2. <i>Source and evolution of the magmatic albitite</i>	176
III.6.3. <i>Silicate melt – iron oxide immiscibility</i>	183
III.6.4. <i>The early magmatic-hydrothermal stage in IOCG systems: insights from the La Berrona deposit</i>	190
III.6.5. <i>Proposed genetic model for the albitite and the magnetite mineralization of the La Berrona area</i>	194
III.7. <i>Conclusions</i>	197
Chapter IV: Final Conclusions	200
References	205
Appendix IA: SEM-CL analysis of hydrothermal quartz: Case histories in magnetite – (±Cu-±Au) deposits	231
Appendix IB: Preliminary characterization of the hydrothermal fluids related to the magnetite-copper deposit of Cala (Huelva, SW Spain)	239
Appendices II (tables in the excel file):	246

Resumen

La Zona de Ossa Morena (ZOM), situada en el suroeste de España, representa una de las áreas geológicas más complejas y mejor estudiadas del cinturón Varisco europeo. Esta complejidad deriva de la evolución tectónica heterogénea que ha registrado la ZOM desde la orogenia Cadomiense (Neoproterozoico – Cámbrico temprano) hasta la orogenia Varisca (Paleozoico tardío). La ZOM se caracteriza por una gran variedad de depósitos minerales relacionados tanto con ambas orogenias como con la etapa de rifting que tuvo lugar durante el Cámbrico temprano y el Ordovícico medio. Los depósitos de óxidos de Fe, Cu-Au y Ni-Cu situados a lo largo del Cinturón de Olivenza-Monesterio (COM, estructura anticlinal situada en la parte central de la ZOM) son de particular importancia e interés por su origen controvertido. Este estudio está enfocado en tres áreas dentro del COM que representan problemas metalogénicos bien definidos: el filón de Cu-Au de la mina Sultana, el depósito de magnetita de La Berrona y la albitita del área de Valuengo, asociada al depósito de La Berrona.

La mineralización de Cu-Au de Sultana se sitúa al sureste del COM y consiste en venas o filones de cuarzo y anquerita encajadas en el Stock Varisco de Sultana así como en las pizarras negras y metagrauvacas Precámbricas de la Serie Negra. La mineralización se compone principalmente de calcopirita, bismutinita y maldonita y desarrolla una alteración sericitica en la roca de caja. Por su parte, el depósito de La Berrona es un cuerpo epigenético de forma cilíndrica encajado en el granito albítico del mismo nombre así como en las calizas de edad Cámbrico temprano y medio de la formación Malcocinado. La mineralización es de tipo remplazante con desarrollo de brechas y stockwork en la parte alta de la intrusión albítica. Esta albitita forma parte de las albititas Cámbricas del área de Valuengo situadas en la parte central del COM, y como La Berrona, algunas de ellas están

asociadas a depósitos de magnetita. La roca presenta una textura porfirítica con predominancia de plagioclasa albita e intruye las calizas, pizarras y corneanas calcosilicatadas del Cámbrico temprano-medio así como las pizarras negras Precámbricas de la Serie Negra.

Los objetivos principales de esta tesis son (1) caracterizar los fluidos e investigar las causas de la precipitación del Cu y el Au en el yacimiento de Sultana, (2) investigar la formación del stock albítico de La Berrona así como su origen magmático o hidrotermal, y (3) caracterizar la evolución magmático-hidrotermal del depósito de magnetita de La Berrona, desde la intrusión del stock albítico hasta el depósito de los metales. Para alcanzar estos objetivos se ha llevado a cabo un estudio detallado de inclusiones fluidas y vítreas mediante su caracterización petrográfica y microtermométrica, combinado con análisis de catodoluminiscencia por microscopio electrónico de barrido (SEM-CL), ablación láser con espectrometría de masas con fuente de plasma de acoplamiento inductivo (LA-ICPMS) y espectroscopía Raman. Además, se han realizado isótopos estables de S e isótopos radiogénicos de Sr-Nd-Pb para confirmar las hipótesis establecidas mediante las inclusiones fluidas y vítreas.

Las imágenes de SEM-CL del filón de Cu y Au de Sultana revelan al menos tres generaciones de cuarzo sugiriendo un relleno polifásico con procesos de disolución y precipitación en espacios abiertos y fracturas. El estudio detallado de inclusiones fluidas combinado con las imágenes de catodoluminiscencia indica que un fluido de baja salinidad (<4 to 15 wt % NaCl eq; promedio de 5 wt % NaCl eq.) con contenidos bajos en CO₂ (10.4 mol %), densidad intermedia y alta concentración en metales (> 537 µg/g Cu, >539 S µg/g) fue atrapado a presiones estimadas de ~800 bares y temperaturas de más de 420 °C. A continuación, y coincidiendo con el proceso de disolución de la primera generación de cuarzo (Q1), el fluido se separa en dos fases por condensación de una fase minoritaria salina (~ 40 wt % NaCl eq.) y una fase vapor de muy baja salinidad (~ 2.4 wt %

NaCl eq.) a una temperatura de alrededor de 350 °C y a 100 – 300 bares de presión. Ambas fases transportan los metales de cobre y posiblemente oro ($335 \pm 123 \mu\text{g/g}$ Cu, $9.5 \pm 6.6 \mu\text{g/g}$ Au) en el sistema. El sulfuro de cobre precipita en los espacios abiertos generados antes o conjuntamente con la precipitación de la segunda generación de cuarzo (Q2). Esta precipitación se confirma con la concentración de Cu, que desciende drásticamente de $700 \mu\text{g/g}$ en las inclusiones salinas y de vapor a menos de $0.1 \mu\text{g/g}$ en las inclusiones secundarias posteriores a la precipitación de la calcopirita. El oro precipita después en las fracturas cortando la calcopirita, debido probablemente a un exceso de azufre en la fase vapor que transportó el oro tras depositarse el Cu.

El reconocimiento de inclusiones vítreas silicatadas (SMI, silicate melt inclusions) en los fenocristales de cuarzo de la albitita de La Berrona demuestra que esta roca es magmática en origen y que no ha sido formada por procesos metasomáticos como se ha sugerido previamente en la literatura. Estas inclusiones vítreas así como algunos glóbulos de óxidos de hierro (IOB, iron oxide blebs) han sido analizadas mediante ablación laser (LA-ICPMS) para establecer su composición química. Las inclusiones vítreas presentan una composición albitica con SiO_2 ($73.2 \pm 1.9 \text{ wt}\%$), Na_2O ($6.8 \pm 1.1 \text{ wt}\%$), K_2O ($0.1 \pm 0.1 \text{ wt}\%$) y CaO ($0.6 \pm 0.4 \text{ wt}\%$) como elementos mayores. En concordancia con el comportamiento compatible e incompatible de los elementos traza en sistemas magmáticos, elementos como el Ba, Sr, V, Zr, Ni y P son compatibles con la mineralogía de la albitita mientras que otros elementos incompatibles y metales como el Cu, Pb, Zn y Mo permanecen en el fundido representado por las inclusiones vítreas. La comparación de la composición de las inclusiones vítreas silicatadas con composiciones obtenidas en estudios experimentales así como el estudio de isótopos radiogénicos sugieren que el fundido albitico se formó por fusión parcial de rocas de la corteza. Así mismo, es probable que la presencia de agua y flúor en el fundido desviara el eutéctico del sistema haplogranítico hacia composiciones

más ricas en plagioclasa albita. Por otra parte, el análisis preliminar de LA-ICPMS de los glóbulos de óxidos de hierro en los fenocristales de cuarzo indica composiciones ricas en Fe, Ti y P sugiriendo la existencia de una fase fundida de esta composición que fue segregada del fundido silicatado.

La mineralización de La Berrona es incuestionablemente de origen hidrotermal, con desarrollo de brechas y stockwork en las zonas altas de la albitita y remplazamiento de magnetita-actinolita-albita de las calizas encajantes y de la propia albitita. La magnetita de la mineralización presenta bajos contenidos en Ti y P lo que sugiere que los fluidos no interaccionaron con la fase inmisible de óxidos de hierro rica en estos elementos.

Los resultados presentados en esta tesis representan casos prácticos que conllevan las siguientes implicaciones: (1) los sistemas de filones de cobre y oro asociados a intrusiones pueden presentar mecanismos de precipitación y transporte de metales similares a los que operan en los depósitos tipo pórfido cuprífero (como por ejemplo separación de fases, enfriamiento, solubilidad retrógrada del cuarzo, entre otros) y también características típicas de venas mesotermales y depósitos de oro metamórfico como el contexto geológico o la composición de fluidos; (2) la roca albítica, típicamente asociada a depósitos de magnetita, puede ser también de origen magmático y no sólo metasomático como se ha venido sugiriendo en la literatura hasta el momento. Esta roca albítica podría tener así una importancia crítica en la formación de depósitos epígenéticos de magnetita. El origen magmático de esta roca es posiblemente la contribución científica más innovadora de esta tesis ya que abre nuevas líneas de investigación para futuros estudios en el ámbito del origen magmático de rocas félsicas ricas en plagioclasa y también estudios relacionados con exsolución de fundidos y fluidos ricos en óxidos de Fe como mecanismo para formar depósitos de magnetita magmáticos e hidrotermales respectivamente. Finalmente, (3) el tratamiento del estudio de inclusiones fluidas y vítreas como inclusiones atrapadas

sincrónicamente en una asociación (FIA: fluid inclusion assemblage o asociación de inclusiones fluidas) es de importancia crítica para obtener datos geoquímicos fiables y realistas. Igualmente, la combinación del estudio de inclusiones fluidas y vítreas con otras técnicas como LA-ICPMS, imágenes de SEM-CL y espectroscopía Raman se ha revelado como una herramienta muy útil para el estudio del origen de los depósitos minerales.

Summary

The Ossa Morena Zone (OMZ) in the southwest of Spain is one of the most complex and best studied areas in the Variscan Belt, and records a heterogeneous tectonic evolution from the Cadomian (Neoproterozoic - Early Cambrian) to the Variscan orogeny (Late Paleozoic). The OMZ host a wide variety of ore deposits related to both orogenies and a rifting and stable platform event that occurred in the Early Cambrian-Mid Ordovician. Particularly important are the Fe oxide, Cu-Au and Ni-Cu orebodies situated along the Olivenza-Monesterio Belt (OMB), a major Variscan anticlinal structure located in the central part of the OMZ. This study is focused on three areas of the OMB that represent well defined metallogenic problems: the intrusion-related Sultana Cu-Au vein deposit, the La Berrona magnetite deposit and some uncommon albititic rocks from the Valuengo area which are related to the La Berrona deposit.

The Sultana Cu-Au deposit is located in the southeast of the OMB and consists of quartz-ankerite veins that are hosted by the Variscan Sultana Stock and the Precambrian black shale and metagreywacke of the Serie Negra Unit. The ore is mostly composed of chalcopyrite, bismuthinite and maldonite with sericitic alteration of the host rock. The La Berrona deposit is a cylindrical epigenetic magnetite orebody hosted by the La Berrona albitite granite and Early to Mid Cambrian limestone of the Malcocinado Formation. The mineralization is replacive with development of breccias and a stockwork system in the upper parts the albitite intrusion. This albitite forms part of the Cambrian albitite granites from the Valuengo area in the central OMB, some of them associated to magnetite deposits. The albitite shows a porphyritic texture with predominance of albite plagioclase and intrudes the Early to Mid Cambrian limestone and related shale and calc-silicate hornfels as well as the Precambrian black shale of the Serie Negra Unit.

The main goals of this thesis were (1) to characterize the fluids and investigate the causes for the precipitation of Cu and Au at the Sultana deposit, (2)

to investigate how the La Berrona albitite stock formed and if it was of magmatic or metasomatic origin, and (3) to characterize the magmatic-hydrothermal evolution of the La Berrona magnetite deposit, from the albitite host rock formation to the deposition of the ore. To achieve these goals fluid and melt inclusions were characterized by detailed petrography and scanning electron microscope-cathodoluminescence (SEM-CL) imaging, and analyzed by combining analytical techniques including microthermometry, laser ablation inductively coupled plasma mass spectroscopy (LA-ICPMS) analyses, and Raman spectroscopy analyses. In addition, S stable and Sr-Nd-Pb radiogenic isotope studies were undertaken to support hypotheses established on the basis of obtained fluid and melt inclusions data.

The SEM-CL images of quartz in the Sultana vein show three generations of quartz implying a multistage vein filling with dissolution and precipitation into open spaces and fractures. The detailed fluid inclusion study developed in correlation with the quartz textures suggest that a low saline (<4 to 15 wt % NaCl eq; average of 5 wt % NaCl eq.), CO₂-bearing (10.4 mol %) intermediate density fluid with high ore-metal concentration (> 537 µg/g Cu, >539 S µg/g) was trapped at estimated fluid pressures of ~800 bar and >420 °C of temperature. Coinciding with the dissolution of the early generation of quartz (Q1), a phase separation occurred by condensation of minor brine (~ 40 wt % NaCl eq.) and a low saline vapor phase (~ 2.4 wt % NaCl eq.) at ~ 350 °C and 100 - 300 bar, both carrying most of the copper and possibly gold (335 ± 123 µg/g Cu, 9.5 ± 6.6 µg/g Au) into the system. Copper sulfides were precipitated into open spaces before or together with the precipitation of a late generation of quartz (Q2). Consequently, Cu concentrations drop from 700 µg/g to less than 0.1 µg/g in the petrographically distinguished secondary fluid inclusions. Gold was later deposited in fractures cutting chalcopyrite, probably due to the excess of sulfur in the vapor phase that transported gold after Cu precipitation.

The recognition of silicate melt inclusions (SMI) in the quartz phenocrysts of the La Berrona albitite demonstrate that this rock is magmatic in origin, and not formed by metasomatic processes as it has been suggested previously in the literature. The SMI as well as few coexisting iron oxide blebs (IOB) were petrographically characterized and analyzed by LA-ICPMS. Silicate melt inclusions show an albititic composition with SiO₂ (73.2±1.9 wt%), Na₂O (6.8±1.1 wt%), K₂O (0.1±0.1 wt%) and CaO (0.6±0.4 wt%) as major elements. In agreement with the compatible/incompatible behavior of trace elements in magmatic systems, elements such Ba, Sr, V, Zr, Ni and P are compatible with the bulk-mineralogy of the albitite whereas incompatible elements as well as ore metals such as Cu, Pb, Zn, As and Mo stay in the residual melt represented by the SMI. Comparison with experimental studies and isotopic data suggest partial melting of crustal rocks as plausible mechanism to form this albititic melt, with additional fluxing of H₂O and possible presence of F that deviate the eutectic of the haplogranite system to the albite component. The study of the IOB of Fe-Ti-P-rich composition suggests the existence of an iron-titanium-phosphorous oxide melt phase that segregated from the silicate melt.

The La Berrona magnetite mineralization is undoubtedly of hydrothermal origin with development of breccia, a stockwork system and magnetite-albite-actinolite replacement of the host carbonate and the albitite rock. The magnetite in the mineralization is low in Ti and P, suggesting that the fluids did not interact with the immiscible iron-oxide phase rich in these elements.

The results presented in this thesis represent case studies that have the following important implications: (1) the intrusion-related copper-gold vein systems can show similar ore precipitation mechanisms as the porphyry copper deposits (i.e. phase separation, cooling, retrograde solubility of quartz), and also have characteristics of mesothermal and metamorphic ore deposits in terms of geological setting and fluid composition; (2) the albitite related to the magnetite deposits is of magmatic origin and it plays an important role in the epigenetic

magnetite deposit formation. This is perhaps the most innovative contribution of this Ph.D. and opens a new research line for future studies in the magmatic origin of plagioclase rich felsic rocks as well as in studies related to iron oxide fluid/melt exolution as major mechanism for the hydrothermal/magmatic Fe oxide - (Cu - Au) deposit formation respectively; and, (3) the careful treatment of fluid and melt inclusions as coevally existing inclusion assemblages is of critical importance in order to obtain reliable and realistic geochemical data. In addition, the combination of fluid/melt inclusions with other techniques such as LA-ICPMS, SEM-CL imaging and Raman spectroscopy has shown to be a powerful tool for the study of ore deposits.

Agradecimientos

Estos años de tesis han sido un viaje de aprendizaje científico y también personal en el que me han acompañado muchas personas. A todas y cada una de ellas les doy las gracias por compartir su tiempo y experiencias conmigo.

No podría dejar de agradecer en primer lugar a Paco Velasco, profesor de yacimientos minerales de la Universidad del País Vasco, quien confió en mí desde el principio y me animó a iniciarme en el mundo científico que tanto he disfrutado. Gracias Paco, espero que te sientas orgulloso de mí. Gracias a Fernando Tornos, mi supervisor, por abrirme las puertas de esta aventura, por darme la oportunidad de hacer esta tesis con libertad y por soportar a veces mi cabezonería. Espero que también te sientas orgulloso de esta pequeña contribución a la ciencia. El profesor Chris Heinrich ha sido una persona clave a lo largo de este viaje sin el cual no hubiera sido posible su buen término. Sus ideas siempre fueron el punto de partida de todos los aciertos de esta tesis. Gracias Chris por tus consejos, tu hospitalidad, tus ánimos y por decir que sí cada vez que te preguntaba si podría quedarme unos meses más en Zúrich. Además de en el ETH de Zúrich, he tenido la gran suerte de realizar otra estancia en la Universidad de Ginebra junto al profesor Lluís Fontboté que me "adoptó" después tan generosamente para poder terminar de escribir allí. Gracias Lluís, por permitirme participar en todo como una más y por ese contrato que salvó mi dignidad. No sólo sois grandes científicos sino también excelentes personas.

De mi época en las oficinas del IGME en Salamanca guardo muy buenos recuerdos. Gracias a Pedro, Emilio, Alejandro, Ícaro, Dulce, Santos y Mery Joe por los buenos momentos. Gracias especiales a Ramón Vicente que es el mejor haciendo su trabajo y también muy buena gente (¡lo conseguí Ramón!). A Jorge Carriedo, porque cuando yo empecé él ya tenía el camino de este proyecto abierto y me enseñó todo lo necesario sobre Cala (cuántos dolores de cabeza nos sigue causando!), Colmenar, la Berrona y Sultana. Gracias Jorgillo!. A Nieves, que llegó con su vitalidad y su aire fresco para animarnos a todos (ánimo pinsesa!!). A Maura Durán, porque, con un poco de yoga y meditación, los sueños se hacen realidad (me alegro de haber formado parte del tuyo Maura, SatNam!).

Mi larga estancia en el ETH de Zúrich ha sido una de las experiencias más bonitas e intensas de mi vida. Todas las personas del grupo de "Minerales y Fluidos" me trataron como una más desde el día que llegué y me enseñaron el verdadero significado de la "excelencia científica". Gracias especiales a Ingo (por decirme un día: Cris, calla y trabaja!) y a Maike, ¡gracias por continuar siendo mis amigos en la distancia!. Gracias también a Tobi por las cervezas de los jueves! A Markus Wälle también le doy las gracias por esos momentos emocionantes y desesperantes al mismo tiempo en el LA-ICPMS y a Jun Hung Seo por ayudarme siempre que me atasqué reduciendo e interpretando datos de LA-ICPMS.

Llegué a Ginebra para quedarme cinco meses y es aquí donde termina este viaje. Muchas gracias a todos, especialmente a Marie Caroline (parce que tu est genial et jamais

perds ta sourise!), Anita and Steph (mercie beaucoup mes petites colloques!), Aldo por su buen humor y amistad, Stefano (y los momentos "Nutella"), Edina (y el pequeño Deszu que aprenderá euskera), Jorren (ups!), Mariel, Roelant, Carol, Lina, Honza y todos los demás. En esta época también conocí (nunca en persona) a Berto Pena, que me hizo ser productiva cuando más lo necesité.

Quiero también agradecer a todos y cada uno de los autores de las referencias de esta tesis, porque este trabajo está hecho de pedacitos del suyo. Gracias especiales a César Casquet y a Chris Heinrich por haber aceptado ser los revisores de la tesis pese a sus agendas apretadas. Mi agradecimiento también para el Ministerio de Ciencia y Tecnología de España y al Instituto Geológico y Minero de España por el soporte económico y logístico. Espero que los políticos nunca olviden que ahora más que nunca en España, "la educación es la más sólida inversión de futuro" (Manolito y Mafalda).

Finalmente...mi última parada... San Sebastián. Muchas gracias a Ana, por estar siempre cerca de mí pese a la distancia ¡lo conseguí por fin Ana! Maria Victoria, te doy las gracias por tus palabras que siempre me reconfortan, y por todo lo que me has enseñado sobre arte, filosofía y la vida (Muito obrigada!!).

Gracias a ti Johannes, porque me has apoyado día a día, me has escuchado, y me has levantado cada vez que me he caído. Danke dass Du bei mir geblieben bist, seit diesem Abend auf der Magnetic Island!!

Esta tesis está enteramente dedicada a mi madre, Consuelo Tomé Sánchez y a mi hermana, Vanesa Tomé, .porque sobran todas las palabras y queda todo el cariño. Gracias de verdad por vuestro apoyo incondicional, vuestros ánimos, las risas y todo lo que ya sabéis. Sois unas luchadoras.

¡Nos vemos en Menorca! Ginebra, 27 de Junio del 2012.

Acknowledgements

These years of thesis have represented a not only scientific but also personal learning journey along which many persons have walked with me. To all of them, thanks for sharing your time and experiences with me.

First and above all, I am grateful to Paco Velasco, Professor of Ore Deposits at the University of Basque Country who trusted on me since the beginning and encouraged me to continue in this scientific world that I have enjoyed so much. Thanks Paco, I hope you feel a bit proud of me. I am also grateful to Fernando Tornos, my supervisor, for opening me the doors of this adventure, giving me the opportunity of developing this thesis with freedom and for standing my stubbornness. I hope you also feel proud of this little contribution to science. The Professor Chris Heinrich from the ETH in Zurich has been a key person for the good ending of this project. His great ideas were always the starting points of all the successes of this thesis. Many thanks Chris for your good advises, your hospitality, your encouragements and for saying “yes” every time I asked you if I could stay a “little more” in the ETH. Besides Zurich, I also had the good luck of spend “few” months working at the University of Geneva with the Professor Lluís Fontboté who “adopted” me and allowed me to stay after the official internship. Thank you Lluís for having considered me as part of the group and for the contract that saved my dignity. During these years I have learnt that being brilliant in any kind of matter always goes hand in hand with being a good person.

From my time in the beautiful Salamanca I have very good memories. I am grateful to my colleagues from the IGME, Pedro, Emilio, Alejandro, Ícaro, Santos and Mary Jou for all the good moments. Special thanks go to Ramón who is the best doing his job and also a great person (¡lo conseguí Ramón!). Thanks to Jorge Carriedo because when I started, he already had opened the path of this project and he taught me all he knew about Cala (how much headache continues causing us Cala!), Colmenar, la Berrona and Sultana. Thanks Jorgillo! Thanks also to Nieves, who came with her vitality and fresh air to cheer us up (ánimo pinsesa!). I will always be grateful to Maura Durán, because, with a little bit of yoga and meditation, all the dreams become true (and I am happy to have been part of yours Maura, Sat Nam!).

My long stay at the ETH in Zurich has been one of the most beautiful and intense experiences in my life. All the people from the “Fluids and Mineral deposits” group considered me as part of the group from the beginning and they showed me what really means “scientific excellence”. Special thanks go to Ingo (for telling me one day: “Cris, shut up and work!), and to Maïke, thank you both for continue being my friends in the distance!. Thanks also to Tobi for the “Thursday-beers” in the ETH bar! I am also very grateful to Markus Wälle for those exciting-depressing moments in the LA-ICPMS lab (including the black holes) and Jun Hung Seo for helping me every time I had some problems reducing and interpreting the LA-ICPMS data.

I came to Geneva for a five months internship and it is here were this journey ends. Special thanks go to Marie Caroline (parce que tu est genial et jamais perds ta

sourise!!...), Anita and Steph (mercie beaucoup mes petites colloques!), Aldo (for his great sense of humor and friendship), Stefano (for the “Nutella moments...”), Edina (and the little Deszö), Jorren (ups!), Andrea, Julie, Aurelio, Mariel, Roelant, Carol, Lina, Honza and all the rest. At this time, I also met (not personally) Berto Pena who helped me to be productive when I more needed it.

I would like to acknowledge to all the authors of the references of this thesis because this work has been done with little pieces of their work. Special thanks to César Casquet and Chris Heinrich for reviewing this thesis despite their tight agenda. I am grateful also to the Spanish Ministry of Science (MICINN) and the Geological Survey of Spain (IGME), for the economic and logistic support. I hope that the politicians don't forget that now more than ever in Spain, “education is the most solid inversion for the future” (Manolito and Mafalda).

Finally... the last stop... San Sebastián. Thank you Ana for being always close to me despite the distance ¡por fin lo conseguí Ana! Maria Victoria,: thank you for your words that always comfort me and for everything you taught me about philosophy, arts and life (Muito obrigada!).

I will be always very grateful to Johannes, because you supported me day after day, you have listened me, and have stood me up every time I have fallen down. Danke dass Du bei mir geblieben bist, seit diesem Abend auf der Magnetic Island.

Now yes, this thesis is entirely dedicated to my mother, Consuelo Tomé Sánchez and my sister, Vanessa Tomé, because words aren't needed to express how much I love you. Thanks for your unconditional support, the good times and everything we already know. You are real fighters!

See you in Menorca! Geneva, 27th of June 2012

Introduction

Approach

The complex geology and geotectonic situation of the Ossa Morena Zone (OMZ) in the southwest of Spain make it one of the most interesting and best studied areas of the European Variscan Belt. In fact, the OMZ is the only terrane of the Iberian Peninsula that records a polyorogenic tectonic evolution including both the Cadomian (Precambrian - Early Cambrian) and Variscan (Late Paleozoic) orogenies.

Reflecting this geological complexity, the OMZ hosts a wide variety of ore deposits that are related to both orogenies and to the rifting and stable platform stages in between. At present, only one deposit is being mined (the Aguablanca magmatic Ni-Cu mine) but many other prospects are under exploration for Fe-Cu-Au, Sn, and Cu-Ni. Particularly interesting are the magnetite (sometimes Cu-Au-rich) deposits that are located along the Olivenza-Monesterio Belt (OMB, Tornos and Casquet, 2005) in the central part of the OMZ. The origin of these deposits is controversial as many of them can be interpreted as volcanosedimentary, skarn, shear-zone related or of replacive type. Tornos and Casquet (2005) defined some of these magnetite deposits as belonging to the IOCG (Iron Oxide – Copper Gold) type as they share similarities in the structural position, hydrothermal alteration, geochemistry and mineral assemblage with this style of mineralization. The magnetite mineralization is sometimes related to Cambrian albitite which is an uncommon rock type found as large and well exposed outcrops in the area. Furthermore, the Variscan calc-alkaline diorite to monzogranite Santa Olalla Plutonic Complex in the southernmost Olivenza-Monesterio Belt is associated with different styles of mineralization, including the skarn and shear-zone related Fe-(Cu) Cala deposit, the intrusion-related Cu-Au Sultana vein system and the Aguablanca Ni-Cu deposit, the latest associated to more mafic rocks.

There are several studies dealing with these intrusion-related magnetite and Cu-Au deposits of the OMB, including those of Casquet and Velasco (1978), Casquet (1980), Velasco and Amigó (1981), Tornos et al. (2002, 2004), Tornos and Chiaradia (2004), Tornos and Casquet (2005), Carriedo et al. (2010) and Carriedo and Tornos (2010). However, little is known about the origin, evolution and characteristics of the fluids related to the ore as well as the ore forming mechanisms.

Melt inclusions represent small portions of melt trapped during the growth of the host crystal while the magma was crystallizing. They provide useful information on the evolution of magmatic systems, such as the melt composition (including the water and volatile content), or the pressure and temperature of crystallization (Anderson and Brown, 1993; Sobolev and Shimizu, 1993; Wallace et al., 1995; Sobolev and Chaussidon, 1996; Hauri et al., 2002).

On the other hand, fluid inclusions have trapped fluids circulating through the hydrothermal systems recording the pressure-temperature-composition (P-T-X) conditions of the ancient hydrothermal fluids. Precipitation of metals-bearing minerals from the fluids is triggered by several physicochemical mechanisms like cooling, decompression, fluid rock interaction, boiling/unmixing and fluid mixing (e.g. Seward and Barnes, 1997).

In the last years, the new analytical developments allow the combination of conventional fluid and melt inclusion studies with SEM-cathodoluminescence (SEM-CL), laser ablation – inductively coupled plasma mass spectrometry (LA-ICPMS), and Raman spectroscopy techniques, and provide new methodologies for a better understanding of the specific ore-forming processes in magmatic-hydrothermal deposits. This has been in part possible thanks to the new fluid and melt inclusion concept treatment, i.e., the fluid inclusion assemblages (FIA, Goldstein and Reynolds, 1994) that should be studied as petrographically coeval groups of inclusions rather than as statistical accumulations of isolated fluid inclusions.

In this thesis, I deal with these concepts focusing the study in three areas that represent three different unresolved questions, i.e. the Sultana vein deposit, the La Berrona albite granite and the La Berrona magnetite deposit.

Evolution and objectives

The Sultana vein deposit, the La Berrona albite granite and its hosting La Berrona magnetite deposit represent three controversial and well defined problems in the metallogeny of the Ossa Morena Zone. On one hand, the Sultana Cu-Au deposit is an example of lode gold deposit with an unusual ore assemblage in which copper sulfides are very abundant. The vein is hosted by a granitic intrusion that is in turn hosted by metamorphic shales and hence, both the magmatic and metamorphic origins for the fluids and the mineralization have to be considered. Indeed, these sources are the most commonly addressed fluid and metal origins in the literature of lode gold deposits without having reached a general consensus. In Sultana, the vein filling has not been affected by shearing or late deformation processes as in most of the lode gold deposits, which has favored the preservation of the fluid inclusion assemblages.

On the other hand, the albite granite and the magnetite mineralization from the La Berrona are also examined. In the first case the albite granite represents a well mapped and exposed body with minor alteration and thus, it exemplifies an excellent natural laboratory to study the controversial magmatic-metasomatic origin of this unusual rock. In addition, the discovery of well preserved silicate melt inclusions for the first time in the literature of albite granites has allowed the detailed characterization of the La Berrona body origin. Finally, the albite granite-hosted La Berrona magnetite deposit has become subject of interest in the recent years due to its similarities with the world class Iron Oxide Copper Gold deposits (IOCG). Common characteristics are the replacive magnetite mineralization, the low sulfide content and the sodic alteration among others.

Therefore, the main objectives of this Ph.D. thesis are:

1. Understand the mechanisms and controls of Cu and Au transport and precipitation at the Sultana vein, as well as the origin of the ore-forming fluids.

Furthermore, compare the observed fluid evolution with that of other Cu-Au-bearing deposits such as orogenic gold, intrusion-related gold or porphyry copper systems.

2. Study and establish the origin of the large albitite bodies in the Valuengo area, with special attention to the La Berrona Stock, discussing their role in the formation of the adjacent magnetite mineralization.

3. Study the geology, mineralogy, hydrothermal alteration and crosscutting relationships in the magnetite La Berrona deposit in order to establish the fluid evolution as a continuum from early magmatic to late hydrothermal stages.

In order to achieve these objectives, fluid and melt inclusion studies are applied combined with the LA-ICPMS, Raman and SEM-CL techniques supported by isotopic and geochemical analyses as well as by field observations.

Organization of this thesis

This thesis is organized in four chapters. The first chapter includes a review of the regional geology and the styles of mineralization in the OMZ. It is mostly based on already published work but also includes personal field observations made before and during this thesis. The chapter is focused on the work carried out in collaboration with Jorge Carriedo (thesis in progress), since both Ph.D. thesis were organized for being elaborated synchronously. Some of the data and ideas presented here come from this joint work.

The second chapter is focused on the fluid evolution of the intrusion-related Sultana Cu-Au vein deposit. After a geological and geochemical review, the fluid evolution within the vein is reconstructed, based on a detailed fluid inclusion study.

A combination of fluid inclusion petrography, SEM-CL imaging, microthermometry, LA-ICPMS, and Raman spectroscopy is applied to unravel the fluid evolution history of the vein-type mineralization and specific ore forming processes. We also examine the role of the dominantly magmatic and metamorphic fluids and discuss the results with those of similar Cu-Au deposits.

The third chapter includes the most innovative part of this Ph.D. where melt inclusions found in the magnetite-related albitite are used to understand the origin of this rock. Silicate melt inclusions (SMI) are studied by conventional petrography, followed by high-temperature microthermometry and LA-ICPMS analysis. Iron oxide blebs (IOB) are found together with the melt inclusions and are interpreted as evidence for the existence of an iron-titanium-phosphorous melt that was segregated from the parental silicate melt. In conjunction with this third chapter, the geological and geochemical characterization of the La Berrona magnetite deposit is shown, including a petrographic characterization of the main lithologies and the orebody. An *in situ* detailed mapping of the relationships between different generations of veins allows establishing a chronology of the different fluid inclusion assemblages and the evolution of the fluids in the magmatic-hydrothermal system.

The fourth chapter includes an overview and general conclusions of the previous chapters.

Two minor studies developed during this thesis are shown in the Appendices. The Appendix IA shows a summary and interpretation of several SEM-CL quartz textures found in five different ore deposits, i.e. Sultana, Cala and La Berrona in the OMZ and Mina Silvita and Taltal in the Central Andes (N Chile). The Appendix IB deals with a preliminary fluid inclusion study of the magnetite-copper deposit of Cala, also situated in the OMB.

Grants and laboratory visits in Bilbao, Zurich and Geneva

Three extended laboratory visits to the University of Basque Country, ETH Zurich, and the University Geneva were financed by the FPI (Formación de Personal Investigador) research grant (BES-2007-16232) of the Science and Innovation Ministry of Spain, which also covered the salary during the four years at the Instituto Geológico y Minero de España (IGME). The aim of the internships is to collaborate with other scientific groups in order to improve the development of the Ph.D. projects.

A four month internship was first developed in the Universidad del País Vasco (March 2008 – July 2008) under the supervision of the Professor Francisco Velasco.

The development of the fluid and melt inclusion study, LA-ICPMS and Raman analysis as well as the acquisition of the knowledge necessary for their interpretation would have not been possible without a 10 months exchange (September 2009-April 2010 and September 2010-December 2010) at the ETH in Zürich under the supervision of the Professor Christoph A. Heinrich. He and the Fluids and Mineral Resources group provided the necessary skills to use these techniques and free access to the laboratories. The LA-ICPMS equipment at the ETH is currently managed by Markus Wälle and is a world class LA-ICPMS laboratory for single fluid inclusion analyses, with very good accuracy even for “problematic” elements such as gold and sulfur.

Finally, a five month internship was also granted at the Université de Genève in Geneva where isotope analyses (sulfur stable isotopes in the sulfides and Sr/Nd and Pb radiogenic isotopes in the albitite) have been performed under the supervision of the Professor Lluís Fontboté.

Chapter I: Regional geology and metallogeny of the Ossa Morena Zone: a review

I.1. Introduction

The Ossa Morena Zone (OMZ) constitutes one of the southernmost terranes of the European Variscan Belt and is one of the few areas in the Iberian Peninsula where there are evidences of polyorogenic deformation, magmatism and metamorphism. It represents one of the major divisions of the Iberian Massif established by Julivert et al. (1974) and is located between the Central Iberian Zone (CIZ) and the South Portuguese Zone (SPZ) (Fig.1).

Geographically, it covers an area of around 300x150 km², extending from Portugal at the WNW to the Guadalquivir basin at the ESE. Due to its tectonic complexity and variety of lithologies the OMZ has been subject of major interest and discussion with abundant studies related to different geological disciplines.

The OMZ hosts a wide variety and abundance of ore deposits with more than 650 occurrences, according to Tornos et al. (2004). Most of them were formed during the Cadomian and the Variscan orogenies as well as the Cambrian-Ordovician rifting event in between. The most dominant ore deposit styles include volcanogenic and sediment-hosted massive sulfides, barite and Zn-Pb SEDEX, iron oxide stratabound mineralization, Fe-rich skarns and IOCG-like replacements, magmatic Ni-(Cu) breccias, Cu-(Au-Bi) veins, W-Sn greisens and veins, orogenic gold deposits and base metal-rich quartz veins with accessory Hg replacements. Detailed studies dealing with the regional metallogeny of the Ossa Morena Zone are those of Locutura et al. (1990), Tornos and Chiaradia (2004) and Tornos et al. (2004).

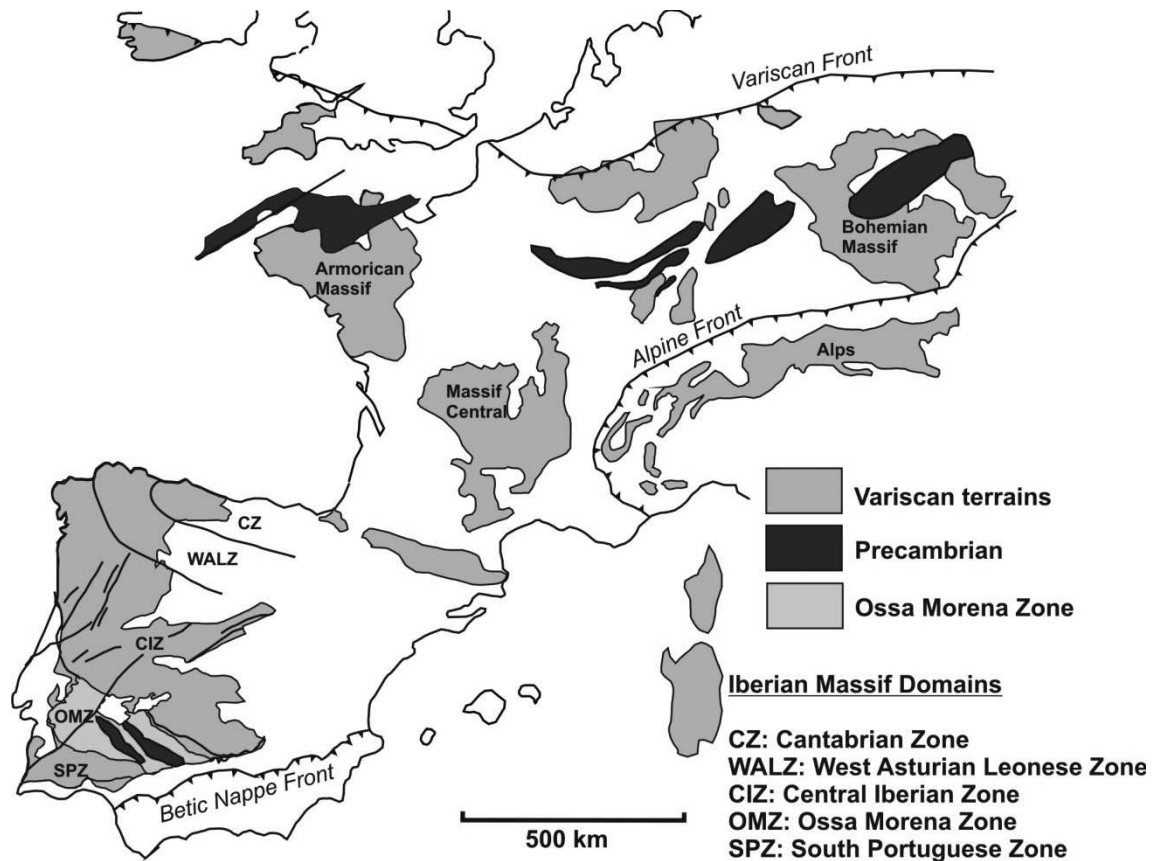


Figure 1. Distribution of the Variscan terranes and zonal divisions of the Iberian Massif established by Julivert et al. (1974). The Ossa Morena Zone (OMZ) is located between the South Portuguese Zone (SPZ) and the Central Iberian Zone (CIZ). Modified after Eguíluz et al. (2000).

I.2. Tectonic evolution of the Ossa Morena Zone: from the Cadomian to the Variscan orogenies

The OMZ is the result of a complex tectonic evolution involving the superposition of two major orogenies (Cadomian in the Neoproterozoic and Variscan in the Mesozoic), both including widespread magmatism and variable metamorphism. This tectonic complexity is reflected by the different interpretations given by the authors working in the area who still continue hypothesizing on the relative effects of both orogenies in the OMZ. In brief, the most accepted setting for the Ossa Morena Zone includes the superposition of two Andean-like continental

margins and related magmatism, with subduction, oceanic destruction and further continent-continent collision (Sánchez Carretero et al., 1990; Murphy and Nance, 1991; Martínez Poyatos, 1997; Eguíluz et al., 2000; Fernández-Suárez et al., 2000; Pin et al., 2002).

During the Neoproterozoic - Early Cambrian Cadomian orogeny, the OMZ represented a continental arc that was accreted to the passive margin of the Autochthonous Iberian Terrane (current Central Iberian Zone or CIZ) which was in turn part of the northern Gondwana continent (Quesada, 1990; Ábalos, 1991; Eguíluz et al., 2000; Bandrés et al., 2002, 2004). This episode produced a tectonic amalgamation that led to the Armorican terrane assemblage (Murphy et al., 1989; Fernández Suárez et al., 2000; Stampfli et al., 2002; Gutiérrez Alonso et al., 2003; Etxebarria et al., 2006). Prior to the second Variscan orogenic event, a Cambrian - Ordovician rifting stage was developed in the OMZ with development of oceanic crust (the Rheic ocean) and production of intense bimodal magmatism. Due to this extensional stage, a fragment of the OMZ left from the Gondwana margin (part of Avalonian?) while the rest of the OMZ continued being part of the Iberian Terrane (Sánchez-García et al., 2008). The rifting stage was followed by a passive margin stage during the Late Ordovician and Early Devonian related to the evolution of the Rheic ocean. (Sánchez Carretero et al., 1990; Eguíluz et al., 2000; Sánchez-García et al., 2003, 2008, 2010). During the Late Paleozoic Variscan orogeny, the OMZ hosted a second magmatic arc related to the likely northward subduction of the Rheic oceanic crust and oblique collision during the amalgamation of Pangea. During the consequent rifting in the Mesozoic with subsequent opening of the Tethys, an exotic terrane nowadays represented by the South Portuguese Zone (SPZ) was attached to the OMZ.

The OMZ is bounded by two major transcrustal first order structures, the Badajoz Córdoba Shear Zone at the North and the Southern Iberian Shear Zone at the South, which are interpreted as the crustal sutures limiting the terranes that were accreted during continent-continent collision (Brun and Burg, 1982; Matte,

1986, Crespo Blanc, 1989; Quesada 1991; Ábalos et al., 1991a; Eguíluz et al, 2000; Simancas et al., 2004).

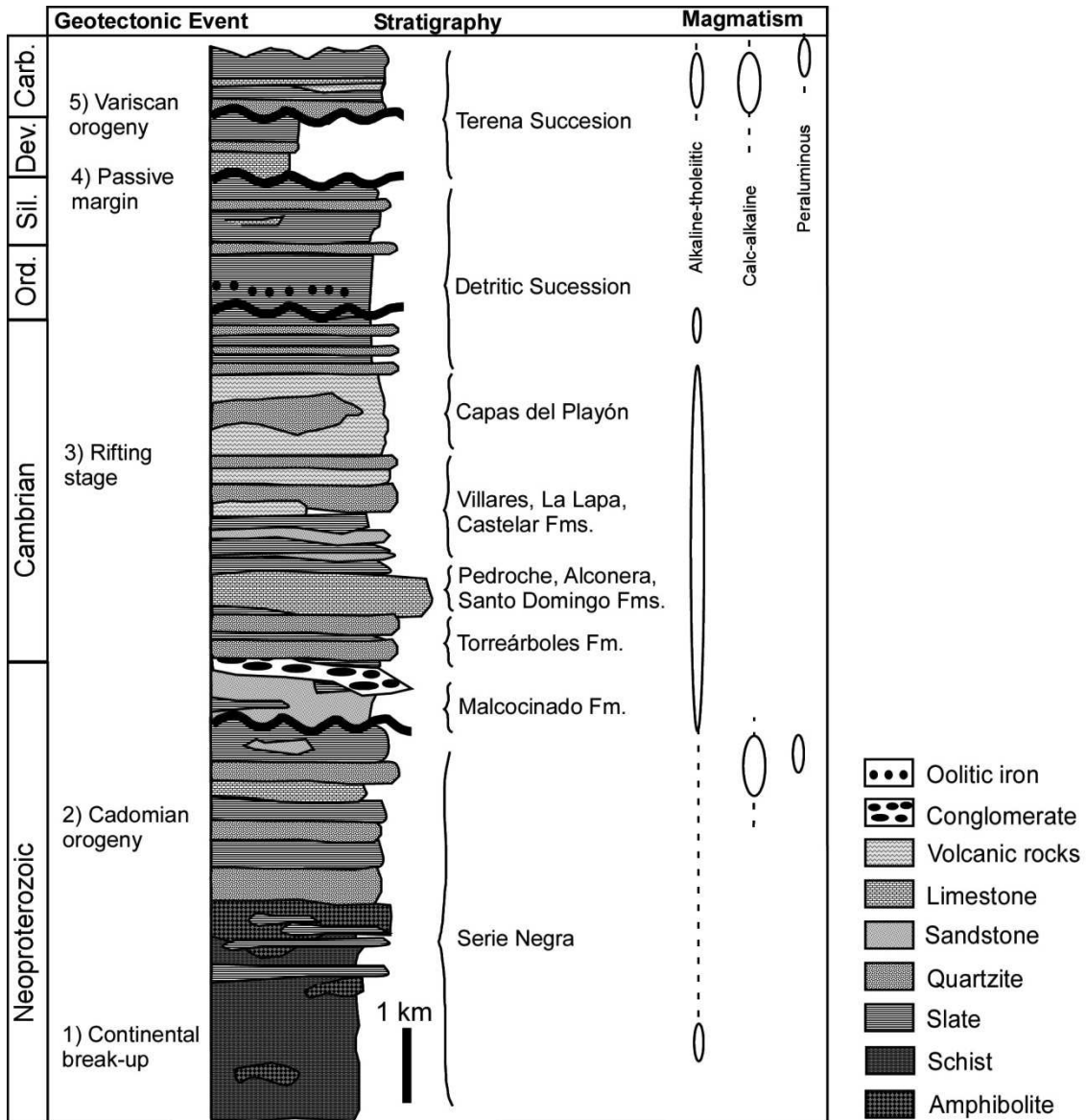
For a more extensive description of the general geology of the OMZ, there are complete reviews in the studies of Apalategui, (1990), Quesada et al. (1991), Eguíluz et al. (2000) and the volumes edited by Martinez and Dallmeyer (1990 - Pre-Mesozoic Geology of Iberia), Casquet (2004 - Journal of Iberian Geology), and Vera (2004 - Geología de España) with the references therein.

I.2.1. The Neoproterozoic Basement

The basement Pre-Cadomian sequence of the OMZ includes the thick Serie Negra Unit, dominated by black shale and metagreywacke with interbedded black quartzite deposited in a passive margin regime (Fig.2). Eguiluz (1987) distinguished two groups of rocks in the Serie Negra Unit: (1) the Montemolín Succession with a monotonous serie of black shale, quartz-schist and amphibolite with intercalation of black quartzite and carbonatic rocks and, (2) the Tentudía Succession with metagreywacke and dark slate and interbedded black quartzite and volcanic rocks. There is not a precise age for the Serie Negra Unit but it is ascribed to the late Neoproterozoic as it is always located below the Cambrian sequence (Azor et al., 2004). According to Galindo and Casquet (2004), Precambrian rocks in the OMZ can be found along three areas: 1) the blastomilonitic corridor to the north of the OMZ, 2) the Olivenza Monesterio Antiform (this study) in the central part and, 3) the Aracena Massif to the south.

Figure 2. Synthetic stratigraphic column of the Ossa Morena Zone and temporal correlation with the main igneous and tectonic events. It consists of: (1) dismembered pre-Cadomian sequences with high grade metamorphic rocks and a thick siliciclastic sequence deposited in a passive margin; (2) backarc to intraarc sequences of late Neoproterozoic-early Cambrian age;

(3) thick volcanosedimentary unit formed during an intracontinental rift phase; (4) passive margin sequence; and, 5) syn-Variscan sedimentary



rocks deposited in restricted basins. Modified after Quesada (1992), Azor et al. (2004) and Tornos and Chiaradia (2004).

I.2.2. The Cadomian Orogeny: Late Neoproterozoic – Early Cambrian

During the Neoproterozoic Cadomian orogeny, the OMZ represented a magmatic arc that was accreted to the Iberian Autochthonous Terrane (northern

Gondwana). The first expression of magmatism in the Neoproterozoic OMZ is located in the Central Unity with very deformed- high to medium grade metamorphic rocks dated at 611 ± 7 Ma (Schafer, 1990). These rocks are related with the rifting episode in the in the beginning of the Cadomian cycle (Apalategui et al., 1985a; Quesada, 1990; Galindo and Casquet, 2004)

The evidences of the existence of the Cadomian orogeny in the architecture of the OMZ are still under controversy as the Variscan deformation has obliterated many of the Cadomian structures. Most authors describe a syn-orogenic volcanic sequence and related epizonal plutonism (the Malcocinado volcanosedimentary Formation and related plutonic rocks (Fig.2); Sánchez Carretero et al., 1989, 1990; Almarza, 1996; Martínez Poyatos, 1997; Pin et al., 1999; Galindo and Casquet, 2004) to this event, synchronous with the development of widespread foliation and low grade metamorphism (Capdevila et al., 1971; Blatrix and Burg, 1981; Eguiluz, 1987; Dallmeyer and Quesada, 1992). These authors also suggest that the Precambrian Serie Negra in the Olivenza Monesterio Antiform recorded two phases of deformation with associated metamorphism that possibly belong to the Cadomian cycle.

However, some authors propose that the tectono-metamorphic fabrics and the metamorphism present in the Precambrian rocks are associated to the Variscan deformation and not to the Cadomian orogeny (i.e. Simancas et al., 2004).

The Malcocinado volcanosedimentary Formation was deposited between the Serie Negra Unit and the Cambrian succession (Fig.2). It is composed by calc-alkaline andesite to rhyolite volcanic rocks interbedded with siliciclastic, carbonatic and volcanoclastic sediments. This sequence is coetaneous with a widespread subvolcanic plutonism that intrudes the Serie Negra Unit (La Bomba, Ahillones, Escribano, Mosquil and Sierra Pedrosa plutons). The Malcocinado Formation is associated to a calc-alkaline magmatism related to the magmatic arc developed above the Cadomian subduction zone (Sánchez Carretero et al., 1989, 1990; Pin et al., 2002).

There is disagreement in the literature about how long lasted the Cadomian cycle in the OMZ. Some authors include the Early Cambrian carbonatic platform sequence as a part of it (Ochner, 1993; Eguiluz et al., 2000; Bandrés et al., 2002) while others support that this sequence represents a transitional period postdating the orogen itself (Quesada, 1991; Giese and Bühn, 1993; Expósito, 2000, Simancas et al., 2004).

I.2.3. The rifting stage: Early Cambrian - Mid Ordovician

After the period of stability with shallow deposition of carbonatic and siliciclastic sediments, a rifting stage took place in the OMZ during the Early Cambrian – Mid Ordovician (Quesada, 1987, 1991, 2006; Liñán and Quesada, 1990; Quesada et al., 1991; Expósito et al., 2003; Simancas et al., 2004). The syn-Cadomian sequence is unconformably overlain by molasse-like sediments (Torreárboles Fm) and shallow marine sediments, including an extensive carbonate platform (Pedroche, Alconera and Santo Domingo Fms) (Fig.2). Sánchez-García et al. (2003, 2008, 2010) have distinguished two periods of magma emplacement during the rifting stage: 1) an Early Igneous Event (EIE) dated at 530 ± 5 Ma, comprised of acid peraluminous rocks with migmatite formation during development of core complex structures and, 2) a Main Igneous Event (MIE) dated between 517 Ma – 502 ± 2 Ma with volcanic, subvolcanic and shallow plutonic rocks that represent a bimodal magmatism with basalt and rhyolite. The EIE is considered to represent the onset of rifting stage in the OMZ. Related to the MIE event, the widespread but localized intrusions of Early Cambrian albitite occur, which are studied in detail in the chapter III of this thesis.

As a result of this extensional event, oceanic crust was formed during the Early Ordovician leading to the opening of the Rheic Ocean to the South, between the current OMZ and the SPZ zones, and of a small ocean between the OMZ and the Iberian terrane to the North along the former Cadomian suture that was also

affected by the rifting stage (Quesada et al., 1994; Sánchez-García et al., 2003, 2008; 2010; Simancas et al., 2004; Azor et al., 2004).

I.2.4. Passive margin phase: Ordovician - Early Devonian

After the rifting stage, a passive margin scenario lasted until the Early-Mid Devonian, when it was disrupted by the early stages of the Variscan Orogeny. Here, shallow marine and siliciclastic sediments were deposited above the Cambrian rift succession in a transgressive environment (the “detritic succession” of the figure. 2) (Robardet and Gutiérrez Marco, 1990; Sánchez-García, 2003; 2008; 2010).

I.2.5. The Variscan orogeny: Mid Devonian - Permian

In a general scale, the collision, subduction, and continental amalgamation of Gondwana derived terranes at the Southeast and Laurasia at the Northwest into the Pangea continent was recorded in the present Western Europe by the Variscan orogeny (Brun and Burg, 1982; Matte, 1986, 2001; Franke, 1989; Shelley and Bossiere, 2000; Stampfli et al., 2002). The Variscan orogeny is the responsible for the present geometrical arrangement of units in the Iberian Massif and in the OMZ itself, as it has been shown in the figures 1 and 4 respectively (Ribeiro et al., 1990; Quesada, 1991, 2006). In the OMZ the Variscan orogeny started in the late Paleozoic with the subduction of oceanic crust beneath the CIZ and the northward oblique subduction of the Rheic ocean under the OMZ (Munhá et al., 1986; Silva, 1990; Quesada, 1991; Quesada et al., 1994; Azor et al., 2004; Ribeiro et al., 2010). After the oceanic crust, the continental crust of the OMZ started to subduct in the early Devonian followed by continental collision with the CIZ. The orogeny continued after the opening of the Tethys and the Atlantic oceans in an extensional phase with oblique collision and coetaneous subduction of the non-Gondwanan continental South Portuguese block beneath the OMZ. This event lasted from the

late Devonian until the late Carboniferous (Fig. 3) (Silva et al., 1990; Ribeiro et al., 1990; Quesada, 1991).

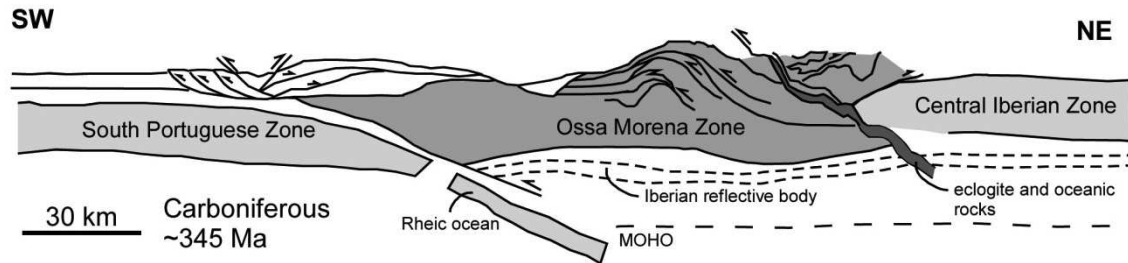


Figure 3. Explanatory cross section of the relationships between the Ossa Morena Zone (OMZ), the Central Iberian Zone (CIZ) and the South Portuguese Zone (SPZ) at the end of the Variscan Orogeny. Modified from Ribeiro et al. (2010) and Azor et al. (2004).

The syn-Variscan sedimentation occurred coinciding with the extensional period between the two compressive episodes of Devonian and Late Carboniferous ages respectively. The Carboniferous sedimentation occurred in two marine basins separated by the emergent terrenes of the OMZ in which continental sedimentation is recorded in small isolated basins (Terena Sucession, Fig.2; Gabaldon et al., 1985; Quesada et al., 1990).

The deformation of the OMZ during the Variscan orogeny was controlled by major structures including SW-verging NW-SE trending ductile shear zones (Azor et al., 1993, 1994) that involved the Cadomian basement (e.g. Monesterio thrust) and large fold nappes, mega folds, and low angle thrusts involving the Paleozoic cover (Quesada et al., 1991). Sinistral subduction and collision also produced superimposed large WNW-ESE strike-slip structures that controlled the present day distribution of lithologies within the OMZ in narrow and long domains which show very different stratigraphy, style of deformation and regional metamorphism (Fig.4). The Variscan regional metamorphism is usually of low grade but there are

some areas, especially those uplifted along the major shear zones such as the Valuengo and the Lora del Rio metamorphic complexes, which show high grade metamorphism with local anatexis (Azor et al., 2004). Related to this transpressional deformation there are extensional zones such as jogs or pull apart zones that were the loci for plutonism.

The Variscan plutonism is widespread in the OMZ and includes calc-alkaline metaluminous intrusive bodies ranging dominantly between gabbro to tonalite and granodiorite (Sanchez Carretero et al., 1990; Casquet, 2004). This plutonism is mainly concentrated in the Olivenza-Monesterio Belt and its southern prolongation, the Santa Olalla Plutonic Complex (Fig. 5).

The Alpine orogeny (Paleogene – Neogene) has probably had only minor influence in the Ossa Morena Zone, with local reactivation of preexisting faults. '

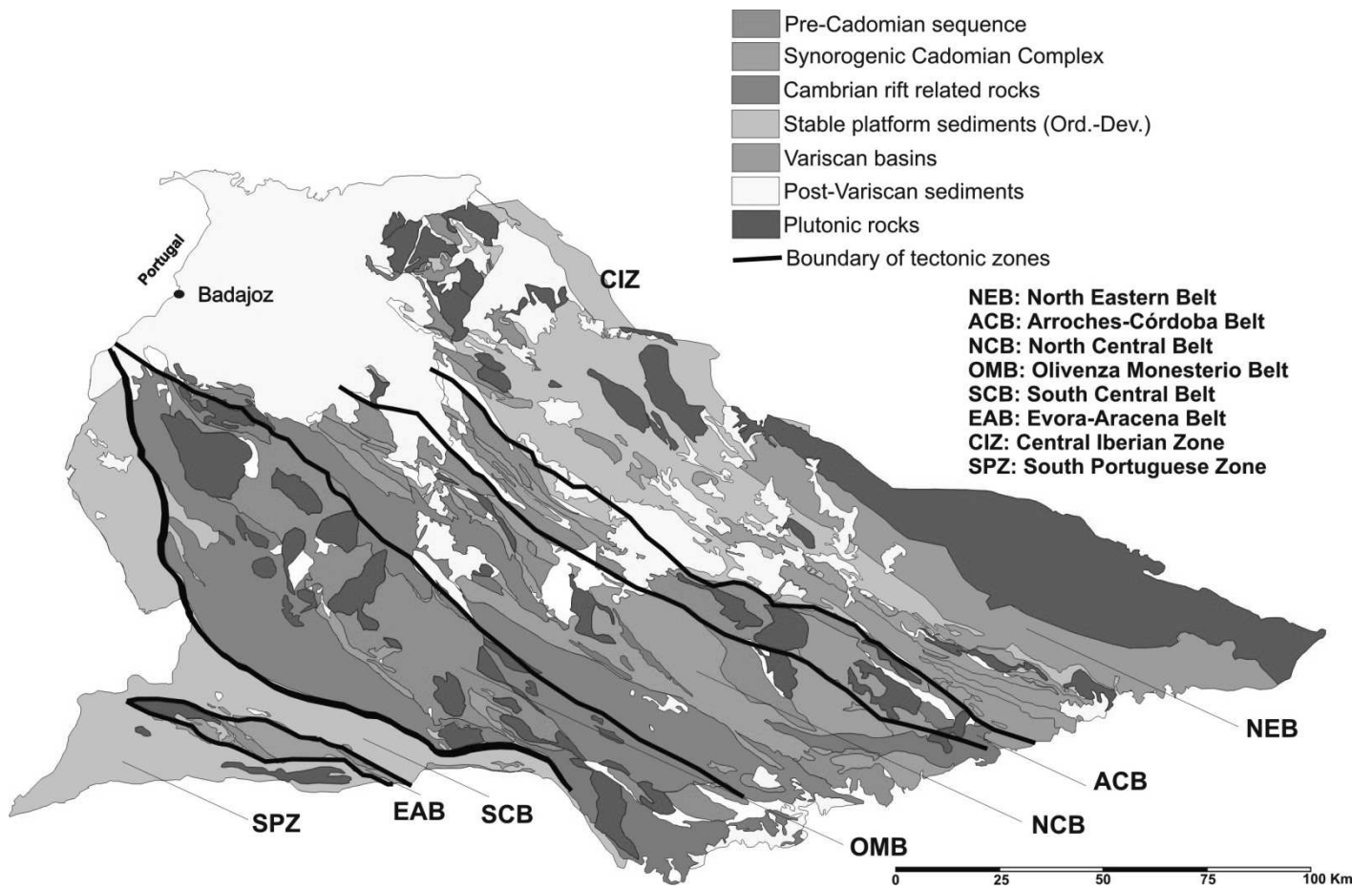


Figure 4. Synthetic geologic map of the Ossa Morena Zone in SW of Spain showing the tectonic zones.

I.3. The Olivenza-Monesterio belt and associated mineralization

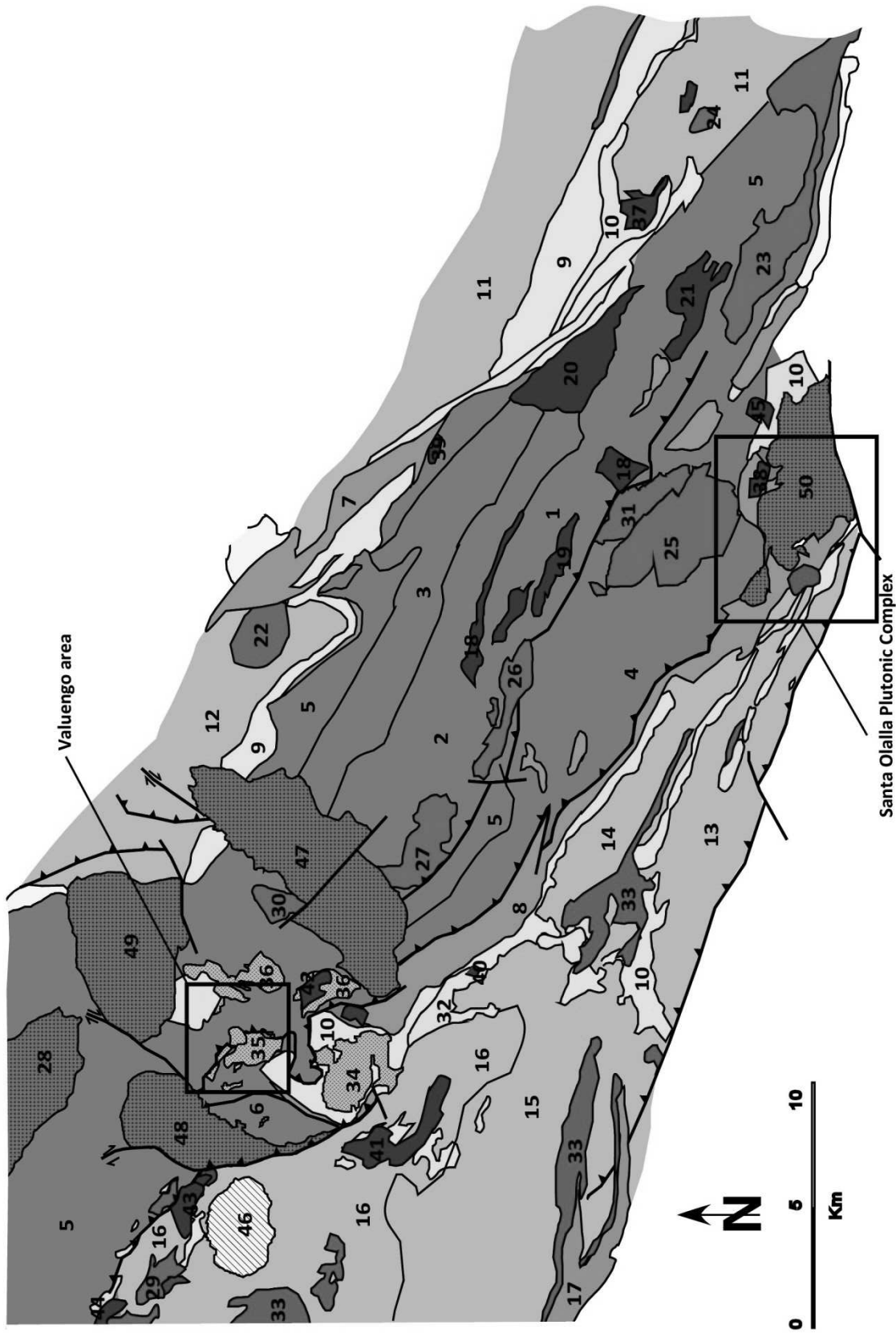
The Ossa Morena Zone has been divided into several tectono-metamorphic belts that are limited by Variscan structures (Oliveira, 1986; Apalategui et al., 1990) and that have different metallogenic characteristics (Fig. 4) (Locutura et al., 1990; Tornos et al., 2004). In this section, the best defined and metallogenetically more significant belt is examined, the so called Olivenza-Monesterio Belt (OMB) (Fig. 5) (Tornos et al., 2004). The OMB corresponds to a major antiformal structure that extends over around 180 km in a NW – SE direction verging to the SW in the central OMZ. The core of this structure is composed of the Precambrian Serie Negra Unit that is overlain by the volcanosedimentary rocks of the Malcocinado Fm and the well exposed Cambrian siliciclastic (Torreárboles Fm.) and carbonatic (Pedroche, Santo Domingo and Alconera Fms.) sediments.

The Olivenza Monesterio Antiform is the result of a first Variscan deformation phase with development of isoclinal folds of E-W direction. A second deformation phase of N60-80E direction refolds the former and they are in turn, refolded by a third phase of N120E direction.

As it is shown in the figure 5, the OMB hosts abundant plutonic rocks of different compositions and ages. Particularly well exposed are the Precambrian Monesterio granodiorite (533±8 Ma to 495±8 Ma, Schäfer, 1990; Ordoñez-Casado, 1998; Ochner, 1990), the pre-Variscan Castillo granite (502±5 Ma to 498±3 Ma, Ochner, 1990; Monero, 2000) and Los Remedios and La Berrona leucogranites (517±2 Ma and 520 Ma, Sánchez-García, 2008 and Carriedo, unpublished respectively), and the Variscan calc-alkaline plutons of the Burguillos del Cerro (338±1.5 Ma, *ref. in* Casquet et al., 2001), Valencia del Ventoso (339 Ma, *ref. in* Salman, 2002), Brovales (340±7, Montero et al., 2000) and the Santa Olalla Plutonic

Complex (341±3 and 347±5, Romeo et al., 2006b and Ordoñez Casado et al., 2008 respectively) (Fig. 5).

One of the key metallogenic features of the OMB is the widespread abundance of iron oxide deposits, with both magnetite and hematite locally accompanied by significant amounts of Cu and Au. Most of them are related to the early Cambrian and Mid Ordovician rift sequence and are hosted by carbonatic and volcanic rocks.



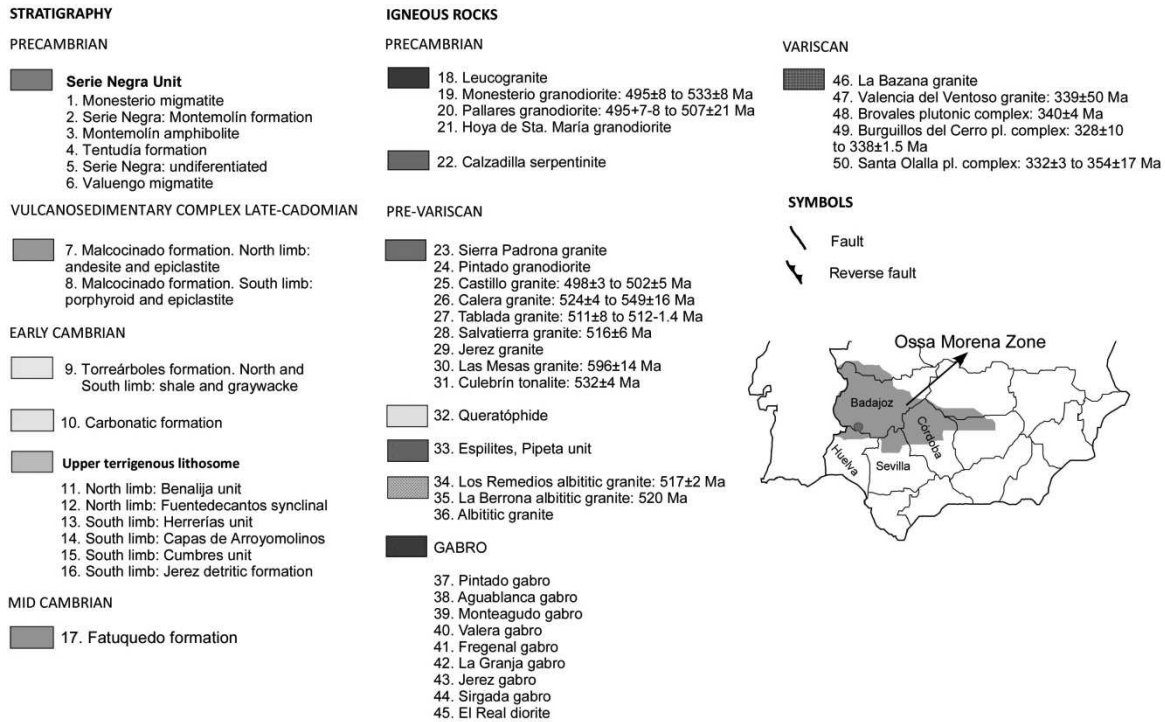


Figure 5. Geologic map of the Olivenza-Monesterio Belt showing the major lithologic units and igneous rocks, modified after García (2003). Both the Valuengo area to the NW and the Santa Olalla Plutonic Complex to the SE of the Belt (black rectangles) are the focus of this study. References for the ages of the main intrusive rocks: 19, Schäfer (1990), Ordoñez-Casado (1998), Ochner (1990); 20, Ordoñez (1998), Schäfer (1990); 25, Ochner (1990), Montero et al. (2000); 26, Salman (1999); 27, Ochner (1990); 28, Ochner (1993); 30, Ordoñez (1998); 31, Montero et al. (2000); 34, Sánchez-García et al. (2008); 35, Carriedo (Ph.D. in prep.); 47, Dupont et al. (1981); 48, Montero et al. (2000); 49, Dupont et al. (1981); 50, Casquet et al. (1998); Montero et al. (2000).

Some of these deposits are clearly syngenetic and have been interpreted as exhalative stratiform, deposited in third order oxic basins coeval with volcanism and related sub-seafloor replacements in carbonatic rocks (El Soldado, Bilbaínia, Bóveda and Alconchel deposits). However, other deposits are clearly epigenetic

(Tornos et al., 2004; Sanabria et al., 2005) including classic calcic and magnesian skarns, shear zone-related replacements (Cala mine) and IOCG-like mineralization (La Berrona and Colmenar deposits), most of them being closely associated with calc-alkaline intrusions and/or albitite (Tornos et al., 2002, 2004; Tornos and Casquet, 2005; Carriedo and Tornos, 2010). Two styles of mineralization are of particular interest in the epigenetic magnetite deposits: (1) Albitite-related magnetite mineralization of both Cambrian and Variscan ages located in the Valuengo area (Berrona, Alfredo and Colmenar deposits, among others) (Carriedo et al., 2010) and, (2) Calcic skarn and superimposed shear zone-related replacements in the Cala mine near the Santa Olalla Plutonic Complex (SOPC) (Velasco, 1986; Velasco and Amigó, 1981). On the other hand, to the South of the Valuengo area, the SOPC hosts several ore deposits, such as the Sultana Cu-Au veinfield system (discussed in the Chapter II of this thesis), the Aguablanca Ni- (Cu) magmatic deposit (Casquet et al., 2001; Tornos et al., 2001; Piña et al., 2006) or the magnetite-rich magnesian skarns of Teuler (Velasco, 1986).

As it has been pointed before, the chapters II and III of this thesis are related to some metallogenic problems in the Santa Plutonic Complex and the Valuengo area, whose general geologic aspects are detailed in the next section.

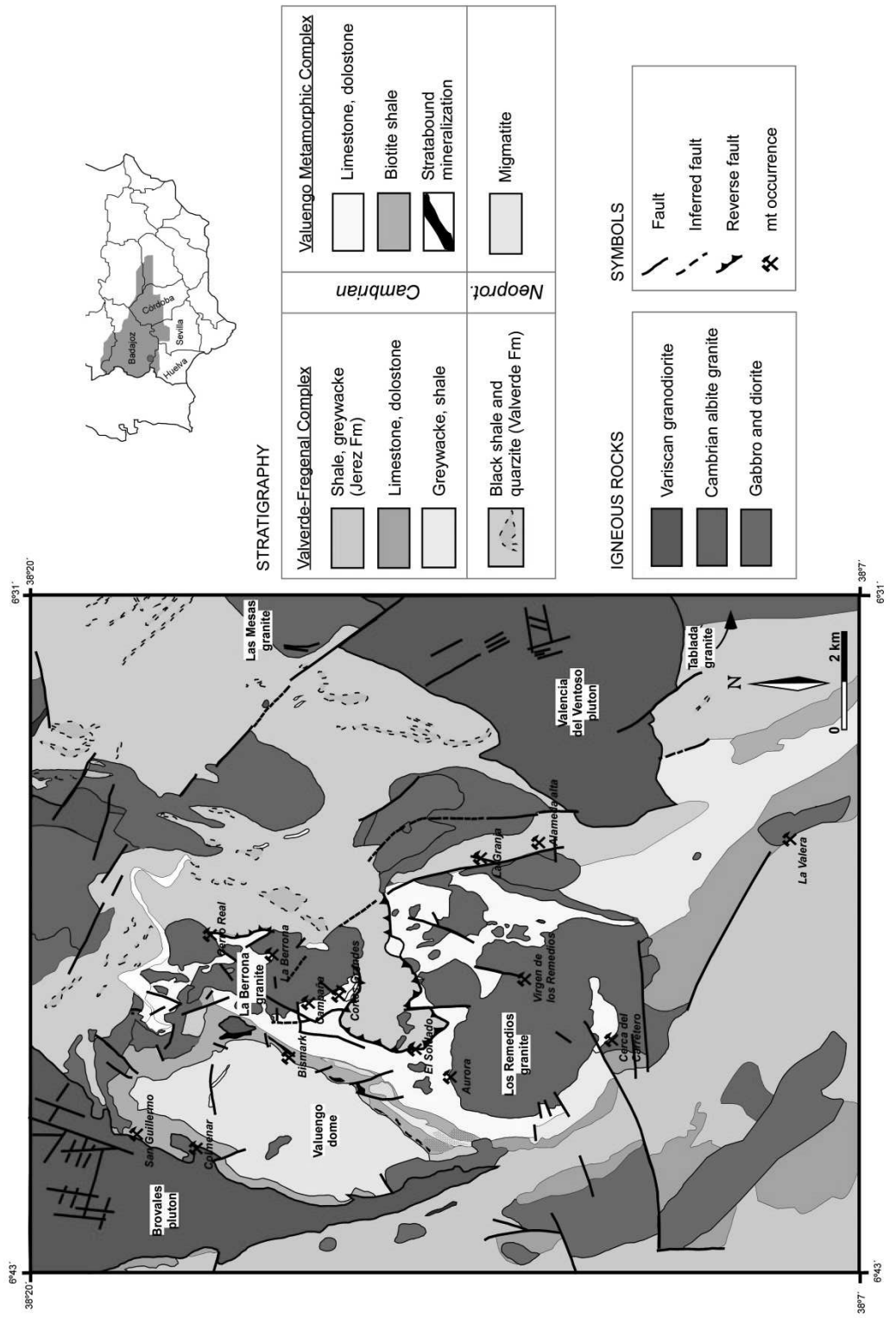
I.3.1. The Valuengo Complex

The Valuengo Complex is one of the few areas in the Ossa Morena Zone where high grade metamorphic rocks can be found (Fig.6). It forms a N-S elongated ellipsoidal structure of 7x4 km² with high grade metamorphic rocks in the core (the gneissic-migmatitic Valuengo Formation of Coullaut et al., 1981). Surrounding these materials there are metapelitic and metavolcanic (both felsic and mafic) rocks with milonitic foliation and middle to high grade metamorphism that are grouped in the Las Mayorgas Formation. These rocks are intercalated by a carbonatic level (the “c” level) which hosts the magnetite deposits of the Colmenar- San Guillermo-Santa

Justa group (Apraiz and Eguiluz, 1996; Tornos et al., 2004; Sanabria et al., 2005). This succession is overlain by a volcanosedimentary complex (probably equivalent to the syn-Cadomian Malcocinado Formation, Apraiz, 1998; Expósito, 2000; Expósito et al., 2003, Fig.2) with milonitic deformation and is followed by a thick (11-150 m) marble serie of low metamorphism at the top. The metamorphism in the core produces widespread anatexis of the rocks and the grade decreases drastically to the eastern edge of the structure where the metamorphism is of medium to low grade. This strong metamorphic gradient is associated to an extensional steeply dipping ductile shear zone which is part of the Monesterio Shear Zone and which has been clearly observed in several open pits of the western part of the dome (Apraiz and Eguíluz, 1996; Expósito, 2000; Expósito et al., 2003). Following this structure to the south, the Monesterio metamorphic complex and the Lora del Río core complex (Apraiz et al., 1993; Apraiz and Eguiluz, 2002; Pereira et al., 2009) share many of the features of the Valuengo Dome.

One big controversy in the Valuengo Dome is that if the metamorphism is pre-Variscan or coetaneous with the Variscan deformation. Some interpretations consider this HT/LP metamorphism as the result of crustal thickening and collapse during the second deformation phase of the Variscan orogeny (Ábalos and Díaz Cusí, 1995; Apraiz and Eguíluz, 1996; Apraiz, 1998). They are based on structural criteria as, for example, the presence of neosomes showing one phase of penetrative deformation. Recent radiogenic isotope and geochronological data of Carriedo (Ph.D., in prep.) has dated as Variscan some dykes of albitite within the shear zone suggesting that the age of the albitite, the related mineralization and the formation of the Valuengo Dome Complex is Variscan, ca. 340 Ma. The Lora del Río Complex, to the south of Valuengo and Monesterio areas has been also interpreted as an extensional core complex structure dated at 340 Ma (Apraiz and Eguíluz, 2002) supporting the Variscan age for the formation of these high metamorphic grade domes.

Figure 6. Geology of the Valuengo area showing the location of the magnetite occurrences. Modified after Fernández et al. (1980).



Other interpretations suggest that the metamorphism is pre-Variscan (Expósito et al., 2003; Azor et al., 2004; Sánchez-García et al., 2003, 2008, 2010) since the mylonitic foliation related to the shear zone is folded by the Variscan recumbent folds. Expósito et al. (2003) have dated both an orthogneiss and undeformed microgranite in the Valuengo Dome, obtaining ages of 532 ± 5 Ma and 480 ± 7 Ma, respectively. In addition, the Monesterio Complex shares many structural features of Valuengo, since high grade metamorphic rocks outcrop enclosed by branch lines of the same Variscan thrust-system. Despite the geochronological data are not very precise, the ages for the Monesterio metamorphic dome range also between 530 and 500 Ma (Schäfer, 1990; Ochner, 1993; Ordoñez Casado, 1998; Montero et al., 1999). These data support the connection of the metamorphism of the Valuengo and Monesterio complexes with the pre-Variscan rifting stage that occurred in the OMZ during the Cambrian-Ordovician (Expósito et al., 2003).

The albitite intrusive bodies bounding the east of the Valuengo Complex are described in detail in the Chapter III of this thesis. There are up to six large intrusive albititic bodies, some of them covering more than 4 km² of surface (Fig. 6) (IGME, 1972). They have associated large but barren calcic skarns with abundant grandite, clinopyroxene and scapolite, as well as some magnetite mineralization related to clinoamphibole rich retrograde skarn (Carriedo and Tornos, 2010). There is a second style of magnetite mineralization that replaced calcsilicate and pelitic hornfels and marble of the Malcocinado Formation and the Early Cambrian sequence, showing features of the IOCG style of mineralization (Carriedo and Tornos, 2010). The La Berrona magnetite deposit associated to the La Berrona albitite comprises one example of this style of mineralization and is described and interpreted in the Chapter III of this thesis. The metallogenic scenario is complicated by the presence of abundant stratiform magnetite-rich lenses of likely exhalative origin that are hosted by the same sequence (Dupont, 1979; Tornos et al, 2004; Sanabria et al., 2005; Carriedo and Tornos, 2010).

The western contact of the Valuengo dome is bounded by the Brovales Pluton, a typical calc-alkaline intrusion of Variscan age (340 ± 7 Ma; Montero et al., 2000) that has produced some calcic skarn on the Cambrian limestone (e.g. Santa Bárbara mine; Tornos et al., 2004).

I.3.2. The Santa Olalla Plutonic Complex

The Santa Olalla Plutonic Complex (SOPC) is a calc-alkaline Variscan pluton dated at 354 ± 17 (Casquet et al., 1998), 332 ± 3 (Montero et al., 2000) and 341.5 ± 3 Ma (Romeo et al., 2006), that is located in the southernmost OMB (Figs. 5 and 7). The complex is limited by the Zufre and Cherneca faults, the former bounding to the south of the Ossa Morena Zone. It intruded two different stratigraphic units: black shale and metagreywacke with thin intercalations of meta-volcanic rocks and black quartzite of Neoproterozoic age (Serie Negra Unit) to the North, and the Early to Mid Cambrian sequence with marble and shale overlain by porphyritic rhyolite and metabasite to the South. The intrusion is elongated in shape with a WNW-ESE trend, covers an area of around 30 km² and when limestone is present, is bordered by skarn dominated by garnetite. In this area, the regional metamorphism is of very low to low grade and is superimposed by a well-defined intense contact metamorphism grading from greenschist to amphibolite facies. Casquet (1980) has proposed a maximum temperature for the contact metamorphism of 700° to 925 °C and a fluid pressure from 0.5 to 1 kbar. The SOPC is interpreted as having a reverse compositional zonation with quartz diorite grading to tonalite in the center and monzogranite in the south.

Three important ore deposits are known in the vicinity of the SOPC: the Aguablanca magmatic Ni-Cu deposit, the Cala magnetite – (Cu - Au) skarn IOCG?-like deposit (Appendix IA) and the Sultana (California, Extremeña) copper-gold veinfield (Chapter II).

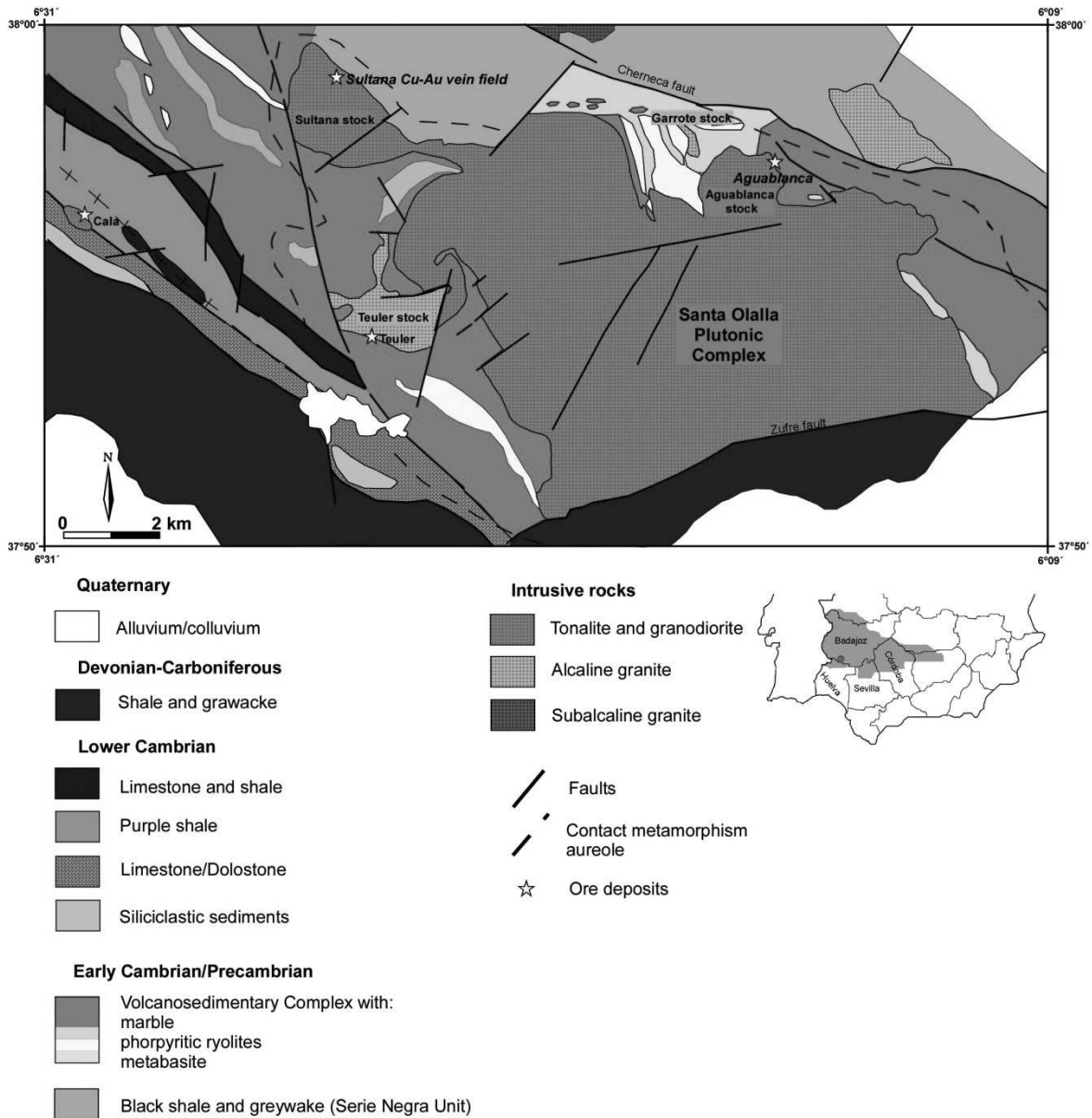


Figure 7. Geology of the Santa Olalla Plutonic Complex. Modified after Apalategui et al. (1980).

I.4. The magnetite – (Cu-Au) mineralization of the OMZ: a controversial origin

The origin of the magnetite – (Cu-Au) mineralization in the OMZ has been controversial for a long time. The coexistence of both exhalative and intrusion-related Fe oxide mineralization in the same zone and hosted by the same lithologies (the limestone and related calcsilicate hornfels and volcanic rocks of Late

Proterozoic and Early Cambrian age) has promoted the discussion about if the late ones are just a metamorphosed stratiform mineralization, an hydrothermal remobilization of the previous ores or a new mineralization related to the igneous rocks. Thus, one of the main questions to resolve is if the intrusion-related mineralization is product of the assimilation of previously mineralized exhalative rocks and further release of iron-rich magmatic hydrothermal fluids or if they form part of superimposed independent mineralizing processes that are genetically unrelated (Doetsch, 1967; Doetsch et al., 1973; Ruiz García, 1974; Vazquez and Fernandez Pompa, 1976; Velasco, 1976; Dupont, 1979; Casquet and Tornos, 1991; Tornos et al., 2002, 2004; Carriedo and Tornos, 2010).

Recent data suggest that the magnetite deposits of the Valuengo dome share many similarities with the IOCG (Iron Oxide Copper-Gold, Hitzman et al., 1992, 2000; Williams et al., 2005) style of mineralization (Tornos et al., 2003; Tornos and Casquet, 2005; Carriedo and Tornos, 2010). They are principally concentrated in the Olivenza-Monesterio Belt (Colmenar, Alfredo, La Valera, La Berrona, El Soldado and Monchi) and most of them are associated to albitite granites. These deposits are dominated by magnetite (\pm hematite), copper sulfides and some gold with variable amounts of Co, Ni and As. Common characteristics of the IOCG deposits include the abundance of iron oxides (>10%) with moderate to low contents of sulfides and quartz, the association with shear zones or crustal scale structures, the high REE-U concentrations and especially the intense alkali-calcic alteration, with a characteristic assemblage including K feldspar or albite and actinolite or diopside with minor amounts of scapolite and biotite (Hitzman et al., 1992; Williams et al., 2005). One of the important characteristics of the IOCG deposits of the OMZ is their polyphase character as they seem to have formed by similar geological processes that took place during different metallogenic events, both the Cadomian and the Variscan orogenies, (530-520 Ma and 340 Ma, Carriedo et al. 2010). However, there is still an open debate about the origin of some of these deposits. An example is the Cala mine, where the discussion about the existence of one (skarn) or two (skarn +

IOCG) types of magnetite mineralization is still intense and controversial (Carriedo et al., 2008, 2000; Carriedo and Tornos, 2010). Another example is the La Valera deposit which shows a structure resembling columnar jointing in the magnetite ore that suggest a magmatic origin for it (Carriedo and Tornos, 2010).

As it is discussed in the Chapter III of this thesis, the understanding of the origin and genesis of the albitite of the Valuengo area has major implications for our knowledge on the formation of the magnetite deposits nearby. It is likely that the albitite could well be the source for the iron both in the hydrothermal (e.g. La Berrona deposit) and in the magmatic (e.g. La Valera deposit) magnetite orebodies in the area. If true, the model proposed in the Chapter III contributes to the already long list of origins of the IOCG deposits worldwide.

I.5. The “Iberian Reflective Body”: a link between the Variscan magmatism and the mineralization

Between 2002 and 2003, a seismic reflection profile (IBERSEIS, Simancas et al., 2003; Carbonell et al., 2004) revealed an image of the hidden crust in the Ossa Morena Zone (Fig. 8). 15-20 km below the current surface, there is a high amplitude reflective 140 km long and 4 km thick band called the “*Iberian Reflective Body*” (IRB). This body has been interpreted as large but discontinuous intrusive sill-like series of mafic intrusions emplaced within the mid-upper crust boundary (Fig. 8B). More recent geophysical data also report a high velocity zone in the refraction modeling and conclude that the crust in the OMZ is laterally variable and that the modeled high velocities are consistent with the existence of mantle-derived rocks (Palomeras et al., 2009, 2011).

Tornos and Casquet (2005) have suggested that the intrusion of such a large stratiform magmatic complex, probably one of the largest detected on earth, induced low pressure-high temperature metamorphism and dewatering of the hosting low grade crustal metamorphic rocks, as well as local partial melting

synchronous with extensive crustal contamination of the juvenile melts. Such a mafic intrusion has major implications on the genesis of the ore deposits of the area and explains the unusual Variscan metallogeny of the OMZ. In fact, it has been proposed that the IRB is the source of magmas and fluids representing the ultimate control on the formation of the Variscan Fe oxide, Cu-Au and Ni - Cu mineralization (Tornos and Casquet, 2005).

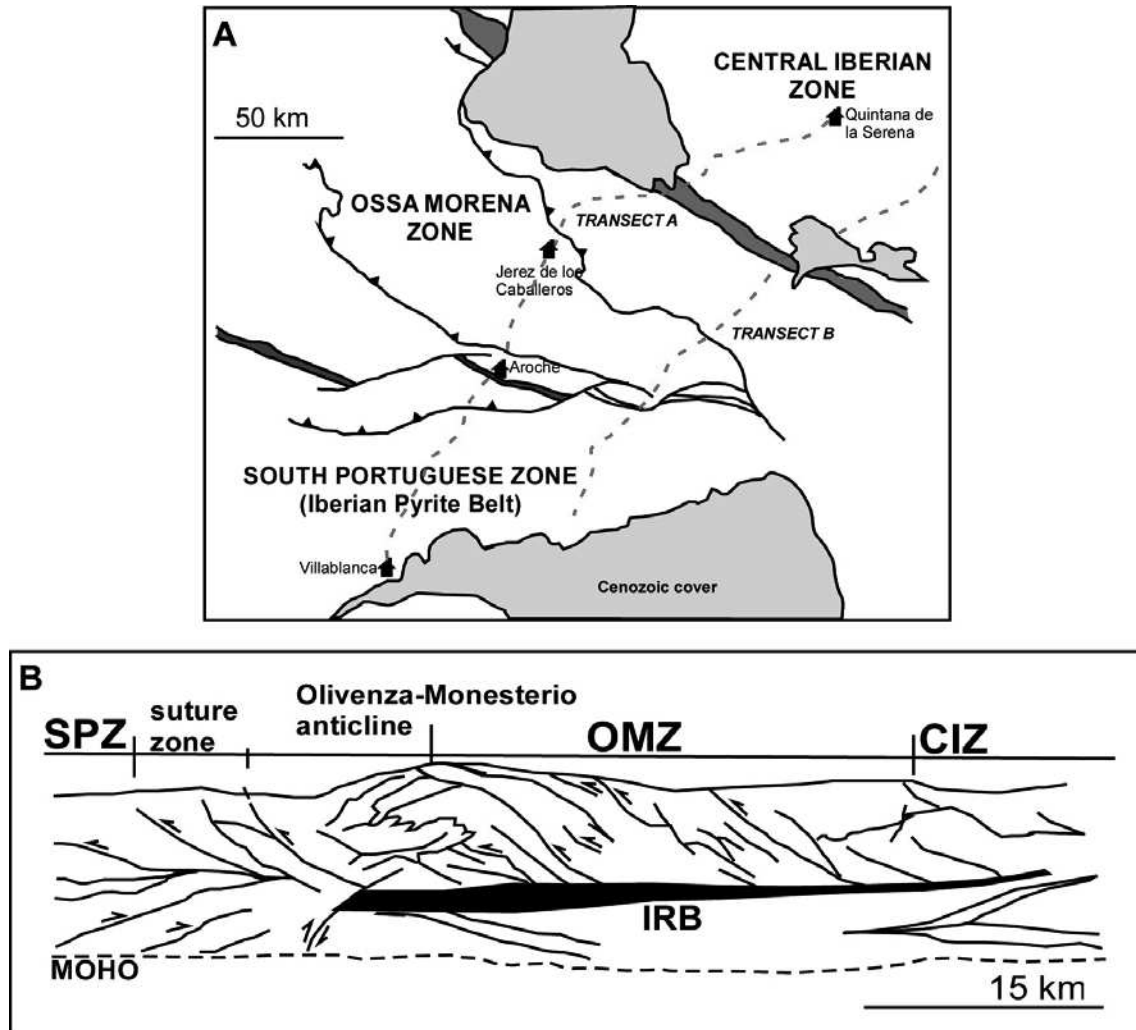


Figure 8. (A) Location map of the transects of the IBERSEIS deep reflection seismic profile (modified after Palomeras et al., 2009). (B) Interpretation of the IBERSEIS profile in the Ossa Morena Zone (OMZ) and northern South Portuguese Zone (SPZ) crosssection (from Simancas et al., 2003). Abbreviations: IRB, Iberian Reflective Body; CIZ: Central Iberian Zone.

I.6. Mining history

Despite the proximity to the world class district of the Iberian Pyrite Belt, which probably put in the shade the mining in the Olivenza-Monesterio Belt, some ore deposits in the Southwest of Spain have been important metal producers in the past century.

The first evidences of mining in the OMB come from the 2000 year BC, when the Iberian cultures (Celtics?) worked some copper and silver veins in the area (Tornos et al., 2004). More clear evidences of historical mining derive from the Romans who intensely exploited Pb, Zn, Cu and Au metals in veins such as Sultana or Abundancia and the Cu (and gold?) in the gossan from the Cala mine. After the Roman period, little evidence of extensive mining exists, except in the 16th century, when some Pb and Cu veins were worked (Tornos et al., 2004).

The modern mining industry emerged during the First World War with the exploitation of magnetite in the San Guillermo-Colmenar-Santa Justa group of Fe-oxide mines, through small open pits and few underground galleries. In 1956 “Minera del Andévalo, S.A.” started exploiting this group of mines as well as the iron and the copper from the Cala mine at the SE (IGME, 1980, Vázquez, 1983). Other stratabound magnetite-hematite deposits such as Bismark, Aurora and El Soldado were also exploited for iron during the WW1 and later on until the fifties. The Cala Mine has remained in operation until 2010, the last years by PRESUR SA. All the concentrate derived from these mines was transported by train to the Riotinto smelter in Huelva.

Currently, only the Aguablanca mine is on production exploiting Ni-Cu sulfides, though at present day (2012) it is momentarily closed for maintenance reasons. No other mines in the area are open at the moment.

On respect to the future, new exploration campaigns are developing in the OMB in the light of the actual high prize of metals. The exploration is mainly based on a reserve reevaluation of old deposits that were exploited for other commodities like iron, but that contain reasonable grades in copper and gold.

Chapter II: Fluid inclusion evidence for magmatic-hydrothermal fluid evolution in the intrusion-related copper-gold Sultana vein deposit at Huelva, Spain

Abstract

The copper-gold-bearing Sultana quartz-ankerite vein system in Huelva (SW of Spain) is related to the Santa Olalla Plutonic Complex (SOPC) which emplacement is dated at ca. 341 Ma, during the Variscan orogeny. The mineralization is hosted by the tonalite of the SOPC as well as by black shale and volcanosedimentary rocks of Late Neoproterozoic age and Early Cambrian calcsilicate hornfels that were affected by an intense contact metamorphism. Combined techniques including detailed fluid inclusion petrography, scanning electron microscope-cathodoluminescence imaging (SEM-CL), microthermometry, Raman spectroscopy analysis and laser ablation-inductively coupled plasma mass spectroscopy (LA-ICPMS) analyses are applied in this study to reconstruct the physical and chemical evolution of the hydrothermal fluids in the Sultana system. The study shows that the first recorded fluid circulating through the vein system was a low saline (<4 to 15 wt % NaCl eq; average of 5 wt % NaCl eq.), CO₂-bearing (10.4 mol %) intermediate density fluid with high ore-metal concentration (>537 µg/g Cu, >539 S µg/g) that was trapped at estimated fluid pressures of ~800 bar and >420°C. When this fluid rose or the fluid pressure evolved from lithostatic to hydrostatic conditions, phase separation occurred by condensation of minor brine (~ 40 wt % NaCl eq.) and a low saline vapor phase (~ 2.4 wt % NaCl eq.) at ~ 350 °C and 100 - 300 bar, both carrying most of the copper and possibly gold (335 ± 123 µg/g Cu, 9.5 ± 6.6 µg/g Au) into the system. Coinciding with the dissolution of an early generation of quartz (Q1) due to its retrograde solubility in a cooling system, both the drop in temperature and boiling triggered the precipitation of chalcopyrite into open spaces before or together with the precipitation of a

late generation of quartz (Q2). Consequently, Cu concentration drops from 700 µg/g to less than 0.1 µg/g in late secondary liquid carbonic fluid inclusions without a proportional decrease in the rest of elements. Gold was later deposited in the fractures of the chalcopyrite, probably due to the excess of sulfur in the vapor phase that could transport gold after the Cu precipitation. The Sultana vein system shares many features with the intrusion-related Cu-Au deposits but shows a large affinity to the Cu-Au porphyry systems on respect to the ore-forming fluid conditions and metal content.

II.1. Introduction

In recent years the combination of conventional fluid inclusion studies with SEM-Cathodoluminescence images and LA-ICPMS (laser ablation–inductively coupled plasma mass spectrometry) analysis in single fluid inclusions have significantly increased the knowledge of the fluid phase relationships and the mechanisms of ore-metal transport and precipitation in hydrothermal systems. One of the most important discoveries is that the low-intermediate density fluids can transport high concentrations of Cu, As and Au and follow different pressure-temperature paths depending on the physicochemical environment (Heinrich, 2005; Williams-Jones and Heinrich, 2005). Precipitation of metals from the fluids is triggered by processes like cooling and/or decompression (Lowell and Gilbert, 1970; Ulrich et al., 2002), fluid phase separation (Burnham, 1980; Seward and Barnes, 1997; Heinrich, 2007), reaction with the host rock (Gustafson and Hunt, 1975; Hedenquist et al., 1998) and/or fluid interaction with external fluids of metamorphic or surficial derivation (Reynolds and Beane, 1985; Heinrich, 2007; Audétat, 2008). These comprehensive studies have been commonly carried out in deposits where the deformation is not significant and is thus easy to differentiate between zones of mineralization and alteration and clear fluid inclusion types can be distinguished (e.g. Bingham Canyon Porphyry Cu-Mo-Au deposit, Landtwing et al., 2010; Butte

Porphyry Cu-Mo deposit, Rusk et al., 2008; Sn-W-F mineralized Mole Granite, Audetat, et al., 2000).

Despite the abundant literature in gold (\pm copper) deposits such as intrusion-related, epithermal, orogenic or IOCG deposits, it is still not well known how the processes of ore transport and precipitation described above operate in these less well known ore systems. The intrusion-related gold deposits (Lang et al., 2003) are diverse, difficult to define and classify as they are formed in different geological settings (Groves et al., 2003b; Phillips and Powell, 2010). Common characteristics to most of the intrusion-related gold systems are (Sillitoe, 1991; Hollister, 1992; Lang et al., 1997; Thompson et. al, 1999; Lang et al., 2000; Newberry, 2000): (1) the metaluminous, subalkaline intrusions hosting or lying close to the mineralization; (2) the presence of CO₂- bearing hydrothermal fluids; (3) an ore assemblage composed by gold with Bi, W, As, Mo, and Te with low sulfide content; and (4) a restricted hydrothermal alteration, except in shallow deposits. One of the most controversial and debated question in these intrusion-related deposits is the origin of both the ore-metals and their transporting fluids. The proposed ore-fluid sources are dispar from metamorphic devolatilization reactions (Phillips and Powell, 2010), mantle degassing (Fyon et al., 1983), magmatic hydrothermal fluids expelled from intrusions (Burrows and Spooner, 1989; Groves et al., 2003) or a combination of them.

In this study the mechanisms of transport and precipitation of a low tonnage-high grade Cu-Au granitoid hosted vein mineralization are discussed. A combination of fluid inclusion study, SEM-CL, LA-ICPMS and Raman techniques is applied to study in detail the physical and chemical evolution of the hydrothermal fluids that circulated through the vein. With significant estimated resources up to 1.8 Mt at 8.2% Cu and 28 g/t Au, the Sultana vein has been one of the richest gold mines in Spain with local grades up to 500 g/t. It represents a good example to examine the evolution of the hydrothermal fluids and ore forming processes within

a vein system, due to its good accessibility, simple mineralogy, high ore grade and the local presence of free-grown quartz crystals that host well preserved fluid inclusions. In addition, evidences on the similarities of the Sultana vein with other copper-gold deposits such as orogenic gold lodes or porphyry gold deposits are provided on the basis of fluid characteristics and ore-metal precipitation mechanisms.

This study accompanies another work oriented to the field relationships and geochemistry of the ore deposit (Tornos et al., in prep.).

II.2. Geological setting

The Sultana vein is located in the northwest part of the Santa Olalla Plutonic Complex (SOPC; Casquet, 1980), in the Ossa Morena Zone (ZOM, SW Iberia) (Fig. 1). The SOPC is a Variscan pluton located in the southern limb of a major folding structure, the Olivenza-Monesterio Antiform (OAM, Fig.5, Chapter I). The complex is limited by the Zufre and Cherneca faults, and intruded two different stratigraphic units: the black shale and metagreywacke with thin intercalations of meta-volcanic rocks and black quartzite (Serie Negra Unit, Eguiluz, 1988) in the north, and the syn-Cadomian Malcocinado Fm and superimposed Early Cambrian limestone in the south (Fig.1). The intrusion is irregular and elongated in shape, with a WNW-ESE trend, covers an area of around 30 km² and is usually bounded by skarn dominated garnetite. The Variscan regional metamorphism is of very low to low grade and is superimposed by a well-defined intense contact metamorphism grading from greenschist to amphibolite facies. Casquet (1980) has proposed an interval of temperature from 700° to 925 °C and pressure from 0.5 to 1 kbar for the contact metamorphism formation. The SOPC is interpreted as having a reverse compositional zonation with quartz diorite grading to tonalite in the center and monzogranite in the south. Minor aplite and microgranite occur as late dikes. Three important styles of Variscan mineralization are known in the vicinity of the

intrusion: the Aguablanca magmatic Ni-Cu deposit (Tornos et al., 2004), the Cala Fe-Cu-(Au) skarn IOCG?-like deposit (Velasco and Amigó, 1981; Tornos and Casquet, 2005; Carriedo et al., 2006) and the Sultana (California, Extremera and Cala) copper-gold vein (Fig.1).

The Sultana Cu-Au vein system is located in the Sultana Stock, which is an apophysis of the SOPC located at the northwest (Fig. 1). The stock is subcircular in shape and is hosted by the Precambrian black shale and greywacke with thin intercalations of meta-volcanic rocks and black quartzite of the Serie Negra Unit and the shale, marble, calcsilicate hornfels, porphyritic rhyolite and metabasites of the Malcocinado Formation overlain by a thick unit of limestone of Early Cambrian age (Eguiluz, 1989; Apalategui et al., 1990). This limestone usually occurs as roof pendants or along the margins of the intrusion and is sometimes replaced by garnet-rich calcic skarn. The stock has a rather monotonous composition, with medium to coarse grained tonalite and granodiorite with local zones enriched in large plagioclase phenocrysts. The Sultana Stock is the only place in the SOPC where the granitic rocks are in direct contact with the black shales of the Neoproterozoic Serie Negra Unit. For an extensive explanation of the geological and the structural setting of the area, we refer to Tornos et al. (in prep.).

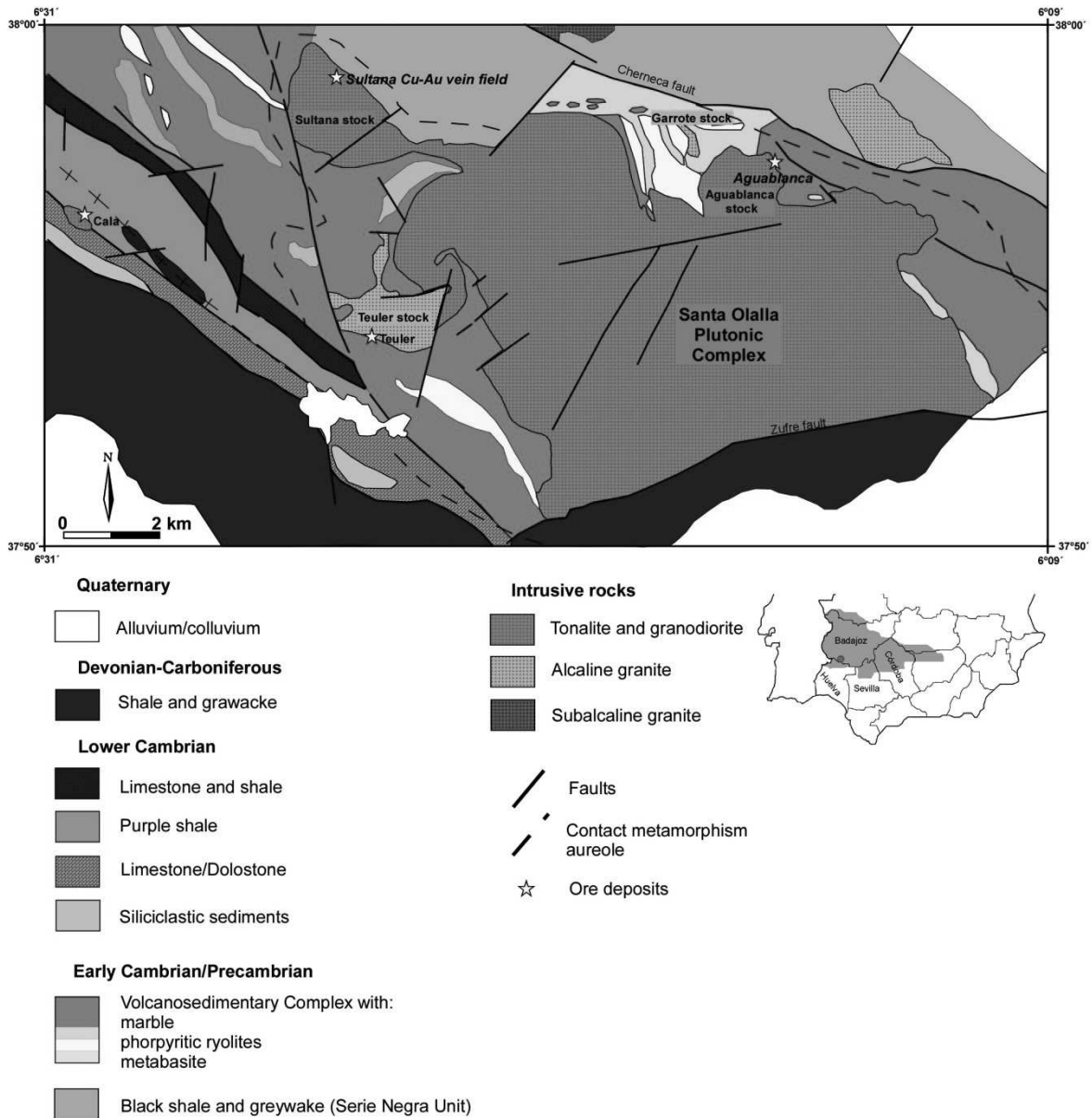


Figure 1. Geological map of the Santa Olalla Plutonic Complex and associated host rocks showing the main lithologies in the area. Modified after IGME, (1986-1987).

II.2.1. Dating of the intrusive events and the mineralization

Well constrained ages for the SOPC show an age of emplacement between 341 ± 3 Ma and 347.7 ± 5 Ma (Romeo et al., 2006; Ordóñez-Casado et al., 2008) during the Variscan orogeny (Table 1). The Sultana Stock was formed at the same age 341 ± 3 Ma (Lunar et al., 2008) whereas the Teuler stock in the south and

Garrote stock in the north were emplaced slightly later (338 ± 2 Ma, Romeo et al., 2006; Lunar et al., 2008).

The mineralization has been dated in the quartz-sericite alteration next to the selvage of the vein, yielding an Ar/Ar age of 331.4 ± 0.7 Ma (Tornos et al., in prep.). Despite not very confident, this age suggests that the vein formed 10 Ma later than the hosting Sultana Stock.

Sample	Method	Mineral	Age (Ma)	References
Santa Olalla P.C	U/Pb	zircon	341 ± 3	Spiering et al., 2005; Romeo et al., 2006
		zircon	348 ± 5	Piña et al., 2006; Ordoñez Casado, 2008
	U/Pb	zircon	332 ± 3	Salman, 2004
	Pb/Pb	zircon	341 ± 3	Lunar, 2008
	Pb/Pb	zircon	341 ± 3	Montero et al. 2000
Sultana Stock	Pb/Pb	zircon	341 ± 3	Lunar, 2008
Sultana vein	Ar/Ar	phengite	331 ± 1	Tornos et al., (in prep.)
Teuler Stock	Pb/Pb	zircon	338 ± 2	Romeo et al., 2006; Lunar, 2008
Garrote Stock	Pb/Pb	zircon	339 ± 3	Romeo et al., 2006; Lunar, 2008
Cala Stock	Pb/Pb	zircon	352 ± 4	Romeo et al., 2006

Table 1. Geochronological data of the most important features in the Santa Olalla Plutonic complex.

II.2.2. The Sultana vein

Crosscutting the Sultana Stock there are at least two systems of veins, one with N110-130°E trend represented by the San Rafael and California mines and a second one with N160°E trend that includes the Sultana vein. Only this late one was accessible to the underground galleries for the realization of this study. The Sultana vein dips between 10° and 60° W and has an irregular pinch and swells morphology with the thickness varying between 0.18 to 1.5 m. It extends laterally for more than 1 km and was mined to a depth of about 100 m. The vein crosscuts earlier subvertical barren ankerite-quartz veins of N0°-90° and N110-130° E trend with some disseminated pyrite (Tornos et al., in prep.).

The vein infill is predominantly formed by quartz, ankerite and chalcopyrite, the latest almost invariably located in the center but also supporting microbreccias (Fig.2A). Tornos et al. (in prep.) has distinguished four superimposed hydrothermal events in the vein (Table 2):

- The earliest stage is composed by highly deformed milky quartz, ankerite, scarce pyrite and arsenopyrite (Fig. 2B).
- Superimposed to the first stage, the main ore assemblage is dominated by chalcopyrite, quartz and ankerite. Quartz is more transparent than the earlier one, with local euhedral growing into open spaces (Fig. 2C).
- Bismuthinite (Bi_2S_3), maldonite (Au_2Bi) and native gold postdate and replace the chalcopyrite; Gold occurs in fractures, coating quartz and chalcopyrite veins, replacing bismuthinite and in some cases, as free grown native gold aggregates during the final stages of crystallization (Fig. 2D).
- The latest stage comprises a low temperature assemblage with quartz, calcite, sphalerite and galena replacing chalcopyrite and filling late veins.

The vein selvage is affected by a dominantly sericitic alteration that is most commonly confined to narrow zones (10-20 cm) adjacent to the vein (Fig. 2E). The assemblage includes fine grained phengite, quartz, ankerite, albite, chlorite, biotite, tourmaline and variable proportions of calcite, epidote and apatite; locally, it has disseminated chalcopyrite and pyrite.

In some areas of the SOPC, the tonalite hosts aplite dikes and miarolitic cavities that can be interpreted as indicative of late stage fluid release while intrusion was solidifying (Fig. 2F). As it is shown later, the euhedral quartz in these cavities host fluid inclusions that are similar to those of the Sultana but, unfortunately, there are no field evidences of synchronous development near or underneath the Sultana vein which could help to establish a link between these cavities and the vein formation.

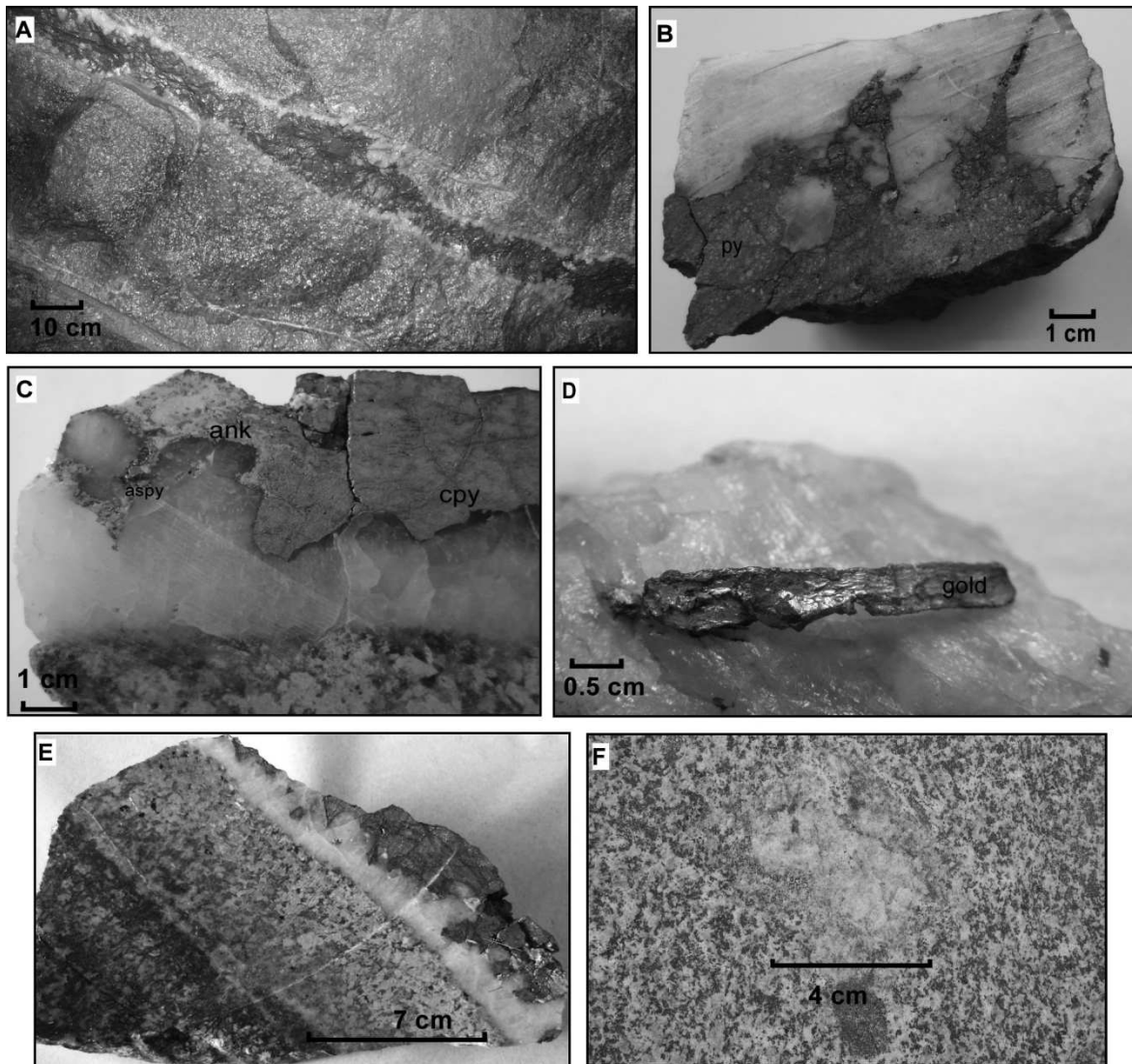


Figure 2. Photographs of the Sultana vein and the magmatic-hydrothermal features of the Santa Olalla Plutonic Complex. **(A)** Aspect of the vein with quartz and chalcopyrite; note the pinch and swell morphology of the vein; **(B)** Quartz-pyrite stage affected by superimposed brittle deformation (sample SUL-py-1); **(C)** Main stage assemblage, including quartz, ankerite, and chalcopyrite replacing earlier arsenopyrite. These sections are optimal for the fluid inclusion study (sample CSU-1); **(D)** Free grown aggregate of gold in quartz (sample from the Museo GeoMinero, Madrid, Spain); **(E)** Aspect of the sericitic alteration in the selvage of the vein (sample CSU-2); **(F)** Possible

miarolitic quartz cavities in the tonalite of the Santa Olalla Plutonic Complex granodiorite.

Mineral assemblage	stage I	stage II	stage III	Wall-rock alteration
Quartz	—————	—————	-----	-----
Ankerite	—————	-----		-----
Pyrite	—————			
Arsenopyrite	—————	-----		
Chalcopyrite		—————		
Native gold		—————		
Bismuthinite		—————		
Maldonite			—————	
Galena			—————	
Sphalerite			—————	
Sericite				—————
Chlorite				—————
Biotite				—————
Tourmaline				—————
Calcite				—————
Epidote				—————

Table 2. Mineral precipitation sequence in the Sultana vein based on Tornos et al. (in prep.).

II.3. Methods

After the thorough field mapping and conventional petrographic and isotope studies carried out by Tornos et al. (in prep.), a detailed fluid inclusion study has been made in order to reconstruct the fluid evolution during the vein formation. Most of the quartz filling in the Sultana vein is milky and poorly transparent with myriads of randomly distributed fluid inclusions showing neither clear crosscutting relationships nor obvious links with quartz and ore precipitation. However, there are zones where the quartz has not been deformed and shows euhedral growing into open space. This quartz corresponds to the second and third mineralization stage (cpy-Au) and host

large and very well preserved fluid inclusion assemblages (FIA) suitable for detailed analysis.

II.3.1. Fluid inclusion petrography

Thirty doubly polished thick sections parallel to the c-axis of the crystals and with a thickness between 200 and 400 μm were prepared for the fluid inclusion petrography. The fluid inclusion petrography is based on the “Fluid Inclusion Assemblage” (FIA) concept defined by Goldstein and Reynolds (1994), as petrographically coexisting fluid inclusions. Fluid inclusions with evidences of postentrapment modifications as well as the single isolated ones were avoided from the study. All the procedure for the petrography was done following the method of Goldstein and Reynolds (1994).

II.3.2. SEM-Cathodoluminescence images

The petrography of the doubly polished sections was performed in combination to cathodoluminescence imaging of the quartz crystals on a scanning electron microscope (SEM-CL). The SEM-CL and associated SEM-BSE (Back Scattered Electron) images were obtained at the Centro de Instrumentación Científica (CIC), University of Granada (Spain). The sections were coated with a film of carbon to prevent electrical charge during irradiation, which was removed for the further fluid inclusion study. The images were taken in SEM Leo 1430 VP equipment with an acceleration voltage of 15kV, 2nA e-probe and a beam current density of 80mA. The working distance was 16 mm. To distinguish between different intensities of cathodoluminescence in quartz, we have classified it as dark-luminescent, gray-luminescent and bright-luminescent.

II.3.3. Microthermometry of fluid inclusions

Microthermometric analyses were performed in two phases during the study, using a Linkam TMS 94 heating-freezing stage at the Instituto Geológico y Minero de España (IGME, Salamanca) and a Linkam THMSG 600 stage at the ETH in Zürich. Calibration was performed using synthetic H₂O-CO₂ fluid inclusions supplied by Linkam Scientific Instruments Ltd. for the eutectic point of CO₂ (-56.6 °C) and synthetic H₂O fluid inclusions for the melting point of ice (0.0 °C) and the critical point of water (374.0 °C). The procedure was dependent upon the phase proportions of fluid inclusion at room temperature. For the CO₂-bearing fluid inclusions, we have followed the procedure of Diamond (1990); it consist on the preheating of the sample to 50 °C and further rapid cooling with liquid nitrogen to -155 °C, leading to the formation of vapor, CO₂ clathrate, ice, salt-hydrates and CO₂-solid. Then, the sample was heated in order to observe the equilibrium phase changes until the total homogenization at a given temperature (T_{htot}). Many times T_{htot} was not reached in order to inhibit decrepitation of the fluid inclusions before Raman and LA-ICPMS analysis. The heating rate was 5 °C/min and close to phase changes it was reduced to 0.5 or even to 0.1 °C/min. For accurate measurements of some phase changes, the “cycling” technique was used (Goldstein and Reynolds, 1994; explained in the appendix IIB). The salinity is expressed in wt % NaCl equivalent and was determined from the final melting of ice (Bodnar and Vityk, 1994), the final melting of clathrate or the final melting of halite (Bodnar and Vityk, 1994), depending on the phases present within the inclusion. The estimation of the salinity is difficult in some CO₂ bearing fluid inclusions (especially in the intermediate density carbonic type, IDc and Liquid Aqueous carbonic, Lc; see below). In these inclusions, liquid CO₂ is difficult to observe and the clathrate melting temperature (T_{mcla}) is very variable within a single FIA. Even more, the system can contain CH₄ and salts which can form a solid solution with the CO₂ clathrate and alter its stability, modifying the calculated salinity. To check any difference, the salinity was also calculated using the T_{mcla} of the H₂O-CO₂-NaCl-CH₄ system (Jacobs and Kerrick,

1981; Brown and Hagemann, 1994). We have made the calculation using both procedures and the salinity did not vary significantly; since the CH₄ content is small in all the carbonic fluid inclusions, we have preferred to simplify the procedure using the method of Diamond (1992).

II.3.4. Raman analysis

Three gas species (CO₂, CH₄ and N₂) were analyzed by Raman Microprobe at the University of Bern in Switzerland selecting a laser beam with $\lambda = 514$ nm for the measurements. In order to correct the eventual contribution of atmospheric N₂ (blank measurements; Burke, 2001), it was subtracted from the N₂ measured in the fluid inclusions. Molar fractions of gas species in each inclusion were calculated following the procedure explained in Burke (2001) and in the Appendix IID of this thesis. A total of 17 fluid inclusions were analyzed by Raman spectroscopy with three or four representative fluid inclusions from each type.

II.3.5. Laser ablation-inductively coupled plasma-mass spectrometry analysis (LA-ICPMS)

Laser ablation - inductively coupled plasma mass spectrometry (LA-ICPMS) measurements were performed at the ETH Zürich, in an Elan 6100 ICP-MS (Perkin Elmer, Canada) combined with a 193 nm excimer laser system (Lambda Physik, Germany). Details about the instrumentation and quantification procedure for fluid inclusion analysis are described in Günther et al., (1998), Pettke et al., (2000) and Heinrich et al., (2003). The imaging optical system permits to adjust the aperture in the laser beam to control the ablation with different pit sizes. After careful cleaning of the sample-chips and the chamber to avoid the external contamination, a petrographic microscope which allows direct observation of the sample was used to locate a previously selected fluid inclusion. The absolute quantification of the signal (Fig. 3) was

obtained by time integration of all element intensities, correction for host mineral contributions (Na, K, Mn, Zn, Cs and Pb), comparison of intensity ratios with the external standard (NBS 610 glass from NIST), and transformation of the element ratios into absolute concentrations using an internal standard. For fluid inclusions, this internal standard is the Na concentration, obtained from the microthermometry as wt % NaCl eq. (Heinrich et al., 2003). The LA-ICPMS conditions for this study are detailed in the Table 3. Data reduction and quantification was done with the SILLS computer software developed at the ETH Zürich (Guillong et al., 2008b). Up to 130 fluid inclusions were analyzed by laser ablation, all of them forming part of representative FIA of all generations of the Sultana vein.

EXCIMER 193 nm ArF laser COMPLEX 110I	
Fluence	30 -35 J/cm ²
Pulse duration	10 - 20 ns
Repetition rate	10 Hz
Pit size	15 and 200 µm
Ablation cell volume	1 cm ³
Cell He gas flow	1.1 L/min (+5 ml/min H ₂)
ELAN 6100 DRC quadrupole ICP-MS	
Nebulizer gas flow	0.85 L/min Ar (can vary due to daily tuning)
Auxiliary gas flow	0.85 L/min Ar (can vary due to daily tuning)
Cool gas flow	15 L/min Ar
RF power	1550 W
Quadrupole setting time	3 ms
DATA AQUISITION	
Readings per replicate	400
Dwell time per isotope	Adjusted to 10 ms (standard)
Isotopes	23Na,29Si, 32S, 39K, 42Ca, 55Mn, 57Fe, 65Cu, 66Zn, 75As,133Cs, 208Pb,197Au, 125Te, 209Bi

Table 3. LA-ICPMS analytical conditions for the fluid inclusions studied in the Sultana vein.

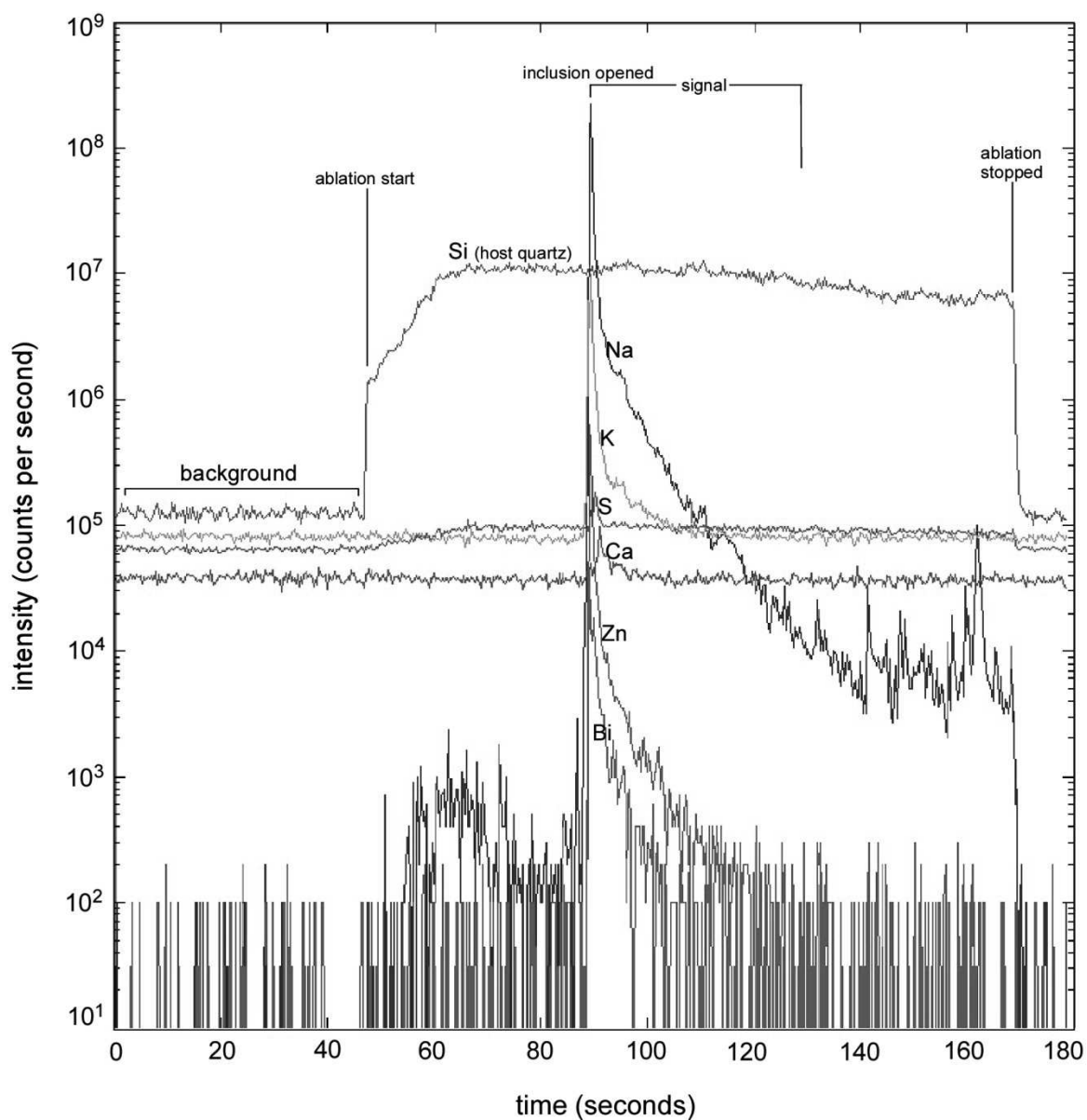


Figure 3. LA-ICPMS signal of a single fluid inclusion (flinc10ma09d04, Lcx) of the Sultana vein. The signal records the elements (only some of them are shown here for better clarity) analysed inside the fluid inclusions. Note the good signal for elements that usually are difficult to identify, such as S or Ca. For the quantification, the signal was integrated from 85 to 125 seconds.

II.4. Vein quartz textures from SEM-cathodoluminescence

The main purpose of the SEM-Cathodoluminescence (SEM-CL) analysis is to try to identify the different types and generations of quartz and their relationship with the precipitation of the sulfides and gold. Cathodoluminescence is a powerful tool since the images reveal textures that are not observable under the transmitted light microscope or backscattered electron imaging (BSE) (Fig. 4). After the SEM-CL analyses, the fluid inclusion assemblages can be assigned to the quartz domains, allowing to the reconstruction of the hydrothermal fluid pulses that circulated through the vein.

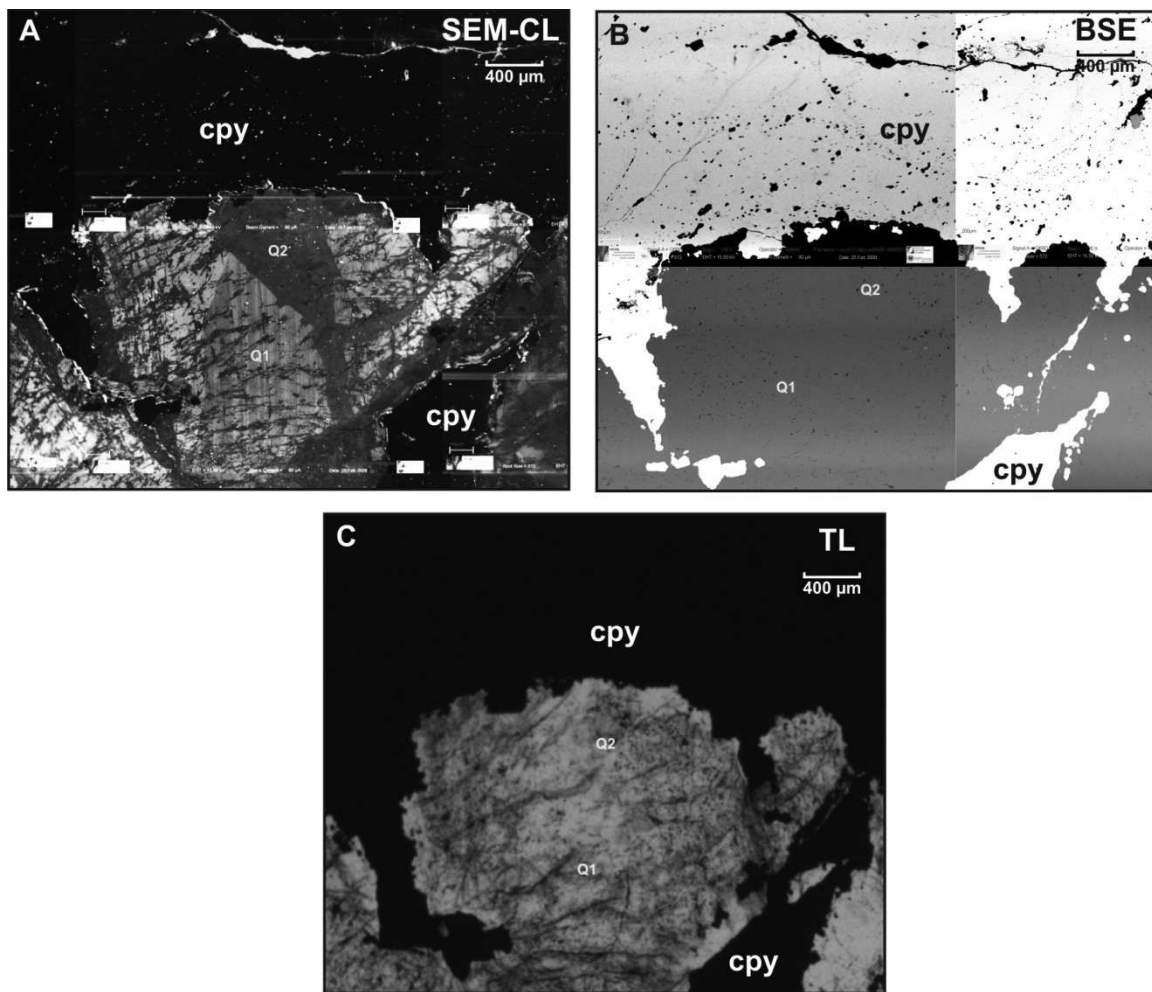


Figure 4. Comparison between images of the same area (sample CSU2) taken by scanning electron microscope cathodoluminescence (SEM-CL) (A), back scattered electron imaging (BSE) (B) and normal transmitted light (TL) (C). The SEM-CL image shows at least two different textures of quartz: an older euhedral zoned quartz (Q1) that is crosscut by a younger generation (Q2) that precipitated along fractures and replaced Q1 as irregular patches. These textures and the relationships between the quartz generations are not visible in the other images, where quartz looks as optically continuous. Note that in the BSE image, the fractures and imperfections within the sulfides can be easily observed.

In the Figure 5A and 5B, we illustrate a hypothetical reconstruction of the evolution of the Sultana vein infill based on the SEM-CL textures. The images reveal a complex growth history with several episodes of quartz precipitation that are consistent through all the studied samples. This evolution can be summarized in at least three clearly separated generations of quartz: the earliest one comprises the bulk of the vein and in hand sample it corresponds to milky texture less massive, usually deformed quartz (Fig. 5A). Q1 is bright-luminescent and shows local euhedral growth zoning indicating crystallization into open spaces (Fig. 5E). This quartz has superimposed dark luminescent patches of grayer luminescence related quartz.

After the precipitation of the Q1 generation, a process of dissolution and microfracturation took place followed by the precipitation of a second generation of quartz (Q2, Fig.5). Q2 shows dark-luminescence and occurs overgrowing or filling microfractures that crosscut Q1. In the center of the veins, close to the sulfides, the Q2 grows into open spaces where perfect euhedral growth along the c-axis is visible (Fig. 5C). This later generation is always and invariably in direct contact with the sulfides suggesting that the ore precipitated after the Q1 dissolution and before or together with the precipitation of Q2. Very similar quartz generation stages have been previously documented in porphyry-copper deposit sulfide veins (e.g. Redmond et al., 2004; Rusk et al., 2008; Landtwing et al, 2010).

A third generation of quartz (Q3) shows very dark-luminescence and occurs filling late fractures that crosscut both the first and the second generation of quartz.

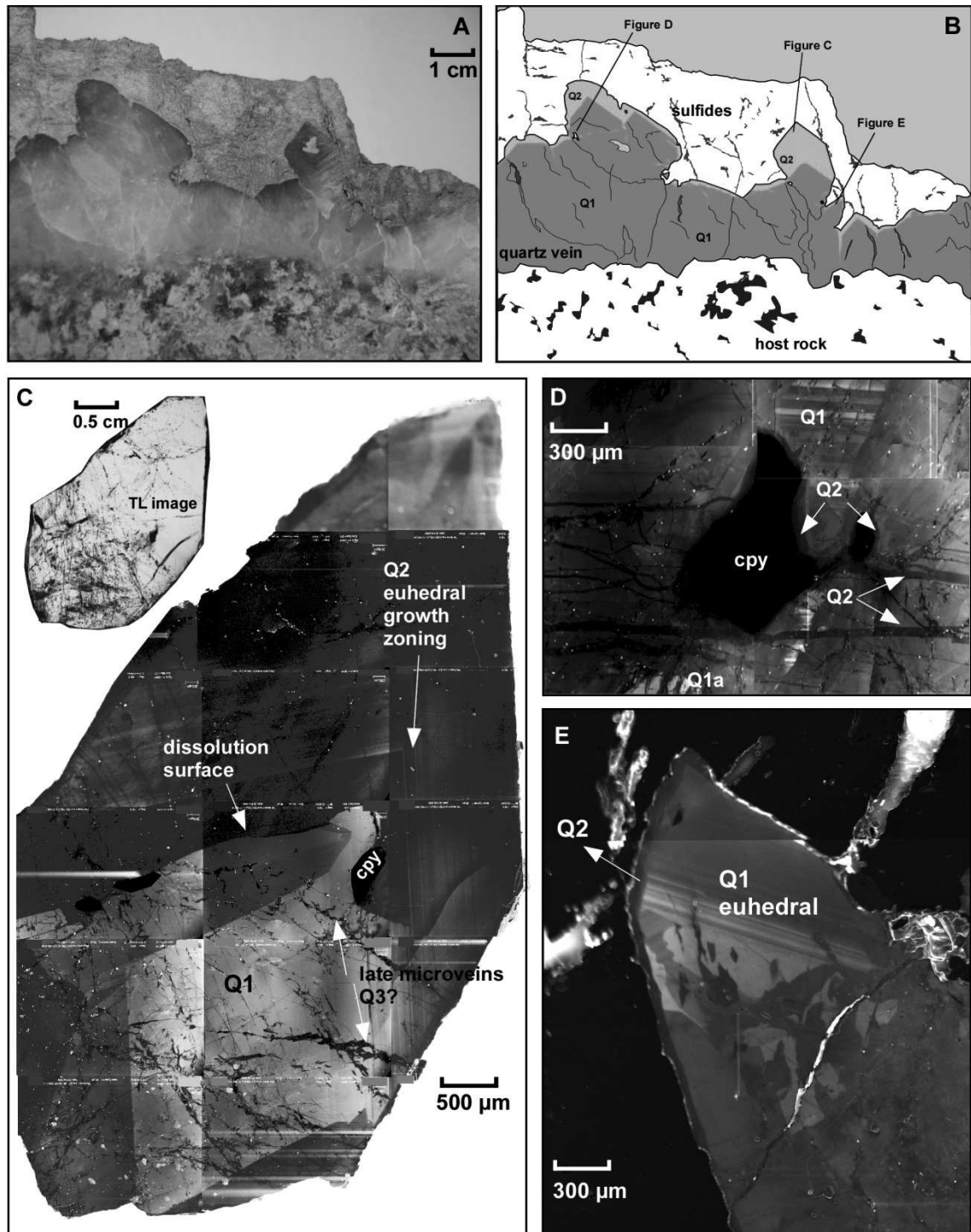


Figure 5. (A and B) Reconstruction of an area from the vein-sample CSU1 based on SEM-CL images. Note that the Q1 quartz generation covers the most part of the vein infill, whereas Q2 (in green color) is only represented by a narrow rim of quartz, filling open spaces as euohedral crystals or filling

fractures; **(C)** Photomosaic of a free standing quartz crystal (sample SUCH3) where the two quartz generations can be observed. This pattern is continuously repeated in many samples with chalcopyrite and quartz in the center of the vein; **(D)** Detail of a small single grain of chalcopyrite that precipitated along a microfracture filled with quartz Q2 (sample CSU1A); **(E)** A detail of a thin film of Q2 superimposing the euhedral zoning of Q1. This Q2 is always in direct contact with the chalcopyrite.

This clear textural evolution can only be observed in the small pods of euhedral quartz crystals within the chalcopyrite. The milky quartz that forms the bulk of the vein, and is interpreted as similar to the Q1 quartz described above, shows no discernible textures in the cathodoluminescence images, with only little variations in the intensity (Fig. 6). Rusk (2009) suggests that this lack of visible textures results from the recrystallization of quartz during low grade metamorphism but also could be due to a major event of deformation. In any case, and as mentioned before, the fluid inclusions are here too small and not good for a detailed petrography

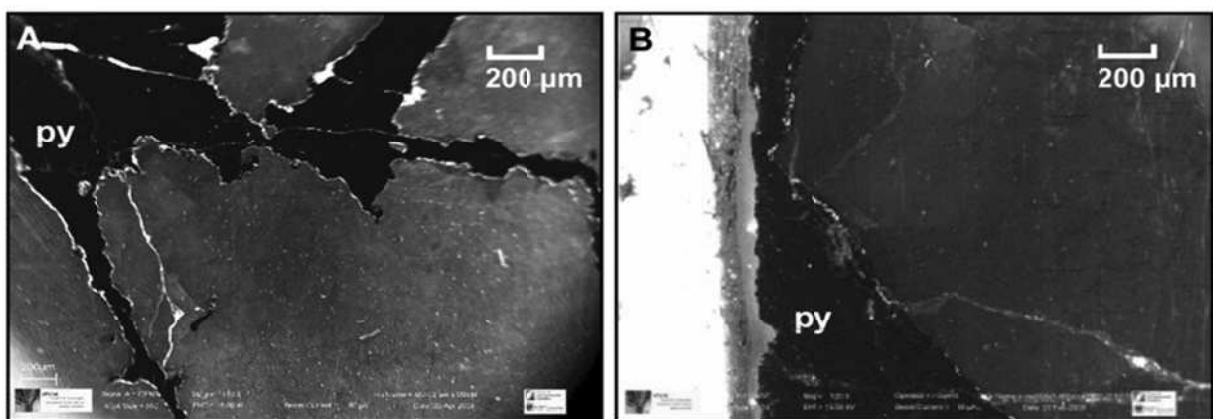


Figure 6. SEM-CL images of samples belonging to the quartz-pyrite early stage (samples SUpy92, **A** and SUpy93, **B**) where the quartz Q1 lacks of visible

textures under SEM-CL. In these veins, there are myriads of fluid inclusions, but they are too small for a suitable petrography and microthermometry

II.5. Types and distribution of fluid inclusions

II.5.1. Fluid inclusion types

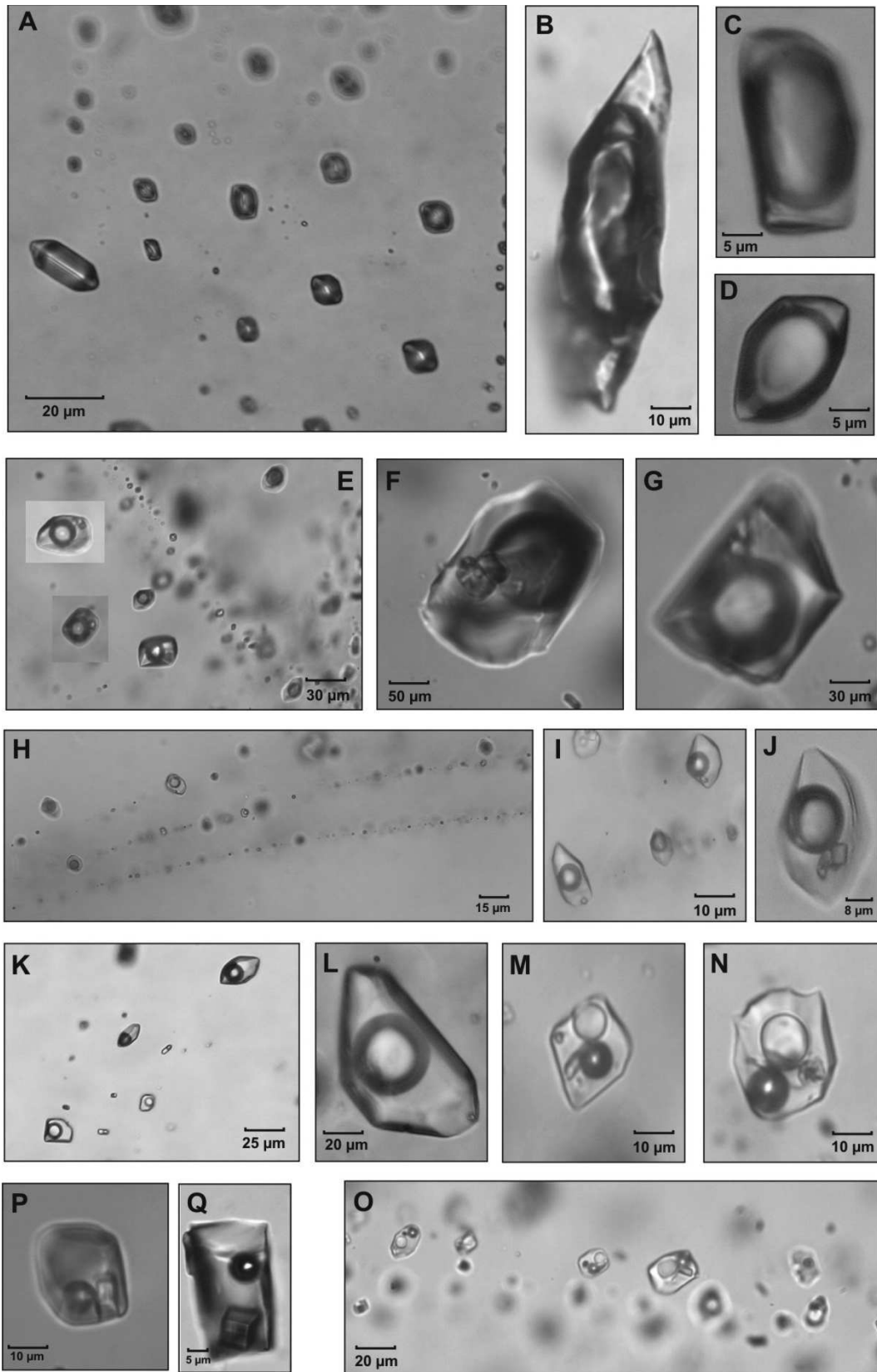
Fluid inclusion types are classified according to their nature and phase volume proportions at room temperature. All of them form part of fluid inclusion assemblages, representing groups of petrographically associated fluid inclusions that occur along growth zones or fractures (Goldstein and Reynolds, 1994). Six types of fluid inclusions are identified as: vapor carbonic (Vc), intermediate density carbonic (IDc), liquid carbonic (Lc, Lcx), liquid aqueous (La), brine (B) and brine polyphase (Bpol) (Fig. 7).

The shapes are mostly negative crystal to rounded isometric. Sizes vary between very large (>100 μm in some IDc fluid inclusions) to very small inclusions (2 – 3 μm in La). The mean size (20 – 25 μm) is good enough for both microthermometry and subsequent LA-ICPMS analysis. Most of the studied fluid inclusion assemblages are pseudosecondary and secondary in origin. Primary fluid inclusions exist but are rare and difficult to work with because of their small size.

Vapor carbonic fluid inclusions (Vc; Fig.7A to 7D) are low density with the bubble (without typically distinguishable liquid CO₂ phase at room temperature) occupying almost the 80-90% of the total volume. In fluid inclusions where the liquid fills less than around 20%, the liquid phase is generally invisible due to internal reflection of the inclusion walls (Ulrich et al., 2001). However, in a few particularly large inclusions with protrusions and pointy tips, all the phases can be distinguished (Fig. 7B).

Intermediate density carbonic fluid inclusions (IDc, Fig.7E to 7G) have almost similar proportions of vapor (40-50 % vol.) and liquid. Liquid CO₂ is usually not distinguishable at room temperature because it's small presence. They always contain one or most commonly two highly refractive transparent crystals.

Figure 7 (next page). Fluid inclusion types at Sultana vein. **(A)** Pseudosecondary trail of vapor carbonic (Vc) inclusions in Q2 growth zone; sample SUCH3. **(B)** Vc fluid inclusion with pointy shape where the liquid aqueous, liquid carbonic and vapor carbonic phases can be easily distinguished; sample SU88. **(C and D)** Two portrait pictures of Vc fluid inclusions. Note that the carbonic liquid phase is not visible here at room temperature, but clathrate nucleate during the cooling runs; samples SUCH3-3-L. **(E)** Pseudosecondary trail of intermediate density carbonic (IDc) fluid inclusions that start in the Q2 quartz generation; sample CSU1-A-1-AF. **(F and G)** Portrait of two IDc fluid inclusions with 30-50% of bubble volume and two transparent crystals; sample CSU2-4-E. **(H)** Parallel secondary trails of liquid carbonic (Lcx) fluid inclusions; sample SUCH1-6.3-P. **(I and J)** Detail of Lcx fluid inclusions in the parallel trails; sample SUCH1-6.3-P. **(K and L)** Liquid carbonic (Lc) fluid inclusions in early secondary trails. These fluid inclusions usually are lack of daughter crystals; sample CSU1A-U. **(M and N)** Two portrait of brine poliphase (Bpol) inclusions with halite, sylvite and 1 or 2 more crystals; sample SUCH 5-S. **(O)** A pseudosecondary trail of Bpol fluid inclusions; sample SUCH3-5-UW. **(P and Q)** Halite saturated brine (B) fluid inclusions; samples SU88 and SUCH1 respectively.



Liquid carbonic fluid inclusions (Lcx, Fig. 7H to 7J) are higher in density (20-30 % bubble vol.) than the IDc ones and usually the liquid CO₂ phase can be observed at room temperature. Most of them also show two small transparent crystals. Another generation of liquid carbonic fluid inclusions (Lc, Fig. 7K and 7L) is petrographically indistinguishable to the Lcx one, except that some of these inclusions do not have daughter crystals, the CO₂ liquid phase is more difficult to observe and principally, that they occur at petrographically different positions.

Brine polyphase fluid inclusions (Bpol, Fig. 7M, 7N and 7O) contain a small bubble (10-20 % vol.) and have up to three daughter crystals including halite and sylvite.

Brine fluid inclusions (B, Fig. 6P and 6Q) consist of an aqueous liquid phase and a halite crystal.

Liquid aqueous fluid inclusions (La) have small bubbles (5-10%) and are highly irregular and flat in shape.

II.5.2. Distribution of the fluid inclusions: relative timing of fluid entrapment

The precise timing of fluid inclusion generations relative to the main sulfides and gold precipitation in Sultana is usually difficult to constrain, even when there is a clear picture of the different stages of quartz growth. In the most earlier and deformed Q1 quartz, fluid inclusions are abundant and randomly distributed making the petrography difficult. This is why we have used systematically the combination of fluid inclusion petrography and SEM-cathodoluminescence images in all samples, in order to assure the correct interpretation of relative timing. The spatial distribution of the fluid inclusion types varies vertically in a single crystal together with the succession of quartz generations as follows (Fig. 8):

The base of the crystal is dominated by highly deformed Q1 (Fig. 8.1), where the fluid inclusion assemblages are usually affected by post-entrapment processes such as opening and refilling, decrepitation, etc. Almost all the fluid inclusion types are randomly distributed in the core of the crystals. Sometimes, brine poliphase (Bpol) and vapor (Vc) inclusions appear together but their possible coeval trapping is very difficult to prove. Parallel trails of liquid carbonic (Lcx) fluid inclusions clearly postdate deformation, and crosscut the crystal boundaries, indicating that they are secondary on respect to the Q1 precipitation. These trails also crosscut the younger Q2 generation, but in some cases the relationships are obscure.

Pseudosecondary (secondary in some cases) trails of intermediate density carbonic fluid inclusions (IDc) are difficult to situate in the vein growth history as they are invariably in Q1 but it is not clear if they crosscut or not the early stages of the second generation of quartz.

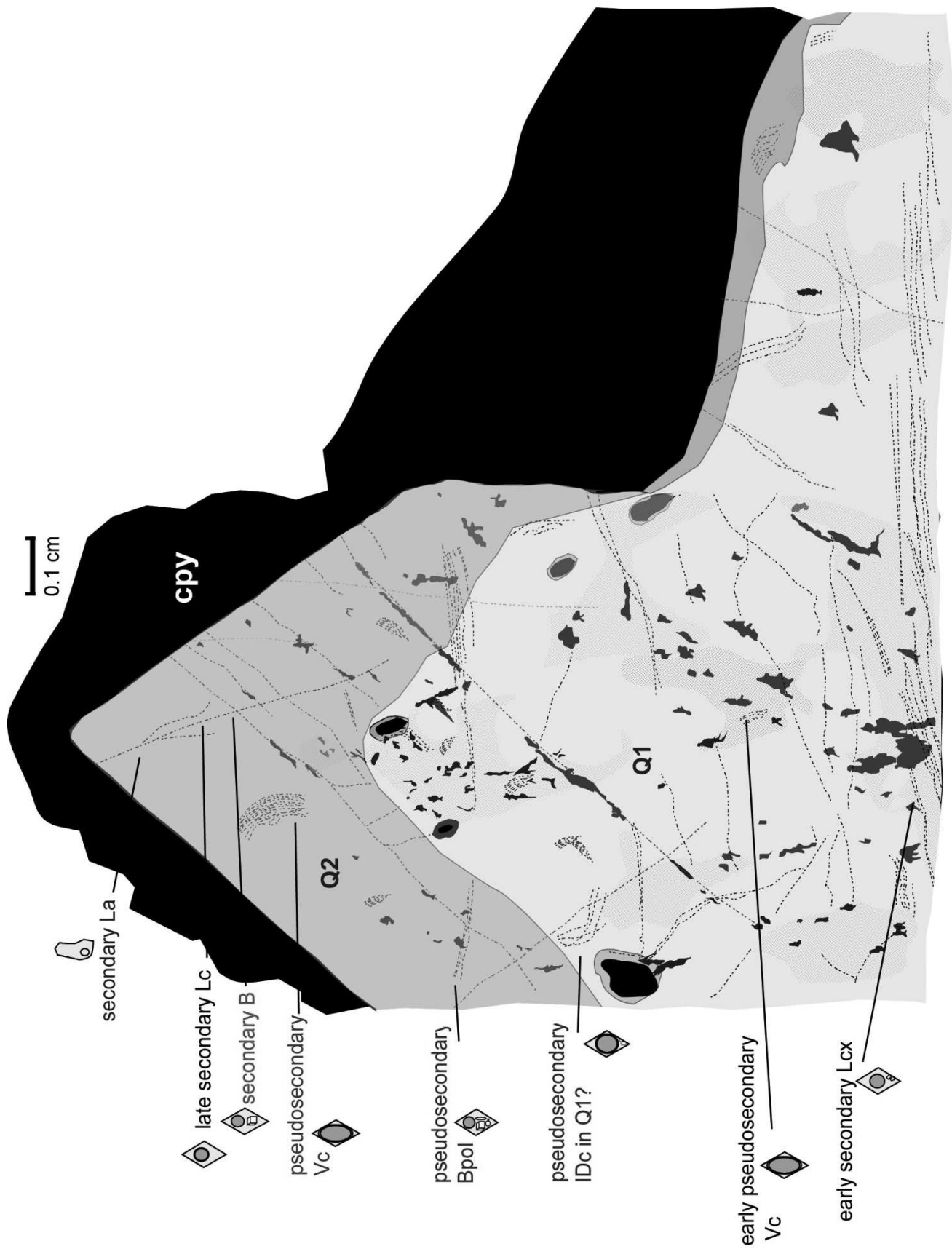
Clear pseudosecondary vapor carbonic (Vc) fluid inclusion assemblages are associated to the growth zones of Q2 (Fig. 8.1). They occur as well defined,

consistent and abundant pseudosecondary trails of fluid inclusions. In two of the studied samples (SUCH3 and SUCH1), the vapor carbonic fluid inclusion assemblages are situated in the same growth zone where brine polyphase (Bpol) fluid inclusion trails start, suggesting their spatial coexistence. Even more, inside two vapor carbonic pseudosecondary trails, a few isolated brine polyphase inclusions can be also recognized.

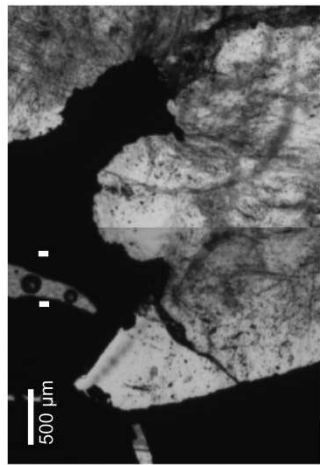
Again, liquid carbonic (Lc) fluid inclusion trails are found as healed fractures crosscutting all the Q2 and continuing along Q1 (Fig. 8.2). However, as they do not crosscut the basis of the Q1, we consider them as secondary but in a later generation than the petrographically undistinguishable parallel trails in Q1.

Liquid aqueous (La) and brine inclusions (B) are clearly the latest recognized generations in the system and they take place as secondary trails crosscutting all the quartz generations. The microthermometry results (see next section) also confirm that these fluids postdate the main mineralization event.

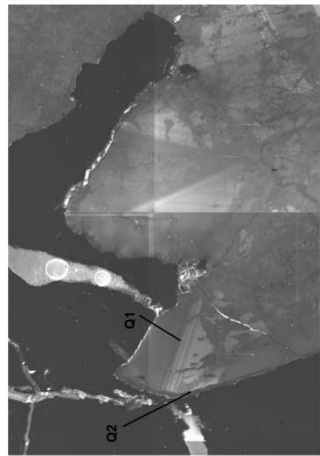
Figure 8. (next page) Sketch of the petrographic relationships in a quartz crystal (sample SUCH2) (Fig. 8.1) and in a sample with intergrown chalcopyrite-quartz (sample CSU2-bis) (Fig. 8.2), summarized from observations in several doubly polished thick sections. The quartz domains interpreted from the SEM-CL are also shown in order to make clear the correlation between the petrography and the quartz generations. Note that in the Fig. 8.2C sometimes is difficult to distinguish between some IDc, Lc and Lcx fluid inclusion generations. Among others, microthermometry and LA-ICPMS analysis on all these fluid inclusion assemblages have been performed.



A. Transmitted light



B. SEM-Cathodoluminescence



C. Petrographic interpretation



II.6. Microthermometric data and Raman results

The determination and interpretation of the temperature of phase changes within the fluid inclusions during heating and cooling runs (microthermometry) has been performed only in clearly defined fluid inclusion assemblages selected from the petrography. There is a moderately to good consistency of the data within most of them indicating a good preservation of the original features in the fluid inclusions. In addition, three or four representative fluid inclusions of each generation were qualitative and quantitative analyzed by Raman spectroscopy in order to know the possible presence of gases other than CO₂ in the vapor phase and their respective molar fractions. A summary of all microthermometric and Raman results is given in the Table 4 and the all data set is given in the Appendix IIB and IID of this thesis.

Low density vapor carbonic inclusions (Vc) show variability in the data due to the small proportion of liquid aqueous phase which makes the observations difficult. The CO₂ presence is confirmed by the solid CO₂ melting (-57° to -58°C) and Raman analysis which indicate high amounts of CO₂ (98.3%) and minor CH₄ (1.7%) within the bubble. The clathrate melting temperatures, obtained by the cycling method in some good assemblages, yield salinities between 2.4 and 3.4 wt % NaCl eq. When visible, the carbonic phase homogenizes via dew point (to the vapor phase) at $25.7^{\circ} \pm 2.4$ °C. Final homogenization temperature occurs at $348^{\circ} \pm 17$ °C determined only in some inclusions with protrusions or pointy tips (Fig. 7B) by bubble expansion into the vapor phase. These measurements indicate minimum temperatures due to the difficulty of the observations.

The temperature of phase changes in the intermediate density carbonic (IDc) fluid inclusions are difficult to interpret, even if they are large in size and good to measure. The presence of liquid CO₂ and the Raman analysis confirm the existence of CO₂ (92.6%) and CH₄ (7.4%) in the vapor phase. The clathrate final melting

temperature is variable, even within the same assemblages (between 0 ° and 8 °C), yielding also variable salinities, between <4 and 15 wt% NaCl eq. When visible, homogenization of CO₂ occurs at 27.7±3.1°C to the vapor and in a few inclusions to the liquid phase. The total homogenization to the liquid phase (from ~370 to ~480°C) could only be measured in some inclusions due to widespread decrepitation before final homogenization. Few of them homogenize via meniscus fading.

Liquid carbonic fluid inclusions (Lc and Lcx) show very consistent data within all the measured FIA. Raman spectroscopy shows the dominance of CO₂ (98.2 to 98.7%) with small amounts of CH₄ (1.3 to 1.8 %) in the vapor phase. The CO₂ liquid phase homogenizes via dew point at 23.9±0.9 °C (Lc) and 24.7±1.7 °C (Lcx). The clathrate melting temperatures yield salinities of 9.7±1.1 (Lc) to 11.4±1.3 (Lcx) wt % NaCl eq. and the total homogenization temperature occurs at 351±8 °C and 352±14 °C for Lc and Lcx respectively, both to the liquid phase.






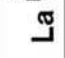

Total homogenization of brine polyphase (Bpol) and brine (B) fluid inclusions occurs into the liquid phase at 348 ° ± 20 °C and 169 ° ± 38 °C with salinities of 40 ± 3.1 and 31.4 ± 1.8 wt% NaCl eq. respectively. In some brine fluid inclusions, the temperature of dissolution of the halite is significantly higher than that of the bubble disappearance. The difference in homogenization temperature between brine and brine polyphase inclusions as well as their different petrographical constrain suggest the existence of two different inputs of brine fluids, one related to the main ore forming event and most probably coexisting with the vapor phase and a later one, with lower temperatures and salinities.

Liquid aqueous (La) fluid inclusions have ice melting temperatures between 6 ° and 9 °C, indicating average salinities of 11.9±2.7 wt% NaCl eq. The final homogenization temperature occurs at 175±63 °C. As the brine inclusions, they are

interpreted as late in the fluid evolution of the vein and unrelated to the main ore; Raman analysis do not show any dissolved gas in the vapor phase.

Microthermometric data of all fluid inclusion types are plotted in the Figure 9 as salinity versus total homogenization temperature. Point symbols represent the fluid inclusion assemblages where both T_{htot} and salinity could be determined in each fluid inclusion and the shaded boxes represent the overall ranges for each type. The plot also shows the rather good internal consistency within the different types of fluid inclusions. Only in some brine (B) inclusions the data are more widespread. Taking in account the homogenization temperatures and the petrography, most of the vein filling and ore precipitation occurred in a narrow temperature range, between 350° and 500 °C. Note that as we discuss later, the trapping pressure and temperatures from the coexisting vapor and brine poliphase fluid inclusions can be shifted due to the presence of CO₂ and salts other than NaCl.

Table 4. (next page) Summary of microthermometric data and Raman spectroscopic analyses. Abbreviations: **Vc**, vapor carbonic; **Bpol**, brine polyphase; **IDc**, intermediate density carbonic; **Lc**, liquid carbonic early secondary trails; **Lcx**, liquid carbonic parallel trails in the base of Q1; **B**, brine; **La**, liquid aqueous; **c**, carbonate crystals; **o**, opaque (daughter? accidentally trapped?) crystals; **Hal**, halite; **Silv**, sylvite; **L**, liquid; **V**, vapor. Bubble infill has been optically estimated under the microscope. The numbers represent the averages of all the fluid inclusions included in each type of FIA with the respective standard deviation. In gas species molar fractions (Raman results), the data are subject to uncertainties due to the volume-area calculations.

	 IDc	 Vc	 Bpol	 Lcx	 Lc	 B	 La
Quartz generation	Psec.-Sec. trails, in Q1, not clear if they start in Q2	Psec. trails + clusters in euhebral Q2	Psec. Trails in euhebral Q2 Not abundant	Sec. parallel trails in deformed Q1	Healed trails + clusters in Q1 and euhebral Q2	Widespread	Widespread
Phases at room T°C	$L + L_{CO2} + V_{CO2} + 2c$	$L + L_{CO2} + V_{CO2} \pm O$	$L + V + Hal + Si/v + c$	$L + L_{CO2} + V_{CO2} + 2c$	$L + V_{CO2} \pm L_{CO2}$	$L + V + Hal$	$L + V$
Bubble Infill (%)	40 – 50	85 – 90	20	15 – 20	15 – 20	15 – 20	15 – 30
Tm CO₂ (°C)	-57.5 ± 0.5	-57.4 ± 0.7		-57.1 ± 0.5	-57.5 ± 0.6		
Tm clathrate (°C)	2.9 ± 3.2	8.7 ± 0.6		3.0 ± 1.6	4.5 ± 0.7		
Thom CO₂ (°C)	27.7 ± 3.1 to vapor or liquid?	25.7 ± 2.4 to vapor		27.4 ± 1.7 to vapor	23.9 ± 0.9 to vapor		
T halite (°C)			329 ± 17			192 ± 39	
Salinity (wt % NaCl eq.)	<4 to 15 very variable	2.4 ± 1	40 ± 3.1	11.4 ± 1.3	9.7 ± 1.1	31.4 ± 1.8	11.9 ± 2.7
Thom total (°C)	426 ± 48 to liquid or critical	348 ± 17 to vapor	348 ± 20	352 ± 14 to liquid	351 ± 8 to liquid	169 ± 38 to liquid or halite	175 ± 63 to liquid
CO₂ molar fraction (%)	92.6	98.3		98.2	98.7		
CH₄ molar fraction (%)	7.4	1.7		1.8	1.3		

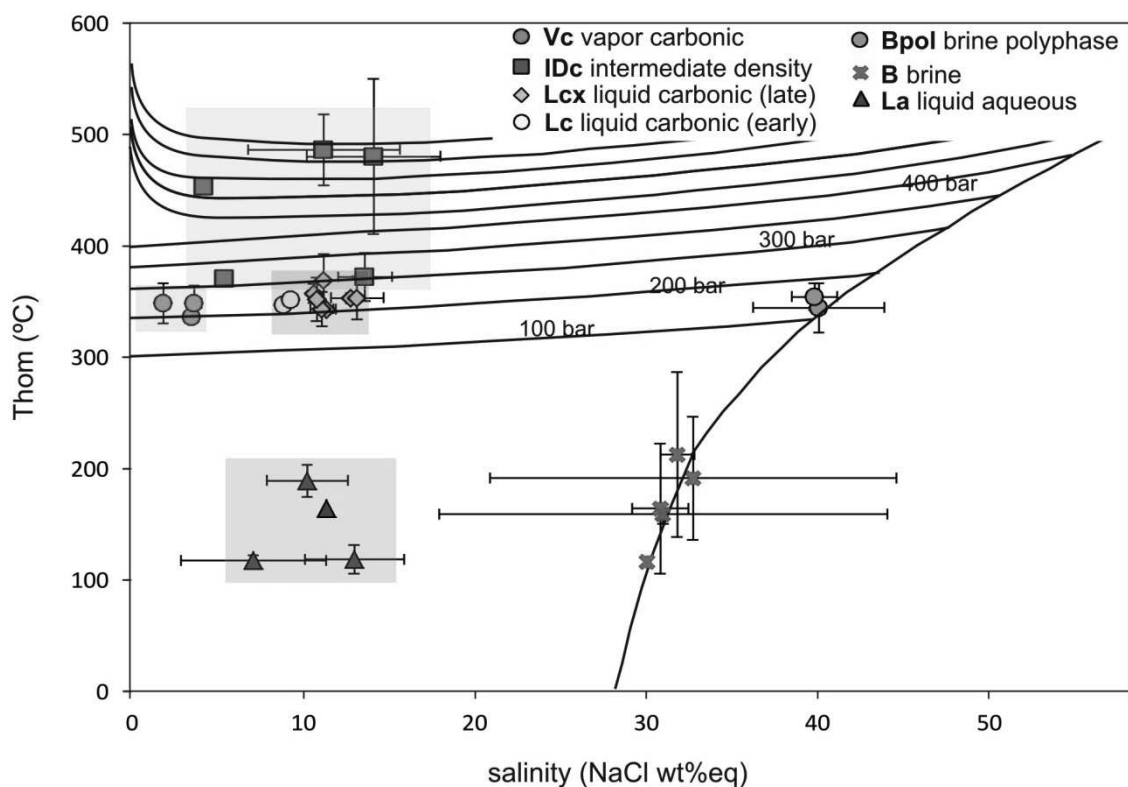


Figure 9. Plot of the salinity (measured from the clathrate, halite and ice melting dissolution temperatures) versus the total homogenization temperatures of all the inclusion types. The different symbols represent the fluid inclusion assemblages where both the Thom and the salinity could be determined in the inclusions and the boxes represent the overall range for each type.

II.7. Density, molar volume calculations and minimum pressure – temperature estimations

The density, CO₂ mol fraction and minimum pressure–temperature estimations of the different fluids that circulated through the Sultana vein are here constrained for latter discussion. One of the requirements to build the model is the determination of the homogenization temperature of the CO₂ (ThCO₂) to liquid, vapor or critical phases. ThCO₂ measurements can have a large error even under detailed observations because the phase changes in the CO₂ phase are difficult to

observe. In order to minimize the error, we tried to select irregular, elongated and pencil shaped fluid inclusions in which the disappearance of the meniscus is more obvious (Fig. 10). In addition, the visual estimation of the volume proportions can also carry large uncertainties due to the absence of a third dimension under the microscope (Bakker et al., 1996; Bakker and Diamond, 2006). These errors in estimating the ThomCO_2 and the volume proportions have a large effect on calculated density and therefore, on the isochore slopes.

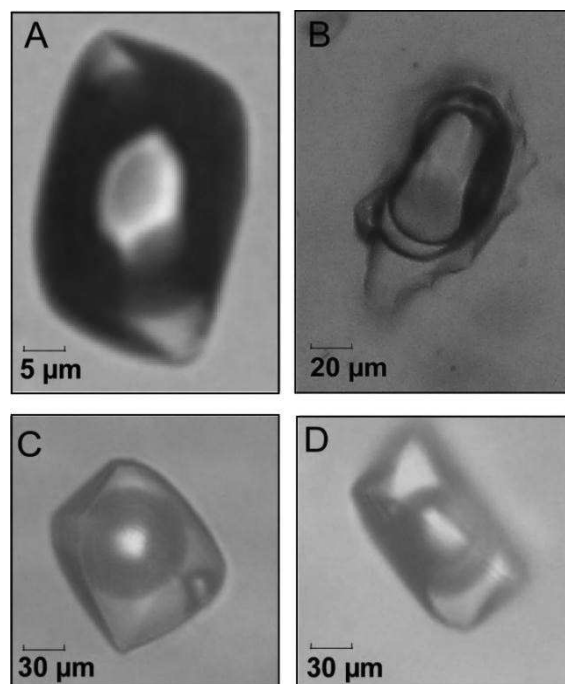


Figure 10. Four examples of fluid inclusions (**A and B**, Vc type and **C and D**, IDc type) where the liquid CO_2 phase is not observable at room temperature (A and C) and where, for the same type of fluid inclusion, it is easily observable thanks to the irregular and elongated shapes (B and D). Measurements are thus dependent on the optical visibility of the fluid inclusions

II.7.1. Density

The density calculations of the brine (B), brine polyphase (Bpol) and liquid aqueous (La) fluid inclusions can be determined assuming the simplified H₂O-NaCl system, and are calculated directly from the microthermometric data. For that, we used the `sowatfinc_inclusion` computer program (Driesner, 2007 and Driesner and Heinrich, 2007, www.geopetro.ethz.ch/people/td/sowat). The carbonic fluid inclusions (Lcx, Lc, Vc, IDc types) can be assumed to belong to the H₂O-CO₂-(CH₄) system. Here, the calculation of the bulk composition and the density needs an additional parameter, the volume proportions of the CO₂ and H₂O phase that is subject to a major error as mentioned before. The volume fractions together with the estimated salinity and the measured ThCO₂ allow calculating the bulk density using the BULK computer program (FLUIDS package, Bakker, 2003; <http://fluids.unileoben.ac.at/Computer.html>).

The estimated bulk densities of the different groups of fluid inclusions are given in Table 5. Note, for example, that the density of the vapor carbonic inclusions (Vc) is close to 0.43 g/cc, and is probably overestimated since under the microscope they seem to be of lower density. In such a way, the density of the intermediate density fluid inclusions is estimated to be close to 0.77 g/cc and as showed in the Figure 6 they look more like of intermediate density.

Type	n	Bulk Density (g/cc)	XCO ₂ (%)	XH ₂ O (%)	XNa ⁺ +Cl ⁻ (%)
Vc	5	0.43	28.7	70	1.1
IDc	9	0.77	10.4	85.5	4.1
Lcx	4	0.83	6.4	87.5	6.1
Lc	3	0.79	6.1	88.5	5.4
Bpol	4	1.08			
B	5	1.12			
La	3	0.94			

Table 5. Calculated bulk densities and CO₂, H₂O and [Na⁺ + Cl⁻] fractions in selected assemblages belonging to all the fluid inclusion types. These results depend on the estimation of the bubble proportions so probably they are overestimated

II.7.2. CO₂ fraction and molar volumes (Vm)

Raman spectroscopy analyses confirm the presence of CO₂ and CH₄ gases in the carbonic-bearing fluid inclusions (Table 4). The CH₄ proportion is low in most of the inclusions and thus, it can be neglected during the estimation of the CO₂ fraction on respect to water and salt content. The CO₂ fraction and molar volumes have been calculated using the same computer program used for the density (BULK, Bakker, 2003), and the results are given in the Table 5.

II.7.3. Minimum trapping pressure and temperature estimations: calculation of the isochores

The estimation of the minimum trapping pressure was obtained from the construction of isochores, defined as lines of constant volume in the P-T space (Goldstein and Reynolds, 1994). Isochores have been calculated from the microthermometric data (salinity and total homogenization temperature) and the fluid composition data (system type and density). In the case of the carbonic fluid inclusions (IDc, Vc, Lc and Lcx), the simplified H₂O-CO₂-NaCl system has been

used. This was done with the ISOC computer program (FLUIDS package, Baker, 2003) with the EOS of (Bowers and Helgenson, 1985; Bakker, 1999b). The isochores for the B, Bpol and La fluid inclusions were calculated with the *sowatfinc_inclusion* computer program (Driesner, 2007; Driesner and Heinrich, 2007) assuming the H₂O-NaCl system. After constructing the isochores, an independent P or T constrain is needed for real trapping conditions estimations except for the clearly coexisting brine polyphase and vapor fluid inclusions. This late ones represent a boiling assemblage and, thus, the temperature and pressure of homogenization are close to the trapping ones. The isochore plot and the interpretation of the P-T conditions are given in the discussion of this chapter (Fig. 16).

II.8. LA-ICPMS microanalytical results: element concentrations in the fluids

In order to reconstruct the chemical evolution of the hydrothermal fluids circulating through the vein, 130 individual fluid inclusions from 21 assemblages of all generations were measured by LA-ICPMS. The Figure11 shows the absolute element concentrations of the fluid inclusion assemblages, sorted according to the petrographically inferred timing sample evolution and between assemblages, sorted according to decreasing Cu concentration. Average element concentrations are also given in the Table 6 with the corresponding standard deviations. In general, the analyses of the vapor-rich inclusions (Vc) are less accurate compared to more saline and brine inclusions due to its lower proportion of liquid and solutes that give not strong signals.

There are no significant differences in the absolute concentrations among major elements (Na, K, Fe, Mn, Pb, Zn, As) in all the generations of fluid inclusions, showing rather uniform values through time (Fig. 11). Ca is sometimes difficult to analyze in the vapor (Vc) and intermediate density (IDc) fluid inclusions because the values are close to the detection limit or below it. In the brine polyphase and

brine inclusions Ca is present sometimes in even higher concentrations than Na (49 wt % and 33 wt % Ca in Bpol over 7.74 wt % and 11 wt % Na in B). Unlike major elements, Cu varies at the assemblage-scale, with lacking of constant values between the fluid inclusions in the same assemblage. This variability has been explained either as indicative of changes in the fluid composition in the source or as due to postentrapment reequilibrations in the fluid inclusions (Li et al., 2009; Zajacz et al., 2009). Copper varies also through the time, decreasing one to two orders of magnitude between the vapor carbonic (Vc, 335 ± 124 $\mu\text{g/g}$ in sample Vcass26L1) - brine polyphase (Bpol, 783 ± 333 $\mu\text{g/g}$ in sample Bpolass30L2) and the early secondary liquid carbonic aqueous (Lcx) fluid inclusions where it is below the limit of detection (except 1 $\mu\text{g/g}$ in sample Lcxass48L15.1) (Fig. 11). The Cu concentration in the intermediate density generations is in the same range of that of vapor and brine polyphase assemblages with a maximum of 537 ± 123 $\mu\text{g/g}$ in the sample IDcassIDAL18. As the variability within types is significantly greater than the variability within assemblages, we consider that the decreasing of the Cu content between different generations (Figure 11) over than one order of magnitude is geologically real and likely due to the precipitation of the chalcopyrite. In addition, Lcx fluid inclusions are clearly secondary in time so the decreasing of Cu content is consistent to its precipitation before the trapping of the Lcx fluid inclusions.

Gold is difficult to analyze as the concentrations are almost always close to the detection limit and the signals are difficult to interpret due to the inclusion quality, size, contamination of the sample, etc. In the vapor carbonic Vcass26L1 assemblage, gold reaches concentrations of 9.5 ± 6.6 $\mu\text{g/g}$ while in the rest of generations is irregular with values between 0.1 and 0.6 $\mu\text{g/g}$. However, due to the high variability and poorly reproducibility of the data it is difficult to establish any realistic trend of variation between the fluid inclusion types.

Sulfur is a particularly important element because it acts as ligand of metals in sulfides and sulfate complexes. Unfortunately, determination of the sulfur by

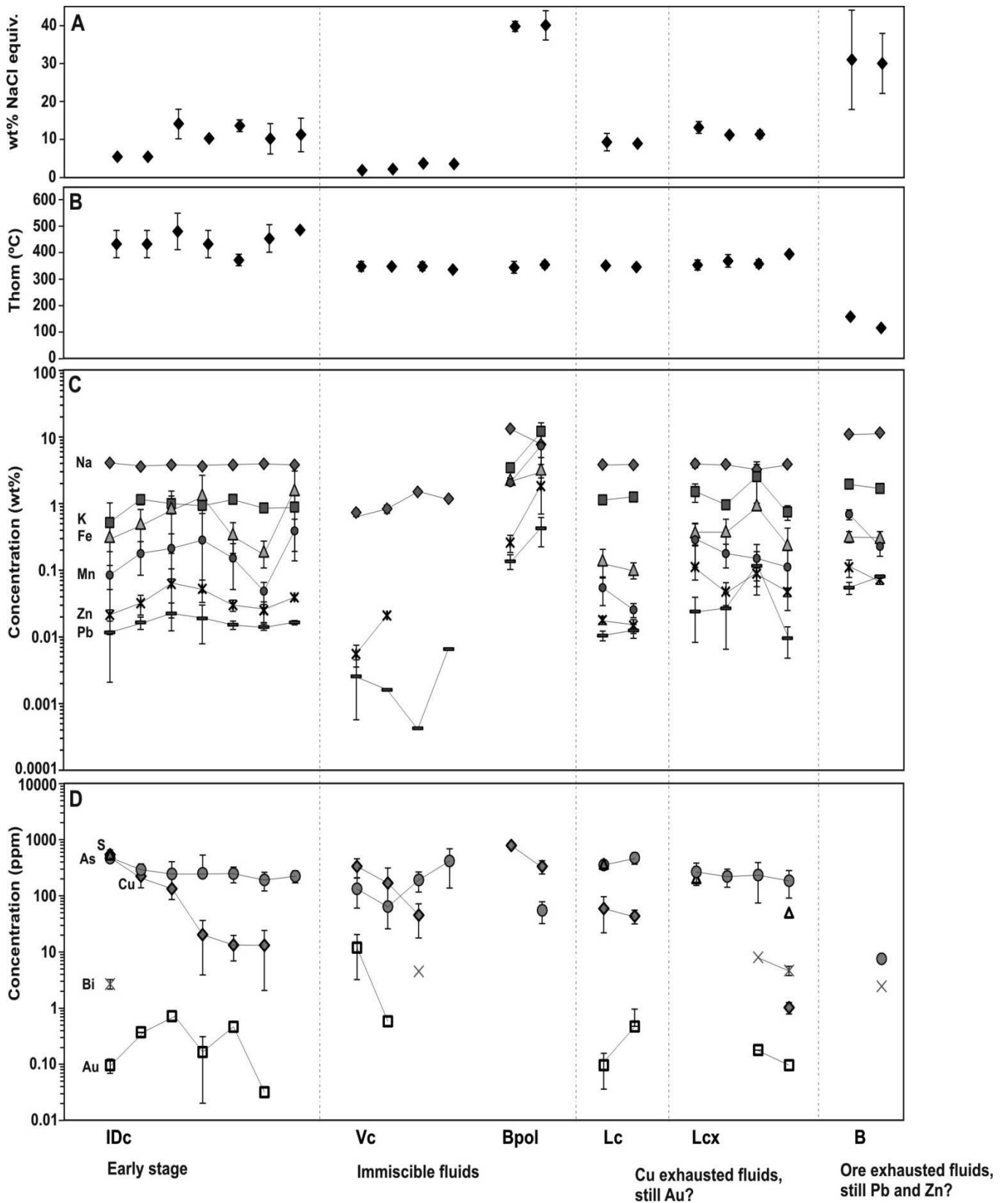
LA-ICPMS in the fluid inclusions is still difficult (Guillong et al., 2008a) even though some recent studies have shown important improvements in its detection and determination (Seo et al., 2009). In any case, some inclusions in this study show neat peaks of sulfur, with concentrations as high as $539.4 \pm 52.5 \mu\text{g/g}$ in the sample IDcassIDAL18 and $372.2 \pm 60.3 \mu\text{g/g}$ in the sample Lcass59L7W. Sulfur is below the limit of detection in the vapor generations but still, the upper limit of detection is very high in comparison to the other types (0.14 % wt in the sample Vcass21L7VU) suggesting a significant presence of S in these low density fluids.

Other elements like Bi and Ce were included in the analytical menu in the lattermost sessions and thus, there is a lack of measurements that makes difficult the establishment of any trend through the evolution of the vein. However, few analyses show that highest concentrations in Bi are in the secondary Lcx fluid inclusions ($8 \mu\text{g/g}$ in the sample LcxassL22).

Late brines (B) have high concentrations in all major elements but less Fe and Ca than brine polyphase fluid inclusions. Ore forming elements like Cu, Au, As, and S are always below the limit of detection whereas Zn and Pb are still very present in these late fluids, with maximum concentrations of $0.11 \pm 0.03 \%$ wt Zn and $803.9 \pm 43.9 \mu\text{g/g}$ Pb in the samples Bass34L10 and Bass38L19 respectively.

Figure 11 (next page). Salinity (A), homogenization temperature (B) and absolute element concentration (C and D) evolution of fluid inclusions in the Sultana vein. The fluid inclusion evolution (from left to right) is based on petrographical constraints. The vertical scale on the elemental concentration plots is logarithmic for highlighting variations in the orders of magnitude. Each point represents a fluid inclusion assemblage and the error bars show 1 σ variability within assemblages. The upper limit of detection of the assemblages where all the values of

a certain element are below the limit of detection are not plotted in the diagram in order to highlight the real values.



Sample	Na µg/g	16	S µg/g	16	K µg/g	16	Ca µg/g	16	Mn µg/g	16	Fe µg/g	16	Cu µg/g	16	Zn µg/g	16	As µg/g	16	Sb µg/g	16	Cs µg/g	16	Au µg/g	16	Pb µg/g	16	Bi µg/g	16
IDcass1DAL18	40824	1971	539	52.5	5192	5171	<2078	851	333	3209	1289	537	123	214	40.7	469	70.0	218	45.3	19.9	2.7	0.1	0.0	116	7.0	2.7	0.5	
IDcass43L9A	38025	1001	<1121	11461	1817	13811	853	1778	931	5064	3159	224	84.2	320	105	294	76.7	36.0	20.2	29.7	5.9	0.4	0.0	164	34.6			
IDcass39L8.1	38236	1443	<1480	10004	3028	<71692		2136	1390	8649	6852	133	164	626	432	246	159	29.1	11.0	28.7	13.3	0.7	0.1	224	101			
IDcass42L11N	36216	2455	<1527	9434	1479	8084	2848	4284	13569	13099	20.2	16.3	525	194	251	280	30.0	13.7	15.1	2.8	0.2	0.1	190	111				
IDcass41L7AF	38063	807	<1933	11609	1623	<63696		1524	1010	3496	1688	13.3	6.4	300	56.4	249	77.6	25.9	7.7	28.0	14.5	0.5	0.0	152	21.9			
IDcass38L8.2	39681	162	<700	8611	750	<22166		486	177	1925	844	13.2	11.1	252	86.6	192	70.3	27.1	15.1	13.0	0.6	0.0	142	15.0				
IDcass37L8.1	38306	1402	<389	8890	1311	<222627		3889	1950	16122	14731	2.2	393	31.3	224	54.1	33.5	8.9	11.8	1.1	<3			165	12.5			
Vcass26L1	7370	950	<32795	<8016		<1275381		<1336		<10811		335	124	55.5	19.8	134	73.3	73.6	92.0	4.0	0.9	9.5	6.6	25.6	19.9			
Vcass4HL7	8368	1155	<10961	<4423		<408725		<440		<5620		169	143	209		64.6	8.7	30.2	2.2	12.0	4.1	0.6		<16				
VcassBL18	15039	228	<1457	<375		<73572		<95		<1128		45.2	27.3	<42		192	74.4	77.2	27.4	2	<1	<1		<4		<5		
Vcass21L7VU	11824	324	<28645	<14404		<925111		<998		<588		<18		<637		415	277	<74		12.1		<0.4		<66				
Bpolass30L2	133652	2376	<4092	34698	5106	100297		20554	1576	22983	1369	783	10.3	2613	756	<30		<12		104	13.7	<1		1371	341			
Bpolass29L2.2	77474	38612	<6858	121905	42042	490880		73240	48805	33022	16406	333	87.6	18293	11306	55.1	23.2	94.9	50.7	498	239	<2		4252	1997			
LCcass59L7W	38620	456	372	60	11445	1039	<14662	548	251	1423	653	59.2	37.2	179	24.5	355	23.1	16.8	1.9	51.4	10.7	0.1	0.1	105	17.3			
LCcass57L7Vdef	38331	601	<2938	12582	1523	<11367		257	62	1021	274	43.6	12.0	148	34.4	476	111	27.6	5.2	57.7	7.6	0.5	0.5	125	29.2			
LCcass5-6L6	38821	4808	207	15196	4667	<50051		2861	2148	3756	1345	<3		1122	1214	268	116	15.6	11.3	43.8	13.9	<0.3		240	156			
LCcass10L5	38765	756	<1247	9586	1146	<46196		1777	691	3850	2003	<4		477	180	222	79.2	40.5	28.8	27.4	6.6	<0.4		268	203			
LCcassxxL22	32584	6411	<1357	25317	17404	<120010		1504	935	9538	676	<4		888	194	234	159	37.9	30.0	29.1	10.9	0.2	0.0	1166	738	8.0		
LCcass48L15.1	38944	640	50	7513	1868	4336	1565	1119	869	2428	1886	1.0	0.2	470	66.2	186	94.5	28.8	15.5	11.5	1.2	0.1		95.3	47.1	4.7	0.9	
Bpass34L10	110790	1325	<2292	19748	2730	233355	19550	6933	1179	3220	607	<9		1108	325	<23		<8		137	20.2	<1		549	114			
Bpass38L19	115565	420	<225	16981	1300	335227	52702	2285	660	3119	701	<5		727	110	7.5	1.1	13.2	7.7	52.2	3.9	<0.5		804	43.9	<2		

Table 6. Absolute elemental concentrations of fluid inclusion assemblages determined by LA-ICPMS. The samples are sorted in terms of time evolution (IDc → Vc + Bpol → Lc → Lcx → late B) inferred from the petrography. The absolute concentrations and corresponding standard deviations are calculated on the basis of the apparent salinity as determined during microthermometry. When all the measurements in the assemblage are below the limit of detection, the upper limit of detection of the assemblage is given (e.g. <20).

II.9. Interpretation and discussion

The fluid inclusion study combined with geological and geochemical data allow presenting an interpretation and discussion of the origin of the ore-metals transporting fluids as well as the ore forming processes that operated in the Sultana Cu-Au vein deposit. The results presented here address some new aspects that have not been entirely resolved in the literature of the intrusion-related magmatic hydrothermal Cu – Au deposits and confirm observations in other styles of mineralization.

II.9.1. Representativeness of the fluid inclusions and postentrapment modifications

After the entrapment of the fluid, deformation and reheating processes can cause changes in the fluid inclusions like their location, shape, volume and chemical composition (see Roedder, 1984; Goldstein and Reynolds, 1994 and Audétat and Günter, 1999 for an extensive explanation about postentrapment modifications in the fluid inclusions). These changes usually lead to inaccurate interpretations, especially in the hydrothermal environments where the temperature and pressure conditions are highly variable in short time. Thus, in a suitable fluid inclusion study is critical to assess if the inclusions are really representative of the fluids that circulated through the hydrothermal system.

Most of the studied fluid inclusions show minor evidence of post-entrapment modifications excluding those in the base of the quartz crystals, where the deformation is larger. The variability of the data derived from the microthermometry and LA-ICPMS elemental concentrations in the assemblages can be considered as acceptable. These considerations indicate that the fluid inclusions are representative samples of the ancient fluids that circulated through the system.

II.9.2. Intermediate density deep fluid and phase separation

The first clear texturally discernible generation of fluid inclusions in the euhedral quartz before the ore precipitation is that of likely coexisting vapor carbonic (Vc) and brine polyphase (Bpol) fluid inclusions. The evidences for this coetaneous trapping are several: they are located in the same growth zones of Q2 (Fig. 8.1), the homogenization temperatures are very similar within a narrow interval of uncertainty ($348^{\circ} \pm 20^{\circ}\text{C}$) and the salinities of the vapor (Vc) and brine polyphase (Bpol) inclusions are extreme (2-3 wt % NaCl eq. vs 40-42 % NaCl eq. respectively) as occurs in the typical “boiling” assemblages. Furthermore, in some vapor rich assemblages (samples VcSUCH3assL and VcCSU1AassX) there are one or two small polyphase fluid inclusions in the mid or at the edge of the assemblage (Figs. 12A, 12B and 12C) indicating their direct coexistence. Intermediate density fluid inclusions (IDc) are located in Q1 “starting” before the Q2 generation while in some assemblages is difficult to ensure that the trails do not start in Q2. However, it seems clear that they are not trapped during the euhedral growing of the Q2 (Fig. 8.1 and 8.2). Although petrographically difficult to classify, these fluid inclusions are potential candidates to represent a pulse of an early magmatic fluid that lead to the phase separation into the brine and the vapor phase. This interpretation is consistent with the fact that the IDc inclusions show the highest homogenization temperatures ($>400^{\circ}\text{C}$, minimum trapping temperatures homogenizing into the liquid phase), low to moderate salinities between < 4 and 15% NaCl eq., and densities between 0.5 and 0.7 g/cc , suggesting that the fluid was trapped as a single phase fluid in agreement with the P-T field of the system NaCl-H₂O (Fig. 13). Very similar intermediate density single fluids are described in detail in the deep zones of some porphyry copper gold deposits, and are considered as representing the parental fluid ascending from deeper parts of the magmatic hydrothermal system prior to unmixing (Redmond et al., 2004; Rusk et al., 2004).

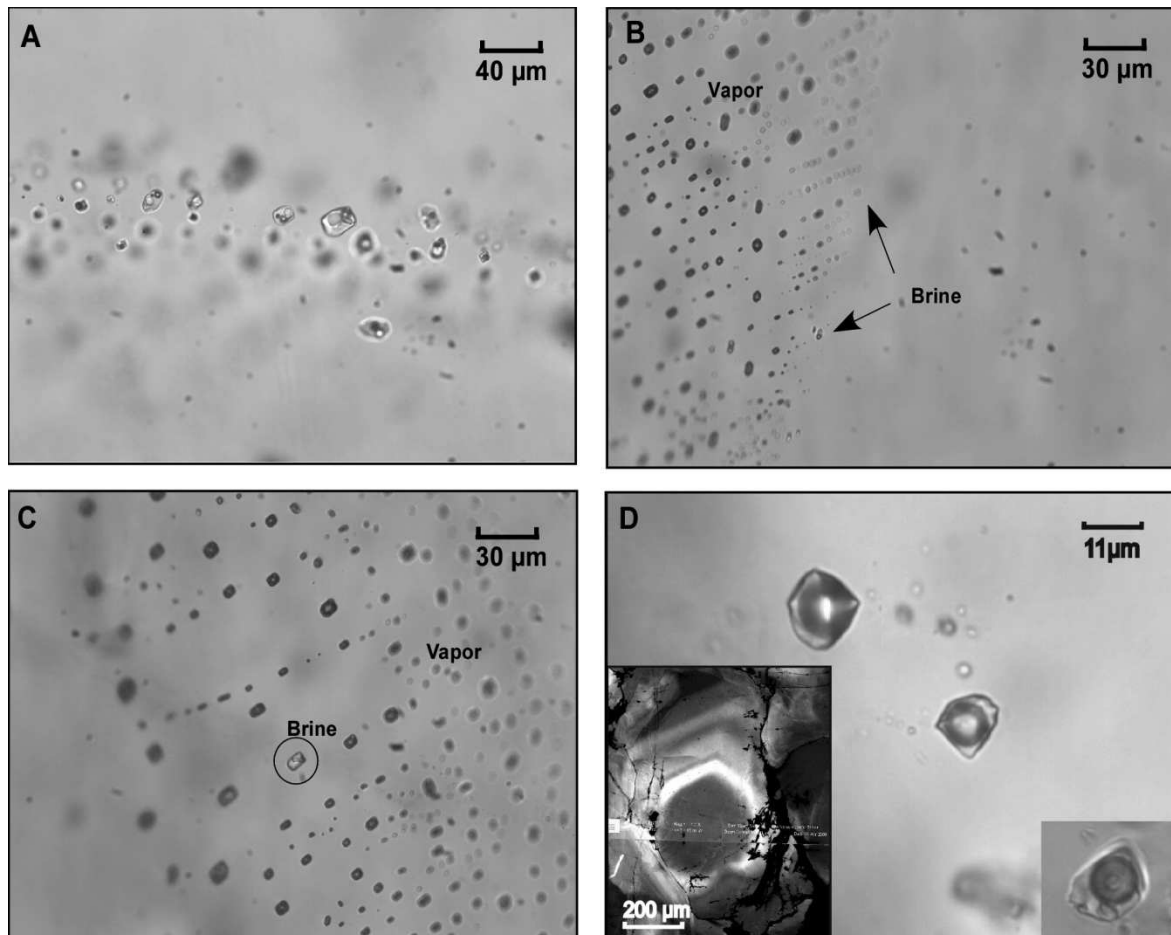


Figure 12. Transmitted light images showing brine polyphase fluid inclusions coexisting in the same growth zone with a vapor carbonic assemblage (A). Small brine polyphase fluid inclusions within (B) or at the edge (C) of vapor-carbonic fluid inclusion assemblages (sample SUCH3assL). (D) Three intermediate density fluid inclusions located in a euhedral growth zone (see the SEM-cathodoluminescence image in the caption) from a quartz cavity in the Santa Olalla host pluton. These fluid inclusions are rare and too small to manage, but they could represent the parental fluid of the system (Sample SO1assID).

Assuming that a single phase fluid with the IDc characteristics was separated into brine (Bpol) and vapor (Vc) phases, the possible physical evolution path in the well-constrained two-phase stability diagram of the NaCl-H₂O system (Driesner and Heinrich, 2007) can be reconstructed. An intermediate density (0.40 – 0.5 g/cc) fluid of 4

to 15 % NaCl eq salinity, temperature higher than 400°C and broadly estimated input pressure of 400 to 800 bar (Fig. 9) will intersect the two phase surface through the vapor side of the critical curve (Fig. 13) separating into a dominant low saline vapor and a little amount of brine by the process of condensation (droplets of hypersaline liquid separating from a dominant vapor) rather than by boiling, that occurs when the input high saline fluid intersects through the liquid side (Liebscher and Heinrich, 2007).

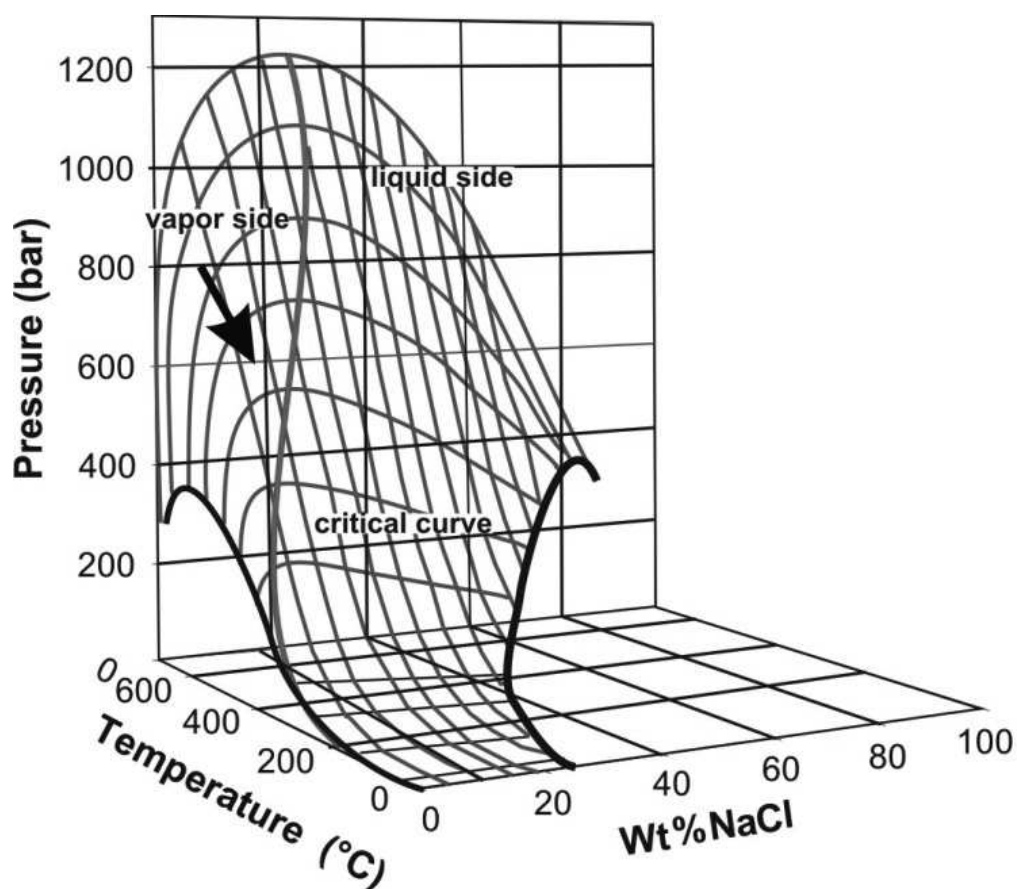


Figure 13. Phase diagram of the H₂O-NaCl system in the P-T-salinity stability space taken from Heinrich et al. (2007) and Driesner and Heinrich (2007). The black arrow represents the evolution of single phase fluid with the characteristics of the IDc group of fluid inclusions at the Sultana vein. The proposed path intersects the vapor side of the critical curve, below which two phase fluids (brine and vapor) coexist. The presence of CO₂ as well as salts other than

NaCl in the fluid inclusions will shift the PTX relationships but at low extent regarding to the moderate content of CO₂ in the inclusions.

The presence of minor brine phase condensation during the immiscibility is confirmed by the element concentrations in the fluids; vapor and intermediate density fluid inclusions are indistinguishable in terms of element/Na ratios in the majority of elements except for the ones that are below the limit of detection (Fig. 14). Brines, on the other hand, are enriched in K/Na, Mn/Na, Zn/Na, Pb/Na and Cs/Na with respect to parental fluid (IDc fluid inclusions). This suggest that vapor was the dominant phase when the separation from an intermediate density fluid occurred and is confirmed also by the high number of vapor assemblages on respect to the brine poliphase ones in the Q2.

Despite not studied in detail, some intermediate density fluid inclusions in the host Santa Olalla Plutonic Complex cavities also show homogenization temperatures as high as 450-500 °C and poorly constrained salinities of 5 to 15 % NaCl eq (Appendix IIB). They are similar to the IDc fluid inclusions studied in the Sultana vein and hypothetically, they could represent the evidences of the very early fluids exsolving from the crystallizing intrusion. However, these inclusions are too small to work reliable and to establish any petrographic constrain (Fig. 12D). Moreover, there is no direct connection between the cavities and the vein, despite hosted by the same intrusion, and more detailed studies are necessary to prove that they are genetically linked.

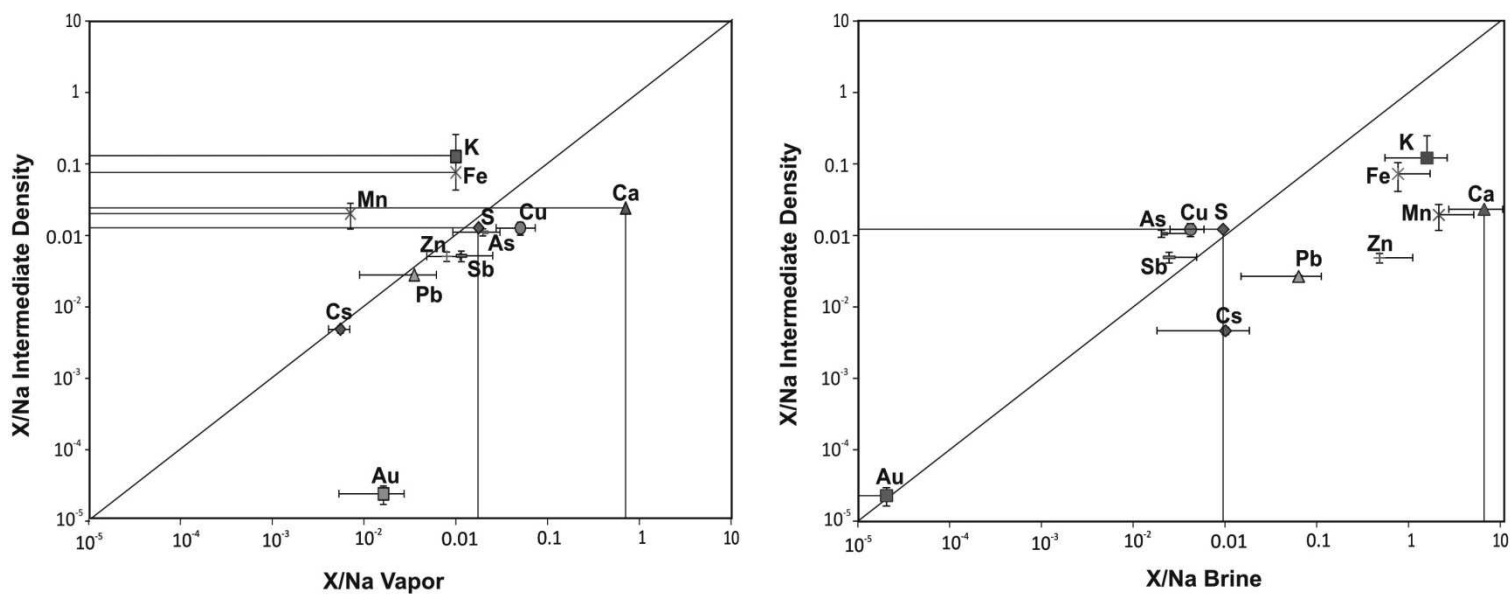


Figure 14. Fractionation of the analyzed elements between intermediate density (sample IDcassIDAL18) and coexisting vapor (A) and brine poliphase (B) fluid inclusions (sample SUCH3ass26and30). Error bars indicate 1σ of the variability within one assemblage.

II.9.3. Did the sulfides and gold precipitated during the quartz dissolution?

SEM - Cathodoluminescence images show that the sulfides are always in direct contact with the second generation of quartz (Q2, Fig.4) strongly suggesting that the ore precipitated during or after the dissolution of Q1 and before or together with the precipitation of Q2. The Q1 shows fracturation, discontinuous boundaries, networks of microfractures, etc. indicating that it suffered several pulses of dissolution-precipitation. Experimental studies of numerical modeling show that in pure water, the solubility of quartz (i.e. the maximum SiO₂ amount that can be dissolved in a certain amount of water) decreases with decreasing the temperature at pressures greater than 750 bar (Fournier, 1999). A drop in pressure (from lithostatic at around 2000 bar to hydrostatic at 700 bar conditions) causes silica oversaturation because the solubility decreases and thus, quartz precipitates in the open spaces of the vein (Fig. 15A, Rusk and Reed, 2002). At lower pressures (\approx 300 bar) and in slightly saline water (2 - 5 wt % NaCl eq.), this direct dependence switches to a reverse solubility-temperature dependence (the "retrograde solubility of quartz") where the solubility increases while cooling and quartz dissolution occurs. Regarding to the SEM-CL images and their textural relationship with the fluid inclusion assemblages, the fluids cooled from temperatures up to 400°C through the retrograde solubility path dissolving quartz until the point which further cooling led to the second generation of quartz precipitation as well as the sulfide precipitation (Fig. 15B). Highly saline fluids do not show retrograde solubility as the solubility of quartz decreases while cooling so probably the vapor carbonic low saline (Vc, 2-3 wt % NaCl eq.) fluid was the dominant quartz dissolution agent during cooling.

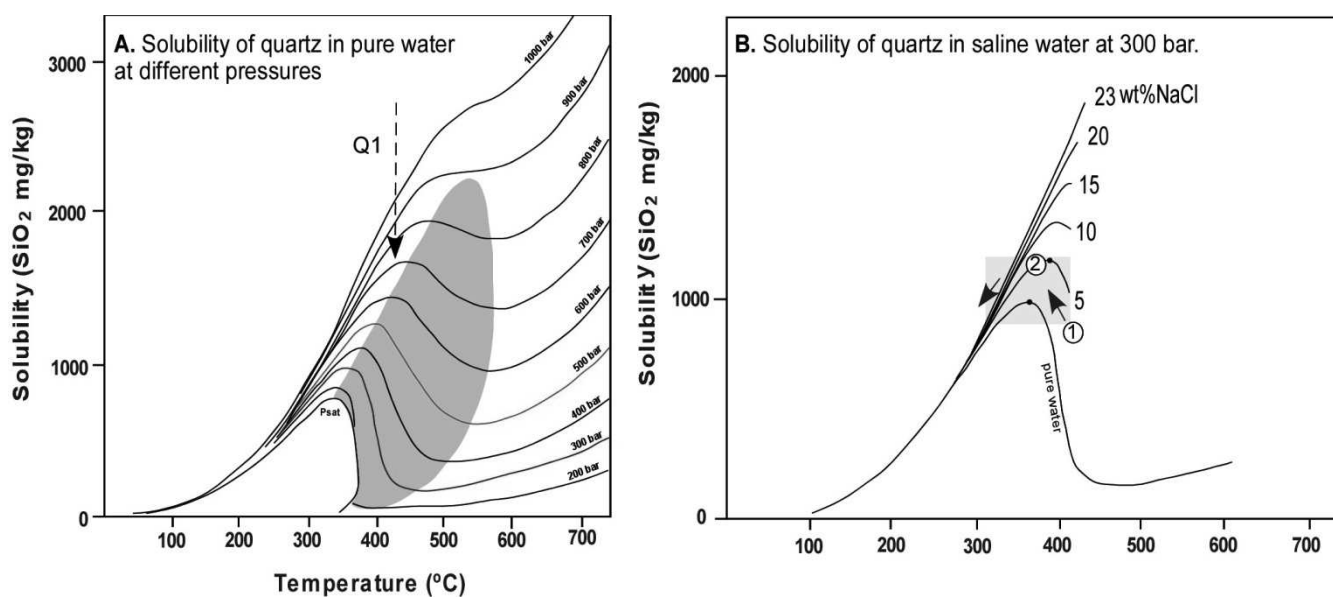


Figure 15. Solubility of quartz in pure water at different pressures (A) and in water with variable salinities at 300 bar (B). The arrow in the pure water diagram shows the hypothetical path followed by the fluids related to the precipitation of the Q1 generation due to the evolution from lithostatic to near hydrostatic fluid pressures (from Rusk and Reed, 2002). When cooling from 450° to 350°C (estimated temperatures of the ID, Vc and Bpol ore-related fluid inclusions in Sultana) the solubility of quartz increases (1) leading to the dissolution of Q1. With further cooling the open space is filled by the second generation of quartz and the sulfides (2). Modified after Fournier (1999).

II.9.4. Pressure and temperature formation conditions of the fluids

The isochore plots show that the trapping conditions for the fluid inclusions are consistent with a wide range of temperatures and pressures (Fig. 16). However, the slope and location of the isochores is subject to large variations due to the uncertainties in the calculation of the densities and the oversimplification of the fluid system. An early intermediate density carbonic (IDc) fluid with average 5 wt% NaCl eq. that homogenizes between 378 and 474°C yields a minimum trapping pressure of around 800-1200 bar without any pressure correction, in

agreement with the pressure emplacement conditions of the Santa Olalla Plutonic Complex (500 – 1000 bar, Casquet, 1980) and consistent with its trapping close to the two phase fluid surface.

In the inclusions trapped under immiscibility conditions (“boiling assemblages”, Vc and Bpol), the absolute pressure estimation can be directly obtained from the isochores (Roedder, 1984; Goldstein and Reynolds, 1994), with estimated trapping pressures of 200 to 400 bar and temperatures of 370 to 400°C. These P-T conditions are slightly higher than those calculated on the basis of the NaCl-H₂O two-phase surface system, i.e., 150-200 bar and 340–350°C (Fig.9). A reason for this inconsistency is that the later are probably underestimated due to the presence of salts other than NaCl and CO₂ gas dissolved in the fluid (Bodnar and Vityk, 1994; Driesner and Heinrich, 2007). These conditions are also in correspondence with the P-T field of the retrograde solubility of silica (Fig. 14).

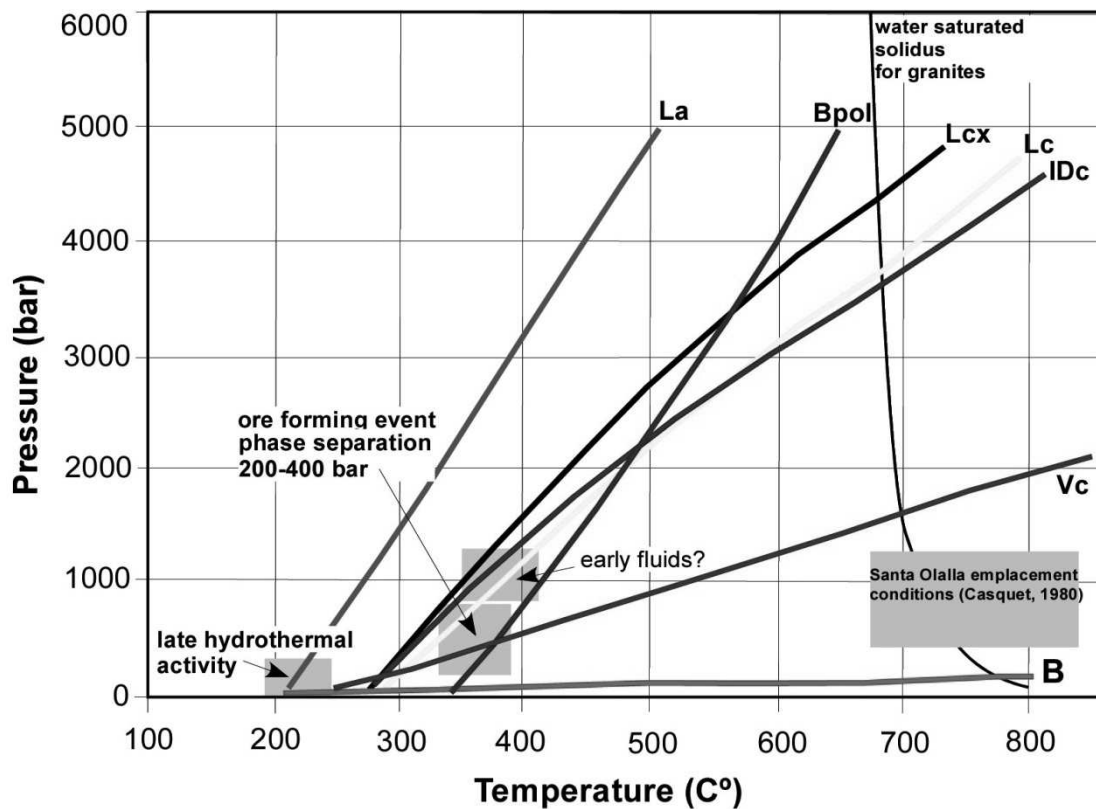


Figure 16. Pressure-temperature plot showing the calculated isochores for the seven types of fluid inclusion. Previously estimated P-T conditions for the hosting Santa Olalla pluton are also shown, corresponding to the trapping pressures for the early ID fluids. The ore forming event occurs approximately between 200 and 400 bar and 450 ° and 350 °C.

II.9.5. Fluid and metal source: magmatic vs. metamorphic origin

In the literature on orogenic (metamorphic) gold and intrusion-related gold systems, there is no consensus about the ultimate source of the ore fluids and metals (see Lang, 2001; Groves et al, 2003; Phillips et al, 2010 for reviews of this type of deposits). Metamorphic rocks are known to be an important source in gold-only deposits by processes of metamorphic devolatilization at the greenschist to amphibolite facies transition (Ridley and Diamond, 2000; Phillips et al, 2010). Fluids in these systems are commonly low saline (<10 wt% NaCl eq.), $\text{CO}_2 \pm \text{CH}_4 \pm \text{N}_2$ -

bearing and trapped at pressure-temperature conditions ranging from 0.5 to 4.5 kbar and 200 to 400°C, respectively. These fluids are usually richer in volatiles and have lower salinities than those associated with intrusion-related systems. Furthermore, they show a clear association with large structures that focused fluid flow, being associated or slightly postdating regional metamorphism. In the intrusion-related gold deposits, metamorphic fluids can be also derived from the hosting volcanosedimentary and pelitic rocks (Powell et al., 1991; Stüwe, 1998; Phillips et al., 2010) as well as from deeper sources, derived from the subducted oceanic crust (Fyfe and Henley, 1973; Groves et al., 2003a). In the recent times, however, a dominantly magmatic source is the most widely accepted source for the fluids and metals in the intrusion-related deposits, including also the porphyry deposits (Bodnar, 1995; Hedenquist et al., 1998;; Baker and Lang, 2001; Heinrich, 2007). Fluids of metamorphic derivation are expected to be present in a setting such that of the Sultana vein, with a granitoid intruding low grade metamorphic rocks dominated by shale, calcsilicate hornfels, marble and volcano-sedimentary rocks. Fluids generated during the well-developed contact metamorphism with transformation of shale into pelitic hornfels and formation of skarn on the calcsilicate and carbonate rocks could well infiltrate in the vein system. Stable isotopes of sulfur in the sulfides of the mineralization have signatures between +9.5 and +15.7 per mil, consistent with the interaction of fluids equilibrated with the hosting metasedimentary rocks (Tornos et al. in prep.). Sulfides in orogenic gold deposits typically have compositions ranging from 0 to +9 ‰ (McCuaig and Kerrich, 1998), something that reflects the dominant derivation of the reduced sulfur from a sedimentary source. Magmatic sulfur has usually values close to 0 per mil (Ohmoto and Rye, 1979) but the exsolved magmatic fluids can carry variable proportions of H₂S and SO₄²⁻ depending on the oxidation state of the magmas and the moment of degassing (Hodkiewicz et al, 2010); furthermore, magmas showing derivation or interaction with crustal rocks can inherit reduced sulfur of sedimentary derivation. Stable isotopes could also indicate more than one source,

given the complexity of wall rocks with variable isotopic compositions as well as the episodically long fluid-path events (Ridley and Diamond, 2000).

It is also evident that the Sultana vein has a direct association with intrusive rocks and, thus, a magmatic source for the fluids is likely. Evidences for a magmatic origin of fluids and metals are the following: (1) the ore association dominated by Cu-Au and the high base metal tenors, not typical of orogenic-metamorphic gold systems; (2) the T-P conditions of ore precipitation, typical of cooling magmatic-hydrothermal systems with higher temperatures and commonly lower fluid pressures than in metamorphic terrains; (3) the existence of evidences of phase separation through condensation of a minor brine fluid, typical of magmatic-hydrothermal environments; (4) the element concentrations in the fluid inclusions that show high copper, sulfur and gold contents in the brine, vapor and intermediate density phases; (5) the retrograde solubility-quartz textures, that are uncommon in metamorphic settings; and, (6) the presence of an intermediate density single phase fluid, which is frequent in deep parts of magmatic-hydrothermal systems. Nevertheless, and as we explained before, isotopes do not support a unique magmatic origin for the fluids and thus, a metamorphic contribution has to be considered. The Table 7 includes a list of these and other geological aspects of both orogenic gold and intrusion-related (including porphyry) deposits that could well fit in the Sultana ore formation, in order to clarify the possible origin and classification of this vein.

The common presence of moderate to high CO₂ contents in fluid inclusions of the intrusion-related veins is well addressed in the literature (Diamond, 1990; Thompson and Newberry, 2000). Despite the presence of CO₂ in fluid inclusions has been widely used as a criteria for the presence of metamorphic fluids (Godfarb et al., 1997), there are abundant evidences of that CO₂, and even CH₄, can separate from crystallizing magmatic intrusions (Sisson and Hollister, 1990; Lowenstern, 1994; Lentz, 1999). Therefore, the presence of CO₂ cannot be used for discrimination

of a genetic origin. In fact, moderate to high amounts of CO₂ are very present in some porphyry-related and epithermal fluid inclusions, as indicated by the formation of clathrate during the cooling runs (Heinrich et al., 2004; Redmond et al., 2004; Ronacher et al., 2004; Rusk, 2008). Here, possible sources of the CO₂ are: (1) fluid separation from a crystallizing silicate melt, with the CO₂ separating early from the melt due to its low solubility (Lowenstern, 1994); (2) devolatilization reactions of carbonate rocks during contact metamorphism; or, (3) a combination of both.

Characteristics	Orogenic gold deposits	Intrusion related gold deposits	Porphyry copper deposits	Sultana Cu-Au deposit
Tectonic setting	Deformed continental margin, mainly of allochthonous terranes	Pericratonic terranes of the miogeocline margin	Convergent plate boundaries (magmatic arc including back-arc)	Deformed continental margin
Structural setting	Structural highs during later stages of compression and transension. Structural complexity	Compressional to extensional transition in fold and thrust belts. Simple vein arrays in brittle regimes	Ranging from moderately extensional through oblique slip to contractional	Southern limb of the Olivenza-Monesterio antiform, Variscan deformation (Mid Devonian - Permian)
Host rocks	Mafic volcanic or intrusive rocks or greywacke-slate sequences	Granitoid intrusions, some in sedimentary rocks	Porphyritic	Granodioritic intrusion, black shale and greywacke
Association with intrusions	Commonly felsic to lapmphyre dikes or continental margin batholiths	Strong association with granitoid stocks	Spatially and genetically associated to commonly felsic, epizonal, porphyritic intrusions	Veins hosted by the Sultana Stock
Mineralization style	Veins, vein arrays, saddle reefs, replacement of Fe rich rocks	Sheeted veins, lesser breccias, veins, and disseminations	Veinlets, disseminated in the altered rock, ore-breccia	Sheeted veins crosscut by late veins
Timing of mineralization	Late tectonic; post (greenschist) to syn (amphibolite) metamorphic peak	Very late tectonic; postregional metamorphic peak	Late magmatic-hydrothermal stage	Late tectonic; post contact metamorphic peak
Metal association	Au-Ag, As, B, Bi, Sb, Te, W	Au-Ag, As, B, Bi, Sb, Sn, Te, W, distal Zn, Pb	Cu-Au, Ag, Mo	Cu-Au, Bi, distal Zn and Pb
Alteration	Varies with metamorphic grade; normally mica - carbonate-Fe sulfide	Mica-K feldspar-carbonate-chlorite-Fe sulfide	Zoned: albite, oligoclase-biotite, K feld.-chlorite sercrite-sericite-quartz, alunite	Mica, ankerite-chlorite, biotite, tourmaline, Fe sulfide
P-T conditions	0.5-4.5 kbars, 220°-600°C; normally 1.5 ± 0.5 kbars, 350° ± 50°C	0.5-1.5 kbars, 200° - 400°C for Au-rich systems	0.2 - 1.5 kbars, 250° - > 700°C	0.2 - 0.4 kbars, 350° - > 450°C
Ore fluids	Low salinity H ₂ O-CO ₂ ± CH ₄ ± N ₂	Variable salinity H ₂ O-CO ₂ , very minor CH ₄ ± N ₂	Low-high salinity, H ₂ O±CO ₂ , fluid phase separation; retrograde solubility of quartz	Low-high salinity, H ₂ O-CO ₂ , minor CH ₄ , fluid phase separation; retrograde solubility of quartz
Metal source	Subduction/subcreted crust and/or supracrustal rocks and/or deep granitoids	High-level granitoids and/or supracrustal rocks	Subduction related composite plutons	Santa Olalla Plutonic calc-alkaline complex, shales?

Table 7. Several characteristic of orogenic gold deposits, intrusion-related gold and porphyry copper deposits compared to the Sultana vein features. Modified after Groves et al. (2003) and Sillitoe (2010).

In the fluid inclusions from Sultana, the CO₂ content ranges between 6.1 and 28.7 mol % with the H₂O dominating in all the fluid inclusion types. The highest CO₂ values, considering the uncertainties derived from the calculations, are in the vapor (Vc) inclusions (28.7% CO₂ and 70% H₂O), lower than the typical CO₂ concentrations in the orogenic-gold deposits (e.g. 71% CO₂ in the vapor fluid inclusions from Brusson, Italy, Diamond, 1990). Rusk et al. (2008) also show CO₂ contents as high as 18 mol % in the fluid inclusions of the Butte porphyry copper deposit (Montana). The methane content is much more common in metamorphic settings than in magmatic environments. However, in the later one, CH₄/CO₂ ratios may be appreciable at the temperatures expected for hydrothermal mineralization in intrusion hosted gold deposits. In the analyzed fluid inclusions, CH₄ is invariably present but with minor contents compared to CO₂ and it could be derived by reduction of carbon compounds in the magmatic fluid or incorporation of carbon during wall-rock. Two possibilities are proposed here to explain a magmatic origin of the fluids together with the metamorphic signature given by the S isotopes in the sulfides: (1) a mixing process between the oxidized magmatic fluids and contact metamorphic fluids derived from the devolatilization of the hosting shale (Sisson and Hollister, 1990); (2) a prior interaction of the melt with metasediments having sulfides enriched in $\delta^{34}\text{S}$. Exsolved magmatic fluids should carry sulfur with positive $\delta^{34}\text{S}$ values.

II.9.6. Fluid chemistry and ore deposition

Recent studies on the solubility of metals at magmatic-hydrothermal conditions show that some elements such Cu and Au preferably fractionate into the vapor phase and others like Fe, Zn and Pb partitionate into the liquid phase (Audétat, 1998, 2000, 2008; Heinrich et al. 1999; Ulrich et al., 1999; Audétat and Pettke, 2003; Kehayov et al., 2003; Picrovsky, 2008; Seo et al., 2009). When plotting the X/Na ratios of elements in the most definitive coexisting assemblage in Sultana (Fig.17), it can be observed that copper, arsenic and antimony are preferentially partitioned into the low density vapor phase. Sulfur is below the limit of detection in both the brine and vapor assemblage whereas gold is below the limit of detection in the brine suggesting its preferential partitioning in the gas phase. On the contrary, elements such as zinc, lead and cesium fractionate into the brine. Manganese, iron, potassium and calcium are below the limit of detection in the vapor phase.

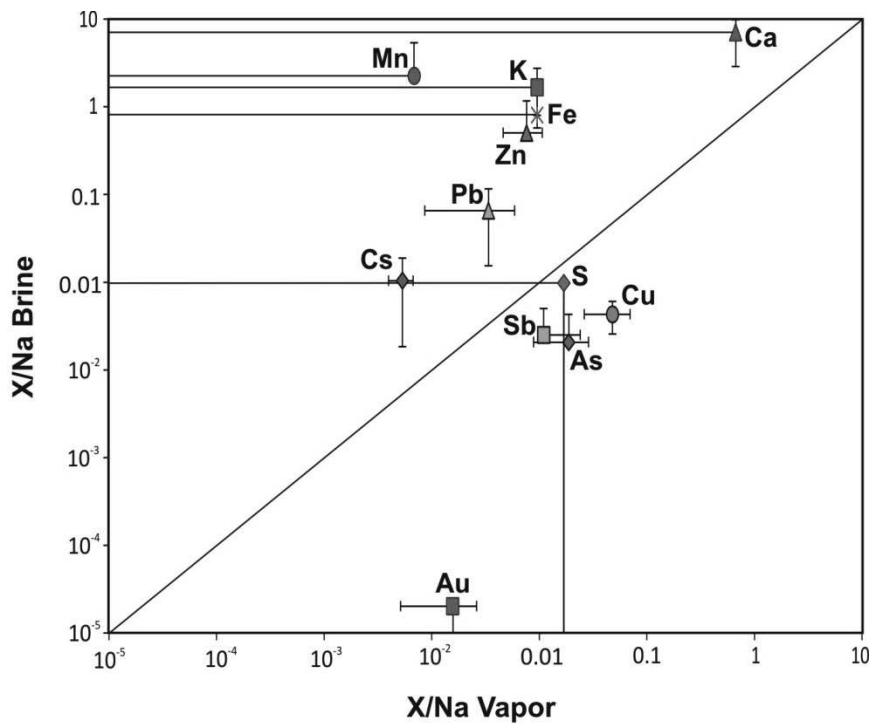


Figure 17. Fractionation of elements between vapor and brine in the best assemblage of coexisting brine and vapor fluid inclusions (sample SUCH3ass26and30) based in the average element concentrations normalized to the Na concentration. Error bars indicate 1 σ of the variability within one assemblage.

Several works have addressed that this metal partitioning is due to the dominant complexation of the metals as hydrosulfide and chloride complexes in the vapor and brine fluid phase, respectively. Special attention has been paid into the critical role of sulfur as a stable copper- and gold-ligand in magmatic fluids (Heinrich et al., 1992; Heinrich et al., 1999; Pokrovski et al., 2008; Zajacz et al., 2008; Seo et al., 2009). These authors propose that Cu and Au are preferentially partitioned in the gas phase, probably related to its preferential complexation with S-rich anions. However, Cu-chloride complexes are also stable in high temperature magmatic fluids (Zajacz et al., 2011).

Recently, Lerchbaumer and Audètat (2011) have experimentally shown that perhaps this model is not always true. They synthesized vapor and brine inclusions from a Cu-H₂O-NaCl and S-rich fluid at 800°C/1.3 kbar, that were later reequilibrated in a second experiment with a similar fluid but at 800°C/700 bar. The results show that the vapor inclusions experienced a dramatic increase in the Cu content after the second experiment while the brine inclusions remained unmodified, leading from a true $D_{\text{Cu}}^{\text{vapor/brine}}$ value of 0.4 ± 0.05 to an apparent value of 8.3 ± 8.9 . They suggest that this behavior is due to diffusional gain, as the quartz-hosted fluid inclusions can diffusively lose or gain Cu after their formation (Lerchbaumer and Audètat, 2009, 2011). If true, these studies will modify the current models on the role of magmatic vapor in the formation of Cu deposits, something considered critical in the most recent models.

The Table 6 shows that the maximum concentration of copper in the intermediate density fluid inclusions (IDc) is 537 ± 123 µg/g with approximately equal concentration of sulfur in the same assemblage, 539 ± 52 µg/g, as it is required for copper and gold transport as hydrosulfide complexes (Seo et al., 2009). These metal concentrations are here considered to represent those in the magmatic fluid flowing into the vein; however, it is likely that the fluid was close to saturation and probably some copper had already precipitated. The existence of fluids with even higher Cu, Au and S contents is consistent with the higher concentration in Cu and S in the coexisting brine and vapor assemblages (Bpol and Vc) with 783 ± 335 µg/g Cu (S is below the detection limit). As it is showed in the Figure 11, the Cu concentration drops from these high values in the brine-vapor assemblages to less than 1 ± 0.2 µg/g in the late Lcx fluid inclusions that likely represent the ore-spent fluids of the system. This is consistent with the precipitation of copper as chalcopyrite (CuFeS₂) in this interval from the vapor and/or the brine fluid, coinciding with the cooling of the fluid from temperatures slightly above 450° to ~350°C and synchronously with the dissolution of Q1. Attempting to establish the

precipitation mechanism of Cu, Hezarkhanai et al. (1999) calculated the solubility of chalcopyrite at different fO_2 , fS_2 , pH and a_{Cl} -conditions, based on a thermodynamic model of alteration and mineralization. They concluded that the solubility is strongly dependent on the temperature, decreasing from 50000 $\mu\text{g/g}$ at 450 °C, to 25 $\mu\text{g/g}$ at 350 °C. In Sultana, it is inferred that a fluid with 500-700 $\mu\text{g/g}$ of Cu similar to that of intermediate density fluid inclusions, was undersaturated at temperatures higher than 400°C but after the phase separation and further cooling to around 350°C, the copper concentration in the fluid was enough to saturate and to precipitate the chalcopyrite. Other factors like fluid oxidation from a more reduced to oxidized fluid could also promoted the copper precipitation.

On respect to gold, the highest concentrations are in the vapor phase with 9.5 ± 6 $\mu\text{g/g}$. Petrographic studies show that maldonite and native gold occur late in the fractures of the chalcopyrite, coating quartz and as native gold aggregates in the late stages of crystallization (Tornos et al., in prep.). A possible explanation for this late deposition of gold is that still remains sulfur in the vapor phase after the chalcopyrite precipitation (around 372 ± 60 $\mu\text{g/g}$), and thus it is still able to transport the gold to lower temperatures in the form of secondary Lc or Lcx fluid inclusions (in which it is above the LOD), perhaps after a contraction of the vapor phase by little cooling (Heinrich, 2004; Seo et al., 2009).

Zinc and lead are deposited in the form of sphalerite and galena in the lattermost stage. As it is shown in the Figure 17, Zn and Pb preferentially fractionate into the brine phase. Probably, these elements did not precipitate during the main ore forming event due to the higher solubility of Zn and Pb in hydrothermal solutions and perhaps due to the lack of enough reduced sulfur in the fluid after the precipitation of the other sulfides during the main ore forming event. Later mixing of the brines with infiltrated cooler meteoric fluids transporting sulfur could favor the precipitation of sphalerite and galena.

II.9.7. Conclusions: Fluid evolution scenario with deep single phase fluid input, phase separation and ore deposition

The combination of the results of the fluid inclusion study with previous geological data allows proposing a scenario for the formation of the Sultana orebody (Fig.18).

The ascent and further epizonal emplacement of the calc-alkaline tonalite melts represented by the Sultana Stock lead to the crystallization and concomitant pulsatile exsolution of magmatic-hydrothermal fluids. Fluid inclusion petrography, microthermometry, Raman and LA-ICPMS microanalysis show that the earlier most fluids separated from the melt were intermediate density ones (represented by the ID_c fluid inclusions), characterized by low salinity (avg. 5 wt% NaCl eq.), significant amounts of CO₂ but little CH₄, high temperature of homogenization (Thom>400 °C) as well as high concentrations in ore-metals (537±120 Cu, 0.7 µg/g Au, 539±52 S). These fluids were trapped at rather deep conditions, with the system likely dominated by lithostatic pressures (800-1200 bar; >1.5-2 km). These fluids were probably responsible of the precipitation of the bulk quartz and ankerite that dominate in the vein system.

Further opening of the vein and transition of the fluid pressure from lithostatic to hydrostatic pressures made the fluid breach the two-phase surface of the H₂O-NaCl-CO₂ system with condensation of a minor brine phase and a dominant low saline vapor. This phase separation occurred at estimated temperatures and pressures of ≈450-350°C and 400-200 bars, respectively, coinciding with the widespread opening of spaces within the vein due to the retrograde solubility of quartz. The sulfides, dominantly chalcopyrite, precipitated here by phase separation and cooling due to the destabilization of the aqueous complexes prior or during the precipitation of a second generation of quartz. The precipitation of the chalcopyrite is supported by the significant decrease of the Cu

content in the fluid inclusions from those predating the ore forming event to those (inclusions Lcx) postdating it (Fig. 11). In fact, the element concentrations are constant through all the fluid evolution of the vein, except for copper, which drops by about an order of magnitude from the brine-vapor stage (500 – 700 $\mu\text{g/g}$) to less than 0.1 $\mu\text{g/g}$ in the late fluids. Even if sulfur is not well detected in most fluid inclusions, it seems that S was the dominant complexing ligand. Gold precipitated later into the fractures of the chalcopyrite. In fact, an excess of sulfur after the deposition of chalcopyrite makes possible the retention of gold in solution, precipitating it late in the evolution of the vein. Galena and sphalerite precipitated even later, most probably in relationship with the mixing of residual magmatic fluids with meteoric waters that cooled the system down to lower temperatures or supplied enough sulfur for the precipitation of Zn and Pb. The role of metamorphic fluids in the system has not been tracked by the fluid inclusion study but the sulfur isotope data suggest that they likely added excess reduced sulfur to the system favoring the precipitation of the sulfides.

The proposed ore forming model is similar to that proposed for porphyry deposits and other intrusion-related Cu-Au systems, with precipitation of the Cu-Fe sulfides synchronously with phase separation, cooling between 450° and 350°C and quartz dissolution. This is a highly effective mechanism for precipitating chalcopyrite and, if enough S and Fe are present, the hydrothermal fluids exhaust almost all their Cu during this short interval of temperature.

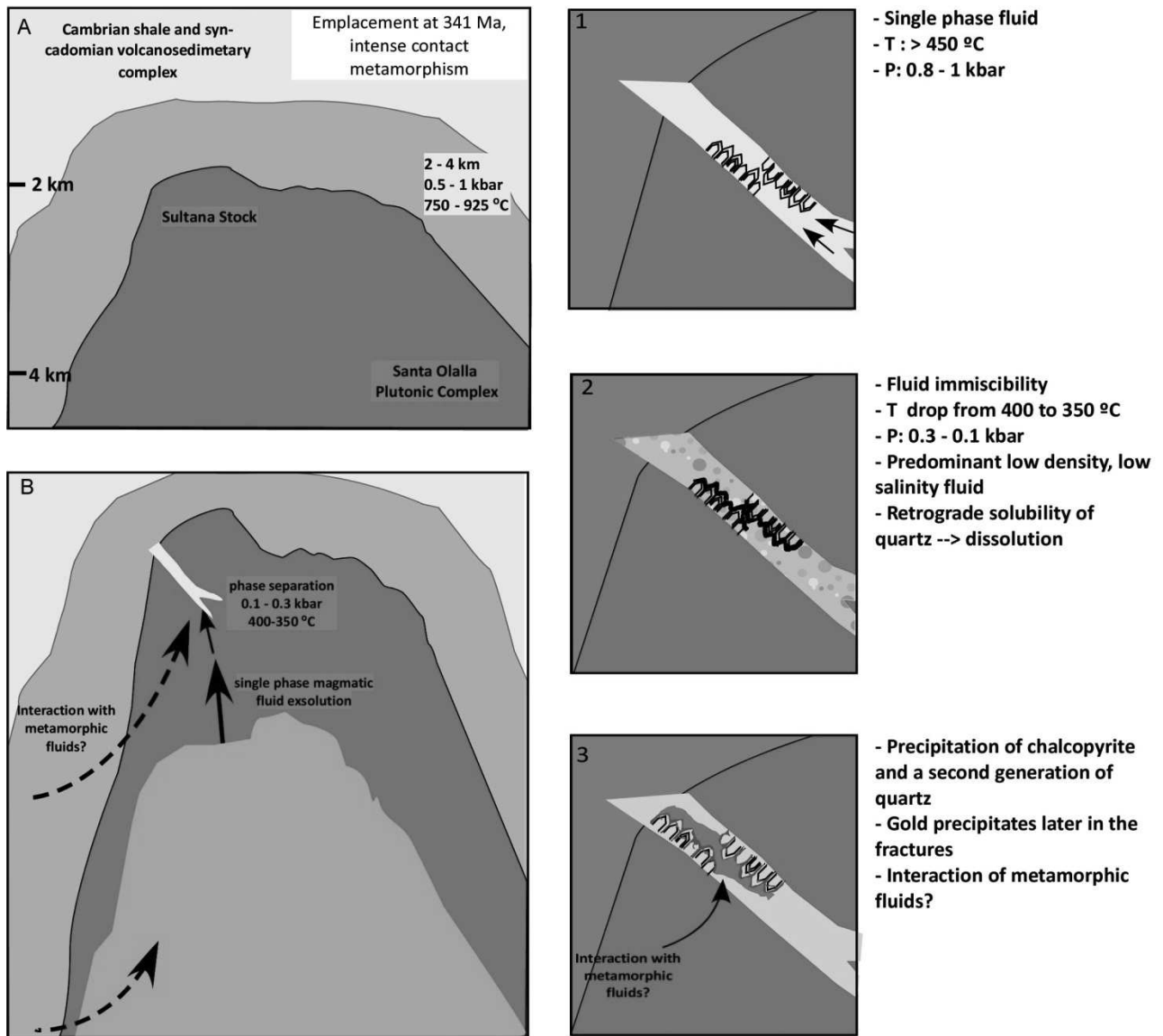


Figure 18. Hypothetic and schematic interpretation of the evolution of the hydrothermal system in Sultana (A and B) and detail of the different stages of vein filling and ore precipitation with respective formation conditions and processes.

Chapter III: Albitite related to magnetite deposits: melt inclusion evidence for a magmatic origin and its role in the genesis of the hydrothermal mineralization

Abstract

Albitite, particularly the one related to magnetite ($\pm\text{Cu}\pm\text{Au}$) and REE ore deposits, has been commonly interpreted in the literature as of metasomatic origin by sodic alteration of igneous or sedimentary rocks. In this study, melt and fluid inclusions in the Cambrian albitite of La Berrona Stock (SW Spain) are characterized and indicate a magmatic origin for this unusual rock. Crystallized silicate melt inclusions in quartz phenocrysts of the albitite were carefully selected and analyzed by laser ablation-inductively coupled plasma mass spectrometry (LA-ICPMS). The silicate melt inclusions have a composition close to that of the host albite with SiO_2 (73.2 ± 1.9 wt%), Na_2O (6.8 ± 1.1 wt%), K_2O (0.1 ± 0.1 wt%) and CaO (0.6 ± 0.4 wt%) as major elements. In agreement with the compatible/incompatible behavior of trace elements in magmatic systems, compatible elements such Ba, Sr, V, Zr, Ni and P are incorporated in the phenocrysts and groundmass whereas incompatible elements as well as ore metals such as Cu, Pb, Zn, As and Mo are enriched in the residual melt represented by the silicate melt inclusions. The quartz phenocrysts also show some opaque melt inclusion of Fe-Ti-P-rich composition suggesting the existence of an immiscible iron-titanium-phosphorous oxide melt phase segregated from the parental silicate melt. In the uppermost zone of the stock, there are some magmatic-hydrothermal breccias and stockwork-like mineralization that are interpreted as representing zones of fluid exsolution. Adjacent to these structures, La Berrona magnetite deposit is undoubtedly of hydrothermal origin, and occurs replacing both the albitite and the host calc-silicate hornfels. Magnetite is associated with albite and actinolite and has features similar to those of the IOCG deposits. Fluid inclusions in the quartz phenocrysts of the albitite, the breccia and early hydrothermal veins indicate the

circulation of high temperature Fe- and CO₂-bearing fluids at temperatures higher than 340 °C. The magnetite in the mineralization has low Ti and P contents, suggesting that the fluids did not interact with the immiscible iron oxide phase rich in these elements. Probably, the separation of the immiscible iron oxide melt depleted the system in Ti-P, leading to the later exsolution of Ti-P-poor magmatic-hydrothermal fluids that formed the hydrothermal mineralization.

Comparison of the silicate melt inclusion composition with experimental studies, the isotope data (⁸⁷Sr/⁸⁶Sr, ¹⁴³Nd/¹⁴⁴Nd and Pb isotopes) and the trace element geochemistry suggest that the albitite derived from the partial melting of upper crustal rocks in water-rich conditions.

This melt inclusion study together with the field relationships, petrography and geochemistry demonstrates that true albitite melts exist and that not all the albitite related to Fe oxide mineralization is consequence of a pervasive sodic alteration.

III.1. Introduction

Albitite is an uncommon rock present in very different geological settings, including ophiolite sequences, metamorphic terrains and hydrothermal environments. The dominant mineral association consists almost entirely of albitite-rich plagioclase and quartz with minor amounts of biotite, clin amphibole and abundant accessory phases like zircon, apatite, magnetite and fluorite. Despite this simple mineralogy, the ultimate source of the albitite has been subject of a large controversy. A metasomatic origin related to the circulation of Na-rich fluids that pervasively alter a granitic protolith is the most documented forming process (Kovalenko, 1978; Chauris, 1985; Hitzman, 1992; Williams, 1994; De Jong and Williams 1995; Barton and Johnson, 1996; Bachiller et al., 1996; Porter, 2002 and 2010; Sillitoe, 2003; Oliver et al., 2004; Castorina et al., 2006; Correveau et al., 2007), usually related to Sn-(Nb-Ta), U or Au mineralization. Of particular interest here is the association of albitite to the Fe oxide-(±Cu±-Au) (IOCG) style of

mineralization which has been intensively described in the literature (Hitzman et al., 1992; Williams, 1994; de Jong and Williams, 1995; Barton and Johnson 1996; Porter, 2002, 2010; Sillitoe, 2003; Oliver et al., 2004; Chen et al., 2010). In this context, albitite is considered as a product of pervasive sodic alteration of either sedimentary or igneous host rocks due to the circulation of fluids in disequilibrium with the protolith. A good example can be found in the Cloncurry Fe oxide - ($\pm\text{Cu}\pm\text{Au}$) district (Queensland, Australia) where the albitite is the dominant rock formed during a pervasive regional sodic ($\pm\text{calcic}$) alteration providing a favorable host rock for fracturation, brecciation and replacive Fe oxide mineralization (Mark, 1998; Oliver et al, 2004). A large number of magnetite deposits in the Cloncurry district contain albitized host rocks (i.e. calc-silicate rocks, marbles and minor pelitic and volcanic rocks of the Corella formation and siliciclastic metasedimentary and mafic metavolcanic rocks of the Soldiers Cap unit), such as Osborne, Starra (Rotherham et al., 1996) and Eloise. Also in the world class magnetite-apatite Kiruna deposit in which the magnetite is considered as the product of the crystallization of an iron oxide-rich melt, albitite formed in relationship to sodic alteration in the deep levels of the system, evolving to potassic and sericitic alteration in the upper levels. Here, the albitite is also associated with breccia fillings in which the magnetite replaced the magmatic, typically volcanic rocks deposited under continental conditions (Nyström and Henriquez, 1994). Of metasomatic origin is also considered the albitite related with other types of mineralization such as in some U - deposits (e.g., Valhalla in Brasil, Polito et al., 2009), REE - mineralization (e.g. Orani area in Central Sardinia, Cargangiu et al., 1997), Sn - (W) mineralization (e.g. Emuford in Australia, Charoy and Pollard, 1989; Aridondack Mountains in USA, McLlelland et al., 2002; Tikus in Indonesia, Schwartz, 1992) and Sn deposits (e.g. El Trasquilón deposit and albititic cupola and the Golpejas deposit in SW Spain, González Aguado and Gumiel, 1984 and Mangas and Arribas, 1987 respectively). Some episyenite (hydrothermal rock formed by the dissolution of quartz and feldespatization of a previous granitoid,

Leroy, 1978) of albitite composition have been also described as host of U, base metal or Sn-W mineralization (e.g. French Massif Central, Cathelineau, 1987; Sierra de Guadarrama, Spain, Caballero, 1993 y 1999; Tornos, 1991).

Magmatic albitite (directly crystallized from an igneous melt) is much less commonly addressed in the literature and is only ascribed to albititic dikes in ophiolite complexes (e.g. Bay of Island in USA, Elthon, 1991; Penjwin ophiolite, Kurdistan Region in Iran, Osman, 2007; Osman and Maekawa, 2007), some peraluminous granitoids (e.g. Kinsman intrusive suit in USA, Clark and Lyons, 1986), few REE-bearing granitoids (Kovalenko and Kovalenko, 1984; Umm Al Suqian Pluton, Asir Region in Saudi Arabia, Sherbini and Quadi and Qhadi, 2004), tonalite - trondhjemite - granodiorite series (TTG) and some intrusive carbonatite related to explosive emplacement of albitite derived from of A-type granites (e.g. the intrusive carbonate-albite complex in Southern Sinai, Egypt, Chaudhri et al., 2003; Azer et al., 2010).

The given criteria in order to determine the magmatic or metasomatic origin of the albitite are generally based on field evidences as for example the size of the outcrop, the presence of transitional zones between non-albitized and albitized rocks, the presence of relics of protolith, and the mode of occurrence. Criteria based on petrographic features are also commonly used, such as the shape and textures of the minerals or the presence of widespread replacive textures. However, the most important criterion for their characterization is the evidence of alteration of K-feldspar and Ca-bearing plagioclase into albitite.

In this study, we describe an albitite stock (La Berrona Stock, Ossa Morena Zone, SW Spain) that is one of the several large outcrops of albitite located in the Valuengo area (Fig. 1) and propose a magmatic origin for it based on a silicate melt inclusion study. Adjacent to this intrusion there is a large magnetite deposit, the La Berrona mine, that is studied in detail in order to establish the relationship

between the albitite and the mineralization. Our results are in clear contrast with the current view for the origin of most of the albitite bodies, particularly those related to Fe oxide-(\pm Cu- \pm Au) deposits, which are usually considered as of metasomatic origin.

Furthermore, the melt inclusion study of La Berrona Stock has shown the presence of some accessory Fe-Ti-P oxide droplets coexisting with the silicate melt inclusions. They are interpreted as representing an immiscible oxide phase that separated from the silicate melt during cooling and crystallization. If true, the existence of such an immiscible iron oxide melt phase is of critical importance for the genetic model as it could represent the source of the iron in the magmatic-hydrothermal fluids exsolving during the crystallization of the albitite.

III.2. Geological setting: the Valuengo area and the associated mineralization

The studied albitite occurrences are located in a geologically complex area near the denominated Valuengo Dome (Fig. 1), in the southern limb of the Variscan Olivenza-Monesterio Antiform (OMA, Fig 3, Chapter I). The Valuengo area is one of the few areas in the Ossa Morena Zone where high grade metamorphic rocks can be found. It consists of a N-S elongated ellipsoidal structure of 7x4 km with high grade metamorphic rocks in the core (the gneissic-migmatitic Valuengo Formation of Coullaut et al., 1981). These rocks are surrounded by the detritic and pelitic rocks with milonitic foliation of the Las Mayorgas Formation, probably equivalent to the syn-Cadomian Malcocinado Formation (Apraiz and Eguiluz, 1996; Apraiz, 1998; Expósito, 2000; Expósito et al., 2003, see Fig.2, Chapter 1). This formation has a characteristic layer of carbonatic rocks which is related to the magnetite deposits of the Colmenar-San Guillermo-Santa Justa group (Coullaut, 1979; Cuervo et al., 1996; Tornos et al., 2004; Sanabria et al., 2005). This succession is then followed by a thick (11-150 m) unit of

limestone, of likely Early Cambrian age. As it can be seen in the Figure 1, the Neoproterozoic low metamorphic grade metasediments of the Serie Negra Unit are overthrusting the previous rocks. These thrusts are probably related to the first deformation phase of the Variscan orogeny (Apraiz and Eguiluz, 1996).

At a regional scale, the contact between the Early Cambrian limestone and overlying volcanosedimentary rocks of the rift sequence are the loci of abundant (sub-) exhalative stratabound iron oxide mineralization that can be traced along both limbs of the OMA (Vázquez and Fernández Pompa, 1976; Coullaut, 1979; Dupont, 1979; Tornos et al, 2004; Carriedo and Tornos, 2010).

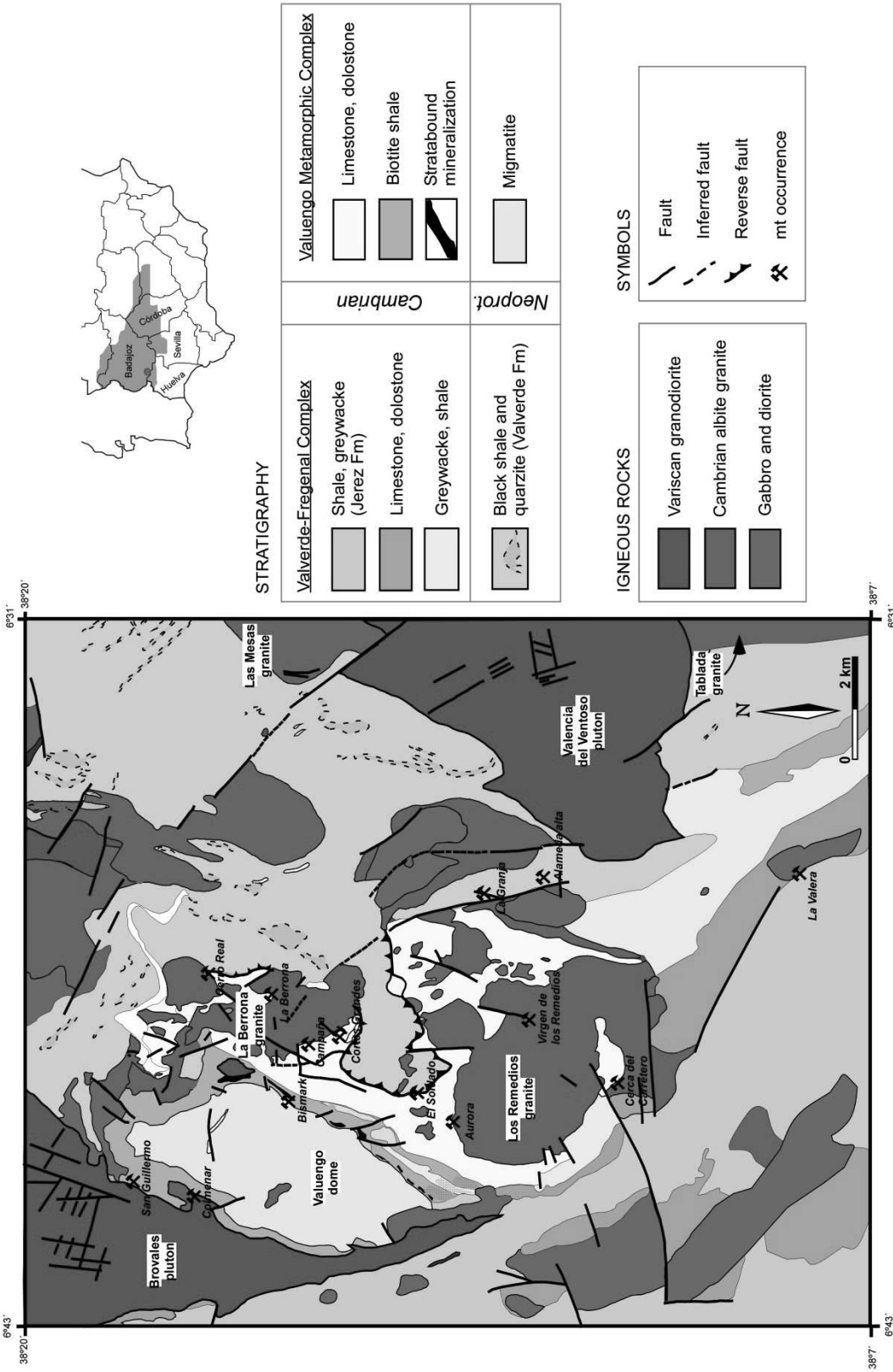


Figure 1. (Previous page). Geological map of the Valuengo area showing the main lithologies, structures and magnetite occurrences. Modified after Fernández Carrasco et al. (1981).

The high temperature/low pressure metamorphism that is especially visible in the core of the Valuengo Dome produced widespread anatexis of the rocks and the grade decreases drastically to the edge of the structure where the metamorphism is of medium to low grade. This strong metamorphic gradient is associated to an extensional steeply dipping ductile shear zone channelized by the Las Mayorgas Formation that has been clearly observed in several open pits of the western part of the dome. Following this structure to the south, the Monesterio metamorphic complex and the Lora del Río Core Complex (Apraiz et al., 1993; Apraiz and Eguiluz, 2002; Pereira et al., 2009) share many of the features of the Valuengo Dome (Fig.3, Chapter 1).

One controversy in the Valuengo Dome is the age of the metamorphism and dome formation, if being pre-Variscan or coetaneous with the Variscan deformation. Some interpretations consider them as related to crustal thickening and collapse during the second deformation phase of the Variscan orogeny (Ábalos and Díaz Cusí, 1995; Apraiz and Eguíluz, 1996; Apraiz, 1998). These interpretations are based on structural criteria such as the existence of neosomes showing only one phase of penetrative deformation. Recent radiogenic isotope and geochronological data of Carriedo (Ph.D. in prep.) are consistent with this model since U-Pb ages of some dykes of albitite within the shear zone suggest that the age of the albitite, the related mineralization and the formation of the Valuengo Dome Complex is Variscan, ca. 340 Ma. The Lora del Río complex, to the South of Valuengo and Monesterio areas has been also interpreted as an extensional core complex structure, dated at ca. 340 Ma (Apraiz and Eguíluz, 2002). Other interpretations suggest that the metamorphism is pre-Variscan (Expósito et al., 2003; Azor et al., 2004; Sánchez-García et al., 2003, 2008, 2010) as the mylonitic foliation related to the shear zone is folded by the Variscan recumbent folds. Expósito et al., (2003) have applied the single zircon Pb-Pb method in both an orthogneiss and undeformed microgranite in Valuengo,

obtaining ages of 532 ± 5 Ma and 480 ± 7 Ma respectively. In addition, the Monesterio Complex shares many structural features of Valuengo with high grade metamorphic rocks cropping out enclosed by branch lines of the same Variscan thrust-system. Despite the geochronological data are not very precise, the ages for the Monesterio Metamorphic Complex range also between 530 and 500 Ma (Schäfer, 1990; Ochner, 1993; Ordoñez Casado, 1998; Montero et al., 1999). These data support the connection of the metamorphism of the Valuengo and the Monesterio complexes with the pre-Variscan rifting stage that occurred in the OMZ during the Cambrian-Ordovician (Expósito et al., 2003).

The albitite bodies are abundant along the eastern and southern margins of the Valuengo Dome, and are located within the zone of major detachment (Fig. 1), which probably controlled the level of intrusion of the albitite. There are up to six intrusive bodies, some of them more than 4 km long (IGME, 1972). The most significant ones are the La Berrona and Los Remedios Stocks, intruding the Early Cambrian limestone and related shale and calc-silicate hornfels but also the late Neoproterozoic black shale (Serie Negra Unit). There are also some albitite dyke warms crosscutting the Burguillos del Cerro Variscan intrusion (Bachiller et al., 1997) or the Las Mayorgas Fm in the Colmenar Mine area (Carriedo and Tornos, 2010). Other albitite intrusions such as the Feria Stock are directly related to Cambrian volcanic rocks. The contacts between the country rocks and the albitite bodies are sharp and sometimes replacive with development of minor barren calcic garnet-rich skarn. The intrusions caused only slight contact metamorphism that is usually non-evident.

The albitite stocks at the east of the Valuengo Dome are dated at Early Cambrian age (La Berrona and Los Remedios). Carriedo and Tornos (2010) addressed an age of ca. 520 Ma in La Berrona (U-Pb SHRIMP) while Sánchez-García et al. (2008) dated Los Remedios Stock by U-Pb Zircon (TIMS) at 517 ± 2 Ma. Currently, these albitite bodies are interpreted as coetaneous and genetically

related to the alkaline to tholeiitic igneous activity developed during the post-Cadomian rifting stage that took place in the Ossa Morena Zone from the Early Cambrian to the Mid Ordovician (Sánchez-García et al., 2003, 2008, 2010). There is an early rift-related igneous suite, of predominantly felsic composition and related to core complex formation and middle to upper crustal migmatization, and a second event, the main rift-related igneous suite, with a younger and voluminous bimodal association emplaced during the climax of the upper crustal extension and basin compartmentalization (Sánchez-García et al., 2003).

On the basis of the geological relationships and the flat REE chondrite-normalized patterns, the albitite intruded during this period is interpreted as associated to the mafic rocks and equivalent to oceanic plagiogranites with N-MORB affinities (Sánchez-García et al., 2003, 2010; Bellido et al., 2010). Etxebarria et al. (2006) also address the similarities on the composition of the albitite with that of the ocean ridge plagiogranite and the fact that some albitite bodies are related to gabbro. The ultimate origin would be the extreme fractionation of a basaltic magma (Sánchez-García et al., 2003, 2008, 2010; Bellido et al., 2010) or the partial melting of a tholeiitic gabbro (Etxebarria et al., 2006).

Some albitite in the Valuengo area is of clear Variscan age. The albitite dyke swarms of Burguillos del Cerro crosscut the homonymous intrusion and are, thus, younger than 340 ± 4 Ma (Montero et al., 2002). They have been dated at 337 ± 7 Ma (Rb-Sr; Bachiller et al. 1997). Also, some small elongated stocks and dykes with aplitic to pegmatitic structures of the western Valuengo area have been dated as Variscan by Carriedo (Ph.D., in prep.). These data suggest that in the Valuengo area there are at least two events of albitite formation.

Close to the Valuengo Dome, the main Variscan plutonic complex in the OMA is located as subcircular groups of large calc-alkaline bodies including the Valencia del Ventoso, La Bazana, Brovales (340 ± 4 Ma, Montero et al., 2000) and

Burguillos del Cerro (330±9 Ma, Bachiller et al., 1996, 1997; ca. 335 Ma, Dallmeyer et al., 1995 and ca. 335 Ma, Casquet et al., 1998) plutons. Some of them have developed calcic skarns on the adjacent Cambrian limestone (e.g., the Santa Bárbara mine in the Brovales pluton and the abundant magnetite deposits around the Burguillos del Cerro pluton, Tornos et al., 2004).

III.2.1. Fe oxide (± Cu ± Au) deposits associated to the albitite in the Valuengo area

As shown in the Figure 1, there are several magnetite occurrences spatially associated to the albitite in the Valuengo area. First considered as being calcic skarns (Coullaut et al., 1972) or as of sedimentary origin associated to the Cambrian volcanism (Doetch, 1967; Dupont, 1979) some of them have been recently reclassified as IOCG (iron oxide-copper gold) style deposits by Tornos et al. (2003), Tornos and Casquet (2005) and Carriedo and Tornos (2010). Main arguments include the relationship with a sodic-(calcic) alteration, the presence of replacive albite-actinolite-magnetite, the high REE-U contents and the abundance of scapolite. Most of the orebodies are small, and only some of them were exploited for iron during the past century with a total production of 2 to 4 Mt @ 55–60% Fe (in the San Guillermo-Colmenar-Santa Justa group, Dupont, 1979). The mineralization occurs as stratabound (Bismark, El Soldado, Las Galerías, Colmenar), replacive skarn and breccia (Santa Bárbara, Colmenar, La Berrona) and stockwork irregular bodies (La Berrona) associated with albitite dykes or intrusions (Carriedo and Tornos, 2010). The ore is mainly composed of magnetite associated with albite and actinolite with minor proportions of adularia, hedenbergite, biotite, quartz, carbonates, ilvaite and titanite. The sulfide content is generally low, with only some chalcopyrite, pyrite, pyrrhotite and trace amounts of millerite and cobaltite, besides significant amounts of titanite, allanite, zircon and apatite (Tornos et al., 2004). In some cases, this epigenetic mineralization

crosscut earlier stratabound magnetite deposits in the host volcanosedimentary rocks (Sanabria et al., 2005; Carriedo et al., 2009).

Also, in the western part of the Valuengo Dome, the Colmenar mine includes complex stratabound actinolite-albite-magnetite replacement bodies associated with the albititic dykes capped by magmatic-hydrothermal breccias (Sanabria et al., 2005; Carriedo and Tornos, 2010).

Besides this hydrothermal mineralization style in the area, there is some different mineralization as in the La Valera Mine, located to the south of the Valuengo Dome (Fig. 1). Coullaut et al. (1980) described pyroclastic rocks of dacitic composition with interbedded layers rich in fragmental magnetite. Here, the presence of some columnar jointing structures and magnetite-supported breccias suggest a magmatic origin for the mineralization, crystallized from an iron oxide melt immiscible from a silicate melt (Carriedo et al., 2009, 2010).

A comprehensive characterization of the geology, mineralogy, isotope geochemistry and geochronology of the magnetite ($\pm\text{Cu}\pm\text{Au}$) deposits of the Ossa Morena Zone can be found in Carriedo and Tornos (2010) and Carriedo Ph.D. thesis (in prep.).

III.2.2. Geology of the La Berrona Stock

The La Berrona Stock is located in the eastern zone of the Valuengo area (Fig.1). It is an N-S elongated intrusion that was emplaced within the limestone, calc-silicate hornfels and shale of the Early Cambrian sequence. Roof pendants and enclaves of limestone and calc-silicate hornfels (partially replaced by calcic skarn) are widespread above the albitite suggesting that the current outcrops are near to the original roof of the intrusion. The eastern limit of the intrusion is a N-S trending and low dipping thrust of likely Variscan age that overthrusts the early Cambrian sequence and the albitite over Neoproterozoic shale and quartzite.

The albitite is a whitish unoriented and massive rock mainly composed of quartz (~ 1 cm, rounded to euhedral) and albite (~ 1cm, rounded to euhedral) phenocrysts with only some potassic feldspar phenocrysts in a fine grained groundmass composed of the same minerals (Fig. 2A). Common accessory minerals are biotite, clinoamphibole, clinopyroxene, magnetite, apatite, zircon, carbonates and fluorite. There are also some remnants of former phenocrysts of mafic minerals (clinoamphibole or biotite) almost totally replaced by albite plus quartz. The plagioclase phenocrysts show the characteristic polysynthetic twinning (Fig. 2B) but occasionally they have an external rim with a more sodic composition, interpreted as due to the presence of a subtle autometasomatic alteration related to the fluid exsolution during the crystallization of the melt, which was also responsible of the replacement of the mafic minerals by albite. Otherwise, the rock does not show any evidence of hydrothermal alteration. The rock shows abundant granophyric textures, mainly of K feldspar with vermicular quartz (Fig. 2C). These textures are indicative of rapid crystallization of a melt with a composition close to that of the eutectic (Winter, 2010). Evidences of replacement of K-feldspar or other minerals (except that of the mafic minerals by albite) have been not observed. The rock is crosscut by wavy and segmented veins that are considered to be formed prior the rock was completely consolidated (Fig. 2D).

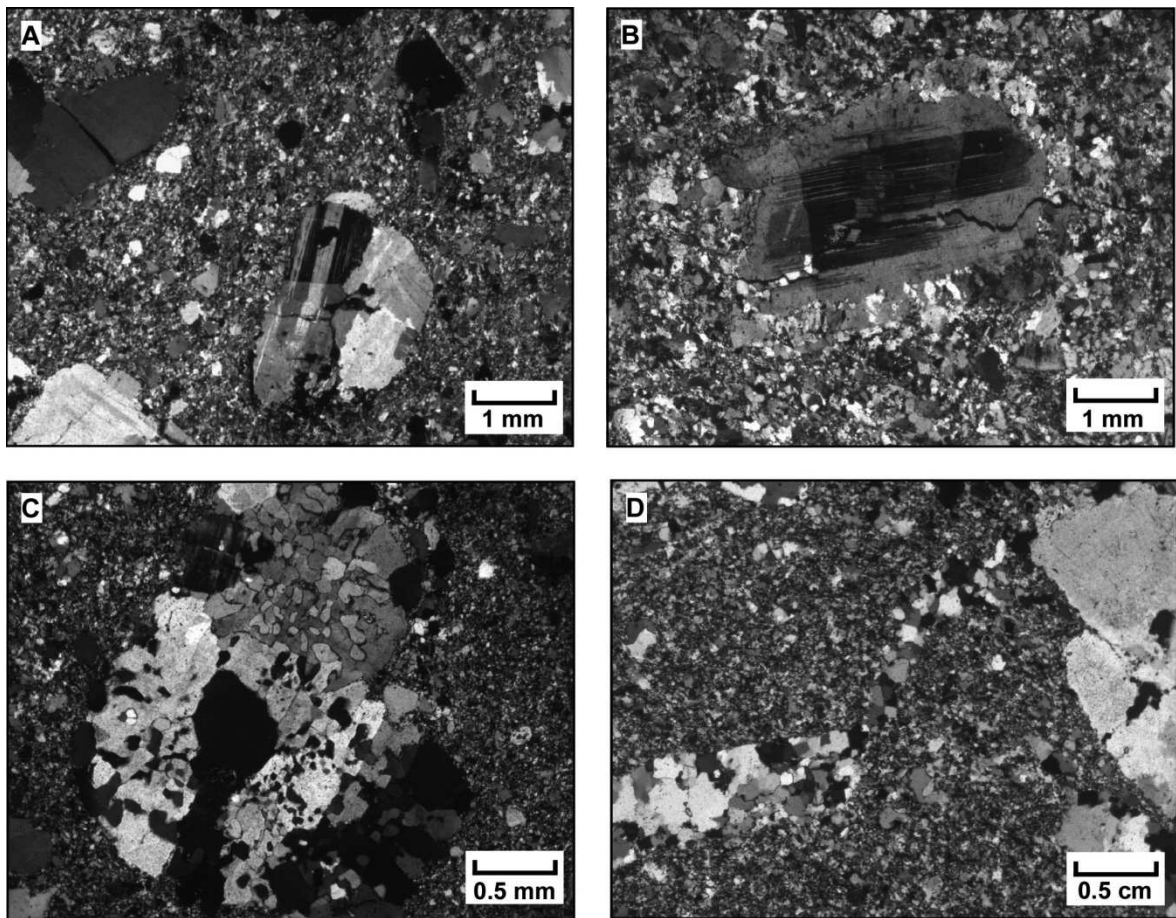


Figure 2. Transmitted light microscope photographs (polarized light) of the albitite. **(A)** Porphyritic texture with phenocrysts of quartz and albitite in a groundmass with the same minerals. **(B)** Plagioclase phenocrysts showing an untwined external zone of albitite, probable product of autometasomatic reaction. **(C)** Myrmekitic texture with intergrown quartz and albitite. **(D)** Quartz A-type vein in the albitite (see Figs. 3F and 3G) with wavy and segmented shapes and crosscutting the groundmass.

The emplacement of the albitite was probably accompanied by the development of a carapace that isolated the melt from the host rocks. The only field evidence of the existence of such a carapace is the fine grained nature of the groundmass (<0.2 mm) that contrasts with the more coarse grained one (0.5-1 mm) within the core of the intrusion.

The conditions of emplacement of the albitite are difficult to establish due to the lack of geobarometers and of noticeable contact metamorphism. Contacts with the host rock are sharp and discordant with magmatic hydrothermal breccias at the top of the intrusion. The minimum estimated temperature of crystallization is ca. 600° to 800 °C as estimated from the melt inclusion data (see below).

Besides the La Berrona albitite, the La Berrona deposit is also studied in detail in this chapter in order to establish the magmatic-hydrothermal fluid evolution reflecting the continuum from the magmatism to the fluid exsolution and the hydrothermal fluid circulation related to the ore formation. In the introduction of this chapter, some examples have been addressed in which some Fe oxide-(±Cu-±Au) mineralization worldwide is related to large volumes of metasomatic albitite (e.g., Rubenach and Lewthwaite, 1992; Perring et al., 2001; Corriveau, 2007). It is proposed in this study that the albitite related to the La Berrona magnetite deposit is of magmatic origin, strongly contradicting the current genetic models for the albitite in these type of deposits (see Oliver et al., 2004 for a good review of metasomatic albitization related to Fe oxide deposits).

III.2.3. Origin of the Fe oxide (±Cu-±Au) deposits: a review

The IOCG sl. style of mineralization include both magnetite-apatite deposits, usually poor in sulfides, and the IOCG ss. deposits, where the iron oxides (magnetite and hematite) coexist with variable amounts of iron and copper sulfides and variable amounts of gold. These two styles of mineralization share characteristics such as the relationship with a hydrothermal alteration dominated by alkali feldspar (both albite and K feldspar), actinolite/calcic pyroxene, biotite, scapolite and the low proportions of quartz and sulfides. These systems are also characterized by the common presence of minerals rich in volatiles such as P, F or B and a significant enrichment in U and REE. Different genetic models have been proposed based on the texture and structure of the ore, the alteration pattern, the

geochemistry and the mode of occurrence. Magnetite-apatite deposits are considered to be product of the direct crystallization of Fe-rich, Ti-poor oxide melts that have been separated from a parental silicate melt (Nyström and Henriquez, 1994; Naslund et al., 2002; Henriquez et al., 2003). However, there are alternative models that invoke a magmatic-hydrothermal (Hitzman et al., 1992) or sedimentary-hydrothermal (Barton and Johnson, 2000) origin for these ores.

There is a type of magnetite-apatite rock, the so-called nelsonite (Watson, 1913, Kolker, 1982) that is an igneous rock rich in Ti-rich magnetite, ilmenite and apatite commonly associated to anorthositic complexes. As the magnetite-apatite rock in the IOCG's clan, nelsonite is interpreted as formed by direct crystallization from a Fe- Ti- P oxide melt that could represent an immiscible magma exsolved from a silicate melt or due to extreme fractional crystallization. Perhaps the major difference of nelsonite regarding the magnetite-apatite ores is the Ti content, which is usually low in the later and high in the former as well as the association to magmatic anorthositic rocks which are common in the former (Kolker, 1982; Dymek and Owens, 2001; Clark and Kontak, 2004).

IOCG mineralization includes both magnetite and hematite (\pm Cu-Fe sulfides, \pm Au) deposits formed by the circulation of hydrothermal fluids that replace sedimentary, volcanic or plutonic rocks. The origin of the fluids is controversial and different models have been proposed. They have been interpreted as exsolved from magmatic sources, both of mafic and felsic composition (Pollard, 2000, 2001, 2006; Perring et al., 2000; Sillitoe, 2003; Tornos et al., 2010). Alternative models propose the infiltration of brines equilibrated with evaporites but driven by magmatic heat (Barton and Johnson, 1996, 2000, 2004). Regardless of the ultimate origin, high saline fluids (that are characteristic of the IOCG) carry metals as Cl-complexes that precipitate by fluid-rock reaction or by fluid mixing (Williams et al, 2005). The vast amounts of fluids involved in these systems produce large zones of alkaline-calcic, Na and K-rich, alteration usually

associated with the growth of calcic minerals, either actinolite or clinopyroxene. Both magnetite-apatite and IOCG styles of deposits can coexist in the same province such as in the Skellefte district in N Europe (Weihed et al., 2005) and in the Central Andes (Tornos et al., 2011).

As pointed before, there are several magnetite deposits directly related to the albitite within the Valuengo Dome area (Fig.1). One of the largest of these deposits, La Berrona, constitutes an accessible and well exposed magnetite deposit that was discovered in 1979 by the Geological Survey of Spain (IGME). The deposit was never exploited but there are two exploration quarries (the “Upper” and “Lower” Quarries) done for metallurgical tests that expose the mineralization and the host rocks. La Berrona deposit has been recently cataloged as IOCG-like deposit by Tornos et al. (2003), Tornos and Casquet, (2005) and Carriedo and Tornos, (2010) as it shares some characteristics of the IOCG deposits as the typical magnetite-albite-actinolite alteration pattern or the poor sulfide content. In this chapter La Berrona deposit is studied in detail in order to establish the magmatic-hydrothermal fluid evolution reflecting the continuum from early magmatic to the late hydrothermal fluid circulation and its relationship to ore formation. In the introduction of this chapter, some examples have been addresses in which Fe oxide-(Cu- Au) mineralization worldwide is related to, in some cases very large volumes of metasomatic albitite (e.g., Rubenach and Lewthwaite, 1992; Perring et al., 2001; Corriveau, 2007).

III.2.4. La Berrona deposit as a case study of magnetite mineralization related to albitite

The La Berrona deposit is situated at the northeastern part of the albitite stock of the same name in the Valuengo area, 20 km east of Jerez de los Caballeros (Badajoz, Spain) and covers a surface area of around 800 m² (Fig. 3). In 1979, the IGME made a drilling campaign and recovered 71 vertical drill cores in a regular

net of 50*50 m, estimating reserves of 26.2 Mt ore with 26.8% Fe, 0.325% P and 2.97% Na₂O+K₂O. Unfortunately all the drill cores were thrown to an unknown place.

The magnetite mineralization replaced an early Cambrian sequence occurring as a roof pendant or lateral to the albitite stock (IGME, 1979; Coullaut et al., 1980). The main orebody covers a surface area of about 500x350 m (IGME, 1979) and has a sub-cylindrical shape of N160°E direction with irregular patches of mineralization below (Fig. 3). In the Lower Quarry it can be observed that both the albitite and the calc-silicate hornfels are irregularly replaced by an albite-actinolite-magnetite alteration assemblage. The main orebody shows a conspicuous banding consisting of mm to cm-thick layers of almost monominerallic magnetite and actinolite with albite and minor amounts of epidote, scapolite, pyrite, pyrrhotite, chalcopyrite, apatite, titanite, calcite and quartz (Figs. 4A and 4B) (Tornos et al., 2004; Carriedo and Tornos, 2010).

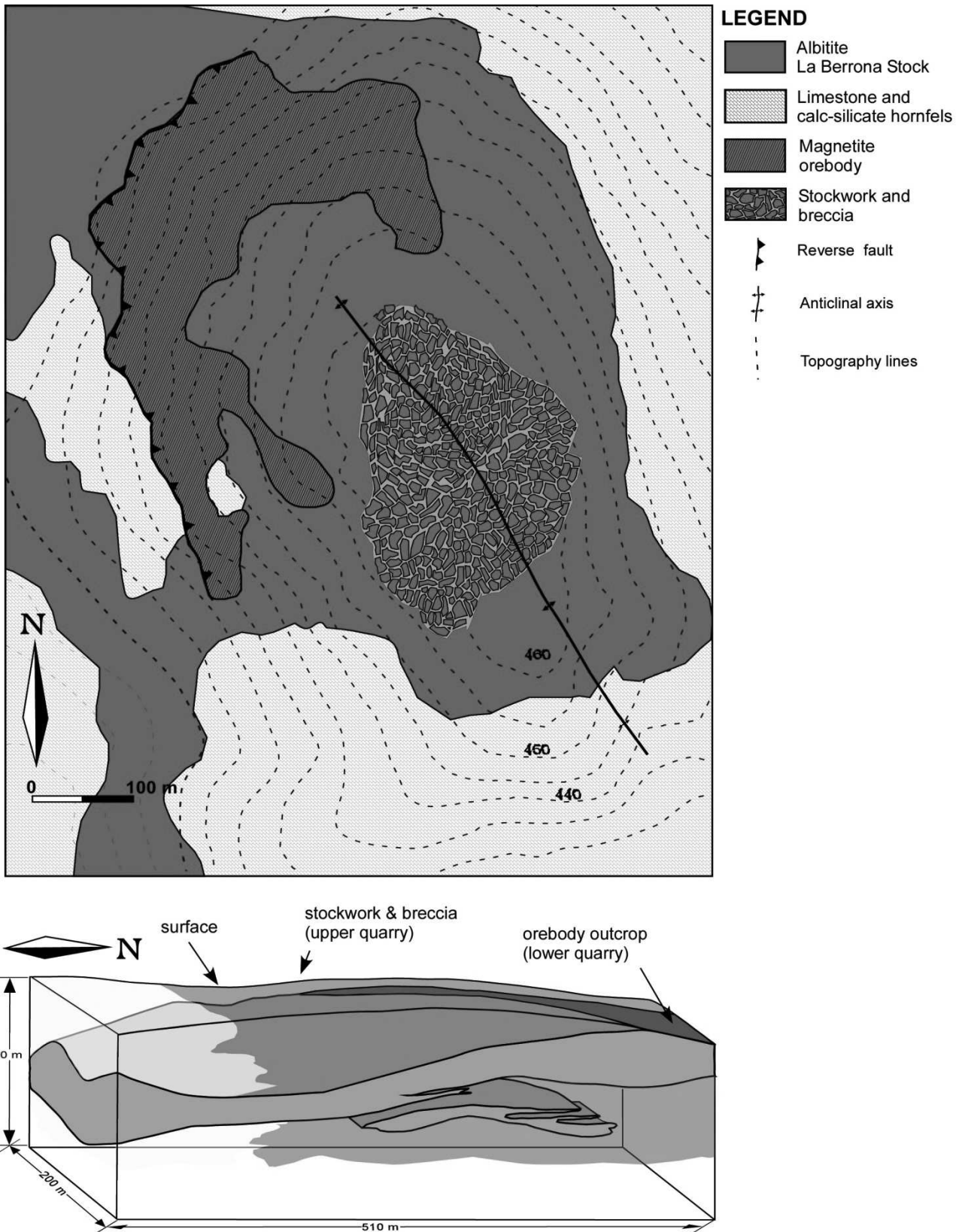
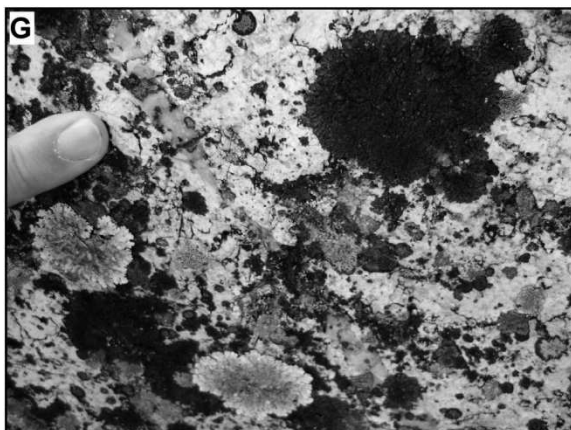
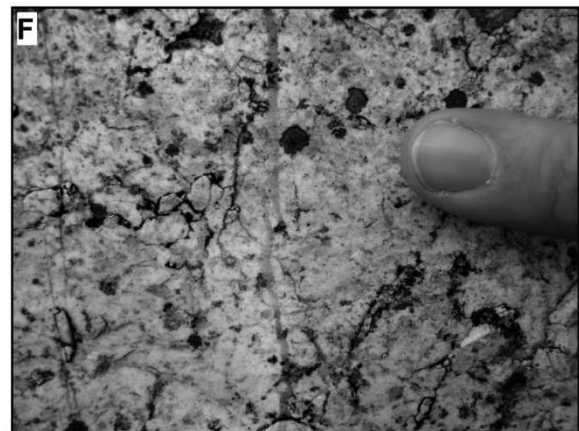
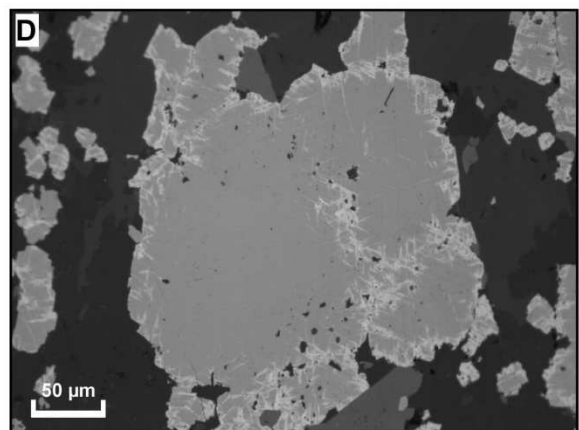
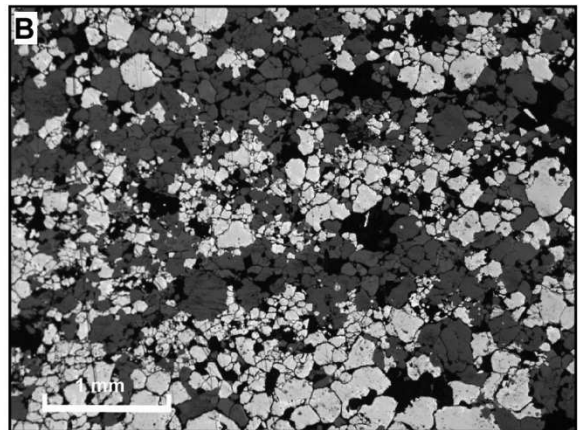


Figure 3. Geological map of the La Berrona deposit (based on IGME, 1975). A simplified 3D model of the orebody is also shown, based on the drill-core logging.

In the Upper Quarry, probably excavated in what was the cooling carapace of the intrusion (see below), there are breccias and a well-developed stockwork system. These bodies are lateral to the replacive mineralization (Fig. 2) but likely represent the zones of upwards fluid circulation generated by fluid overpressure during the exsolution of an aqueous phase from the silicate melt. The breccia consists of fragments of albitite supported by a fine grained hydrothermal groundmass of magnetite, actinolite and quartz (Figs. 4C and 4D). The albitite fragments are both angular and subrounded with equant to elongated shapes and sizes ranging from 2 to 20 cm, showing a jigsaw pattern. They show an irregular and subtle replacement by fine grained actinolite and magnetite. The stockwork system is marginal to the breccia and here the magnetite fills irregular fractures between heterometric angular fragments of altered albitite (Fig. 4E). The mineralization has been replaced by supergene hematite in areas exposed to the surface, although this hematite is not related to the ore formation but to secondary alteration processes.

Within the albitite and the mineralization there are different types of quartz veins and hydrothermal vugs that are suitable for fluid inclusion studies. The uppermost albitite is crosscut by quartz veins having irregular, wavy, and sometimes segmented shapes with widths ranging between 1 and 3 cm (Fig. 4F and 4G). These veins are broadly equivalent to the A-type veins described in porphyry copper deposits (Gustafson and Hunt, 1975) and other magmatic-hydrothermal systems. They are interpreted as formed before the rock was completely solidified, i.e., close to the brittle-ductile transition. Crosscutting the breccias, there is a second generation of quartz veins with constant widths of 5 to 8 cm. These veins have parallel walls and a continuous trace that is lacking in the first generation of A-veins and are thus interpreted as late brittle veins (Fig. 4J). The magmatic-hydrothermal breccias locally include small cavities filled with quartz, actinolite, biotite and calcite (Fig. 4H). These cavities are probably

synchronous with the vugs having the same assemblage and found in the banded ore within the Lower Quarry (Fig. 4I).



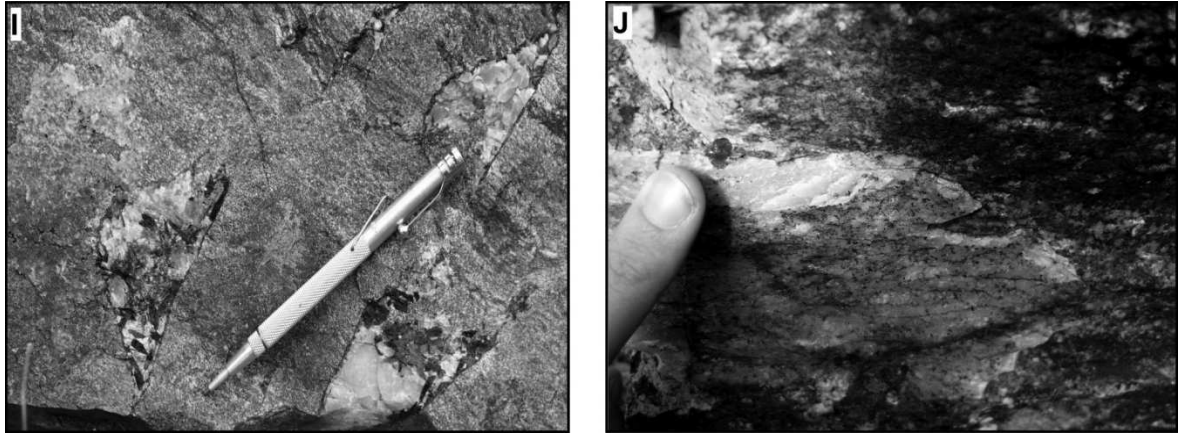


Figure 4. Microscope and field photographs showing the nature of the magnetite mineralization and the styles of quartz veining and filling at La Berrona. **(A)** Bands of almost monomineralic magnetite and albitite with clin amphibole replacing the calc-silicate and the pelitic hornfels in the Lower Quarry. **(B)** Reflected light image of bands of magnetite (grey white) intergrown with actinolite and alternating with albitite. **(C)** Magmatic-hydrothermal breccia with clasts of fresh albitite in a groundmass of magnetite, albitite, actinolite and quartz. **(D)** Reflected light image of the pseudomorphosis of martite along borders and fractures of a grain of magnetite. **(E)** Stockwork system with the fractures filled by magnetite and actinolite in the Upper Quarry. Note that the albitite shows only minor alteration. **(F)** Thin early A-vein with a segmented shape. **(G)** Discontinuous and wavy A-vein. **(H)** Small cavities with quartz, actinolite, biotite and calcite in the magmatic-hydrothermal breccia. **(I)** “Pockets” of quartz, actinolite and calcite in the banded magnetite ore. **(J)** Late veins with parallel walls not segmented as the A-veins in the figures F and G.

III.3. Sampling and Methods

Albitite samples were collected in the La Berrona Stock area, both within areas close to the magnetite mineralization and the magmatic-hydrothermal breccias and away the zones with evidences of hydrothermal activity. Samples were also collected in the La Berrona orebody in order to test the potential for fluid inclusion studies in the deposit. Normal and double polished sections of 150-300 μm in thickness were made and examined under the transmitted light microscope for mineral, melt inclusion and fluid inclusion petrography. After a detailed characterization, some samples were selected for melt and fluid inclusion analysis. They include: (a) quartz and plagioclase phenocrysts in the albitite for melt inclusions studies; and, (b) quartz phenocrysts in the albitite, early (A type) and late quartz veins crosscutting the albitite and the quartz-rich cavities in the breccias and banded magnetite ore for fluid inclusions. Melt and fluid inclusions were evaluated in terms of size, shape, frequency and phases present at room temperature. Special care was taken avoiding the inclusions with signs of postentrapment modifications (Nielsen, 1998; Audéat and Gunther, 1999; Webster, 2006; Zajacz et al., 2008).

III.3.1. Homogenization tests of the melt inclusions

The homogenization experiments were performed on a high temperature THMSG 1500 Linkam stage at the ETH Zurich. This microthermometric stage is capable of heat the sample to 1500 $^{\circ}\text{C}$ and the phase changes in the melt inclusions can be observed by the microscope fitted to it. The silicate melt inclusions (SMI) were heated to high temperatures in order to test if they homogenize or not at geologically realistic temperatures. Theoretically, the homogenization temperature of melt inclusions is equivalent to the trapping temperature and hence, the temperature range of the crystallization of the melt can be estimated. Although a

commonly used technique (e.g. Thomas and Klemm, 1997; Webster et al., 1997; Danyushevsky et al., 2002; Davidson, 2004; Student and Bodnar, 2004; Severs et al., 2007), the microthermometry of melt inclusions entails problems that are sometimes impossible to solve. One of these problems is that the melt inclusions often decrepitate during the transition of quartz from α to β at 573 °C (Ghiorso et al., 1979; Danyushevsky et al., 2002). Decrepitation of younger secondary fluid inclusion trails that crosscut the melt inclusions can also provoke fracturing of both melt inclusion and the host mineral during the heating runs (Webster et al., 1997). Moreover, diffusion (of H₂O in most of the cases) can occur between the host phenocryst and the melt inclusion misleading the true melting temperatures. An alternative method to reproduce the temperature at which the melt inclusions were entrapped is to homogenize them under confining pressure in a cold seal pressure vessel to prevent volatile loss by leakage or decrepitation (Student and Bodnar, 2004; Zajacz et al., 2008). The major disadvantage of the pressure vessel is that is not possible to observe the phase changes in the melt inclusions, and only an estimation of the last melting temperature can be acquired. Owing to all these difficulties, the microthermometry is not used anymore to determine the trapping/crystallization temperatures of the melt inclusions but rather to get an idea of their melting behavior and principally, to obtain a homogeneous glass for further microprobe and Raman analyses.

In this study, thirteen silicate melt inclusions of different sizes and shapes were selected for heating experiments (Appendix IIB). In order to avoid as much as possible the decrepitation and diffusion processes, we followed the heating run procedure established by Student and Bodnar (2004) that is explained in the Appendix IIB of this thesis.

In most of the cases, the melt inclusions (principally the largest ones) did not reach the homogenization temperature due to prior decrepitation. In others, the poor visibility (mostly due to the groundmass melting) prevented the

observation of phase changes at temperatures higher than ~400°C. When this observation was possible, the majority of the recognizable changes (melting of a phase) occurred between 600° and 800 °C. This range of melting temperatures is considered only as estimation and not the true homogenization/trapping temperature as discussed above. However, it is a guess of the minimum crystallization temperatures of these melts.

III.3.2. Fluid inclusion petrography and microthermometry

The fluid inclusion petrography and microthermometry were carried following the procedure explained in the Chapter II of this thesis. Microthermometric analyses were performed on a Linkam TMS 94 heating-freezing stage at the Instituto Geológico y Minero de España (IGME, Salamanca). The stage was calibrated using synthetic H₂O-CO₂ fluid inclusions supplied by Linkam Scientific Instruments Ltd. for the eutectic point of CO₂ (-56.6 °C) and synthetic H₂O fluid inclusions for the melting point of ice (0.0 °C) and the critical point of water (374.15 °C). The procedure was dependent upon the phase proportions of the fluid inclusion at room temperature. The complete data set of fluid inclusion microthermometric data is shown in the Appendix IIB.

III.3.3. LA-ICPMS analyses

More than 100 silicate melt inclusions (SMI), 12 being iron rich (iron oxide blebs; IOB) and 20 fluid inclusions were analyzed by laser ablation - inductively coupled plasma mass spectrometry (LA-ICPMS) to determine their absolute element concentrations. The complete procedure for LA-ICPMS analysis on melt inclusions is described by Günther et al. (1997, 1998), Audétat et al. (1998), Ulrich et al. (1999), Halter et al. (2002), Heinrich (2003) and references therein. The advantage of using the LA-ICPMS technique when working with crystallized melt inclusions is that they do not have to be homogenized, quenched and being

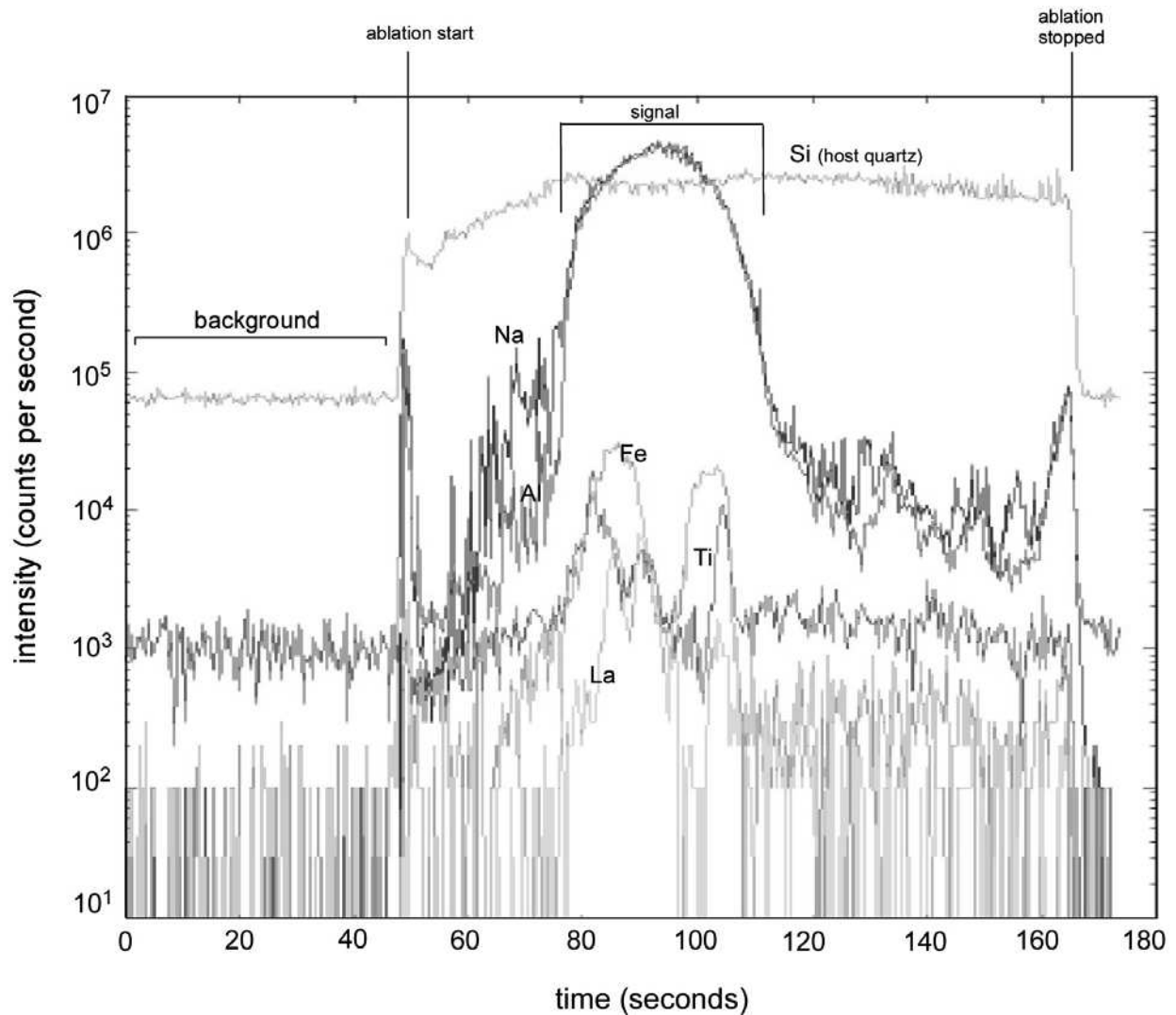
exposed to the surface prior to the analyses as it is required by other techniques such as EPMA, SIMS and PIXE. The LA-ICPMS analyses were made at the ETH Zürich, with an Elan 6100 ICP-MS (Perkin Elmer, Canada) spectrometer combined with a 193 nm Excimer laser system (Lambda Physik, Germany). The conditions for the melt inclusion analyses are summarized in the Table 1. The selected wafers were first cleaned thoroughly with acetone and aqua regia and later they were repolished for avoiding as much as possible any surface contamination. In order to obtain homogeneous signals, only inclusions located beneath the quartz surface were selected. Both the silicate melt inclusions and the iron oxide blebs were analyzed following the same procedure except for the data reduction.

EXCIMER 193 nm ArF laser COMPLEX 110I	
Fluence	30 -35 J/cm ²
Pulse duration	10 - 20 ns
Repetition rate	10 Hz
Pit size	15 and 200 µm
Ablation cell volume	1 cm ³
Cell He gas flow	1.1 L/min (+5 ml/min H ₂)
ELAN 6100 DRC quadrupole ICP-MS	
Nebulizer gas flow	0.85 L/min Ar (can vary due to daily tuning)
Auxiliary gas flow	0.85 L/min Ar (can vary due to daily tuning)
Cool gas flow	15 L/min Ar
RF power	1550 W
Quadrupole setting time	3 ms
DATA AQUISITION	
Readings per replicate	400
Dwell time per isotope	Adjusted to 10 ms (standard)
Isotopes	23Na, 29Si, 25Mg, 27Al, 29Si, 31P, 32S, 39K, 42Ca, 45Sc, 47Ti, 51V, 53Cr, 55Mn, 57Fe, 59Co, 60Ni, 65Cu, 66Zn, 75As, 85Rb, 88Sr, 90Zr, 93Nb, 95Mo, 111Cd, 118Sn, 133Cs, 137Ba, 139La, 140Ce, 157Gd, 172Yb, 175Lu, 181Ta, 182W, 208Pb

Table 1. LA-ICPMS analytical conditions for the melt inclusion analysis.

An external standard (NIST 610 SRM) was used to calibrate the analytical sensitivity and convert the signal of the mixed host and melt inclusion into

elemental ratios. In order to obtain the absolute element concentrations, an internal standard (an element with a known concentration in the melt inclusion) is required to quantify the contribution of the host mineral and the melt inclusion to



the mixed laser ablation signal (“deconvolution” of the mixed signal; Fig. 5).

Figure 5. LA-ICPMS signal of a single silicate melt inclusion (sample10ma05b07) hosted by a quartz phenocryst in the albitite from La Berrona. The signal records the elements (only La, Ti, Fe, Na and Si are shown here for better clarity) analyzed within the melt inclusion.

The selection of the internal standard is critical and the possible uncertainties that it entails have to be taken into account in each specific case. Halter et al. (2002b) has proposed four methods through which the internal standard for the melt inclusions can be obtained, all of them from external sources: (1) to consider the concentration of an element, which does not vary significantly during the melt differentiation, as being constant in the melt inclusions within a same rock; (2) to define a characteristic element concentration or ratio from the bulk differentiation trend rocks of the same system; (3) to guess a constant distribution coefficient of an element between the host and the melt; and, (4) from volume measurements of the inclusions and the ablated pit. Zajacz et al., (2008) proposed an additional method (perhaps the most accurate one) which consists of compare coetaneous and cogenetic melt inclusions in co-precipitated minerals to quantify their composition without depending on an external source for the internal standard. Unfortunately, the melt inclusions found in the plagioclase phenocrysts of the albitite are not good enough for the study, ruling out the use of this late method. The uncertainty due to the internal standardization is in the order of 20-30% (Audétat et al., 1998). Despite being rather high, it is acceptable when compared to the large changes in the concentrations of certain elements during the melt fractionation. After evaluating the rest of the options, the Al_2O_3 content of the bulk rock has been chosen as the internal standard because: (1) The variation of the aluminum content is quite constant in the bulk rock analyses of the albitite from La Berrona (12.7 to 16.5 wt% Al_2O_3) as well as in other coetaneous albitite found nearby (Sánchez-García et al., 2003) (13.5 to 16.2 wt% Al_2O_3 ; Table 2); and, (2) Al is one of the most constant element in magmatic rocks showing little variations during the fractional crystallization.

Rock suit	Al ₂ O ₃ content (wt%)
Felsic-intermediate rocks with OIB affinity	14.7 (max: 17.3; min: 9.4)
Mafic rocks with OIB-EMORB affinities	15.1 (max: 17.7; min: 9.5)
Mafic rocks with N-MORB affinities	16.2 (max: 22.1; min: 8.9)
Plagiogranite with N-MORB affinity	13.5 (max: 16.0; min: 12.5)
Albitites Valuengo area (this study)	13.5 (max: 16.5; min: 10.8)

Table 2. Al₂O₃ values of the rift-related Cambro-Ordovician igneous rocks in the Ossa Morena Zone. All the values are taken from Sánchez-García et al., (2008) except for the albitite from the La Berrona Stock area which belong to this study.

The absolute element concentrations of the iron oxide blebs were calculated assuming the same external standard (NIST 610) as for the SMI (Halter et al., 2002). However, the selection of the internal standard for the IOB is difficult as there are no previous references of LA-ICPMS analysis on oxide droplets in the literature. In the references of LA-ICPMS analysis of sulfide melt inclusions, the internal standard is selected assuming that the inclusions are stoichiometric ((Fe, Cu)S₂) in their composition (Halter et al., 2004 a and b). Following this procedure, magnetite was used as an internal standard for the calculation of element concentrations in the IOB. The stoichiometric composition of the ilmenite was also considered as an internal standard to test the differences on respect to magnetite, as Ti is remarkably present in the IOB. The differences on the element concentrations using these two internal standards are small so the magnetite composition was selected.

LA-ICPMS analyses in minerals were performed in: (1) the host quartz phenocrysts; (2) the plagioclase phenocrysts; 3) the accessory magnetite, and; (4) the magnetite from the orebody. Stoichiometric SiO₂, Al₂O₃ and Fe₃O₄ were used as internal standard for quartz, plagioclase and magnetite respectively.

LA-ICPMS analysis of fluid inclusions were conducted at the ETH Zürich, following the procedure explained in the Chapter II of this thesis. The Na concentration obtained from the microthermometry of the fluid inclusions was used as an internal standard.

The mean LA-ICPMS composition of melt inclusion assemblages, fluid inclusions and iron oxide blebs are shown in the Tables 3, 4 and 5 respectively.

	MIA 1	15	SMI 2	MIA 3	15	MIA 4	15	SMI 5	SMI 6	MIA 7	15	SMI 8	SMI 9	SMI 10	MIA 11	15	SMI 12	MIA 13	15	MIA 14	15	MIA 15	15
SiO ₂	73.42	0.03	71.75	74.64	0.67	74.53	0.29	74.91	74.32	74.93	0.42	72.66	65.97	67.25	71.38	0.20	73.67	72.38	0.17	72.96	0.14	73.90	0.49
Al ₂ O ₃	12.71		12.71	12.71		12.71		12.71	12.71	12.71		12.71	12.71	12.71	12.71		12.71	12.71		12.71		12.71	
Fe ₂ O ₃	0.46	0.28	3.12	0.27	0.23	0.60	0.05	0.15	0.18	0.32	0.27	1.17	5.87	9.62	1.61	0.16	0.87	1.49	0.02	1.26	0.05	1.20	0.39
CaO	BLOD		0.27	BLOD		0.50		0.45	1.08	0.63	0.00	1.02	BLOD	BLOD	1.57	0.00	BLOD	0.72	0.00	0.58	0.03	BLOD	
TiO ₂	0.14	0.00	BLOD	0.08	0.07	0.09	0.02	0.16	0.11	0.07	0.06	0.10	BLOD	0.05	0.13	0.00	0.12	0.15	0.02	0.13	0.01	0.13	0.06
MnO	0.01	0.00	BLD	0.01	0.00	0.01	0.00	0.01	0.01	0.01	0.00	0.01	0.01	0.01	0.00	0.00	BLOD	0.01	0.00	0.00	0.00	0.01	0.00
K ₂ O	0.10	0.02	0.17	0.08	0.00	0.14	0.001	0.19	0.08	0.16	0.07	0.09	BLOD	0.16	0.13	0.01	0.11	0.15	0.08	0.09	0.00	0.13	0.04
MgO	0.004	0.002	0.01	BLOD		0.02	0.01	0.00	0.04	0.01	0.01	0.02	BLOD	BLOD	BLOD		BLOD	0.01	0.00	0.00	0.00	0.01	0.01
Na ₂ O	7.45	0.13	7.29	7.10	0.27	6.65	0.15	6.43	6.43	6.46	0.12	7.07	7.50	6.98	7.77	0.23	7.07	7.22	0.03	7.35	0.08	6.84	0.12
P ₂ O ₅	0.04	0.00	0.02	0.06		0.02	0.01	0.01	0.06	0.03	0.01	0.28	BLOD	BLOD	0.05	0.00	0.03	0.04	0.00	0.03	0.00	0.01	0.01
Total	94.34		95.33	94.95		95.27		95.02	95.02	95.33		95.12	92.06	96.79	95.35		94.57	94.87		95.13		94.94	
Sc	n.m.		n.m.	n.m.		n.m.		n.m.	n.m.	n.m.		n.m.	n.m.	n.m.	n.m.		n.m.	n.m.		n.m.		n.m.	n.m.
V	n.m.		n.m.	n.m.		n.m.		n.m.	n.m.	n.m.		n.m.	n.m.	n.m.	n.m.		n.m.	n.m.		n.m.		n.m.	n.m.
Cr	n.m.		n.m.	n.m.		n.m.		n.m.	n.m.	n.m.		n.m.	n.m.	n.m.	n.m.		n.m.	n.m.		n.m.		n.m.	n.m.
Co	n.m.		n.m.	n.m.		n.m.		n.m.	n.m.	n.m.		n.m.	n.m.	n.m.	n.m.		n.m.	n.m.		n.m.		n.m.	n.m.
Ni	n.m.		n.m.	n.m.		n.m.		n.m.	n.m.	n.m.		n.m.	n.m.	n.m.	n.m.		n.m.	n.m.		n.m.		n.m.	n.m.
Cu	7		8	2	0.2	1		2	8	2	0.2	1	BLOD	n.m.	10		5	3	0.2	6	2	4	4
Zn	6	2	13	5	1	13	1	8	15	8		13	25	7	5		12	15		8	1	47	13
As	4	0.1	2	2	1	3	1	7	7	6	3	8	BLOD	BLOD	BLOD		BLOD	6	1	3	1	4	1
Rb	1		9	1	1	4	1	5	2	5	1	2	BLOD	BLOD	5	1	1	4	3	2	0.1	4	2
Sr	73	5	65	62	8	100	4	101	74	64	15	115	95	n.m.	106	5	103	139	27	115	4	105	25
Zr	144	9	277	198	10	126	10	166	111	129	51	126	BLOD	n.m.	133	10	107	109	1	141	5	158	39
Nb	n.m.		n.m.	n.m.		n.m.		n.m.	n.m.	n.m.		n.m.	n.m.	n.m.	n.m.		n.m.	n.m.		n.m.		n.m.	n.m.
Mo	n.m.		n.m.	n.m.		n.m.		n.m.	n.m.	n.m.		n.m.	n.m.	n.m.	n.m.		n.m.	n.m.		n.m.		n.m.	n.m.
Cd	n.m.		n.m.	n.m.		n.m.		n.m.	n.m.	n.m.		n.m.	n.m.	n.m.	n.m.		n.m.	n.m.		n.m.		n.m.	n.m.
Sn	n.m.		n.m.	n.m.		n.m.		n.m.	n.m.	n.m.		n.m.	n.m.	n.m.	n.m.		n.m.	n.m.		n.m.		n.m.	n.m.
Cs	2	0.3	1	1	1	4	0.1	5	2	1	0.5	1	1	2	1	0.4	0.3	2	1	1	0.1	5	2
Ba	3	2	8	2	0.2	13	5	10	2	13	8	5	BLOD	n.m.	4		19	10	2	10	1	16	7
La	10	0.4	6	6	3	10	0.2	BLOD	13	16		BLOD	5	4	8		8	11	1	15	0.2	9	3
Ce	26	1	19	15	8	26	3	BLOD	33	37		BLOD	bid	BLOD	17	7	21	27	4	34	0.4	27	1
Gd	4	2	5	5	5	5	0.5	BLOD	3	6		BLOD	BLOD	BLOD	5	0.2	3	4	2	4	0.2	7	3
Yb	5	2	7	5	5	5	0.2	6	5	3	1	7	5	5	9	1	6	10	2	6	0.2	8	1
Lu	1	0.1	1	1	1	1	0.0	1	1	1	0.1	1	1	0.4	1	0.2	1	1	0.1	1	0.01	1	0.2
Ta	1	0.2	3	1	1	1	0.0	1	2	0.5		1	BLOD	2	1	0.1	1	1	0.0	1	0.03	1	0.2
W	n.m.		n.m.	n.m.		n.m.		n.m.	n.m.	n.m.		n.m.	n.m.	n.m.	n.m.		n.m.	n.m.		n.m.		n.m.	n.m.
Pb	3	0.4	2	4	0.2	6	0.4	6	7	4	1	18	3	15	3	0.5	6	9	4	9	0.5	8	4

	MIA 16	15	MIA 17	15	MIA 18	15	MIA 19	15	SMI 20	MIA 21	15	MIA 22	15	SMI 23	MIA 24	MIA 25	15	MIA 26	15	SMI 27	MIA 28	15	
SiO ₂	74.28	0.50	73.77	0.52	73.40	0.34	73.80	0.44	73.64	71.39	0.15	72.68	0.16	73.88	73.05	72.75	0.17	72.22	0.16	68.70	72.91	MIA 28	15
Al ₂ O ₃	12.71		12.71		12.71		12.71		12.71	12.71		12.71		12.71	12.71	12.71		12.71		12.71	12.71		15
Fe ₂ O ₃	0.70	0.62	0.65	0.46	1.22	0.30	1.02	0.92	0.96	2.14	0.19	1.74	0.11	1.00	1.36	1.56	0.06	1.62	0.69	6.72	1.48		0.19
CaO	0.39	0.14	0.33	0.04	0.35	0.03	0.40	0.03	BLOD	0.64	0.03	BLOD		BLOD	0.58	0.43	0.08	1.71	0.00	0.10	0.63		0.00
TiO ₂	0.12	0.01	0.13	0.01	0.17	0.04	0.05	0.04	0.04	0.17	0.08	0.07	0.04	0.10	0.13	0.17	0.09	0.06	0.03	0.23	0.13		0.01
MnO	0.01	0.00	0.00	0.00	0.00	0.00	0.00	0.00	0.00	0.01	0.01	0.00	0.00	BLOD	0.00	0.00	0.00	0.00	0.00	0.00	0.01		0.00
K ₂ O	0.11	0.06	0.11	0.00	0.05	0.04	0.10	0.01	0.10	0.26	0.04	0.16	0.08	0.06	0.12	0.12	0.01	0.08	0.01	0.05	0.22		0.03
MgO	0.09	0.05	0.01	0.00	0.02	0.01	0.01	0.01	0.01	0.07	0.05	0.10	0.10	BLOD	0.01	0.01	0.00	BLOD		0.03	0.02		0.01
Na ₂ O	6.64	0.08	7.36	0.14	6.55	0.55	6.97	0.30	7.18	7.82	0.03	7.39	0.10	7.05	7.14	7.35	0.06	7.40	0.06	7.13	7.07		0.01
P ₂ O ₅	0.03	0.01	0.00	0.00	0.01	0.01	0.03	0.01	0.02	0.02	0.01	0.05	0.01	0.03	0.05	0.04	0.01	0.05	0.00	0.01	0.04		0.00
Total	95.07		95.07		94.49		95.09		94.66	95.22		94.90		94.84	95.14	95.16		95.85		95.68	95.21		
Sc	n.m.		n.m.		n.m.		n.m.		n.m.	n.m.		n.m.		n.m.	n.m.	n.m.		n.m.		n.m.	n.m.		
V	n.m.		n.m.		n.m.		n.m.		n.m.	n.m.		n.m.		n.m.	n.m.	n.m.		n.m.		n.m.	n.m.		
Cr	n.m.		n.m.		n.m.		n.m.		n.m.	n.m.		n.m.		n.m.	n.m.	n.m.		n.m.		n.m.	n.m.		
Co	n.m.		n.m.		n.m.		n.m.		n.m.	n.m.		n.m.		n.m.	n.m.	n.m.		n.m.		n.m.	n.m.		
Ni	n.m.		n.m.		n.m.		n.m.		n.m.	n.m.		n.m.		n.m.	n.m.	n.m.		n.m.		n.m.	n.m.		
Cu	5	4	8	4	9	5	6	4	4	6	5	4	1	5	3	3	0.3	BLOD		BLD	12		
Zn	28		13	8	12	5	21	8	7	99	1	25	7	8	17	19	1	18	12	BLD	28		4
As	5	2	3	2	2	1	2	1	4	6	3	3	0.5	4	3	3	1	3		1	6		1
Rb	4	3	3	0.3	2	1	4	2	3	13	0.3	10	6	1	3	4	1	2		1	11		2
Sr	82	16	126	11	112	6	112	23	118	112	32	137	21	117	101	97	5	102	1	89	152		22
Zr	134	13	209	14	230	28	109	15	106	108	19	109	22	120	131	134	5	152	41	99	122		10
Nb	n.m.		n.m.		n.m.		n.m.		n.m.	n.m.		n.m.		n.m.	n.m.	n.m.		n.m.		n.m.	n.m.		
Mo	n.m.		n.m.		n.m.		n.m.		n.m.	n.m.		n.m.		n.m.	n.m.	n.m.		n.m.		n.m.	n.m.		
Cd	n.m.		n.m.		n.m.		n.m.		n.m.	n.m.		n.m.		n.m.	n.m.	n.m.		n.m.		n.m.	n.m.		
Sn	n.m.		n.m.		n.m.		n.m.		n.m.	n.m.		n.m.		n.m.	n.m.	n.m.		n.m.		n.m.	n.m.		
Cs	3	2	1		1	0.3	2	1	1	3	1	2	1	1	1	1	0.0	1	0.2	0.2	3		1
Ba	10	6	6	2	3	1	3	2	4	4		8	2	4	2	5	1	8		2	21		
La	11	5	27	12	33	5	12		9	4	1	10	9	9	11	19	10	10	2	3	9		0.4
Ce	25	10	69	29	52	30	29		23	17	2	27	19	25	30	50	18	25	4	5	22		1
Gd	4	0.5	8	0.3	8	2	6		5	5	3	4	1	3	6	8	0	4	0.4	2	6		0
Yb	5	0.4	6	0.2	8	1	4	2	5	6	3	7	1	7	6	9	2	7	1	4	7		1
Lu	1	0.02	1	0.1	1	0.1	1	0.3	1	1	0.4	1	0.02	2	1	1	0.2	1	0.0	1	1		0.0
Ta	1	0.01	1	0.1	1	0.3	0.4	0.3	1	2	1	1	0.3	1	1	2	1	1	0.1	1	1		0.2
W	n.m.		n.m.		n.m.		n.m.		n.m.	n.m.		n.m.		n.m.	n.m.	n.m.		n.m.		n.m.	n.m.		
Pb	5	2	3	2	3	2	3	1	5	1		6	2	6	3	4	1	4	1	1	9		2

	MIA 29	15	MIA 30	15	MIA 31	15	MIA 32	15	SMI 33	MIA 34	15	SMI 35	MIA 36	15	SMI 37	SMI 38	MIA 39	15	MIA 40	15	MIA 41	15	SMI 42
SiO ₂	68.76	4.97	74.53	0.44	72.91	0.27	72.62	0.29	74.51	73.95	0.99	74.09	74.22	0.37	74.51	73.94	73.22	0.48	73.37	0.64	74.04	0.55	74.90
Al ₂ O ₃	12.71		12.71		12.71		12.71		12.71	12.71		12.71	12.71		12.71	12.71	12.71		12.71		12.71		12.71
Fe ₂ O ₃	5.02	4.52	0.57	0.28	1.39	0.24	1.90	0.12	0.97	1.69	0.70	1.43	1.03	0.13	1.19	1.32	1.44	0.08	1.20	0.55	0.96	0.45	0.32
CaO	0.36	0.18	0.19	0.08	0.50		0.55		0.61	0.56	0.12	0.36	0.47	0.32	BLOD	0.30	0.46		BLOD		0.50	0.07	BLOD
TiO ₂	0.57	0.70	0.09	0.07	0.08	0.04	0.14	0.02	0.12	0.14	0.04	0.16	0.10	0.01	0.10	0.12	0.07	0.06	0.10	0.02	0.11	0.02	0.09
MnO	0.01	0.01	0.00	0.00	0.00	0.00	0.00	0.00	0.00	0.00	0.00	0.00	0.00	0.00	0.00	0.00	0.00	0.00	0.00	0.00	0.00	0.00	0.00
K ₂ O	0.40	0.44	0.09	0.05	0.11	0.04	0.10	0.01	0.11	0.09	0.02	0.17	0.10	0.01	0.09	0.11	0.14	0.01	0.14	0.05	0.10	0.00	0.06
MgO	0.05	0.06	0.00	0.00	0.03	0.00	0.01	0.00	BLOD	0.10	0.12	0.02	0.01	0.00	0.00	0.02	0.02	0.01	0.03	0.02	0.01	0.00	0.02
Na ₂ O	6.87	0.11	6.89	0.24	7.34	0.09	7.33	0.05	6.08	6.03	0.05	6.17	6.45	0.12	6.25	6.59	6.78	0.18	7.04	0.17	6.63	0.05	6.71
P ₂ O ₅	0.02	0.01	0.03	0.02	0.04	0.00	0.05	0.00	0.04	0.03	0.01	0.04	0.02	0.01	0.03	0.04	0.03	0.00	0.04	0.02	0.03	0.00	0.02
Total	94.76		95.10		95.11		95.40		95.15	95.30		95.15	95.11		94.89	95.14	94.88		94.62		95.10		94.84
Sc	n.m.		n.m.		n.m.		n.m.		n.m.	n.m.		n.m.	n.m.		n.m.	n.m.	n.m.		n.m.		n.m.		n.m.
V	n.m.		n.m.		n.m.		n.m.		n.m.	n.m.		n.m.	n.m.		n.m.	n.m.	n.m.		n.m.		n.m.		n.m.
Cr	n.m.		n.m.		n.m.		n.m.		n.m.	n.m.		n.m.	n.m.		n.m.	n.m.	n.m.		n.m.		n.m.		n.m.
Co	n.m.		n.m.		n.m.		n.m.		n.m.	n.m.		n.m.	n.m.		n.m.	n.m.	n.m.		n.m.		n.m.		n.m.
Ni	n.m.		n.m.		n.m.		n.m.		n.m.	n.m.		n.m.	n.m.		n.m.	n.m.	n.m.		n.m.		n.m.		n.m.
Cu	7		3	0.02	3	1	4		6	17		4	4	1	4	4	4	3	5		3	1	BLOD
Zn	38		16	1	9	5	17	3	13	7	4	14	10	2	7	23	14	2	19	11	12	4	15
As	5	4	4	3	4	2	4	1	2	2	1	6	3	1	4	3	3	1	4	2	2	1	BLOD
Rb	7		3	2	5	1	3	0.2	3	3	2	7	2	1	1	4	7	3	6	3	4	1	1
Sr	116	16	87	17	99	5	97	1	108	103	15	87	100	16	99	108	104	7	105	8	99	11	124
Zr	126	0.4	111	21	132	13	131	3	120	141	15	141	107	10	145	136	128	13	123	7	121	5	57
Nb	n.m.		n.m.		n.m.		n.m.		n.m.	n.m.		n.m.	n.m.		n.m.	n.m.	n.m.		n.m.		n.m.		n.m.
Mo	n.m.		n.m.		n.m.		n.m.		n.m.	n.m.		n.m.	n.m.		n.m.	n.m.	n.m.		n.m.		n.m.		n.m.
Cd	n.m.		n.m.		n.m.		n.m.		n.m.	n.m.		n.m.	n.m.		n.m.	n.m.	n.m.		n.m.		n.m.		n.m.
Sn	n.m.		n.m.		n.m.		n.m.		n.m.	n.m.		n.m.	n.m.		n.m.	n.m.	n.m.		n.m.		n.m.		n.m.
Cs	3		3	2	1	0.4	1	0.1	BLOD	1	0.3	1	1	0	BLOD	2	1	0.4	1	0.3	1	0.4	2
Ba	2		12	11	4	2	4	0.1	6	6	4	8	4	1	2	6	8	3	10	3	3	0.2	1
La	10	3	11	8	9	2	12	3	bid	19	10	8	5	1	9	13	11	2	7	5	13	0.2	bid
Ce	18	2	32	24	26	4	30	2	bid	45	20	23	16	3	23	36	28	1	18	11	32	0.3	bid
Gd	5	2	4	4	5	0.2	7	1	12	7	2	6	5	0.1	4	6	4	2	5	2	4	1	11
Yb	7	4	6	4	6	1	8	3	7	8	3	6	6	0.4	5	7	5	2	5	2	5	1	5
Lu	1	0.3	1	0	1	0.1	1	0.3	1	1	0.4	1	1	0.1	1	1	1	0.0	1	0.1	1	0.2	0.5
Ta	2	1	1	1	1	0.3	1	0.5	1	1	0.2	1	1	0.1	1	1	1	0.2	1	0.2	1	0.0	1
W	n.m.		n.m.		n.m.		n.m.		n.m.	n.m.		n.m.	n.m.		n.m.	n.m.	n.m.		n.m.		n.m.		n.m.
Pb	5	3	3	2	5	2	3	0.1	4	3	2	4	3	1	2	6	4	1	5	2	4	1	9

	MIA 43	15	MIA 44	15	MIA 45	15	SMI 46	SMI 47	MIA 48	15	MIA 49	15	SMI 50	SMI 51	MIA 52	15
SiO ₂	71.14	1.72	73.69	0.59	73.78	1.12	74.66	34.27	72.01	1.34	74.55	0.56	74.41	74.88	75.15	
Al ₂ O ₃	12.71		12.71		12.71		12.71	12.71	12.71		12.71		12.71	12.71	12.71	
Fe ₂ O ₃	0.76	0.00	0.87	0.09	1.05	0.37	0.71	0.00	1.83	0.68	0.97	0.31	0.08	0.25	0.11	0.03
CaO	2.82		0.75	0.57	0.84		BLOD	3.97	0.83	0.50	BLOD		BLOD	BLOD		
TiO ₂	0.32	0.27	0.13	0.01	0.17	0.10	0.15	0.26	0.12	0.02	0.32	0.19	0.08	0.15	0.20	0.05
MnO	0.03	0.00	0.01	0.00	0.01	0.01	0.01	0.10	0.01	0.00	0.02	0.01	0.01	0.01	0.00	0.00
K ₂ O	0.09	0.04	0.13	0.08	0.21	0.13	0.13	0.88	0.31	0.05	0.10	0.01	0.07	0.08	0.09	0.03
MgO	BLOD		0.05	0.03	0.05	0.03	0.02	0.00	0.04	0.03	0.02	0.02	BLOD	0.02	0.06	
Na ₂ O	6.57	0.03	6.72	0.12	6.64	0.15	6.72	8.37	7.29	0.12	7.02	0.33	6.90	6.94	6.78	0.16
P ₂ O ₅	0.00		0.02	0.02	0.02	0.01	0.03	0.04	0.04	0.00	BLD		0.00	0.03	0.02	0.02
Total	94.44		95.08		95.48		95.13	60.60	95.19		95.71		94.25	95.05	95.12	
Sc	n.m.		n.m.		n.m.		n.m.	n.m.	11	2	7		10	6	10	0.2
V	n.m.		n.m.		n.m.		n.m.	n.m.	1	0.4	3		BLOD	2	1	0.5
Cr	n.m.		n.m.		n.m.		n.m.	n.m.	BLOD		BLOD		BLOD	BLOD	BLOD	
Co	n.m.		n.m.		n.m.		n.m.	n.m.	BLOD		BLOD		BLOD	BLOD	BLOD	
Ni	n.m.		n.m.		n.m.		n.m.	n.m.	1		8		BLOD	BLOD	1	
Cu	BLOD		8	4	2		4	BLD	5	3	4		BLOD	3	3	
Zn	62		11	9	25	14	13	BLD	44	19	30	8	10	10	11	
As	n.m.		6	6	3		4	BLD	7	0	BLOD		n.m.	3	3	0.2
Rb	5		4	3	7	5	5	BLD	13	2	3	1	1	1	2	0.3
Sr	106	24	90	20	126	68	84	BLD	191	46	104	4	73	74	60	5
Zr	51		93	62	154	17	133	212	142	2	107	0.0	134	126	136	19
Nb	n.m.		n.m.		n.m.		n.m.	n.m.	10	1	14	3	7	6	12	4
Mo	n.m.		n.m.		n.m.		n.m.	n.m.	3	0.2	7	4	5	BLOD	2	0.0
Cd	n.m.		n.m.		n.m.		n.m.	n.m.	2.5		BLOD		BLOD	BLOD	BLOD	
Sn	n.m.		n.m.		n.m.		n.m.	n.m.	20		BLOD		BLOD	BLOD	13	1
Cs	4	3	3	2	5	5	2	n.m.	8		2	1	2	2	1	0.3
Ba	8		7	5	2		10	n.m.	n.m.		10		3	3	1	0.04
La	2		11	4	6	2	9	5	13	2	7	5	n.m.	9	8	2
Ce	n.m.		27	8	13	2	22	10	32	3	26		n.m.	23	23	4
Gd	5		3	1	2	0.4	4	2	6	1	4		n.m.	2	6	1
Yb	15		4	2	5	1	4	2	6	1	4		19	4	7	0.2
Lu	2		1	0.1	1	0.2	1	1	1	0.1	1		2	0.4	1	0.001
Ta	3		1	1	1	1	1	0.4	1	0.2	1	0.4	1	1	2	0.1
W	n.m.		n.m.		n.m.		n.m.	n.m.	5	2	5		4	4	2	1
Pb	n.m.		4	3	3	2	3	n.m.	12	5	7	4	n.m.	5	2	0.02

Table 3. Average composition and standard deviation (1σ) of silicate melt inclusion assemblages (MIA) and single silicate melt inclusions (SMI) hosted by quartz phenocrysts in the albitite analyzed by LA-ICPMS. BLOD: Below the limit of detection; n.m: not measured.

	FIA (1Brine) 1σ		FIA (2Vapor) 1σ		FIA (3Vapor) 1σ	
Al₂O₃	0.04	0.01	0.08	0.04	<i>BLOD</i>	
Fe₂O₃	1.47	0.71	<i>BLOD</i>	0.51	1.26	0.69
CaO	8.05	3.32	<i>BLOD</i>		<i>BLOD</i>	
TiO₂	<i>BLOD</i>		0.06		<i>BLOD</i>	
MnO	0.19	0.14	0.05	0.04	0.08	0.01
K₂O	10.35	3.53	1.01	0.45	1.27	0.40
MgO	0.03	0.01	<i>BLOD</i>		<i>BLOD</i>	
Na₂O	16.17	1.52	4.31	0.20	4.16	0.18
P₂O₅	<i>BLOD</i>		<i>BLOD</i>		<i>BLOD</i>	
Sc	<i>BLOD</i>		<i>BLOD</i>		<i>BLOD</i>	
V	<i>BLOD</i>		<i>BLOD</i>		<i>BLOD</i>	
Cr	<i>BLOD</i>		<i>BLOD</i>		<i>BLOD</i>	
Co	9		<i>BLOD</i>		<i>BLOD</i>	
Ni	<i>BLOD</i>		<i>BLOD</i>		<i>BLOD</i>	
Cu	<i>BLOD</i>		40		<i>BLOD</i>	
Zn	2175	993	<i>BLOD</i>		407	
As	193	81	<i>BLOD</i>		<i>BLOD</i>	
Rb	593	183	27		<i>BLOD</i>	
Sr	8910	3939	1069	213	1313	619
Mo	<i>BLOD</i>		<i>BLOD</i>		<i>BLOD</i>	
Cd	<i>BLOD</i>		<i>BLOD</i>		<i>BLOD</i>	
Sn	<i>BLOD</i>		302		<i>BLOD</i>	
Cs	63	27	26	12	<i>BLOD</i>	
Ba	3808	2188	417		714	206
W	<i>BLOD</i>		70		<i>BLOD</i>	
Pb	405	248	73	10	157	67

Table 4. Average composition and standard deviation (1σ) of the fluid inclusions from the La Berrona deposit. 1Brine: brine fluid inclusions in the quartz phenocryst, sample 10nv30a01-10; 2Vapor: vapor fluid inclusion assemblage in quartz phenocryst, sample 10nv30c01-06; 3Vapor: vapor fluid inclusion assemblage in A vein, sample 10nv30b01-10. Major elements are shown in wt% and trace elements in $\mu\text{g/g}$. BLOD: below the limit of detection.

IOB	Fe	Ti	P
	wt%	wt%	µg/g
10ma02c10.xl	48.2	28.8	608
10ma04b06.xl	48.2	0.2	<74
10ma04b07.xl	48.2	9.4	<67
10ma05a05.xl	48.2	37.4	848
10ma04c06.xl	48.2	94.1	1120
10ma04c07.xl	48.2	53.6	2340
mt ore			
10nv30d03.xl	48.2	0.004	16.3
10nv30d04.xl	48.2	0.004	14.8
10nv30d05.xl	48.2	0.005	11.5
10nv30d06.xl	48.2	0.011	9.9
10nv30d07.xl	48.2	0.005	19.0
10nv30d08.xl	48.2	0.006	17.2
10nv30d10.xl	48.2	0.004	10.9
mt br			
10nv30e04.xl	48.2	0.004	16.5
10nv30e05.xl	48.2	0.005	73.5
10nv30e06.xl	48.2	0.004	68.0
10nv30e07.xl	48.2	0.002	11.2
10nv30e08.xl	48.2	0.002	19.7
10nv30e10.xl	48.2	0.007	15.8
mt groundmass			
10oc18b09.xl	48.2	0.153	728
10oc18e04.xl	48.2	0.308	75
10oc18e06.xl	48.2	0.325	70
10oc18f06.xl	48.2	0.149	227

Table 5. Fe, Ti and P compositions of the iron oxide blebs (IOB), the ore magnetite (mt ore), the breccia-related magnetite (mt br) and the accessory magnetite in the groundmass of the albitite. Note that the magnetite stoichiometric composition ($\text{Fe}_2\text{O}_3=68.97$ wt%) has been used as internal standard in the LA-ICPMS.

	BE7	BE8	BE9	BE13	BE37	BE42	BE44	BE14	BE41	BE35	BE40	BE 19b	BE36b	BE53b
SiO ₂	78.44	78.36	77.10	78.16	77.61	77.49	75.66	78.67	69.34	64.48	65	55.5	60.8	60.6
Al ₂ O ₃	13.10	13.08	12.71	12.89	10.82	13.38	13.30	12.78	14.41	15.57	16.50	8.9	10.5	8.9
Fe ₂ O ₃	0.50	0.38	0.60	0.69	1.30	0.49	0.79	0.14	2.43	2.89	2.25	15.4	12.6	15.6
CaO	0.43	0.21	0.78	0.15	1.75	0.17	0.94	0.31	2.69	3.14	2.95	8.5	5.7	5.6
TiO ₂	0.17	0.23	0.19	0.19	0.11	0.24	0.21	0.20	0.60	0.68	0.59	0.2	0.1	0.2
MnO	0.02	0.02	0.02	0.02	0.03	0.02	0.02	0.02	0.01	0.03	0.02	0.1	0.02	0.03
K ₂ O	0.11	0.13	0.12	0.06	0.10	0.19	0.10	0.08	0.12	0.23	0.12	0.1	0.2	0.1
MgO	0.33	0.10	0.88	0.08	1.47	0	0.65	0.27	1.04	3.21	2.91	4.3	3.2	2.6
Na ₂ O	6.54	7.21	7.24	7.27	6.31	7.51	7.92	7.14	7.91	9.03	9.06	5.6	6.2	5.4
P ₂ O ₅	0.05	0.05	0.05	0.02	0.02	0.02	0.07	0.05	0.05	0.12	0.14	0.1	0.02	0.01
Total	99.68	99.78	99.68	99.53	99.51	99.51	99.66	99.66	98.60	99.38	99.53	98.46	99.32	98.98
Sc	4	4	5	8	8	BLOD	9	4	6	12	11	89	46	96
V	5	7	5	4	8	7	4	5	28	43	43	51	36	44
Cr	70	85	105	97	14	16	14	2	16	9	10	58	16	79
Co	BLOD	BLOD	BLOD	BLOD	53	61	52	2	23	23	10	26	48	1.6
Ni	1	2	2	1	24	23	23	3	25	30	29	9	30	9
Cu	1	0.2	BLOD	0.4	2	1	3	BLOD	9	BLOD	BLOD	4	2	2
Zn	3	2	4	1	4	2	2	BLOD	3	BLOD	BLOD	14	6	9
Ga	20	23	21	22	17	22	21	22	21	26	25	21	21	19
Ge	1	1	1	BLOD	4	4	3	1	2	2	2	2	5	2
As	2	3	1	2	1	1	2	3	3	2	1	BLOD	1	2
Se	BLOD	0.1	BLOD	1	BLOD	BLOD	BLOD	1	BLOD	2	0.2	BLOD	BLOD	1
Br	2	1	1	1	0.4	0.2	1	2	0.3	0.4	1	1	1	1
Rb	2	4	3	2	0	10	1	0.4	2	2.6	1.2	3	3	3
Sr	64	74	79	64	33	50	71	50	94	57	91	122	109	115
Y	19	57	31	26	34	62	40	15	85	59	63	165	115	114
Zr	240	268	265	245	222	254	258	228	537	607	551	242	184	238
Nb	8	11	8	8	2	8	11	12	11	11	11	2	4	3
Mo	0.2	0.4	1	1	1	0.3	0.3	BLOD	0.4	BLOD	BLOD	1	2	1
Ag	BLOD	BLOD	BLOD	3	BLOD	BLOD	BLOD	6	BLOD	BLOD	BLOD	1	2	1
Cd	BLOD	BLOD	BLOD	BLOD	BLOD	BLOD	BLOD	BLOD	BLOD	BLOD	BLOD	7	5	5
Sn	11	14	7	4	10	7	8	BLOD	9	BLOD	BLOD	40	26	34
Sb	2	3	2	1	2	1	2	BLOD	1	BLOD	BLOD	BLOD	BLOD	3
I	4	2	6	3	1	1	0.4	4	2	2	1	BLOD	1	2
Cs	4	BLOD	2	4	1	3	BLOD	BLOD	BLOD	BLOD	BLOD	2	3	4
Ba	9	23	13	16	10	15	10	BLOD	21	BLOD	BLOD	11	14	35
La	9	18	14	19	33	6	12	BLOD	12	BLOD	BLOD	68	26	34
Ce	28	37	29	27	79	27	30	BLOD	BLOD	BLOD	BLOD	154	90	73
Nd	11	16	12	14	32	16	12	4	32	19	13	67	45	42
Sm	4	8	7	5	7	9	7	7	9	4	7	21	9	9
Hf	6	9	8	6	8	7	10	7	15	18	17	12	8	9
Ta	1	2	2	2	3	1	3	BLOD	3	BLOD	BLOD	2	BLOD	3
W	3	5	5	1	BLOD	BLOD	BLOD	2	BLOD	117	73	10	150	1
Tl	0	1	1	5	BLOD	BLOD	0	BLOD	0	BLOD	BLOD	1	1	5
Pb	2	3	2	BLOD	1	1	1	BLOD	2	BLOD	BLOD	3	2	1
Bi	0.3	BLOD	BLOD	18	1	BLOD	BLOD	BLOD	BLOD	BLOD	BLOD	2	2	4
Th	16	19	17	4	15	15	18	16	16	16	14	11	2	6
U	4	5	5	BLOD	3	4	4	1	5	4	4	8	5	1
ASI	1.124	1.056	0.944	1.049	0.792	1.040	0.896	1.031	0.799	0.748	0.809	0.364	0.503	0.469
Q	38.7	35.5	32.1	35.3	36.3	31.2	27.2	35.9	17.8	2.8	3.7	1.3	7.8	12.7
Or	0.7	0.8	0.7	0.4	0.6	1.1	0.6	0.5	0.7	1.4	0.7	0.3	1.0	0.8
Ab	55.3	61.0	61.3	61.5	53.4	63.6	67.0	60.4	66.9	76.4	76.7	45.9	52.7	45.3
An	1.8	0.7	1.8	0.6	0.9	0.7	0.4	1.2	3.5	1.3	4.0	0.0	0.2	0.1

Table 6. Major and trace element whole rock composition of the analyzed albitite.

Major elements are in wt% and trace elements in $\mu\text{g/g}$. The Aluminum Saturation Index (ASI) is calculated on the basis of normative quartz, albitite and orthoclase. BLOD: below the limit of detection.

III.3.4. Bulk rock analyses

The bulk rock composition of the albitite, including major, trace and REE elements, was obtained by XRF (X-ray fluorescence) and ICP-MS (Inductively Coupled Plasma - Mass Spectroscopy) analyses at the Instituto Geológico y Minero de España laboratories (IGME, Madrid). For the major elements, XRF analyses were done on fused glass beads fluxed with $\text{Li}_2\text{B}_4\text{O}_7$ in a Panalytical MagiX analyzer with rhodium pipe. Trace elements were measured in the same equipment by the ProTrace software. Na was analyzed by atomic sorption in a VARIAN FS-220 equipment by fluxing with LiBO_2 . The lost of ignition (LOI) was performed at 950°C . Trace elements were analyzed on pellets fluxed with LiBO_2 and acid digestion and measured in a Agilent 7500 equipment. Both the bulk rock and the trace element compositions are listed in the Table 6.

III.3.5. Sr-Nd-Pb radiogenic isotope analyses of the albitite

Three samples of fresh albitite were analyzed for Sr, Nd and Pb isotope composition at the Department of Mineralogy of University of Geneva. The isotope ratios were measured on a Thermo TRITON mass spectrometer on Faraday cups in static mode. Re filaments were loaded with Pb using the silica gel technique. Pb isotope ratios were corrected for instrumental fractionation by a factor of 0.07% per amu based on more than 90 measurements of the SRM981 standard and using the standard values of Todt et al. (1996). External reproducibilities (2σ) of the standard ratios are 0.05% for $^{206}\text{Pb}/^{204}\text{Pb}$, 0.08% for $^{207}\text{Pb}/^{204}\text{Pb}$ and 0.10 % for $^{208}\text{Pb}/^{204}\text{Pb}$. Sr was loaded on single Re filaments with a Ta oxide solution and measured at a pyrometer controlled temperature of 1490°C . $^{87}\text{Sr}/^{86}\text{Sr}$ values were internally corrected for fractionation using a $^{88}\text{Sr}/^{86}\text{Sr}$ value of 8.375209. Raw values were corrected for external fractionation by a value of + 0.03‰, determined by repeated measurements of the SRM987 standard ($^{87}\text{Sr}/^{86}\text{Sr} = 0.710250$). External reproducibility (2σ) of the SRM987 standard is $7\ \mu\text{m/g}$. Nd was

loaded on double filaments with 1 M HNO₃. ¹⁴³Nd/¹⁴⁴Nd values were internally corrected for fractionation using a ¹⁴⁶Nd/¹⁴⁴Nd value of 0.7219 and the ¹⁴⁴Sm interference on ¹⁴⁴Nd was monitored on the mass ¹⁴⁷Sm and corrected by using a ¹⁴⁴Sm/¹⁴⁷Sm value of 0.206700.

III.3.6. SEM-Cathodoluminescence images of quartz

SEM-Cathodoluminescence (SEM-CL) images of quartz phenocrysts, quartz veins and quartz filling cavities were acquired at the Centro de Instrumentación Científica (CIC), University of Granada (Spain). The double polished thin sections were coated with carbon to prevent electrical charge during irradiation that was later removed for the fluid and melt inclusion petrography. The images were taken on a SEM Leo 1430 VP equipment with an acceleration voltage of 15kV, 2nA e-probe and a beam current density of 80mA. The work distance was 16 mm.

III.4. Results I: The albitite problem

As it has been pointed before, the albitite-rich rocks and particularly those related to magnetite mineralization have been usually considered as of metasomatic origin. In this section we study the albitite from La Berrona in order to test if the albitite is a primary rock or a product of a metasomatic alteration. The methodology used here includes the comparison of the geochemistry of the host albitite with that of the silicate melt inclusions.

III.4.1. Petrography of melt inclusions

III.4.1.1. Silicate melt inclusions (SMI)

The SMI occur as groups of two to ten randomly distributed inclusions or isolated within the host quartz phenocrysts (Fig.6). Unfortunately, the SEM-cathodoluminescence imaging on quartz does not show any internal texture such

as growth zones or fractures that could control the disposition of the melt inclusions. The SMI have mostly rounded to elliptical shapes and the apparent sizes range from 10 μm to up to 100 μm . Most of them are recrystallized although the smallest ones preserve their original glassy state due to the inhibiting effect of the small pore size (Holness et al., 2011). About the 10% of the SMI contain a shrinkage bubble (covering approximately 15 % of the total volume of the SMI) which is usually completely hidden by the crystallized phases. A cubic opaque crystal as well as an opaque “drop” shaped opaque bleb are observed in most of the studied SMI (Figs.6A, 6B, 6C and 6D). This could represent an iron-titanium oxide phase exsolved from the silicate melt.

Figure 6. (next page): Melt inclusions hosted by quartz phenocrysts. **(A)** Two partially crystallized SMI coexisting in the same phenocryst (sample CBE2-chip7.2-ph11); the portrait picture shows the LA-ICPMS pits after the ablation. **(B)** Five SMI showing very constant phase proportions (sample CBE2bis-chip3-Ph.D.). **(C)** Two SMI located at different depth into a quartz phenocryst (sample CBE2-chip7.1-ph1). **(D)** A completely recrystallized SMI (sample CBE2-chip7.2-ph12). **(E)** Two Iron Oxide Blebs (IOB) within a quartz phenocryst. Note the wormlike shape of the bleb in the detailed inset (sample CBE9.2-chip6-ph2). **(F)** Two IOB coexisting in the same phenocryst. Note that one of them has been trapped together with some silicate melt (sample CBE9.2-chip5-ph8).

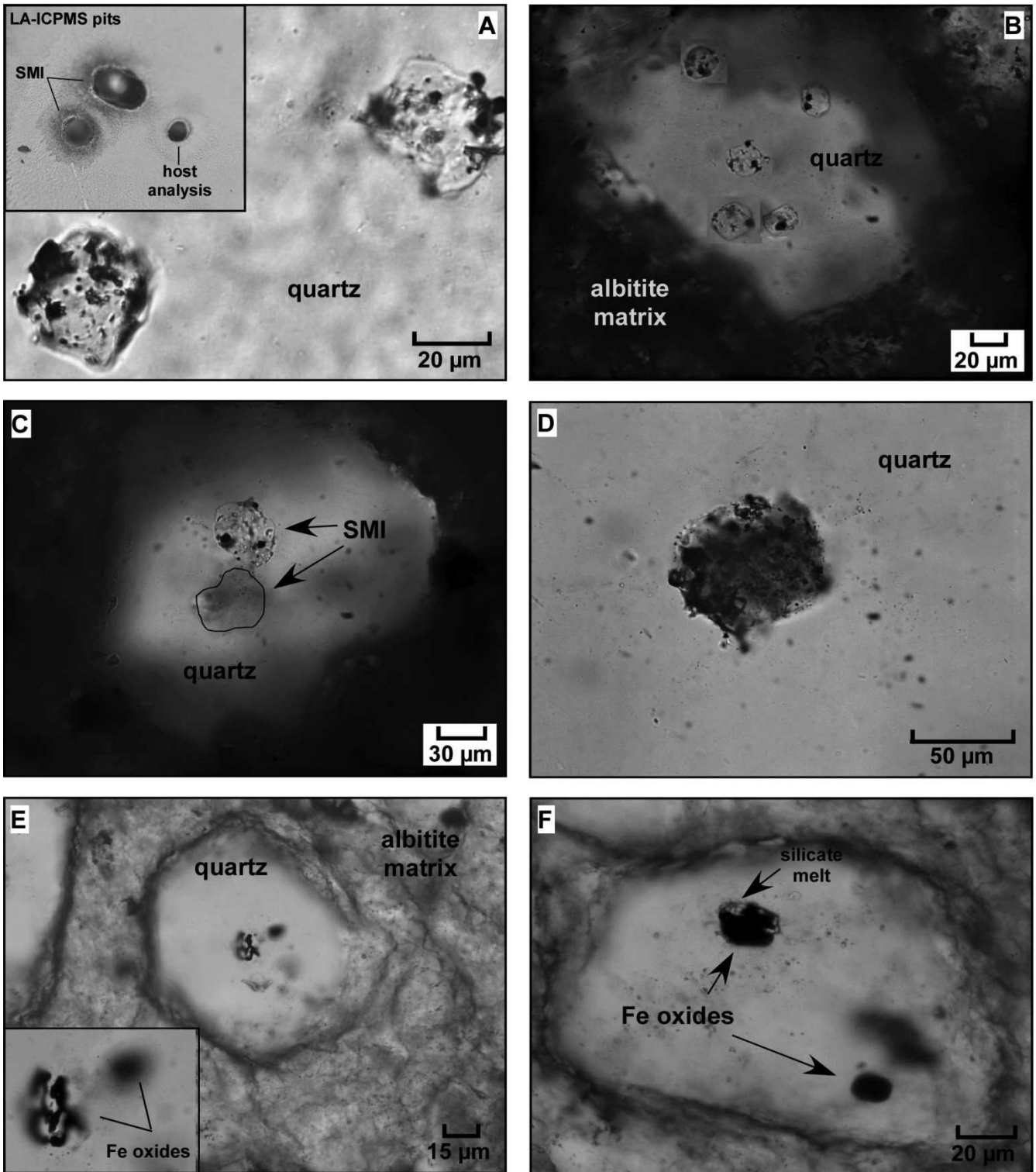


Figure. 6.

III.4.1.2. Iron oxide blebs (IOB)

In a significant less proportion than the SMI, few opaque blebs (IOB) have been found trapped in the quartz phenocrysts (Fig 6E and 6F). They occur isolated or as groups of two and usually near SMI. The sizes range from 20 to 70 μm and they show irregular, rounded and wormlike shapes suggesting entrapment as a liquid phase (Halter et al., 2004). Some of the IOB contain a minor transparent silicate fraction that, as explained later, possibly represents heterogeneous trapping of coexisting silicate melt and iron oxide melt.

III.4.2. Data evaluation: representativeness of the melt inclusions

A requirement to obtain reliable results in a melt inclusion study is that the inclusions were preserved as isolated systems after their entrapment (Roedder, 1984; Lowernstern, 2003). This indispensable condition cannot be sometimes fulfilled due to several pre- syn- and post-entrapment processes that modify the composition of the melt inclusions (Frezzoti, 1992; Thomas, 2003; Student and Bodnar, 2004). In this section, the four most important entrapment processes are discussed in order to ensure the validity of the data: (1) heterogeneous trapping of mineral phases; (2) crystallization of the host crystal onto the melt inclusion walls; (3) alteration of the melt inclusions by hydrothermal fluids; and, (4), the boundary layer effect.

III.4.2.1. Heterogeneous trapping of mineral phases

A common process during crystallization in intrusive systems is that already crystallized mineral grains (usually feldspar) are trapped heterogeneously with silicate melt and a coexisting aqueous fluid phase (Rapien et al., 2003). The resulting heterogeneous inclusions are obviously not representative of the system and have to be identified and excluded from the melt inclusion study since they

can lead to misleading interpretations (Zajacz et al., 2008). In this study, few SMI host a presumably single feldspar crystal coexisting with some melt or fluid (Fig.7). They are interpreted as reflecting heterogeneous trapping and thus, they are not further considered. In order to identify heterogeneously trapped feldspar phases that would not have been recognized during petrography in the remaining inclusions, a significant number of SMI were analyzed and their composition was compared with that of the feldspar in the albitite (Fig. 8). The results show that the SMI are depleted in feldspar-compatible elements such as Ba and Sr and conversely, they are strongly enriched in typical feldspar incompatible elements such as HFSE (high field strength elements: Zr, Nb, Ta, etc.). This demonstrates that the SMI in the albitite are representative of the residual melt and do not include or represent heterogeneously trapped feldspar phases.

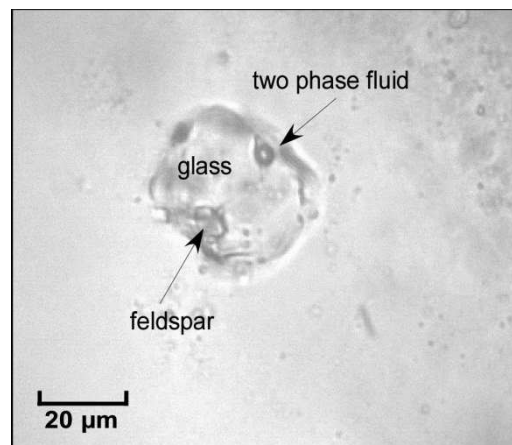


Figure 7. Heterogeneous entrapment of silicate melt, a feldspar crystal, and fluid (sample CBE1-chip2).

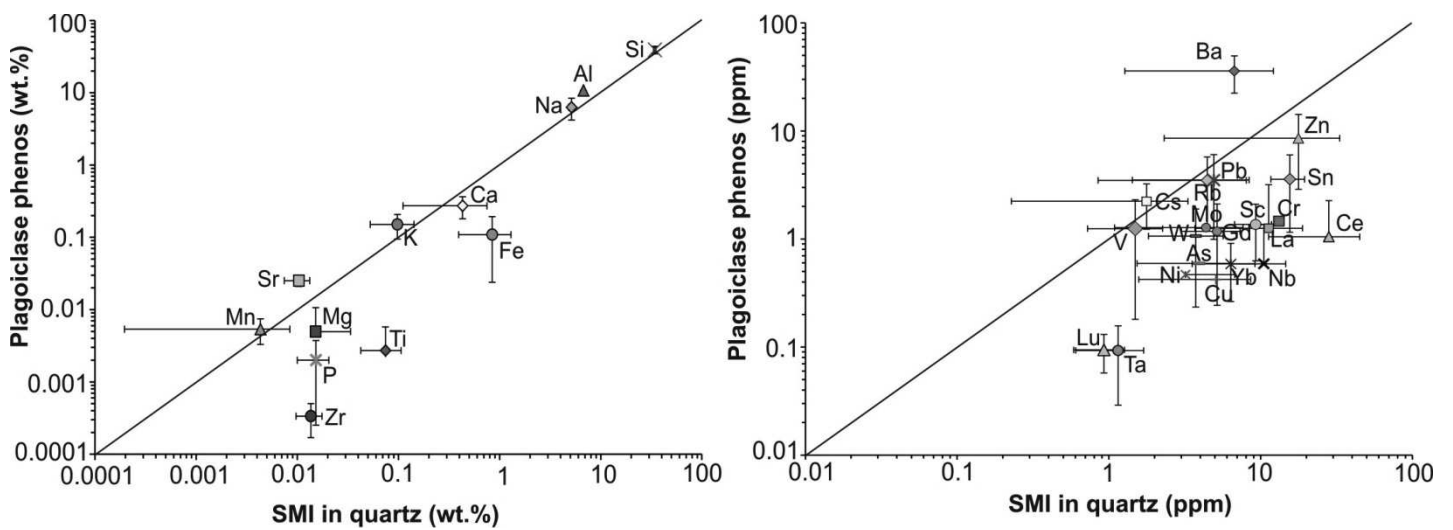


Figure 8. Comparison between the composition of the SMI and the albite phenocrysts analyzed by LA-ICPMS in order to evaluate evidences of synentrapment modifications. The concentrations of elements are given as averages with their respective standard deviations (1δ).

III.4.2.2. Crystallization of the host crystal onto the SMI walls

The original composition of the SMI can be also modified by crystallization of the host crystal onto the SMI walls while cooling (Thomas, 2003). The quartz-hosted SMI that are affected by this process usually show a marked depletion of the silica content because it has crystallized as quartz in the SMI walls. In this study, the signal of the LA-ICPMS analyses obtained during the ablation of the individual SMI show that there is a slight enrichment of silica towards the edge of the inclusions (Fig. 4). However, the change is small, and if any, the precipitation of silica into the walls of the SMI was negligible and the SMI composition has not been significantly modified by crystallization in the walls.

III.4.2.3. Alteration of the SMI composition by hydrothermal fluids

One of the major problems in this study is the fact that pervasive hydrothermal alteration can modify the composition of the melt inclusions. In fact, a common feature in magmatic-hydrothermal systems is that different generations of both magmatic and external fluids can invade the system. In such a process, intense alteration can not only replace the whole rock but also change the composition of the melt inclusions. Likely evidences of such a process are the presence of secondary fluid inclusions in fractures or even as primary fluid inclusions within the outermost growth zones of the quartz phenocrysts. The circulation of these secondary fluids along fractures alters the original composition of the SMI, sometimes provoking their decrepitation. As explained in the next sections, the quartz phenocrysts host two types of fluid inclusions, namely brine fluid inclusions and CO₂-bearing low density fluid inclusions. The former ones clearly crosscut some SMI and decrepitate them. Signs of this decrepitation are evident in the larger SMI having diameters up to 100 µm, which show haloes of minute fluid inclusion around the SMI, radial cracks, etc. (Student and Bodnar, 2004). In fact, the SMI that are crosscut by fluid inclusion trails failed to homogenize during the heating runs supporting their non-validity and hence, they were avoided from the study.

III.4.2.4. The boundary layer effect

When a crystal is growing from the melt, a boundary layer is formed in the crystal surface through which the diffusion of elements from the melt to the crystal occurs (Albarede and Bottinga, 1972; Thomas, 2003). This thin layer of melt is depleted in the compatible elements regarding the bulk melt since they tend to diffuse into the crystal. It has been suggested (Watson, 1982; Roedder, 1984; Anderson, 2003; Lowenstern, 2003) that this effect can affect the representativeness of the melt inclusions because they preferentially trap incompatible element-rich

melt portions rather than the bulk melt portions. However, some studies on this effect (Lu, 1995; Thomas, 2003) have shown that the boundary layer effect is minimum in inclusions greater than around 25 μm and hosted by quartz since most of the trace elements are incompatible with this mineral (Thomas, 2003). Most of the SMI in the albitite are large ($> 50 \mu\text{m}$) and, as it has been shown in the Figure 8, they are enriched in incompatible elements on respect to quartz, plagioclase and also on respect to the bulk rock composition (Fig. 12) so it does not seem that the boundary layer effect has noticeably affected the composition of the SMI.

After evaluating the possible pre-, syn-, and post- entrapment processes that can modify the composition of the SMI, we conclude that carefully selected melt inclusions are representative of the true melt from which the bulk rock was formed and that their compositions are reliable for further studies.

III.4.3. Bulk rock and SMI compositions: a comparison

The hydrothermally unaltered albitite (collected in areas away from the mineralization) is mainly composed of silica ($\text{SiO}_2 = 77.7 \pm 0.9 \text{ wt}\%$), alumina ($\text{Al}_2\text{O}_3 = 12.8 \pm 0.8 \text{ wt}\%$) and sodium oxide ($\text{Na}_2\text{O} = 7.1 \pm 0.5 \text{ wt}\%$) (Table 6). The anorthite ($\text{CaAl}_2\text{Si}_2\text{O}_8$) and orthoclase (KAlSi_3O_8) normative content in the rock are low (0.7 to 1.8 wt% and 0.6 to 1 wt% respectively) on respect to the normative albite ($\text{NaAlSi}_3\text{O}_8$) content (55.3 to 67 wt%) which is the dominant feldspar in the rock. The normative quartz ranges between 27.2 and 38.7 wt%.

Three samples of the altered albitite with an albite-actinolite-magnetite hydrothermal assemblage from the mineralized breccias show a lower content in silica ($\text{SiO}_2 = 58.9 \pm 2.5 \text{ wt}\%$) and slightly less alumina ($\text{Al}_2\text{O}_3 = 9.5 \pm 0.7 \text{ wt}\%$) and sodium oxide ($\text{Na}_2\text{O} = 5.7 \pm 0.4 \text{ wt}\%$) than the unaltered albitite (Fig. 9). Conversely, this brecciated albitite shows much more iron oxide content than the unaltered

albitite ($\text{Fe}_2\text{O}_3 = 14.6 \pm 1.4 \text{ wt\%}$ and $0.6 \pm 0.3 \text{ wt\%}$ respectively), due to the magnetite replacement in the former. It also shows a higher content in magnesia ($\text{MgO} = 3.3 \pm 0.7 \text{ wt\%}$ and $0.5 \pm 0.5 \text{ wt\%}$ in the brecciated and unaltered albitite respectively) and in CaO ($\text{CaO} = 6.6 \pm 1.3 \text{ wt\%}$ and $0.6 \pm 0.5 \text{ wt\%}$ respectively) due to the actinolite-magnetite replacement in the breccias. All the breccia-related albitite analyses were not considered in the comparison of the albitite with the SMI below as they are interpreted as altered by the hydrothermal fluids and thus, do not represent the original rock composition.

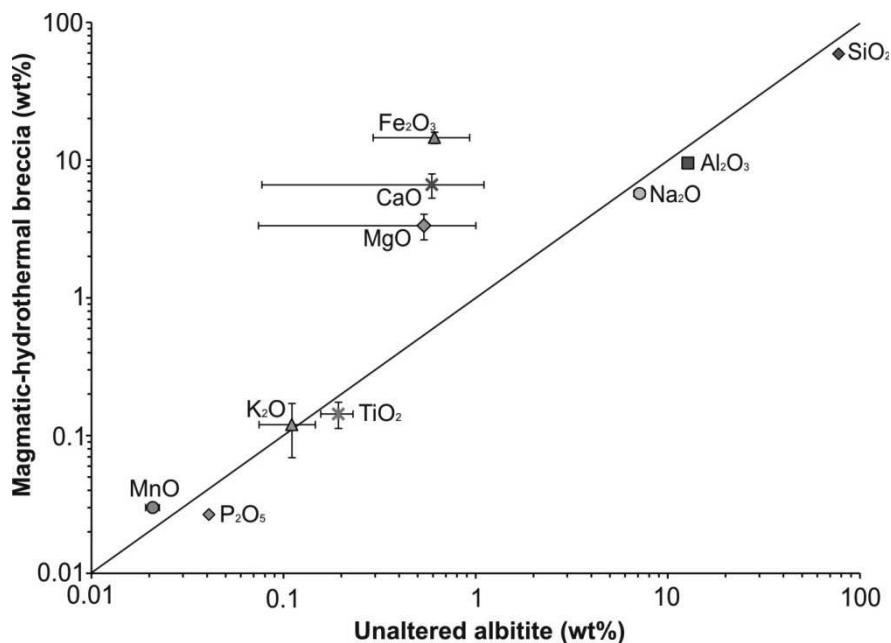


Figure 9. Major element comparison between the unaltered albitite and the magmatic-hydrothermal breccia. The significantly higher contents in CaO, FeO and MgO in the breccia are interpreted as due to the hydrothermal alteration and crystallization of actinolite. Error bars indicate 1δ standard deviation.

As has been described in previous sections, the SMI likely represent the composition of the melt at the time of their entrapment, during the growth of the quartz phenocrysts. Here, the bulk rock composition (major and trace elements) of

the albitite rock is compared with the composition of the SMI in order to confirm that the SMI are remnants of the melt from which the albitite crystallized. The elemental compositions of the SMI analyzed by LA-ICPMS and the bulk composition of the albitite rock are given in the Tables 3 and 6, respectively. The SMI have an average composition similar to that of the host albitite (Figs. 10 and 13), with still very high but slightly lower contents in silica ($\text{SiO}_2 = 73.2 \pm 1.9 \text{ wt\%}$) than the host rock but similar sodium oxide ($\text{Na}_2\text{O} = 6.8 \pm 1.1 \text{ wt\%}$), potassium oxide ($\text{K}_2\text{O} = 0.1 \pm 0.1 \text{ wt\%}$) and calcium oxide ($\text{CaO} = 0.6 \pm 0.4 \text{ wt\%}$). The SMI also show similar but more scattered iron and titanium oxide contents ($\text{Fe}_2\text{O}_3 = 1.2 \pm 0.6 \text{ wt\%}$ and $\text{TiO}_2 = 0.1 \pm 0.1 \text{ wt\%}$ respectively) than the bulk rock composition probably due to the presence of variable amounts of Ti-bearing magnetite within the SMI. The P_2O_5 content is slightly lower in the SMI ($0.03 \pm 0.0 \text{ wt\%}$) than in the bulk rock ($0.06 \pm 0.04 \text{ wt\%}$).

Regarding to the Figure 10, the albitite shows no clear evidences of evolution by fractional crystallization. Both the melt inclusions – trapped early in the crystallization of the melt – and the bulk rock have homogeneous silica contents and rather small variations in other elements. Furthermore, there are no evidences of fractional crystallization such as presence of more mafic terms.

The aluminum saturation index (ASI=molecular ratio $\text{Al}_2\text{O}_3/(\text{CaO}+\text{Na}_2\text{O}+\text{K}_2\text{O})$) values of the SMI range from 0.8 to 1.3 and of the bulk rock from 0.7 to 1.1 indicating both peraluminous and metaluminous compositions (Fig. 11A). The plot of both the SMI and the bulk rock compositions in the TAS diagram show subalkaline and calc-alkaline character with rhyolitic to dacitic compositions consistent with highly evolved rocks (Fig. 11B and 11C). Their normative mineral compositions plot close to the albite apex in the trondhjemite field of the An-Ab-Or diagram (Fig.11D). In the Q-Ab-Or plot, both SMI and bulk rock compositions plot close to the Q-Ab side (Fig. 11E) showing very low content in the orthoclase component.

The chemical index of alteration (CIA=molecular wt% $[\text{Al}_2\text{O}_3/(\text{Al}_2\text{O}_3+\text{CaO}+\text{Na}_2\text{O}+\text{K}_2\text{O})]*100$) in both the albitite and the SMI range from 44 to 53 and from 44 to 56 respectively, and are within the range of fresh granitic rocks (45-55) established by Nesbitt and Young (1982). Conversely, the breccia-related albitite in the La Berrona magnetite mineralization shows CIA values ranging from 27 to 32, consistent with their hydrothermal origin.

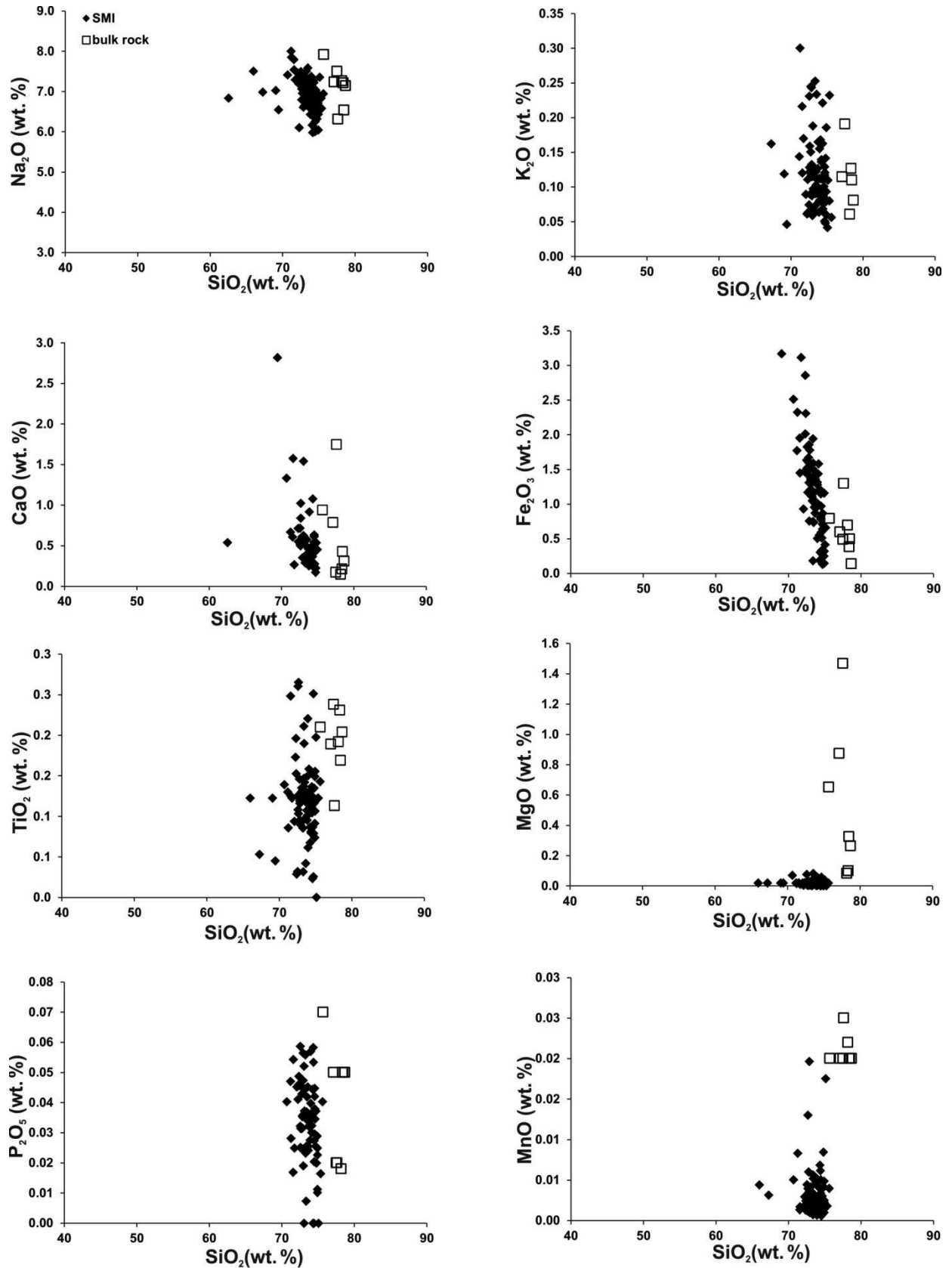


Figure 10. Major element concentrations plotted as a function of the silica content for the SMI and the bulk albitite of the La Berrona Stock.

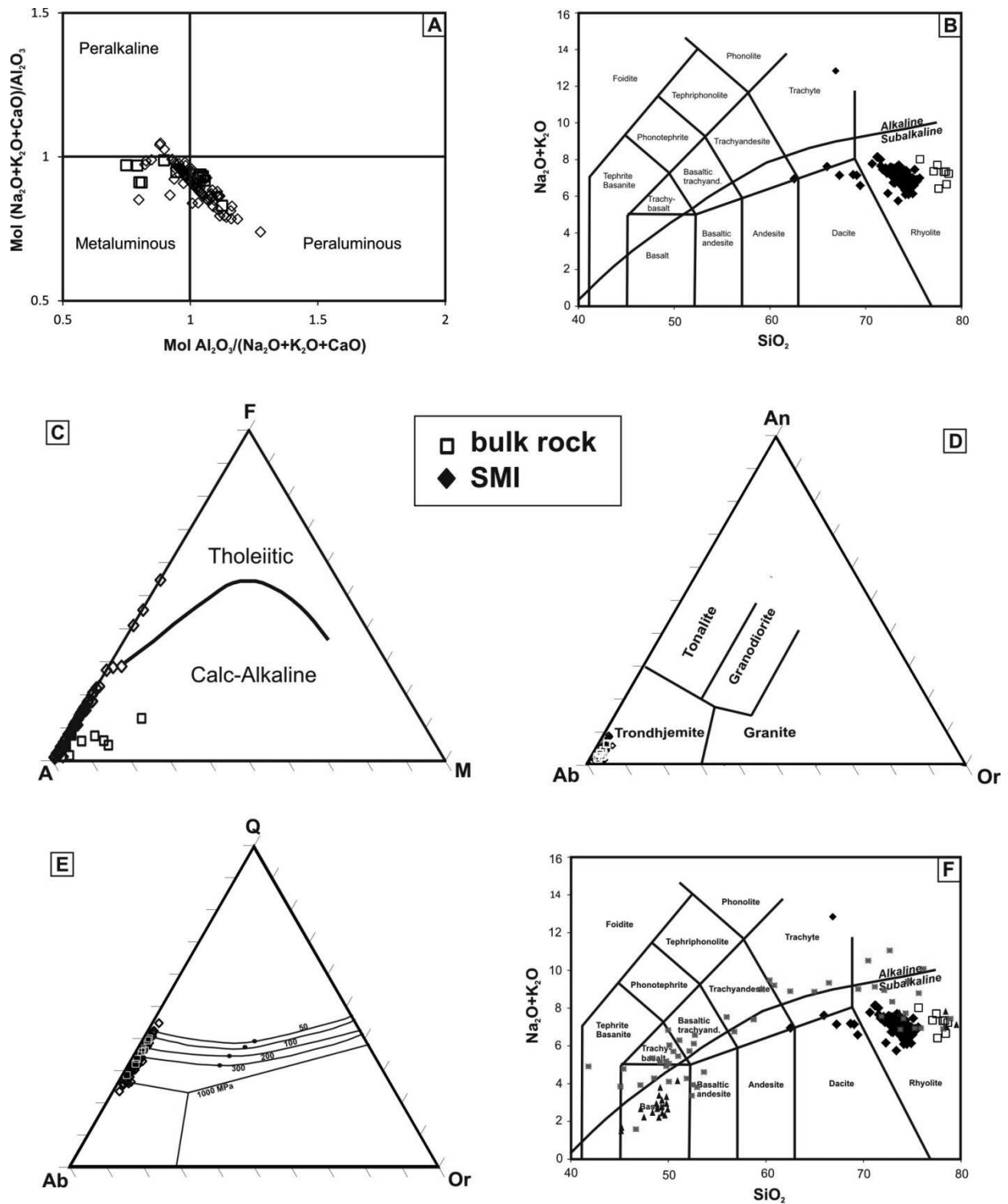


Figure 11. (A) Aluminum saturation index ($\text{ASI} = \text{mol Al}_2\text{O}_3/(\text{Na}_2\text{O}+\text{K}_2\text{O}+\text{CaO})$) versus the alkali index ($\text{mol Na}_2\text{O}+\text{K}_2\text{O}+\text{CaO}/\text{Al}_2\text{O}_3$) for silicate melt inclusions (SMI) and albitite rock from the La Berrona Stock. (B) Chemical classification of the SMI and the albitite bulk rock using the total alkalis versus silica (TAS) diagram. (C) Composition of the SMI

and the host albitite in the AFM diagram. **(D)** Normative anorthite, albite and orthoclase compositions of the SMI and the albitite bulk rock (after Barker, 1979). **(E)** Normative quartz, albite and orthoclase compositions of the SMI and the albitite bulk rock. The cotectic lines and compositions of the eutectic in the Q-Ab-Or haplogranite system as a function of pressure are shown for comparison (data from Tuttle and Bowen, 1958). **(F)** Classification of the Early and Mid Cambrian rifting stage suite of rocks (taken from Sánchez- García et al., 2008). Open squares: bulk rock; solid diamonds: silicate melt inclusions; red asterisks: Rift-related IOB affinity group; solid triangles: Rift-related N-MORB affinity group.

When plotted in a chondrite normalized multi-element spider diagram, both the SMI and the bulk rock compositions show a strong enrichment in incompatible elements such as Th and Ta and a pattern broadly consistent with the upper continental crust (Fig.12A). This pattern is different to that expected in rocks with a juvenile derivation. The REE pattern compared to the average chondrite composition of the albitite shows a classical seagull shape with a negative Eu anomaly and a HREE/LREE ratio of 0.246. This pattern is not consistent with a juvenile source but more classical of plutonic rocks derived from crustal sources (Fig. 12B).

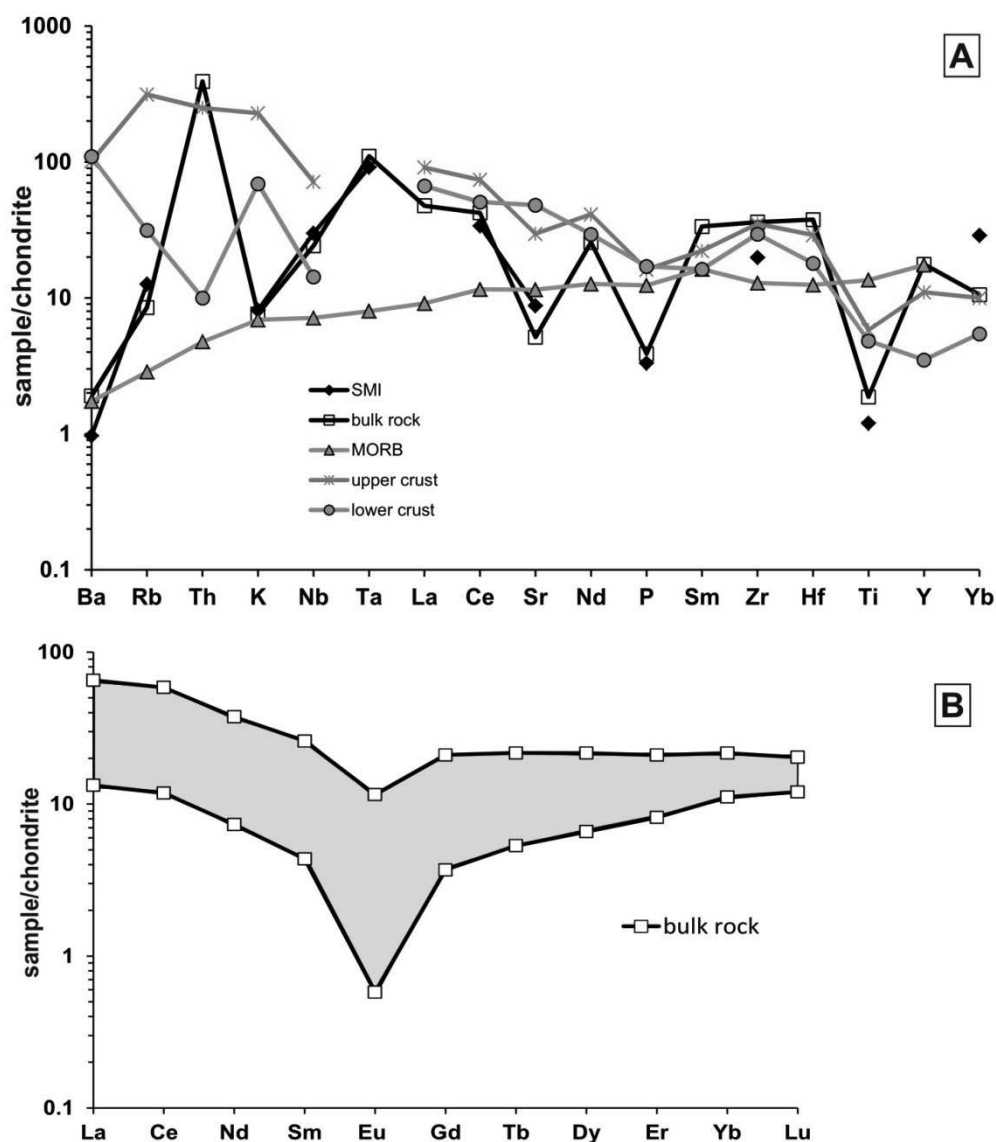


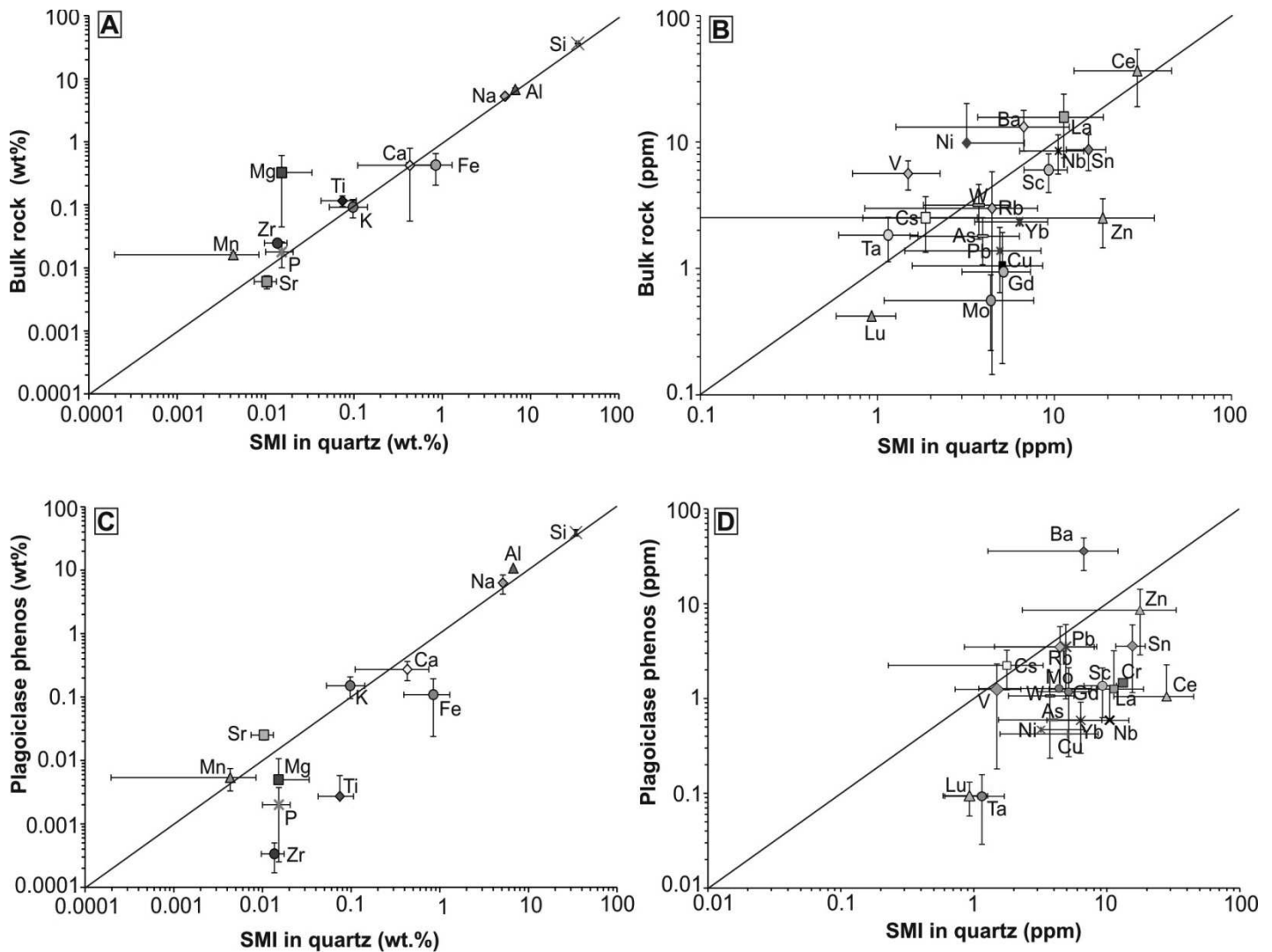
Figure 12. (A) Chondrite normalized diagram of the average compositions of the albitite and the hosted melt inclusions. Mean compositions of the MORB (Saunders and Tarney, 1988) and upper (Taylor and McLennan, 1981) and lower (Weaver and Tarney, 1984) crust are also shown for comparison. Note that, despite the lacking of analyses of some elements in the SMI (i.e. Th, La, Sm, Hf, Y) both the bulk rock and the SMI show a very similar pattern. (B) Chondrite normalized (Palme and O'Neal, 2004) rare earth element diagram for the albitite.

In the Figure 13, the SMI major and trace element concentrations are compared to those of the albitite bulk rock (A and B) and again, to the composition

of the plagioclase phenocrysts (C and D). On respect to major elements, both the SMI and the bulk rock composition show similar concentrations, except for Mg and Mn that are enriched in the later. Regarding to the trace elements, the SMI are enriched in typical incompatible elements such as Sc, Nb, Lu, Gd, Yb, Sn and other elements like ore metals (Cu, Mo, Pb, As and Zn). Conversely, the SMI are depleted in bulk rock compatible elements such as, Ba, Zr, P, V, Cr or Ni. These elements enter in the structure of the bulk rock minerals, as for example Ba in plagioclase, Zr in zircon, P in apatite V in magnetite or Ni in the amphibole. This compatibility effect is better shown in the SMI vs plagioclase plot (Fig. 13 C and D) where all the trace elements, except Sr and Ba, are enriched in the SMI. Sr and Ba are enriched in the plagioclase due to their strong compatibility with this mineral. These fractionation plots indicate that the element distribution is in agreement with their behavior in magmatic systems in which some elements have preference either for the melt phase (incompatible elements) or the mineral phase (compatible elements). Unfortunately, the calculation of partition coefficients ($K_d = C^{\text{mineral}_{\text{elementi}}} / C^{\text{melt}_{\text{elementi}}}$) is not possible as reliable SMI have been only found in quartz and not in other minerals like apatite, zircon or plagioclase in which the SMI would be in equilibrium.

The La Berrona albitite body is considered to be part of the Cambrian-Ordovician rift-related igneous rocks as the U-Pb dating suggest (320 Ma, Carriedo, Ph.D. in prep.). Their genetic relationship with the group of rocks of this event is not clear. Igneous rocks associated with the rifting event show compositions from basalt to high silica rhyolites (Sánchez-García et al., 2008) separated in two major events (Fig.11F). First, the early rift igneous suit, of predominantly acid composition and related to core complex formation and mid upper crustal migmatization (Early Igneous Event) and second a younger volumetrically dominant rift-related igneous suit, a bimodal association emplaced during the climax of upper crustal extension and basin compartmentalization

(Main Igneous Event) (Sánchez-García et al., 2003). In the TAS diagram (Fig. 11F), these two compositional trends can be observed, one evolving from basaltic to more felsic compositions that belong to the Main Igneous Event and the other in the silica rich composition region, where both the Early Igneous Event rocks and the more felsic rocks of the Main Event are included. Both the samples of the La



Berrona Stock and the SMI plot in the high silica region of the TAS diagram.

Figure 13. Comparison between the composition of the SMI and the albitite bulk rock composition as analyzed by LA-ICPMS. The concentrations of elements are given as averages with their respective standard deviation (1δ).

III.4.4. Heterogeneous entrapment of immiscible phases?

III.4.4.1. Testing immiscibility between silicate melt and brine / vapor fluids

In some quartz phenocrysts, SMI occur together with brine and/or vapor (CO₂)-bearing fluid inclusions opening the possibility of entrapment of the melt inclusions in a volatile/fluid saturated magma synchronously with the exsolution of the fluid. If true, a fluid exsolution took place early in the crystallization of the melt, implying the existence of high water-rich melts. Brine inclusions often crosscut the entire quartz phenocryst as secondary trails and thus, they are clearly later than the SMI ruling out their possible coexistence. On respect to the (CO₂)-bearing fluid inclusions, there is textural evidence for their coexistence with the SMI only in one assemblage (CBE-2-chip1-3, Fig. 14), that could indicate a possible immiscibility between a melt and a vapor phase. However, the SMI of this assemblage are different from the other SMI that are addressed here so it is not possible to ensure that this process has occurred in the system. In all the other cases, the vapor (CO₂)-bearing fluid inclusions occur as clusters or isolated and not necessarily together with the SMI.

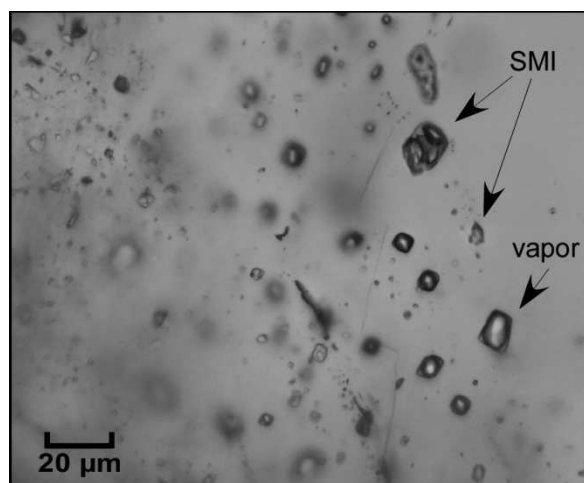


Figure 14. Assemblage of coexisting vapor (CO₂ bearing) fluid inclusions and two possible SMI (sample CBE-2-chip1-3).

III.4.4.2. Testing immiscibility between silicate melt and iron oxide phase

The implications of the presence of Fe-Ti-P oxide blebs (IOB) in the albitite are significant because: (1) they can track the existence of an iron oxide melt that could have been exsolved from the silicate melt represented by the SMI; and, (2) this phase could be the source of the iron for the related magnetite mineralization. Therefore, the evaluation of the real meaning of the IOB is critical for the ore forming model and has to be very precise in order to ensure that these inclusions do not represent trapped crystals of magnetite but a true immiscible iron oxide phase.

The Figure 15 shows the Fe and P vs. Ti contents of the IOB hosted by the quartz phenocrysts in the fresh albitite, together with those of the magnetite occurring as accessory mineral and the magnetite from the La Berrona ore deposit. This figure shows that these types of magnetite have different compositions and plot as independent groups. The IOB show the higher concentrations in Ti and P and are easily discriminable from the accessory grains and the hydrothermal magnetite (Fe does not change because Fe₂O₃ is used as internal standard in the

LA-ICPMS data reduction) with respect to the rest of the groups. Only one of the petrographically characterized IOB (sample 10ma04b06) plots in the group of the accessory magnetite, probably due to its erroneous determination as an IOB.

In addition, most of the studied SMI contain a little drop of an opaque phase besides the crystal shaped magnetite phase and conversely, all the IOB host a portion of silicate melt that is trapped together with the oxide phase. This suggest that both the SMI and the IOB could represent end members of a process of melt immiscibility. However, intermediate stages with ca. 50% oxide phase and ca. 50% silicate melt phases have not been observed. All these facts, together with the presence of wormlike textures and the rounded shapes of the IOB indicate that they represent a true Fe-Ti-P oxide melt and not magnetite grains in the groundmass of the albitite.

The Figure 16 shows a comparison between the major elements in the coexisting SMI and the likely immiscible IOB in what is considered the best and most representative sample (10ma02c10 IOB and 10ma02c09 SMI, Fig. 16B) in order to define the element fractionation between them. The IOB is enriched in Fe and Ti and, in less proportion, in P, while the silicate melt inclusion is enriched in Si, Na and Al. This partition of elements is in agreement with the experimental studies on the behavior of Fe-Ti-P melts exsolved from silicate rich liquids (Philpotts, 1967; Watson, 1976; Naslund, 1983).

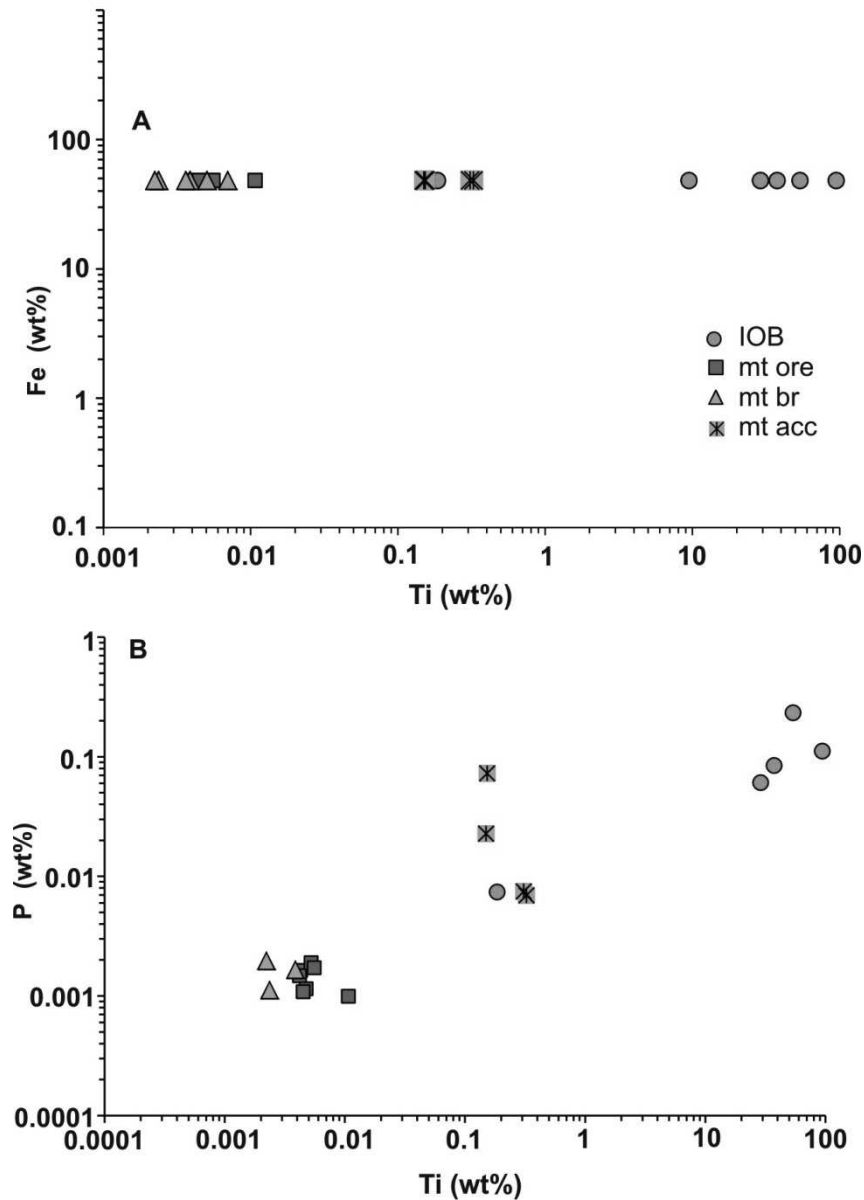


Figure 15. Fe (A) and P (B) vs. Ti concentration of the four types of magnetite existing in the La Berrona area, including IOB, accessory magnetite in the groundmass of the albitite (mt acc), magnetite in the groundmass of the magmatic-hydrothermal breccia (mt br) and banded magnetite from the La Berrona deposit (mt ore). Note that one of the magnetite grains considered petrographically as an IOB plots in the group of the accessory magnetite.

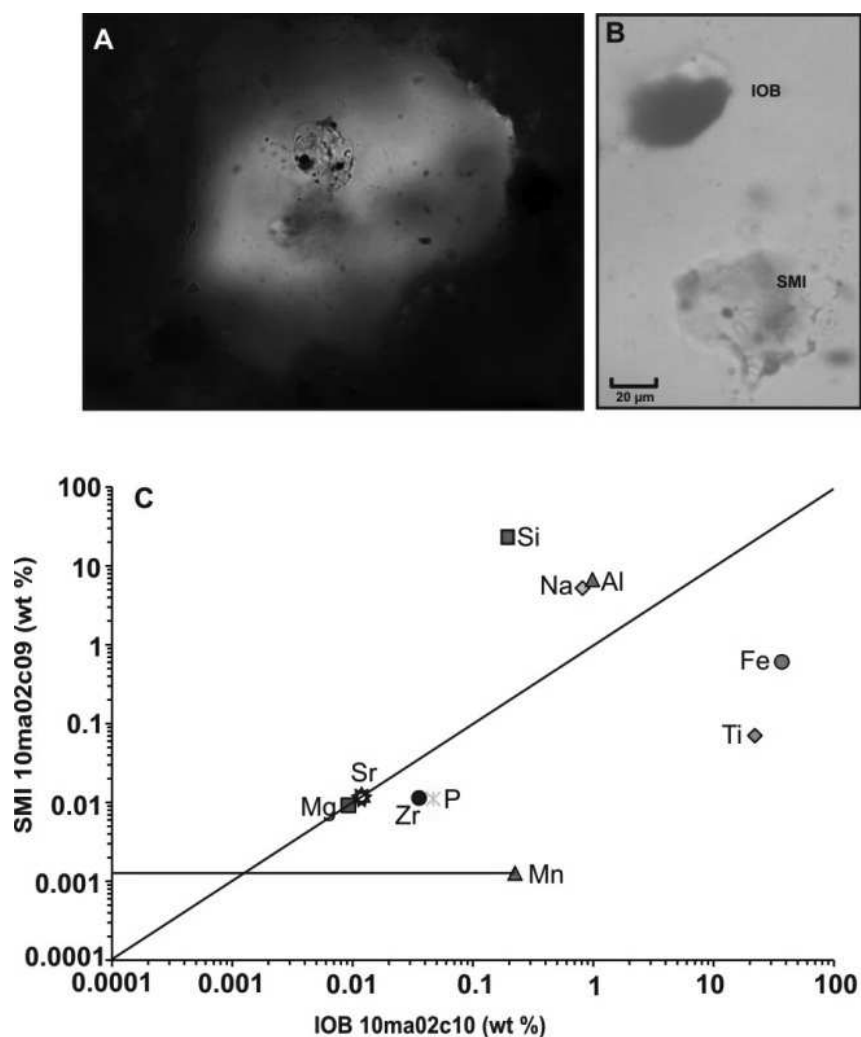


Figure 16. (A) SMI in which an opaque cubic crystal as well as an opaque drop can be distinguished. This opaque drop could represent some iron oxide melt trapped with the silicate melt during the early stages of melt immiscibility. (B) A silicate melt inclusion (SMI, 10ma02c10) coexisting with an iron oxide bleb (IOB, 10ma02c10) in the same quartz phenocryst. (C) Comparison between the compositions of the IOB and SMI. Fe, Ti, Mn, P and Zr are fractionated into the iron oxide melt.

III.4.5. Preliminary Sr-Nd-Pb isotopic data

Two whole rock samples of the albitite from the La Berrona Stock have been analyzed for Sr, Pb and Nd isotopes. These rocks have $^{87}\text{Sr}/^{86}\text{Sr}$ initial (back-calculated to 520 Ma) values of 0.708352 and 0.708214, respectively. $^{143}\text{Nd}/^{144}\text{Nd}$

values yield values of 0.511576 and 0.511141 and a ϵNd of -7 and -16 respectively. However, this late value is too low and probably reflect an erroneous determination of the Sm-Nd contents of the rock. The Pb isotopic values are also radiogenic with $^{206}\text{Pb}/^{204}\text{Pb}$ values of 33.306 and 73.74, $^{207}\text{Pb}/^{204}\text{Pb}$ values of 16.416 and 18.681 and $^{208}\text{Pb}/^{204}\text{Pb}$ values of 48.708 and 81.015. These isotopic signatures are similar to the data reported by Carriedo (Ph.D. in prep.) were a complete data set of radiogenic isotopes in the albitite of Valuengo area are shown.

Attempting to find the possible source rocks for the albitite, there are only few available isotopic compositions of the rocks of the Olivenza-Monesterio Belt. The Early to Mid Cambrian granitoids of Monesterio and Táliga (number 19 in the Figure 5 of the Chapter I) have $^{87}\text{Sr}/^{86}\text{Sr}_i$ values from 0.707 to 0.708 and ϵNd values -3.1 to -4.4 while Salman (2002) calculated a $^{87}\text{Sr}/^{86}\text{Sr}_i$ value of 0.701 and a ϵNd values of +0.9 in the Calera de León (number 26 in the Figure 5). These data are interpreted as processes involving partial melting or assimilation of the Meso Proterozoic crust, that represents the current lower crust in the OMZ (Galindo and Casquet, 2004). The primitive values in Calera de León suggest participation of mantle derived magmas or partial melting of mafic rocks. Despite a detailed isotopic study of the oldest rocks (possible crustal protholits) of the OMB is not available, Casquet et al., (2001) established a general range with values of $^{87}\text{Sr}/^{86}\text{Sr}_i$ values between 0.707 and 0.7225 and ϵNd values between -12 and -5 for Precambrian and Cambrian metasedimentary rocks in the area.

The high $^{87}\text{Sr}/^{86}\text{Sr}$ and the negative ϵNd values of the albitite are more consistent with the dominant derivation of the albitite from a crustal source rather than from a depleted mantle as would be expected if derived from a juvenile melt as proposed by Sánchez-García et al. (2003). In this context, it looks consistent that the albitite melts were produced by the partial melting of the late Neoproterozoic-early Cambrian sequence during the high temperature-low pressure

metamorphism that took place synchronous with the formation of the metamorphic domes.

III.5. Results II: Fluid inclusion study in the La Berrona deposit

A fluid inclusion study has been performed in order to characterize the nature of fluids that circulated through the magmatic-hydrothermal system in the La Berrona deposit and test their relationship with the related albitite. The petrography and further analyses were performed in the quartz where the fluid inclusion assemblages (FIA) are best preserved and where, in most cases, SEM-cathodoluminescence images are available.

III.5.1. Fluid inclusion characteristics and SEM-Cathodoluminescence images

Three types of fluid inclusions have been observed and classified on the basis of their nature and phase proportions at room temperature (Table 7): (1) Vapor-rich fluid inclusions (Vc), which have low densities with the vapor bubble filling about the 75 – 80% by volume of the inclusion. They are CO₂ – bearing although the double bubble of CO₂ liquid-vapor is not always observable due to metastability. They show rounded to negative-crystal shapes with sizes ranging from 10 to 50 μm; (2) Brine fluid inclusions (B) hosting a halite crystal in addition to other transparent reddish and/or opaque crystal(s) that seems to be hematite and/or magnetite. Their shapes are rounded to irregular with sizes always below 25 μm; and, (3) Liquid aqueous (La) fluid inclusions which are two phase-liquid rich inclusions, with irregular shapes and sizes. Both the brine and the liquid aqueous inclusions do not show evidences of the presence of CO₂.

	Vc in phenocrysts	B in phenocrysts	Vc in A-veins	B in A-veins	La in cavities and pockets	La in late veins
Disposition and quartz generation	Groups of 5 to 10 fluid inclusions in clear zones of quartz. No clear relationship with the SMI.	Secondary trails crosscutting phenocrystals.	Consistent assemblages in clear zones of quartz. No clear relationship with B.	Secondary trails. Sometimes isolated or as groups of 2 to 5.	Clouds of tiny fluid inclusions. Very difficult petrography. At least two quartz generations.	Clouds of tiny fluid inclusions. Very difficult petrography. Few trails of B inclusions.
Phases at room T (°C)	$L+L_{CO_2c}+V_{CO_2}$	$L+V+Hal+Hem$	$L+L_{CO_2}+V_{CO_2}$	$L+V+Hal+Hem$	$L+V$	$L+V\pm Hal$
Bubble infill (%)	75 - 80	20	75 - 80	15 - 20	15 - 40 irregular	15 - 20
Tm clathrate (°C)	5.0 ± 1.7		5.9 ± 1.2			
Thom CO₂ (°C)	26.9 ± 2.51 to L		24.2 ± 2.52			
Thalite (°C)		334 ± 42		310 ± 74		
Salinity (wt% NaCl eq.)	8.9 ± 2.7	39.1 ± 5.6	7.3 ± 2	39.8 ± 5.7	n.m.	n.m.
Thom total (°C)	$387 \pm 28^*$	157 ± 7	$337.5 \pm 2.5^*$	152 ± 15	167 ± 31	150 ± 47

Table 7. Summary of microthermometric data of fluid inclusions in La Berrona deposit. Abbreviations: Vc, vapor carbonic; B, brine; La, liquid aqueous; Hal: halite; Hem: hematite; L: liquid; V: vapor. Bubble infill has been optically estimated. The numbers represent the averages of all the fluid inclusions included in each type of FIA with the respective standard deviation. (*) Only 5 and 2 vapor fluid inclusions could be measured for Thom in the phenocrystals and in the A-veins respectively due to widespread decrepitation of most of them.

III.5.1.1. Fluid inclusions in the quartz phenocrysts of the albitite

As it has been pointed out in a previous section, some quartz phenocrysts in the albitite host both vapor (V) and brine type (B) fluid inclusions. Unfortunately, the SEM-cathodoluminescence images of the phenocrysts do not show any texture that can be correlated with the fluid inclusion assemblages. However, their mode of occurrence is enlightening as the vapor inclusions occur as well delimited groups (Fig. 17A and 17B) while the brine fluid inclusions are disposed as secondary trails crosscutting all the phenocryst (Fig. 17C).

When observable, vapor fluid inclusions show clathrate melting temperatures (T_{cla}) of $5.0 \pm 1.7^\circ\text{C}$ that yield salinities of $8.9 \pm 2.7\%$ wt NaCl eq. The homogenization of the CO_2 occurs to the liquid phase at $26.9 \pm 2.5^\circ\text{C}$. Due to the low density of the vapor inclusions, the observation of the total homogenization temperature was difficult. Therefore, only five fluid inclusions yielded minimum homogenization temperatures of $387 \pm 28^\circ\text{C}$ while the rest of measured vapor fluid inclusions decrepitated at around 326°C .

The secondary brine inclusions in the quartz phenocrysts are commonly irregular with clear signs of post-entrapment modifications such as necking down and variable phase proportions. Only a few well preserved assemblages were measured yielding salinities of $39.1 \pm 5.6\%$ NaCl eq. and total homogenization temperatures of $157 \pm 7^\circ\text{C}$. Vapor and brine fluid inclusion are unambiguously not contemporaneous owing to their different mode of occurrence and total homogenization temperatures.

III.5.1.2. Fluid inclusions in the A-veins

As the quartz phenocrysts, A-veins do not show clear SEM-CL textures to correlate with the fluid inclusion types (Fig. 17D). However, these veins host several vapor fluid inclusion assemblages that are similar in the mode of occurrence and in the microthermometric behavior to the vapor fluid inclusions in the quartz phenocrysts (Fig. 17E). Brine fluid inclusions are also very similar to those of the phenocrysts with almost all of them showing a hematite crystal (Fig. 17F and 17G). Several good assemblages of Vc fluid inclusions have clathrate melting temperatures (T_{cla}) of $5.9 \pm 1.2^\circ\text{C}$ and salinities of $7.3 \pm 2\%$ NaCl eq. The total homogenization temperatures could be measured only in two fluid inclusions at $337.5 \pm 2.5^\circ\text{C}$. Brines have salinities of $39.8 \pm 5.7\%$ NaCl eq. and total homogenization temperatures of $167 \pm 31^\circ\text{C}$.

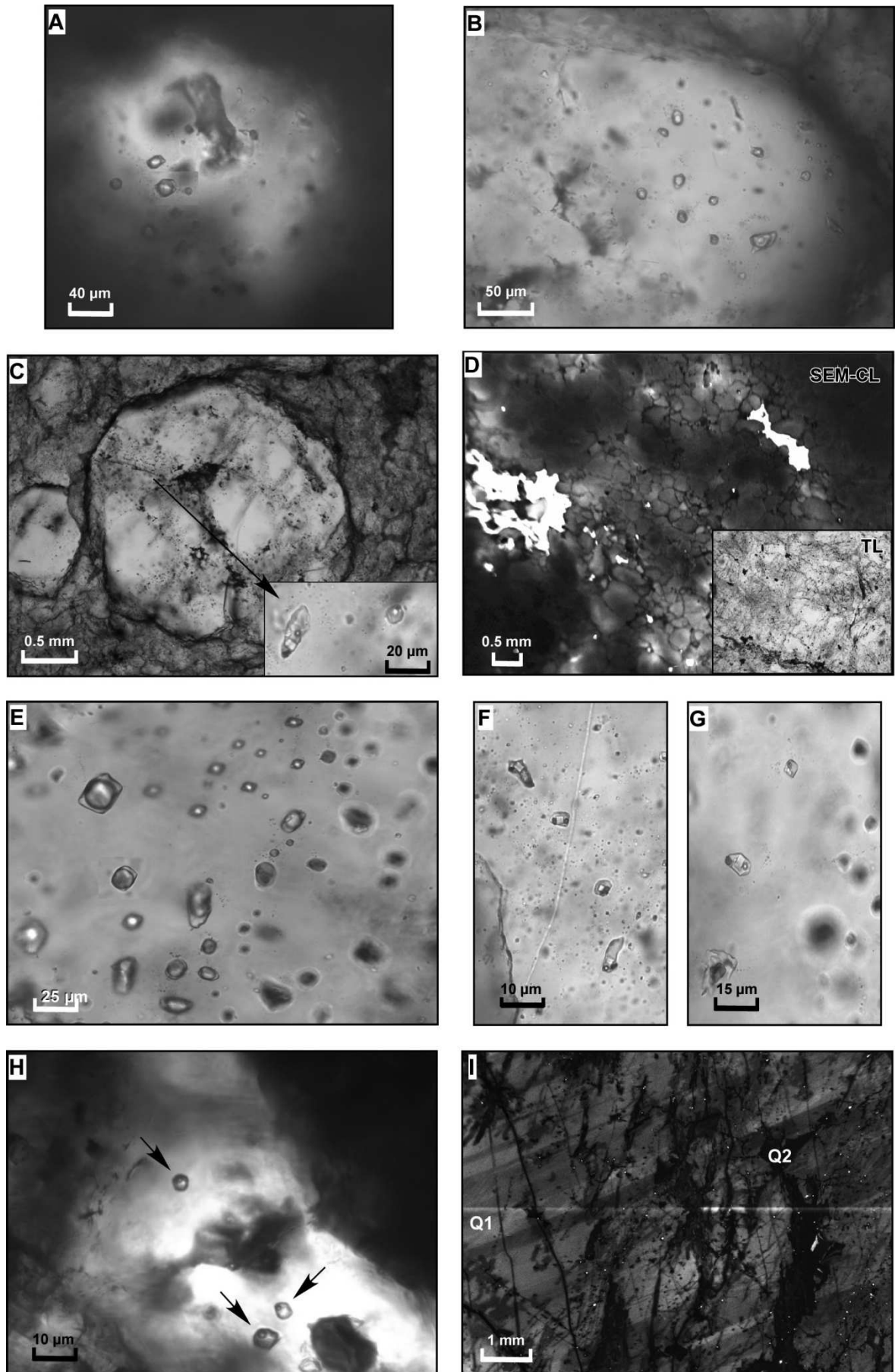
III.5.1.3. Fluid inclusions in the open cavities and “pockets”

Only liquid aqueous (La) fluid inclusion assemblages were observed in the quartz and the calcite filling cavities in the breccia (Fig. 17H). It was not possible to observe the ice melting temperature and the total homogenization temperatures ranged between 135°C and 197°C.

The SEM-CL images of the calcite-quartz “pockets” in the magnetite orebody reveal the existence of at least two generations of quartz (Fig.17I). The first generation is zoned with bands of CL-gray and CL-dark quartz and patches of CL-gray quartz. The second generation is related to branching microfractures healed by CL-dark quartz. However and despite the good CL images, only clouds of small liquid aqueous fluid inclusions could be observed in both generations of quartz (Fig. 17J and 17K). The larger fluid inclusions show similar microthermometric behavior as the La fluid inclusions in the breccia-cavities, with final homogenization temperatures below 200°C. There are some brine fluid inclusions with a hematite crystal similar to the B inclusions found in the quartz phenocrysts and in the A-veins.

III.5.1.4. Fluid inclusions in the late veins

SEM-CL images for the late veins are not available, but the presence of cloudy, milky quartz and the lack of clear zones indicate that these rocks have been affected by several superimposed stages. The quartz includes abundant small fluid inclusions with no discernible FIA; liquid aqueous-rich and some brine inclusions are observed. Their appearance and microthermometric behavior is very similar to the secondary fluid inclusions of the previous stages, with homogenization temperatures below 200 °C. Most of the fluid inclusions in late veins are too small for reliable microthermometric data.



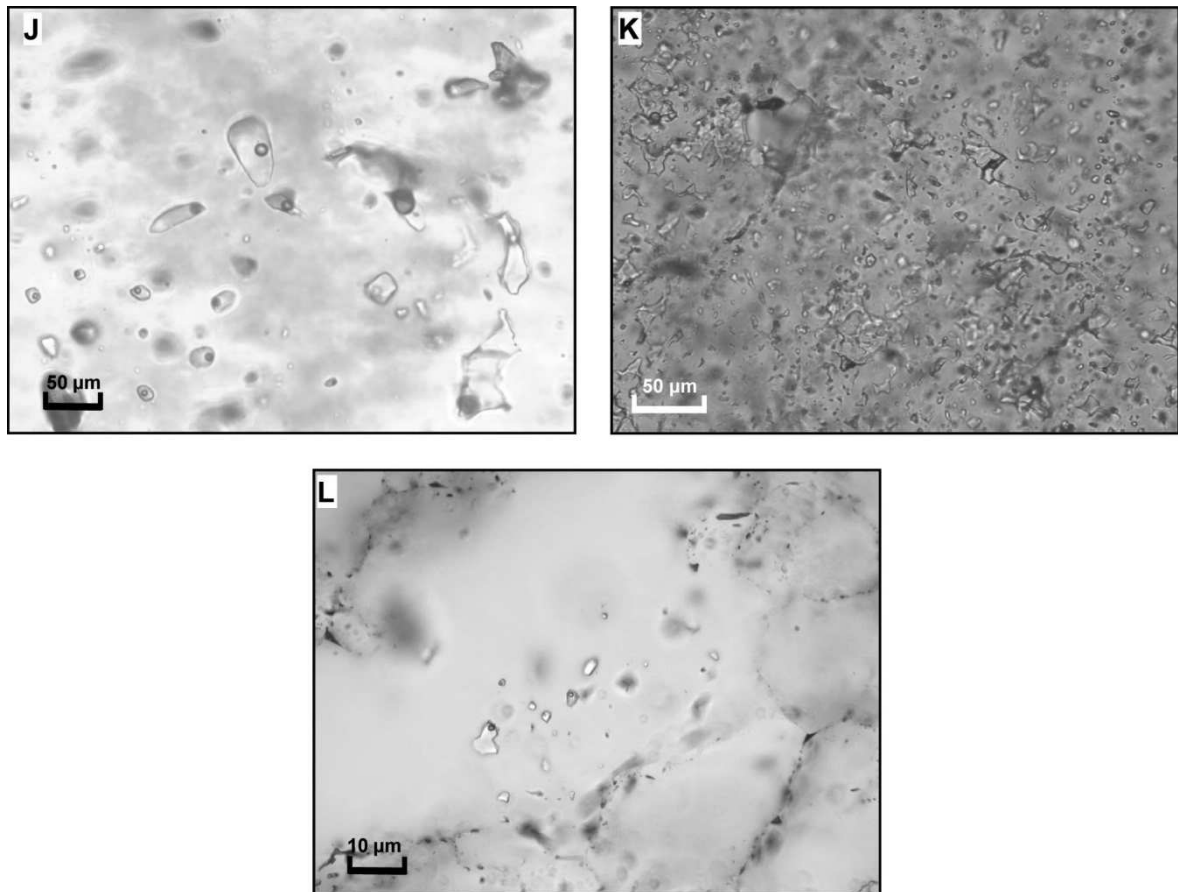


Figure 17. Summary of fluid inclusion types and SEM-CL images in the La Berrona deposit. **(A and B)** Vapor carbonic (Vc) fluid inclusions in quartz phenocrysts of the albitite. **(C)** Secondary trails of brine fluid inclusions (see the inset) crosscutting the quartz phenocryst. **(D)** SEM-CL image of an A-vein highlighting the edges of the quartz grains. Note that there is no euhedral growth that could allow to correlate the fluid inclusion arrays. **(E)** Consistent vapor carbonic fluid inclusion assemblage in an A-vein. The presence of vapor CO₂ is only recognizable during the microthermometric runs. **(F and G)** Brine (B) fluid inclusion in an A vein. A reddish transparent crystal (hematite) can be recognized in addition to halite in most of them. **(H)** Two phase liquid aqueous fluid inclusions in the quartz filling breccia cavities. **(I)** SEM-CL image of the quartz filling “pockets” in the banded magnetite, showing the presence of at least two generations of quartz.

(J) Two phase liquid aqueous fluid inclusions in the quartz filling “pockets”. These fluid inclusions are very similar to the La inclusions of the breccia quartz cavities. (K) Clouds of decrepitated liquid aqueous and brine fluid inclusions in the zones of Q2 quartz generation in the pockets. (L) Liquid aqueous fluid inclusions in late veins.

III.5. 2. LA-ICPMS analysis of the fluid inclusions

Seven vapor and brine fluid inclusion assemblages in the quartz phenocrysts and in the A-veins were analyzed by LA-ICPMS in order to constrain the composition of the fluids that circulated in the La Berrona magmatic-hydrothermal system. Unfortunately, only three fluid inclusion assemblages (one B and V in the phenocryst and one V in the A-veins) showed confident signals good enough to reduce and calculate the absolute element concentrations (Table 4; Fig.18).

The brine assemblage is characterized by high contents in Na₂O (16.2 ± 1.5 wt%), K₂O (10.3 ± 3.5 wt%), CaO (8.05 ± 3.3 wt%), and Fe₂O₃ (1.5 ± 0.7 wt%). Vapor assemblages show lower contents in Na₂O (4.3 ± 0.2 wt% and 4.2 ± 0.18 wt% in the vein and phenocryst respectively), K₂O (1.01 ± 0.4 wt% and 1.3 ± 0.4 wt% resp.) and the MgO is below the limit of detection. The vapor assemblage in the vein has Fe₂O values below the limit of detection, whereas the vapor assemblage of the phenocryst shows a Fe₂O mean value of 1.3 ± 0.7 wt%, suggesting a high iron content in the vapor phase. However, more analysis are needed to confirm this high Fe contents in the vapor CO₂ bearing fluid inclusions. The TiO₂ content in this assemblage is below the limit of detection.

Most of the analyzed trace elements are below the limit of detection in the vapor fluid inclusions (Fig.18). However, they show high contents in Sr (1069 ± 213 $\mu\text{g/g}$ and 1313 ± 619 $\mu\text{g/g}$ in the A-vein and quartz phenocrysts, respectively) followed by Ba (417 $\mu\text{g/g}$ and 714 ± 206 $\mu\text{g/g}$) and Pb (73 ± 10 $\mu\text{g/g}$ and 157 ± 67 $\mu\text{g/g}$). Sr is also the most abundant element in the secondary brines from the phenocryst with concentrations of 8910 ± 3939 $\mu\text{g/g}$, followed by Ba with concentrations of 3808 ± 2188 $\mu\text{g/g}$. This enrichment in Ba-Sr-Pb is unlikely to occur in the residual magmatic-hydrothermal fluids after the crystallization of feldspar or plagioclase unless there is excess of these elements in the fluid. The only likely alternative is that the fluids interacted with feldspar-rich rocks the albitite or the host rocks.

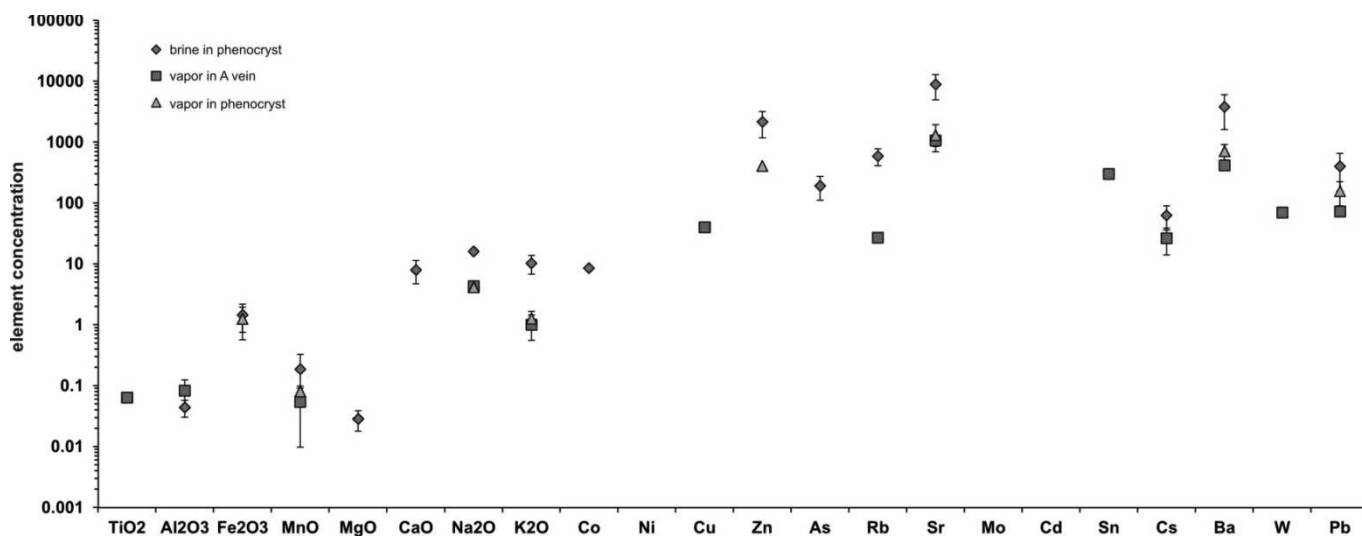


Figure 18. Average element concentration for the three fluid inclusion assemblages that give reliable LA-ICPMS signals. B phenocryst: sample CBE2late-chip8; Vc A-vein: sample CBE2-chip1-veinA; Vc phenocryst: sample Berrona3. Major and trace elements are given in wt% and $\mu\text{g/g}$ respectively.

III.6. Discussion

III.6.1. Distinguishing albitites: a metasomatic vs. a magmatic origin

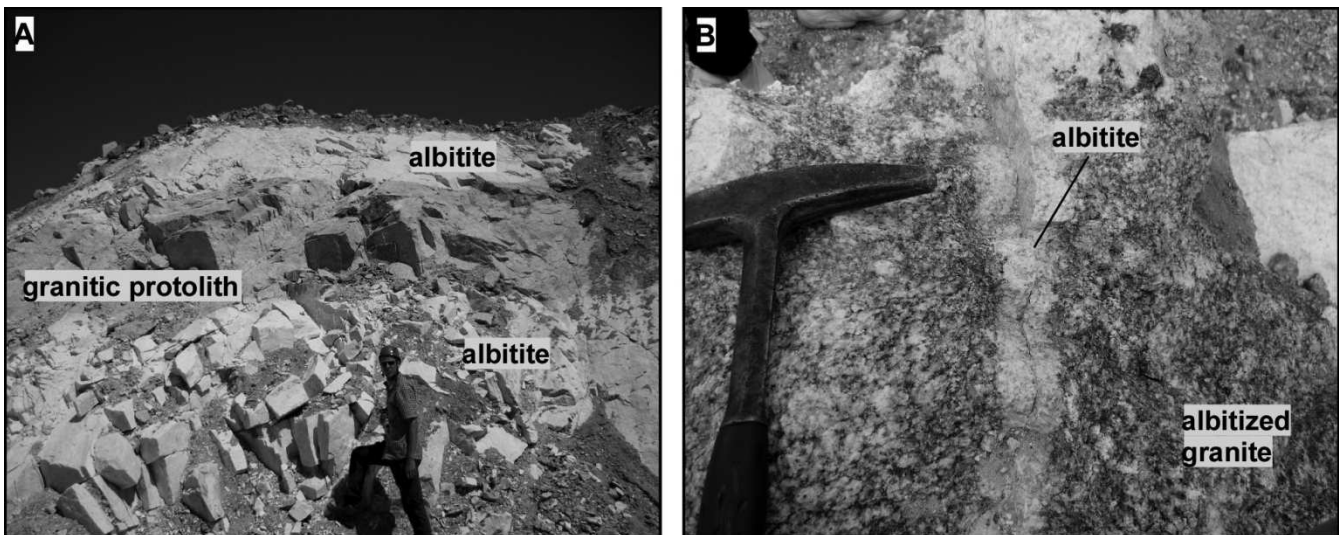
Despite formed in very different settings, all the albitite rocks elsewhere share similar assemblages with only variations in the silica content. Most of the albitite occurrences in the world, and particularly those related to iron oxide- ($\pm\text{Cu}$ - $\pm\text{Au}$) deposits are considered as of metasomatic origin, with the exception of plagiogranite in ophiolitic complexes, TTG suites and greenstone belts and some A-type granite.

III.6.1.1. Two models explaining the same rock: evidences and their validity

At a global scale, the metasomatic model for the genesis of albitite involves the circulation of Na (\pm Ca)-rich aqueous fluids that are in disequilibrium with the host rock (commonly a granitoid but also metasedimentary rocks) that react and produce an almost monomineralic rock dominated by albite with lesser amounts of quartz and clinoamphibole. Fluids related to this process are typically highly saline (18 - 30 % NaCl eq.), hot (400 - 500°C) and usually CO₂-rich (Mark et al., 1998; Oliver et al., 2004). In this fluid context, the albitization is caused by the preferential growth of albite over K feldspar involving the circulation of fluids with high Na/(Na+K) ratios. This can be due to the fact that a fluid in equilibrium with a two feldspars-bearing rock, the Na/(Na+K) ratio increases in the presence of CO₂ or volatiles (Orville, 1963; Lagache and Weisbrod, 1977; Pollard, 2001) or due to the leaching of Na-rich rocks such as evaporites (Barton and Johnson, 2000) or their ancient equivalents. Later in the evolution of the system, due to the unmixing of the H₂O-CO₂-NaCl \pm CaCl₂-KCl fluids, the drop in the Na content due to the precipitation of albite or cooling, K feldspar becomes the stable feldspar phase leading to a superimposed potassic alteration. Here, a 0.01 increase in equilibrium Na/(Na+K) is equivalent to a temperature decrease of 25 °C (Lagache and Weisbrod, 1977). This particularly explains the early albitization in Fe oxide-Cu-Au districts or porphyry systems that is commonly overprinted at lower temperatures by K-rich metasomatism with the development of K feldspar or biotite.

A remarkable world class example of the Na-rich metasomatic alteration is that observed in the well-known albitite from central Sardinia, with more than 90 km² of exposed albitite that is currently exploited as a feldspar resource (Carcangiu et al., 1997; Biddau et al., 2001; Palomba et al., 2001; Castorina et al., 2006). In these rocks, the granitic protolith is progressively altered to an "albitized granitoid" that finally evolves into a completely albitized rock (Fig.19).

The magmatic model is less described in the literature, except for the plagiogranite in ophiolitic suites, which formation process is reasonably well explained (Aldiss et al., 1981; Elthon, 1991; Liang et al., 1995; Floyd et al., 1998; Koepke et al., 2004). Other primary magmatic albitite is that related to the alkaline granitoids, usually due to the crystallization of Na (\pm Li \pm F)-rich magmas of A- or S-type melts formed either by fractional crystallization or partial melting of crustal rocks (Kovalenko and Kovalenko, 1984; Schmitz and Burt, 1990; Schwartz, 1992; Azer et al., 2010). However, the specific magmatic processes that lead to this



particular rock are still poorly understood.

Figure 19. Photographs of the albitite from the Is Paduleddas deposit (central Sardinia) showing the relationships between the granitic protolith and the albitite (A) and the partially albitized granite crosscut by an albitite vein (B).

The evidences given in the literature for discriminating the formation of albitite via metasomatic or magmatic processes are the following:

- 1) Field evidences:
 - a) Metasomatic model

- i) Presence of replacive textures indicating a metasomatic evolution pattern from the unaltered granitic protolith through a transitional albitized rock to a massive albitite (Fig. 19) (e.g. Charoy et al., 1989; Mark, 1998; Palomba, 2001)
 - ii) Structurally controlled Na - rich rocks occurring along faults, veins, lithologic contacts and breccias (Fig. 19B) (e.g. Palomba, 2001; Charoy et al., 1989; Mark, 1998).
 - iii) Existence of relics of the protolith rock in the albitite (e.g. Palomba, 2001).
- b) Magmatic model
- i) Clear spatial, chronological and genetic association of the albitite to magmatic rocks such as ophiolitic suites or A- or S-type magmatism (e.g. Sherbini and Quadi and Qhadi, 2004; Koepke et al, 2004; Elthon, 1991).
 - ii) Absence of a transitional metasomatic column.
 - iii) The occurrence of typical magmatic structures as well as the presence of typical intrusive-like cartographic shapes.
 - iv) Sharp contacts with the host rock, presence of xenoliths and uniform mineralogy, with absence of evidences of albitization of the country rocks (Sherbini and Quadi, 2004).
- 2) Petrographic evidences
- a) Metasomatic model
 - i) Replacement of the K feldspar (microcline) by Na-rich plagioclase (albite - oligoclase) (Palomba, 2001, Charoy et al., 1986; Mark, 1998, Oliver et al., 2004). Sometimes the K feldspar is completely replaced but commonly it shows resorbed grain boundaries or occurs as relics in the grains of Na-rich plagioclase; albite-rich rims are widespread around the K feldspar or replacing the groundmass of the rock. Additionally, the albite fills open spaces created by the dissolution of former quartz.

The albite can locally preserve the general shape and twin pattern of the original K feldspar (Castorina et al., et al., 2006). This petrographic criterion is the most commonly used in the literature as indicator of the presence of a metasomatic alteration.

- ii) Great variability of the grain size of the Na plagioclase.
- iii) Presence of associated mineralogical changes, such as the replacement of biotite by epidote, muscovite or chlorite. Also, the presence of secondary hydrothermal minerals such as quartz and/or hydrothermal zircon distributed along grain boundaries and microfractures (Drummond, 1986; Palomba, 2001; Charoy et al., 1989)
- iv) Evidences of quartz dissolution in the albitized zones. i.e, episyenitization. This is an important alteration process since it enhances the permeability of the rock, increasing the circulation of hydrothermal fluids (e.g. Charoy et al., 1989, Caballero, 1993, 1999, Cathelineau, 1983; Boulvais, et al., 2007).

b) Magmatic model

- i) Lack of systematic pervasive replacement of K feldspar or relics of K feldspar within the albite (Sherbini and Quadi and Quadi, 2004).
- ii) "Snowball quartz" texture consisting of laths of albitite disposed concentrically along the growth zones of the quartz (Schwartz, 1992; Xu et al., 1987; Pollard, 1988). However, some authors (Beus, 1966, Boguslavskiy et al., 1966; Bazarov et al., 1973 and Sabet et al, 1976) consider this texture as indicative of a metasomatic origin (Schwartz, 1992; Sherbini and Quadi, 2004).
- iii) Presence of well-preserved primary silicate melt inclusions (this study).

3) Geochemical evidences

a) Metasomatic model

- i) Depletion of some major elements such as SiO₂, K₂O and/or CaO and in less proportion, of Fe₂O₃ and MgO, in the metasomatic albitite regarding

the protolith. Strong enrichment of Na₂O, locally accompanied by that in CaO and Al₂O₃ (Polito et al., 2009; Castorina et al., 2006; Palomba, 2001; Oliver et al., 2004; Schwartz, 1992; Mark, 1998, 2000).

- ii) Depletion of some trace elements such as Ba and Rb - due to the destruction of K feldspar and biotite during albitization - Pb, Cl, Zn, Co, Cr, Sr, Eu, U and Th. In most cases, there is a significant enrichment in the newly formed Na plagioclase (Schwartz, 1992; Palomba, 2001; Chauris et al., 1985). There is also an accompanying enrichment in Zr, F, Y, and Li.
- iii) REE-enrichment due to the widespread crystallization of some hydrothermal minerals, like LREE in newly formed epidote and HREE in titanite as in the albitite from central Sardinia, Palomba, 2001; Biddau et al., 2002; Carcangiu et al, 1997).
- iv) Lack of geochemical trends consistent with magmatic differentiation in the Harker diagrams and in the normative quartz-albite-orthoclase plots. Schwartz (1992) quotes to the significant deviation in the quartz-albite-orthoclase plot from the pseudo ternary minima to the pure albitite.

b) Magmatic model

- i) High contents in SiO₂, Na₂O, Rb, Ba and low contents in MgO, K₂O, CaO and TiO₂ in the albitite, in agreement with the partitioning of elements between a melt and the crystallizing minerals (Sherbini and, 2004, Schwartz, 1992, this study). Presence of an Eu negative anomaly consistent with the fractionation of plagioclase.
- ii) Presence of high F and/or Li contents, indicative of the formation of the albite during the late stages of fractional crystallization of unusual Li-F rich granitic melts (Kovalenko and Kovalenko, 1984).

The above field and petrographic evidences should be systematically used as criteria for the discrimination between magmatic and metasomatic albitite. However, the geochemical evidences are more dubious and sometimes contradictory. In order to evaluate the validity of the geochemical evidences as usable criteria, we have compared in a chondrite-normalized spider diagram (Fig. 20) the trace element composition of different albitite interpreted either as magmatic or metasomatic, including those related to iron oxide-(\pm Cu- \pm Au) mineralization. From this plot it can be inferred that all the albitite rocks, regardless of their origin, show very similar trace element patterns. In addition, both the depletions and gains of the major and trace elements can be explained as either magmatic or metasomatic fractionation processes. These results support that the geochemical criteria alone are not diagnostic for the ultimate, magmatic or metasomatic origin of the albitite.

Probably, the most convincing evidence for a magmatic origin of the albitite from the La Berrona and elsewhere is the existence of melt inclusions that have a chemical composition similar to that of the host rock and very likely represent the melt from which the bulk rock was formed. Perhaps this is the most definitive argument proving the existence of true primary albitite melts.

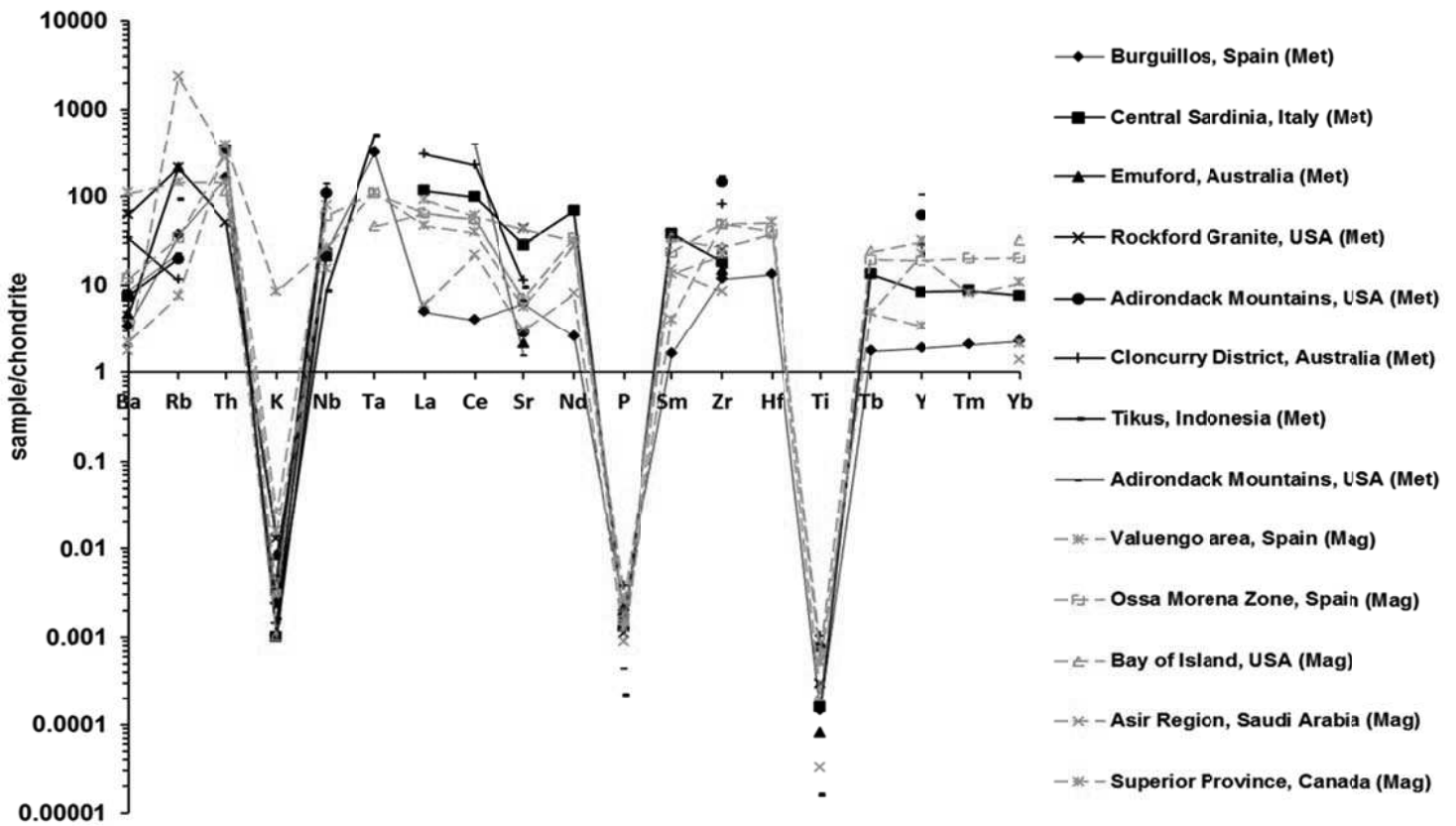


Figure 20. Chondrite-normalized spider diagrams of different occurrences of albitite worldwide. Note that the geochemical pattern is similar in all of them even if the albitites are considered as of metasomatic (black solid line and “Met”) or of magmatic origin (blue broken line, and “Mag”). Legend: Burguillos, Spain: altered leucogranite (Bachiller et al., 1996); Central Sardinia, Italy: altered granitoid (Castorina et al., et al., 2006); Emuford, Australia: albitite rich tin mineralization (Charoy et al., 1989); Rockford Granite, USA: metasomatic trondhjemite; Adirondack Mountains, USA: metamorphic albitite (McLellad et al., 2002); Cloncurry district, Australia: Fe oxide (Cu-Au) related albitite (Oliver et al., 2004); Tikus, Indonesia: Sn-W related albitite; Adirondack, USA: albitite gneiss; Valuengo area, Spain: magmatic albitite related to magnetite mineralization (this study); Ossa Morena

Zone, Spain: plagiogranite (Sánchez-García et al., et al., 2003); Bay of Island, USA: plagiogranite in an ophiolitic complex; Asir Region, Saudi Arabia: REE-rich albitite (Sherbini and Quadi and Quadi, 2004). Superior Province, Canada: TTG related trondhjemite.

III.6.1.2. The albitite from La Berrona: why magmatic?

As described in the section 5.4 and in the Figures 10 and 11, the SMI have an average major element composition very similar to that of the albitite host (with $\text{SiO}_2 = 73.2 \pm 1.9$ wt% in the SMI and 77.7 ± 0.9 in the bulk rock, $\text{Na}_2\text{O} = 6.8 \pm 1.1$ and 7.1 ± 0.5 wt%, $\text{K}_2\text{O} = 0.1 \pm 0.1$ and 0.1 ± 0.04 wt% and $\text{CaO} = 0.6 \pm 0.4$ and 0.6 ± 0.5 wt%). The trace element distribution between the melt inclusions and the albitite is in agreement with the element fractionation behavior in a magmatic system. In addition, the petrographic and chemical features of the SMI rule out the possibility of at least significant pre-, syn- or post-entrapment processes that could change the primitive composition.

The key question is if the SMI could have been trapped in the quartz phenocrysts and afterwards being altered by the late hydrothermal fluids that produced a hypothetical albitization of the host granitoid. The major argument against such a statement is that if the rocks are hydrothermally altered, the compatible/incompatible behavior of the trace elements between the SMI and the albite plagioclase and the bulk rock composition would not be fulfilled (Fig. 13). On the other hand, all the selected SMI show a strong phase consistency with similar solid/melt phase ratios and also strong consistency on the LA-ICPMS element concentrations in all the dataset. It is unlikely that the hydrothermal alteration would have affected homogeneously all the analyzed melt inclusions within the quartz phenocrysts.

A magmatic model for the La Berrona Stock and equivalent albitite bodies in the Valuengo area is also supported by field evidences, such as the lack of an hypothetical protolith in any of the intrusions, the absence of metasomatic contacts nor relicts of precursor rocks within the albitite and the sharp contacts with the country rocks. Furthermore, the albitite shows typical primary igneous textures with little post-crystallization alteration. Thus, all the evidences presented here point towards a magmatic origin for the studied albitite and contradict the current view of that all the albitite related to Fe oxide-(\pm Cu- \pm Au) deposits is of metasomatic origin.

III.6.2. Source and evolution of the magmatic albitite

III.6.2.1. *Hypotheses on the origin and classification of high silica – low K/Na magmatic rocks*

Different models have been proposed in the literature to explain the origin of high silica (>70 wt %) – high Na/K melts. Most of them agree with their derivation from the partial melting of crustal rocks but the contribution of mantle-derived material can be also important either as part of hybridation or as heat supplier in the partial melting process. In other cases, as in plagiogranites in ophiolitic sequences, the contribution of the mafic phase is dominant, as they are formed during extreme differentiation of juvenile magmas. However, the identification of the source rock is not always easy as its primary geochemical/mineralogical signature imprint is usually obliterated by further processes of assimilation and mixing upon the ascent of the melt.

High silica – high Na/K igneous rocks dominated by Na-rich plagioclase and quartz have been usually known as *albitite*, *plagiogranite*, *trondhjemite*, and/or *peraluminous leucogranite*. There is no single classification scheme for them and the only common feature is the high content in silica and sodium as well as the low

contents in K, Ca and Mg. *Trondhjemite* is considered to be part of the *tonalitic*, *trondhjemitic* and *granodioritic* (TTG) igneous suites that are commonly found in Archean greenstone belts, but also in other more recent magmatic provinces such as the Iberian Pyrite Belt (Schutz et al., 1987). They are commonly interpreted as due to product of the melting of an amphibolitic protolith at temperatures ranging from 850° to 1100 °C (Barker and Arth, 1976; Rapp et al., 1991; Wyllie et al., 1997, Patiño Douce, 1997, 1998). In some cases, Na-rich metasomatic rocks have been erroneously called *trondhjemite* (e.g. Drummond, 1989) leading to the misunderstanding of the term. The descriptive term *plagiogranite* is commonly used for plagioclase-rich rocks found in ophiolitic sequences exclusively, that are considered to be formed by partial melting of oceanic gabbro. Alternatively, the denominated *oceanic plagiogranite* (not necessarily related to an ophiolite) are considered to be products of the fractional crystallization of a MORB system (Coleman and Peterman, 1975; Sánchez-García et al., 2003; Koepke, 2004). *Peraluminous SiO₂-rich leucogranite* is commonly used for felsic igneous rocks product of the partial melting of continental crustal rocks during the dehydration melting of muscovite rich metasediments during regional metamorphism, i.e., the S-type granitoids. Also, they can be the product of the extreme fractional crystallization of granitic series, i.e., the most evolved terms of granitic series (Patiño Douce, 1997, 1998). The term *leucogranite* is ambiguous and includes all the quoted igneous leucocratic rocks regardless of their origin.

Among all the names listed above, the general term *albitite* is preferred here to describe these high silica (>70 wt %) albitite plagioclase-rich rocks because it avoids any genetic connotation but highlights the most significant feature of the rock, i.e. the absolute dominance of albitite. This denomination is more specific as other rocks such as *trondhjemite* show wider range in plagioclase composition ranging between albitite to oligoclase. There are two exceptions for which other terms are recommended to use: (1) in the common case in which the Na-rich

alteration is not pervasive but structurally controlled and localized, the term *Na-rich altered rock* or *albitized rock* should be used rather than the term *albitite*; and, (2) when the geological setting is unquestionable, such as in the TTG (tonalite, *trondhjemite*, granodiorite) series or the *plagiogranite* in ophiolitic suites, the specific names should be used (i.e. *trondhjemite* and *plagiogranite*).

III.6.2.2. Comparison with experimentally calculated melt compositions and interpretation of the source and evolution of the albititic melt composition

The obtained data allow for the first time in the study of albitite, to compare the composition of naturally formed melts of albititic composition with already published experimental calculations of similar melt compositions. The Figure 21 shows a comparison of the major element composition of the SMI with the compositions of melts produced by experimental partial melting of various lithologies, such as mica-rich metasediments (greywacke, pelites of mafic and felsic derivation), amphibolite, quartz amphibolite and calc-alkaline granite. The composition of the SMI clearly overlaps with the compositions of the experimental melts formed by dehydration melting of mica-rich rock sources such as greywacke or pelite (Figs. 21A, 21B and 21C). Conversely, the composition of the SMI does not match with melts formed by melting of amphibolite (as most of trondhjemitic rocks do) or calc-alkaline igneous rocks (Fig. 21D and 21E). The albititic melt and the mica-rich rock (greywacke and pelite) -derived melts also coincide in that they are highly enriched in silica, with up to 70 wt% of SiO₂. On respect to the rocks that these melts produce after crystallizing, peraluminous leucogranite is the only rock derived from the anatexis of the pelite and greywacke that shows similar compositions and as high silica content as the melt from which they crystallized (Fig. 21F). Therefore, this rock is considered as product of crustal anatexis without any participation by hybridation, assimilation and/or fractionation of primitive mafic rocks. The albitite from La Berrona also shows similar compositions as the

melt from which it crystallized with very similar content in silica (Fig. 10) suggesting that they also formed by melting of crustal rocks. In addition, the bulk rock composition of the albitite overlaps with the compositions of peraluminous leucogranite rocks in the Figure 20F and they are differentiated only by the high Na/K ratio in the albitite. All the patterns showed above are in agreement with crustal melt derived origin for the albitite with minor, if any, participation of mantle material. However, and despite not having been studied in detail by the authors, the albitite in the northern Olivenza-Monesterio Antiform has been interpreted in the literature as derived from extreme fractionation of a basaltic magma (E-MORB and N-MORB, Sánchez-García et al., 2003, 2008, 2010; Bellido et al., 2010) or partial melting of a tholeiitic gabbro (Etxebarria et al., 2006). These interpretations are based on trace element geochemistry (Bellido et al., 2010), the similarities on the composition of the albitite to the ocean ridge plagiogranite composition (Etxebarria et al., 2006) and the fact that some albitite outcrops are spatially related to gabbro (Etxebarria et al., 2006). Here, it is suggested that the overwhelming difference in volume of the albititic granites compared to the basic rocks in the Valuengo area (no mafic dykes or xenoliths have been found in the La Berrona Stock, Fig. 1) indicates that minor mantle derived melts contributed to the origin of these felsic rocks. In addition, the trace element compositions show similar patterns as the crustal rocks (Fig.12) as well as the REE patterns suggesting no mantle contribution. The preliminary isotopic data also confirm the restricted contribution of mafic magma in the formation of the rock.

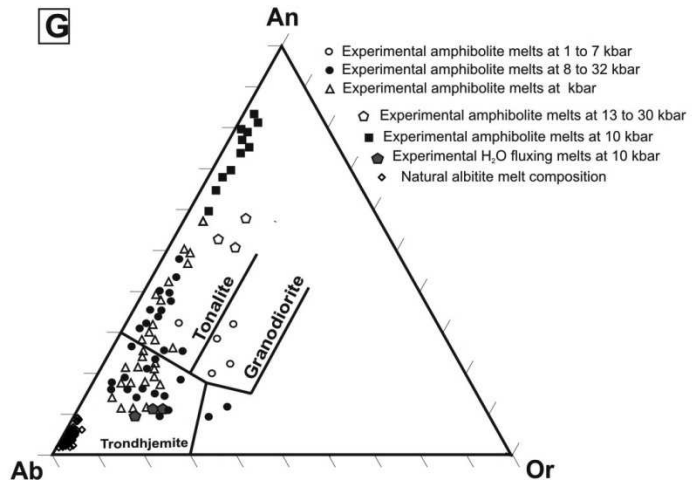
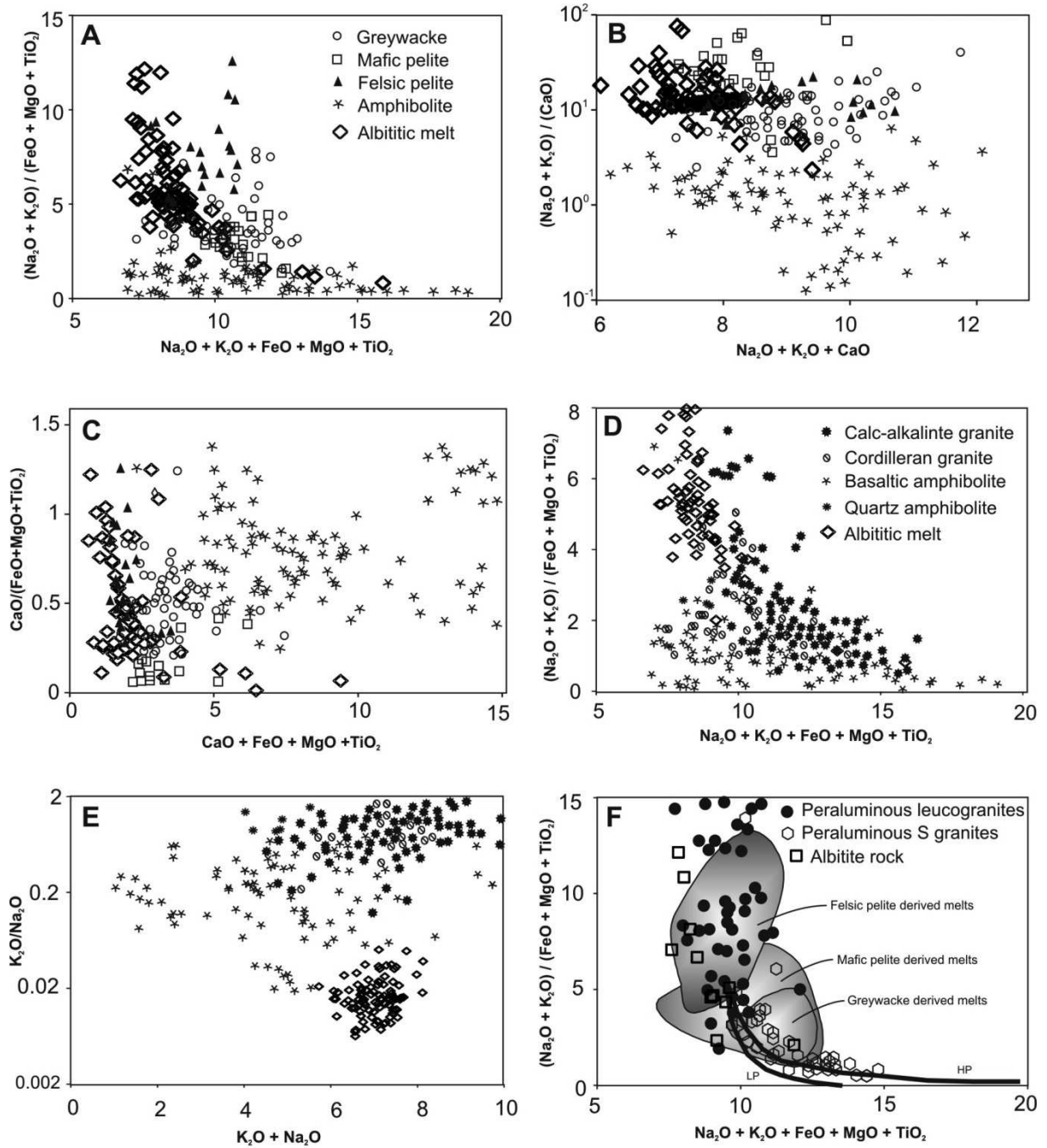


Figure 21. (A to E) Composition of igneous melts generated during the experimental anatexis of various source rocks (from Patiño Douce, 1999 and references therein). The composition of the SMI at La Berrona is plotted with the results of the experimentally obtained melts. All the values are in wt%. **(F)** Bulk rock composition of peraluminous and S-type granite rocks compared to the bulk composition of the albitite from Valuengo. The lines represent trends of hybridation of a mafic melt with a metapelite at low ($P \leq 5$ kbar) and high ($P \geq 12-15$ kbar) pressures (from Patiño Douce, 1999). **(G)** Albite-orthoclase-anorthite triangular system showing the granite classification of Baker (1979), and the compositions of trondhjemite source melts and peraluminous leucogranite melts (all the experimental data are taken from Rapp et al., 1991 except for the experimental H₂O fluxing melt data which are taken from Patiño and Harris, 1998). Note that the albitite melt compositions from this study are much more enriched in albite component than the rest of experimental melts.

III.6.2.3. Why rich in albite plagioclase?

The origin of the high Na₂O/K₂O ratio that controls the formation of the albitite and that makes it so uncommon remains unresolved. The SMI data show that the albitite melt is even more enriched in the albite component than the experimentally obtained peraluminous leucogranite and trondhjemitic melts derived by dehydration melting of pelite and amphibolite, respectively (Fig. 21G).

Several authors have demonstrated that the addition of F and Li to a melt lowers the solidus temperature of the haplogranite (Ab-An-Or) system, shifting the ternary minimum towards the albite side (Glyuk et al., 1980; Manning, 1981; Schwartz, 1992). Fluorine cannot be analyzed with LA-ICPMS and Li is always

below the limit of detection in the SMI so is difficult to know if these elements are enriched in the albititic melt. However, there is no fluorite, lepidolite or other F – Li bearing accessory minerals in the rock, although in some mineralizations nearby (e.g. El Soldado mine, Tornos et al., 2004) there is abundant fluorite intergrown with the magnetite. El Soldado is a replacive deposit on Early Cambrian limestone and a suitable place for the formation of fluorite, thus suggesting the abundance of F in the magmatic system that would favor the formation of albite over K-feldspar or more Ca-rich plagioclase.

A high Cl content in the melt could also have caused preferential fractionation of potassium in the magmatic-hydrothermal fluids released during fluid saturation related to boiling during crystallization causing enrichment in sodium (Burnham and Nekvasil, 1986). In this case, K would have precipitated as K- feldspar later in veins or as potassic alteration around the intrusive, something that has not been observed in the albitite.

Another possible process is the melting under water rich conditions. The presence of H₂O lowers the solidus temperature of plagioclase and quartz inducing the partial melting of the rock at lower temperatures than if it would have melted by incongruent breakdown of micas at higher temperatures (Conrad et al., 1988; Patiño Douce and Beard, 1995; Patiño Douce, 1996; Iwamori, 1997; Winter, 2010). The experiments of Patiño Douce and Beard (1995) and Patiño Douce, (1996) show that the proportion of Na₂O, CaO and K₂O (the first two hosted by the plagioclase and the later by the micas and K feldspar) in the produced melt will depend not only on the source rock composition but also on the H₂O content and fluid pressure conditions. If the pressure is sufficiently high to stabilize garnet as residue, the generated melt produced under H₂O rich condition (1 – 2 wt% water) becomes enriched in the albite component and depleted in anorthite because Ca stays in the grossular garnet. Furthermore K₂O would be also depleted in the melt because micas are stable in the residue (Patiño

Douce, 1996; Patiño Douce and Harris, 1998; Winter, 2010), favoring the formation of melts with high Na/(Na+K) ratios in addition to the presence of volatiles and CO₂. In addition, experimentally calculated melts formed by the dry melting of a metapelite have Rb/Sr ratios of > 5 whereas in water-rich melts the ratio is < 2 (Harris et al., 1993), consistent with the composition of the albitite in La Berrona, with a Rb/Sr ratio of 0.04.

However, despite the water saturated theory is plausible to explain the high Na₂O content in the albititic melt, more parameters are necessary to know such as the pressure at which it was formed, the water content in the melt inclusions and the potential residual assemblage in the commencement of the crustal anatexis process. Taking this in account, our favorite model involves the water-saturated partial melting of F-, and perhaps CO₂, bearing sediments during the high T/low P metamorphism. The generated melts are expected to be silica-rich and with high Na/K ratios. The likely candidates to represent the melted protolith are the chemical sediments interbedded with siliciclastic sediments, iron formations and limestone of the Early to Mid Cambrian sequence.

III.6.3. Silicate melt – iron oxide immiscibility

The existence of an immiscibility field between an iron oxide melt and a silicate melt has been supported by a large number of experimental works since Roedder in 1951 delimited a two liquid field in the silica-rich region of the K₂O-Al₂O₃-FeO-SiO₂ system. Experimental studies have demonstrated that iron is dissolved in the silicate melt at high temperatures but at low temperatures an immiscible Fe oxide rich phase can separate from it (Phillips, 1967; Naslund, 1983). However, and despite the considerable number of papers on this topic (Table 8), descriptions of direct observation of coexisting immiscible silicate melt and Fe oxide melts are rare. Hurai et al. (1998) found primary inclusions of coexisting immiscible Fe oxide melt and silicate melt in the core of zircon crystals

in Pliocene to Pleistocene alkali basalt of the Western Carpathians. Naumov et al. (1993) also found Fe oxide globules coexisting with rhyolite glass in quartz phenocrysts of an ignimbrite in central Slovakia. In addition, Markl (2001) observed macroscopically visible evidences of liquid immiscibility between Fe-Mn-Nb-REE-rich and Na-Al-rich melts in agpaitic dykes in the Ilimaussaq intrusive complex (South Greenland). Spheres of a Fe-Ti-P oxide-rich phase in rhyolitic glass from a subvolcanic magma chamber were also described by Clark and Kontak (2004) in the Cenozoic Antatuta Complex in Peru. At a larger scale, field evidences of crystallization of a Fe oxide melt have been addressed in the magnetite-apatite deposits such as El Laco in Chile (Park, 1961; Naslund et al., 2003; Tornos et al., 2011) and the Kiruna deposit in Sweden (Nyström and Henriquez, 1994), among others. However, and even though these are well studied deposits, there is still significant controversy about the real magmatic origin of these magnetite-apatite deposits (e.g., Naslund, 2004). Furthermore, magnetite- ilmenite/Ti-rich magnetite-apatite rocks known as nelsonite are also considered as the products of the direct crystallization of Fe-Ti-P oxide melts separated from a silicate rich magma or of extreme fractional crystallization (Philppots, 1967; Kolker, 1982; Barton and Johnson, 1996; Naslund et al., 2002; Clark and Kontak, 2004).

References	Experimental evidences
Roedder, 1951	Delimitation of an extensive two - liquid field in the silica - rich region of the system $K_2O - Al_2O_3 - FeO - SiO_2$ at relatively low temperatures (1170°C)
Gibbon and Tuttle, 1967	Delimitation of the two - liquid-vapor - FeO_x field in the hydrous system $FeO - Fe_2O_3 - SiO_2 - H_2O$ at 1120 °C/2 kbar
Philpotts, 1967 ; Naslund, 1983	Evidence of immiscible separation of Fe - Ti - P melts from silicate rich liquids. Fe dissolves readily in silica - rich melts at high temperatures and upon cooling, immiscible silica rich and Fe rich liquids will separate.
Watson, 1976	P is strongly partitioned into Fe oxide melt at 1180 °C in the system $K_2O - Al_2O_3 - FeO - SiO_2 - P_2O_5$
Freestone, 1978	The immiscibility field of Roedder (1951) is expanded with small added amounts of TiO_2 and P_2O_5
Visser and Kosler van Gross, 1979	The extent of immiscibility is enhanced with increasing the pressure and concentration of P_2O_5 at elevated temperatures
Roedder, 1979; Philpotts, 1982; Philpotts and Doyle, 1983	Immiscibility separation occurs between melts of ferropyroxenite composition (25- 40 %wt FeO_{tot} , 35-45 %wt SiO_2) and plagiogranite (71 - 79 wt% SiO_2)
Philpotts, 1982	Delimitation of a immiscible two - liquid field on the basis of natural igneous suites in the system $Na_2O - K_2O - Al_2O_3 - MgO - FeO - MnO - TiO_2 - CaO - P_2O_5 - SiO_2$
Weidner, 1982	Syntesis of Fe oxide melts under CO_2 saturated conditions in the system $Fe - O - C$ at temperatures of ~850 °C
Naslund, 1983; Naslund et al., 2002	Type I immiscibility / tholeiitic basalt. Oxygen fugacity has a strong effect on liquid immiscibility in iron rich silicate melts
Larocque et al., 2000	There is a continuum between FeS liquids and Fe - S - O liquids that are immiscible with silicate melts. They are characerized by high Fe and low Ti.
Lester, 2002	The addition of volatiles (CO_2 , H_2O , P, F or SO_3) to the system lowers the temperature of the iron rich melts to temperatures lower than 1200 °C
References	Natural evidences
Park, 1961; Frietsch, 1978; Nystroem and Henriquez, 1994; Naslund, 2002	Field evidences of direct crystallization of an iron oxide melt forming the magmatic magnetite bearing Iron Oxide Copper and Gold (IOCG) ore deposits (e.g. El Laco)
Roedder and Weiblen, 1970, 1971	Evidence of immiscibility in the residual glasses of many lunar rocks and in some terrestrial basalts
Philpotts, 1976, 1982	Occurrence of immiscible Fe oxide glasses (iron rich spheres) enclosed by silica rich glasses in the mesostasis of tholeiitic basalts
Lundberg and Smellie, 1979	The Kiruna type iron ores (Sweden) are the result of Fe oxide - silicate melt immiscibility aided by a high volatile content
Naumov et al., 1993	Description of melt inclusions from quartz phenocrystals of ignimbrites with Fe oxide globules coexisting with rhyolite glass
Nystroem, 1994; Naslund et al., 2002	Kiruna type magnetite deposits are products of crystallization of Fe oxide dominated melts or magmas
Hurai et al., 1998	Observation of globules of Fe dominated (59-69 wt% FeO_{tot}) and Ti dominated (43.5 wt% TiO_2) oxide melts in igneous xenolites from Pliocene to Pleistocene alkali basalts of the Western Carpathians
Markl, 2001	Macroscopically visible liquid immiscibility between an Fe - Mn - Nb - REE rich and a Na - Al - rich melt in the Ilimaussaq complex, South Greenland
Clark and Kontak, 2004	Fe - Ti - P melt formation by magma mixing in the Antauta Subvolcanic center (Peru). They are associated to Nelsonite and hydrothermal magnetite deposit formation
Lledó, 2005	Even P_2O_5 poor andesitic magmas generate immiscible Fe - P oxide melts Hydrous (10 -20 % H_2O) Fe oxide and Ti oxide liquid is exolved from trachybasalt-to rhyolite melts during fractionation of the parental alkali basalt over the temperature range of 1180-900 °C
Chen et al., 2010	The Marcona magnetite deposit (Peru) is related to immiscibility between P -rich and Fe oxide - rich liquids
Tornos et al., 2011	Melt inclusions in plagioclase phenocrysts from El Laco reflect a complex crustal mixing process between a mafic magma a silica-rich component that promoted the separation of the iron-rich melt

Table 8. Summary of the most relevant references about experimental and natural

evidences for the existence of an iron (titanium – phosphorous) oxide melt phase.

It has been demonstrated in the previous sections that the IOB (iron oxide blebs) represent true droplets of an immiscible Fe-Ti-P oxide phase and not magnetite occurring as accessory mineral in the albitite. Their close association with the SMI in some phenocrysts show that the melt saturated in iron oxide at some stage during cooling. This immiscibility probably occurred in several steps, from the exsolution of small Fe oxide droplets in the SMI (Fig. 6B and 6C) to the almost complete exsolution of the iron oxide phase (Fig. 6E and 6F).

The presence of both IOB and magnetite in the melt and the later exsolution of Fe-rich fluids suggest that the formation of Fe-rich phases in the system was controlled by episodic events of saturation-supersaturation. First, the early separation of an immiscible Fe-P-Ti melt dropped the Fe content of the silicate melt that did not attain saturation until the late crystallization of accessory magnetite in the groundmass. However, the system kept enough Fe in the melt to be able to exsolve it in the magmatic-hydrothermal fluid to produce the La Berrona ore deposit. This complex and unusual process was probably favored by the absence of Fe-rich phases in the albitite [C1].

Unfortunately, only 12 IOB were found, from which only six LA-ICPMS signals (i.e. individual IOB analyses) were good enough to be reliable. Therefore, the aim of this section is to remark the existence of an immiscible oxide phase coexisting with the albitite silica rich melt as well as to make a preliminary approximation to the composition of the oxide phase. More analyses are needed for a more thoughtful interpretation of their geochemistry and formation processes.

In the Figure 22, the IOB analyses are plotted along with the composition of the accessory magnetite in the albitite, the magnetite in the magmatic-

hydrothermal breccia and the magnetite ore as it has been already shown in the Figure 15. The figure now includes the compositions of the SMI and the albitite bulk rock. As in the Figure 15, different groups can be clearly distinguished; the IOB show much higher Ti and Fe concentrations and slightly higher concentrations in P than the other samples. Conversely, the hydrothermal ore magnetite shows the lowest content in P and Ti, while the accessory magnetite has intermediate compositions.

In order to discuss the relationships plotted in the Figure 22A, a preliminary evolutionary model is proposed in the Figure 22C. According to it, a Fe-Ti-P oxide phase represented by the IOB is exsolved during the cooling of the albitite melt. Here, some elements such Ti, P and Zr are partitioned into the oxide phase while Si, Na and Al remain in the silicate melt, as it has been shown in the Figure 16. Watson (1976) demonstrated experimentally that P is strongly partitioned into the Fe oxide rich melts at 1180 °C in the leucite - fayalite - silica system. In addition, several studies have demonstrated that the presence of P extends the immiscibility field of the system to lower temperatures (Visser and Kosler van Gross, 1979) and hence, the presence of P could have triggered the immiscibility of an iron oxide melt. On respect to the existence of high Ti concentrations in the IOB, nelsonite-like melts, magnetite cumulates and some immiscible oxide melts (including the experimental ones from the Table 8) have high Ti contents that are determined by the distribution coefficient between the silicate and the iron oxide melt. The origin for the high Ti contents in nelsonite is either related to the partial melting of high Ti-P crustal rocks or by extreme fractional crystallization. Conversely, the accessory magnetite in the groundmass of the albitite is formed from the residual melt after the iron oxide melt separation. Its relatively low Ti content can be explained by different models, including its growth after the preferential fractionation of most of the Ti into the first separated phase, the IOB. Also, it can be due to the T-dependant solubility of the Ti in

magnetite (Spencer and Lindsley, 1981), with the late magnetite being Ti-depleted regarding the early one. However, this magnetite has similar Ti and P contents that the bulk rock (Fig. 22B) and there is no free rutile, suggesting that the melt was already impoverished in Ti when the accessory magnetite crystallized. Finally, and as it is discussed in the next section, the magnetite ore is precipitated from the hydrothermal fluids. The lack of Fe-bearing phases in the albitite (except the IOB and the accessory magnetite) suggests that the bulk of the iron was exsolved within the aqueous fluid and precipitated by replacement.

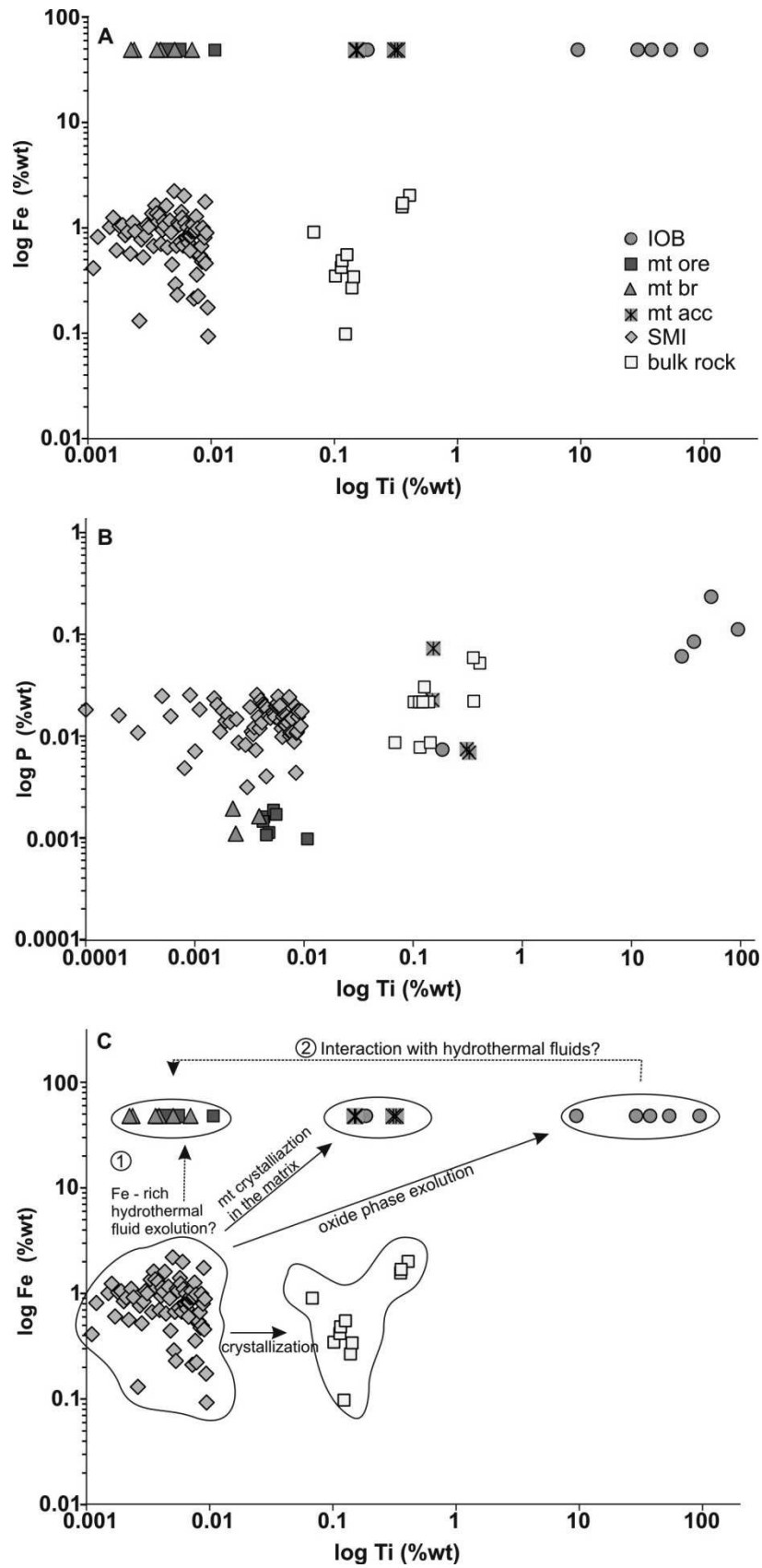


Figure 22. Fe vs. Ti (A) and P vs. Ti (B) binary plots for the compositions of the IOB (iron oxide blebs), the albitite bulk rock composition, the accessory

magnetite in the groundmass of fresh albitite (mt acc), the SMI (silicate melt inclusions), the magmatic-hydrothermal breccia (mt br) and the magnetite from the La Berrona iron deposit (mt ore). The possible genetic relationships between the different groups are also shown in (C) and explained in the text.

III.6.4. The early magmatic-hydrothermal stage in IOCG systems: insights from the La Berrona deposit

Several magnetite deposits worldwide have a dubious origin, as they show characteristics of purely hydrothermal, purely magmatic and of both magmatic-hydrothermal origins. On the contrary, many other deposits are unquestionably of hydrothermal origin, as is the case of La Berrona. As described above, the presence of replacive textures, the hydrothermal breccias and the relationship with sedimentary rocks attest this origin. In addition, there are evidences that suggest a clear genetic relationship between the albitite and the magnetite mineralization in La Berrona, such as:

- The close spatial association between the magnetite orebody and the albitite stock, with the magnetite replacing the albitite and the host rocks.
- The presence of magmatic-hydrothermal breccias and stockwork-like magnetite mineralization in the upper parts of the intrusion.
- The presence of magnetite in the groundmass of the magmatic-hydrothermal breccia, suggesting that magnetite started to precipitate during the early stages of the magmatic-hydrothermal evolution.
- The presence of high temperature, CO₂-bearing, and Fe-rich fluid inclusions in the quartz phenocrysts of the albitite as well as in the early A-veins.
- The high Fe content in the melt evidenced in both the silicate melt inclusions and the iron oxide blebs.

- The existence of other hydrothermal magnetite deposits in the Valuengo area that are always spatially related to the albitite.

The magmatic-hydrothermal breccia and the stockwork-like ore in the upper parts of the intrusion are explained as the product of magmatic fluid saturation and exsolution in a crystallizing magma, as has been intensely discussed in the literature of magmatic- hydrothermal deposits (e.g., Burnham, 1979; Burnham and Ohmoto, 1980; Hedenquist and Lowernstern, 1994; Student and Bodnar, 2004). There is general agreement about that in shallow systems during fluid separation, the fluid pressure overcomes the local rock stress, promoting the cracking of the already crystallized carapace and the host rocks. These fractured rocks are considered to be the ideal channelways for the circulation of the hydrothermal fluids that lead to the subsequent alteration and mineralization.

The second and dominant style of mineralization is the banded magnetite that occurs replacing both the albitite and the hosting calc-silicate hornfels in the Lower Quarry. As it is shown in the Figure 23, both types of hydrothermal magnetite have the same major and trace element contents and are related to the same albite-actinolite alteration, so it is likely that they formed within the same hydrothermal system.

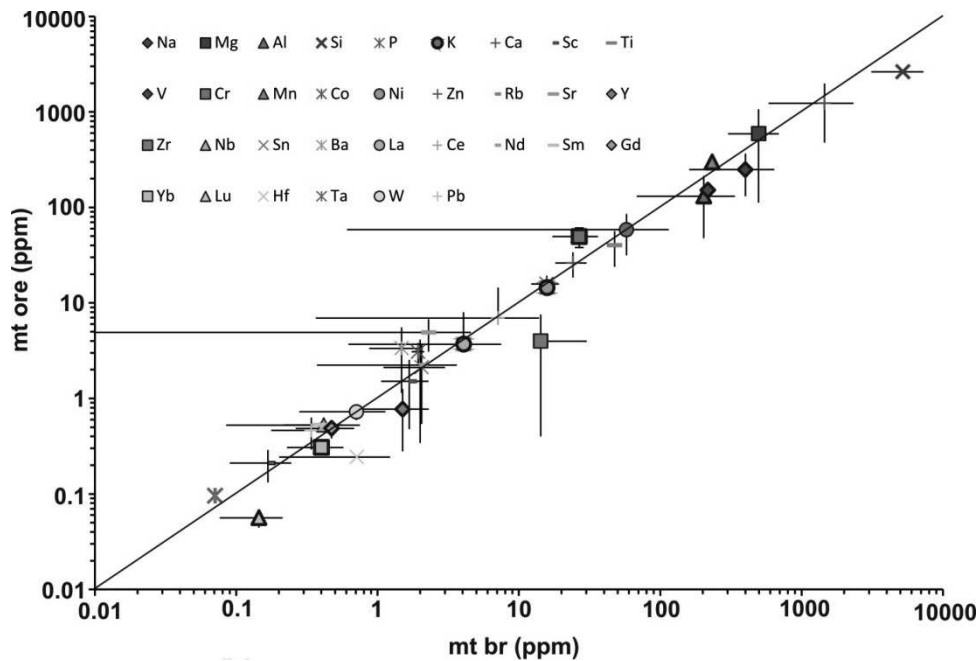
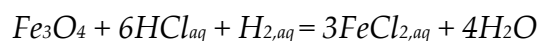


Figure 23. Major and trace element comparison between the banded magnetite (mt ore) and the magnetite in the magmatic-hydrothermal breccias (mt br).

Experimental data indicate that Fe is transported as FeCl_2 complexes in single phase hydrothermal fluids (Chou and Eugster, 1977; Boctor et al, 1980; Frantz et al., 1980; Simon et al., 2004). Chou and Eugster (1977) proposed that the solubility of magnetite is controlled by the equilibrium



In this sense, exsolved silica- and iron-rich saline fluids react with the carbonate host rock increasing the pH of the fluid with concomitant destabilization of the iron chloride complexes and precipitation of actinolite, albitite and magnetite.

In La Berrona, there is not clear coexistence between the SMI and the CO_2 -bearing fluid inclusions (except in the suspicious assemblage of the Figure 14) consistent with their coetaneous entrapment in a fluid saturated scenario. However, these inclusions have high minimum homogenization temperatures

($387 \pm 28^\circ$ and $337 \pm 2^\circ$ °C in the phenocrystals and A veins respectively) and show high Fe content (1.3 ± 0.7 wt% in the analyzed assemblage). In addition, they only occur both in the phenocrysts and in the early A veins and not in the late veins crosscutting the mineralization. Thus, these CO₂-rich aqueous inclusions seem to be a potential ore forming fluid of magmatic-hydrothermal derivation. Simon et al. (2004) demonstrated experimentally that the volatile (CO₂-bearing) exsolution at pressures close to the critical pressure enhances the capacity of the magmatic vapor of transporting Fe, which would be in agreement with the high Fe content and the CO₂ content in the vapor-bearing inclusions. Brine fluids have been also proposed in the literature as source for the iron in IOCG systems (i.e. Barton and Johnson, 2000). Brine fluid inclusions in the phenocrysts and A-type veins in La Berrona are clearly secondary and have homogenization temperatures of $157 \pm 7^\circ$ and $152 \pm 15^\circ$ °C, respectively. They are also Fe-rich, with daughter crystals of hematite. These inclusions also occur in the late veins and late quartz cavities that post-date the mineralization so their role in the magnetite precipitation is dubious.

One of the major points already posed in the previous section is if there is any relation between the ore forming fluids and the iron oxide phase represented by the IOB. There are two possibilities to the fluids be enriched in Fe (options 1 and 2 in the Figure 22C) during the melt-fluid exsolution: (1) the magmatic-hydrothermal fluid is exsolved from the crystallizing melt and the Fe is partitioned into the fluid phase; and, (2) a Fe-poor fluid interacts with the iron oxide phase enriched in Fe which fractionates in the fluid (in the sense of Nadeau, 2010). In the first case, the fluid is enriched in iron because, except the small amounts of IOB and the accessory magnetite, there is no sink for iron in the albitite and most of it fractionates into the exsolving aqueous phase. In the second case, the fluids interact with IOB and the Fe is partitioned to the fluid phase. If this second case is considered, the question about why the magnetite is not also enriched in Ti remains unresolved, as the oxide phase is enriched in Ti. In

nelsonite type deposits, the magnetite mineralization is enriched in Ti and P as it crystallizes directly from a Fe-Ti-P oxide phase similar to that of the La Berrona deposit (Kolker, 1982; Dymek et al., 2001). However, the mineralization in La Berrona is of clear hydrothermal origin and not enriched in Ti and P so the hydrothermal fluids did probably not interact with the iron oxide phase before at the moment of the exsolution. More likely, the Fe was incorporated in the hydrothermal system due to its incompatibility in the silicate melt.

III.6.5. Proposed genetic model for the albitite and the magnetite mineralization of the La Berrona area

The Figure 24 shows a schematic genetic model to explain the magmatic-hydrothermal system in the La Berrona Stock and deposit based on the geological, mineralogical and melt and fluid inclusion data documented in this chapter.

Stage A. The albitite stock probably represents a sub-rooted intrusion that was emplaced para-autochthonously not far from its site of generation and ascended along extensional structures during the rifting event in the Early Cambrian-Mid Ordovician times. The geochemical and geological data suggest that the albitite melt generated by water-rich partial melting of upper crustal rocks, likely shallow marine pelite, calc-silicate hornfels and Fe- and volatile-rich chemical sediments of the late Neoproterozoic Las Mayorgas Formation during a high temperature-low pressure metamorphism. The high water, volatile (F) and CO₂ content of the melt is interpreted as the main reason of the increase in the Na/(Na+K+Ca) ratio of the generated leucosome. There are no evidences of the involvement of mafic juvenile rocks in the genesis of the albitite which composition is close to that the original melt and has not been affected by processes of fractional crystallization.

The melt rose up until the layer of the Early Cambrian limestone at relatively shallow depths. The process inhibiting further ascent is probably similar

to that described by Lowenstern (2001), i.e., the interaction of the carbonatic rocks via assimilation or decarbonatization (skarn formation) with the igneous melt increases the fluid pressure leading to supersaturation, release of magmatic-hydrothermal fluids, drop of the solidus temperature and crystallization of the melt. The first crystallized and most external zone of the albitite produced a carapace of crystallized rock in the contact with the host rocks, keeping an internal zone of molten albitite that gradually crystallized.

Stage B. During the gradual crystallization of the melt, an immiscible Fe–Ti–P oxide melt is separated from it, recorded by the presence of the IOB coexisting with the silicate melt inclusions. The proportion of this Fe–Ti–P phase was negligible in La Berrona but probably much more abundant in other places such as in La Valera, where it formed massive orebodies of magnetite.

Stage C. During its crystallization, the rock attained one or more events of fluid saturation due to secondary boiling, promoting fluid exsolution. Due to the nature of the melt, the albitite could only sequester small amounts of water in the forming silicates and most of the fluid separated as an immiscible Si- and Fe-rich CO₂-bearing aqueous fluid. The iron that was not incorporated into the IOB was fractionated into the fluid due to its incompatible nature in these rocks (with no Fe-bearing phases other than the IOB and the accessory magnetite). It is unlikely that the Fe was incorporated in the fluid via interaction with the Fe–Ti–P melts.

Stage D. Overpressure related to volume increase due to releasing of the magmatic-hydrothermal fluid (and perhaps undetected fluid phase separation) broke up the carapace forming the magmatic hydrothermal breccias and the magnetite stockwork. These rocks were affected by an albite-actinolite-magnetite hydrothermal alteration. In the lower zones of the system the dominant magnetite mineralization occurs, formed by replacement of the calc-silicate hornfels and the albitite. The magnetite is related to the circulation of the magmatic-hydrothermal

fluids and hosted by an alteration zone similar to that of the magmatic-hydrothermal breccias and stockwork, with albite-actinolite-magnetite. The precipitation of the magnetite is due to the reaction of the ore forming fluids with the carbonatic rocks, leading to an increase of the pH of the fluid and destabilization of the Fe-chloride complexes.

The La Berrona orebody lacks of significant contents of base metals. The fluid and melt inclusion data suggest that the melt and the hydrothermal fluids transported negligible Cu and Zn, inhibiting the formation of chalcopyrite and sphalerite. The ultimate cause of these low contents would be the absence of fractional crystallization during the formation of the albitite as the Cu-Zn content would be inherited directly from the source. Despite it transported appreciable Pb, the high Pb solubility at temperatures above 100-150°C inhibited the formation of galena and Pb was lost in the system. Another limiting factor for the precipitation of sulfides is the low amounts of reduced sulfur in the system (there are no evidences of H₂S in the albitite), the separated IOB has no sulfides, and the host rocks lack of significant amounts of H₂S.

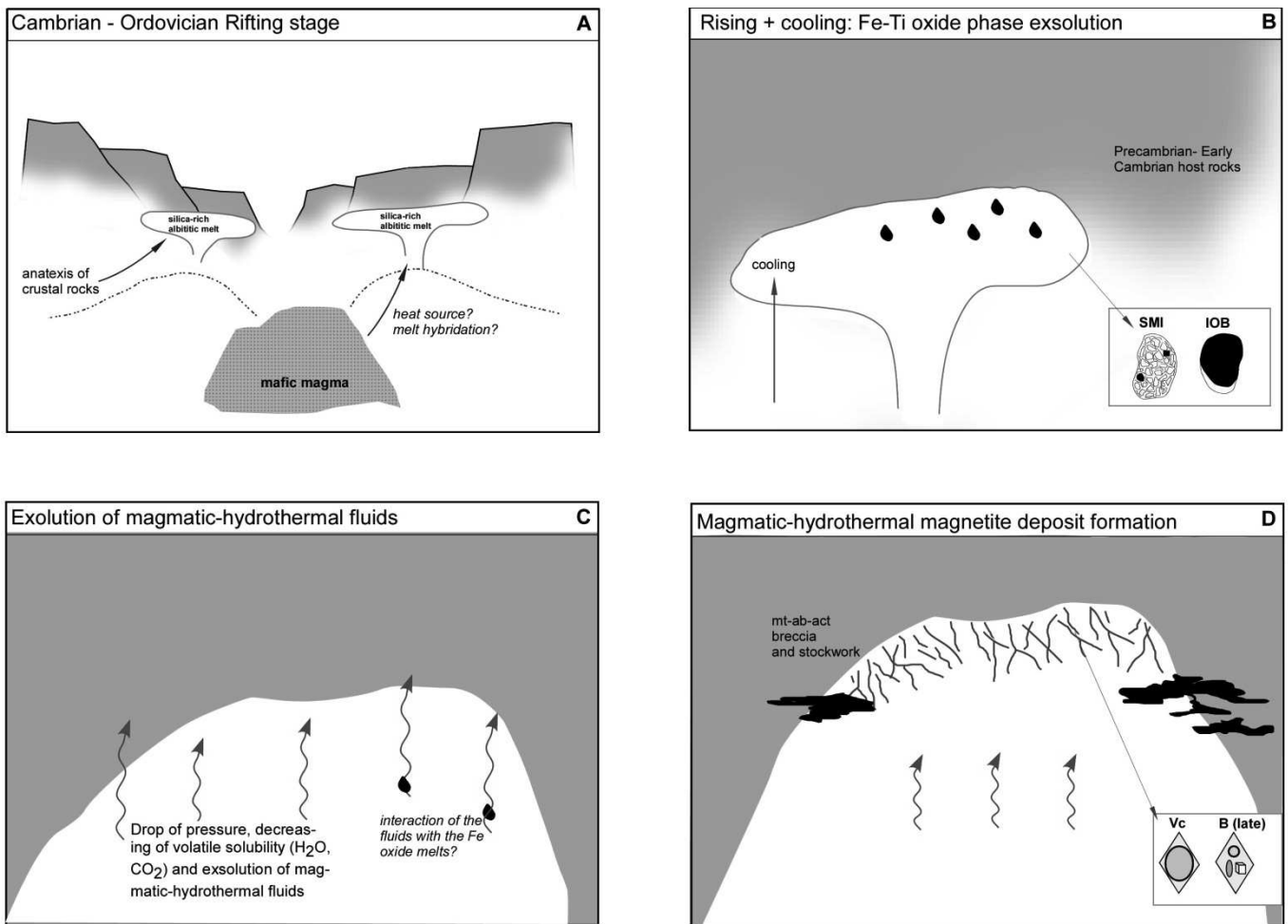


Figure 24. Proposed genetic model of the magmatic-hydrothermal system in the La Berrona Stock area from the formation of the albitite (A) by anatexis, through exsolution of a Fe oxide phase (B) to the exsolution of fluids (C) and formation of the magmatic hydrothermal magnetite deposit (D).

III.7. Conclusions

This first study of silicate melt inclusions observed in albitite has proved that this rock can be of magmatic origin despite it is commonly considered as of metasomatic origin. The LA-ICPMS analyses of the silicate melt inclusions show

similar chemical composition to that of the host bulk rock and the trace elements have the compatible/incompatible behavior expected in magmatic systems. The field, petrographic and radiogenic isotopic evidences support this magmatic origin for the albitite. If true, this model demonstrates that not all the albitite-rich rocks related to magnetite (IOCG) deposits are of metasomatic origin but that some of them can represent igneous melts.

A simple evolution model is proposed in which the Cambrian albitite rock is formed by partial melting of upper crustal rocks without a noticeable contribution of mafic melts. The high Na/K ratios are explained as due to the melting of pelitic rocks under water-saturated conditions and in the presence of fluorine and, perhaps, CO₂. These rocks are very similar to those reported by Carriedo (Ph.D. in prog.) occurring as a leucosome in the Las Mayorgas Fm. The observation of Fe-Ti-P-rich melt inclusions coexisting with silicate melt inclusions suggest the existence of an iron-titanium-phosphorous melt phase segregated from the silicate melt.

Fluid inclusions in phenocrysts and early veins close to the mineralization of La Berrona indicate Fe rich CO₂-bearing fluids that were formed at high temperatures. Fe behaved as incompatible element and fractionated to the fluid phase during the exsolution of the fluids. The low Ti and P content in the magnetite mineralization suggest that the fluids did not interact with the Fe-Ti-P rich oxide phase. Reaction of the magmatic fluids with the host calc-silicate and carbonatic rocks would produce a replacive ore with formation of an albitite-actinolite-magnetite rock with many features typical of the IOCG style of mineralization.

The major outcomes of this work are: (a) albitite related to magnetite mineralization can be a primary magmatic rock; (b) the study of melt inclusions is critical for the understanding of the genesis of these unusual rocks and is a key

technique for deciphering their true origin; (c) the albitite melts can exsolve a Fe-Ti-P oxide immiscible phase; and, (d) magmatic albitite can produce magnetite mineralization forming ore deposits sharing many of the features of the IOCG style and thus, it can be an important point for our understanding of this conflictive style of mineralization.

Chapter IV: Final Conclusions

The selection of the intrusion-related Sultana Cu-Au vein deposit, the La Berrona albitite and related magnetite mineralization as subject of this thesis is product of an extensive evaluation of the fluid and melt inclusion potential among several iron-copper-gold ore deposits located in the Olivenza-Monesterio Belt in the SW Spain.

The study involved detailed petrography, including SEM-CL, and geochemistry of fluid and melt inclusions. Both fluid and melt inclusions were analyzed by LA-ICPMS that seems to be the most powerful microanalytical technique available for this kind of analyses. Two major unsolved questions were approached: (1) the origin and temporal and spatial evolution of fluids in the high grade-low tonnage Cu-Au Sultana deposit and, (2) the origin of the albitite and its relationship with the associated IOCG-like magnetite deposits in the La Berrona area.

Magmatic fluids had a critical role in the fluid evolution forming the intrusion-related Sultana Cu-Au vein deposit, and carried copper and possibly gold to the depositional site at temperatures above 450 °C. The ore precipitation mechanism appears to be related to phase separation into brine and a vapor phase combined with decreasing temperature and space opening in the vein due to the dissolution of the quartz. In fact, Cu concentration drops from 700 µg/g to less than 0.1 µg/g in the late fluid inclusions without a proportional decrease in the rest of the analyzed elements. Gold was later deposited in fractures of chalcopyrite, probably due to the excess of sulfur in the vapor phase that transport gold after the Cu had precipitation. The role of metamorphic fluids in the ore formation remains enigmatic, but they could have interacted with the magmatic fluids at some stage in the evolution of the fluids.

Melt inclusions found in the quartz phenocrystals of the La Berrona albitite stock clearly demonstrate the magmatic origin for the rock. The results of LA-ICPMS analyses show an albititic composition with SiO₂ (73.2±1.9 wt%), Na₂O (6.8±1.1 wt%), K₂O (0.1±0.1 wt%) and CaO (0.6±0.4 wt%) as major elements. In agreement with the compatible/incompatible behavior of trace elements in magmatic systems, the elements Ba, Sr, V, Zr, Ni and P are compatible with the bulk-mineralogy of the albitite whereas incompatible elements Cu, Pb, Zn, As and Mo remain in the residual melt represented by the silicate melt inclusions in the albitite rock. Comparison with experimental studies and isotopic data suggest partial melting of crustal rocks as plausible mechanism to form this albititic melt under H₂O-rich conditions and possible presence of fluorine that deviate the eutectic of the haplogranite system to the albite component. Quartz phenocrystals show some sporadic opaque melt inclusion of Fe-Ti-P rich composition suggesting the existence of an iron-titanium-phosphorous oxide melt phase segregated from the silicate melt.

The La Berrona magnetite mineralization is of hydrothermal origin with development of breccia, a stockwork system and magnetite-albite-actinolite replacement of the host carbonate and the albitite rock. Analyzed fluid inclusions from quartz phenocrystals and early quartz veins show high temperature fluids (Thom ~350 °C) and high content in Fe, and could therefore be interpreted as ore-forming fluids. The magnetite is low in Ti and P, suggesting that the fluids did not interact with the immiscible iron-oxide phase rich in these elements.

The most important contribution of this thesis to the scientific community is the discovery and first detailed characterization of silicate melt inclusions in albitite rocks related to magnetite deposits. This finding sets the basis for a new research line that links the pure petrology of silica-albite-rich rocks and ore deposit studies involving potentially economic magnetite (±Cu±Au) mineralization.

Capítulo IV: Conclusiones Finales

La elección de los depósitos minerales de Cu-Au de Sultana, y de magnetita de La Berrona, así como de la roca albítica asociada a este último como tema principal de esta tesis es producto de una extensa evaluación del potencial de las inclusiones fluidas y vítreas en algunos depósitos de hierro-cobre-oro situados a lo largo del Cinturón de Olivenza-Monesterio, en el SO de España.

Este estudio se basa en una petrografía detallada de inclusiones fluidas y vítreas combinada con imágenes de catodoluminiscencia y análisis geoquímicos. Tanto las inclusiones fluidas como las vítreas han sido analizadas mediante ablación láser (LA-ICPMS) que es actualmente la técnica microanalítica más apropiada para este tipo de análisis. Dos cuestiones importantes han sido tratadas a lo largo de esta tesis: (1) el origen y evolución espacial y temporal de los fluidos hidrotermales en el depósito de alta ley-bajo tonelaje de Cu-Au de Sultana y, (2) el origen de roca albítica (albitita) y su relación con los depósitos de magnetita en el área de La Berrona.

Los fluidos de origen magmático representan un papel fundamental en la evolución de los fluidos hidrotermales que dieron lugar al filón de Cu-Au de Sultana ya que son los responsables de transportar el cobre y posiblemente el oro al lugar de precipitación a temperaturas por encima de los 450 °C. La precipitación de los metales se debe principalmente a una separación de este fluido magmático en una fase minoritaria salina y otra fase mayoritaria de vapor, junto con un descenso de temperatura y apertura de espacio debido a la solubilidad retrógrada del cuarzo. Consecuentemente, el contenido en Cu desciende de 700 µg/g en las inclusiones pseudosecundarias previas a la precipitación del Cu a menos de 0.1 µg/g en las inclusiones secundarias posteriores a la mineralización, sin observarse un descenso proporcional en el resto de elementos analizados. El oro fue depositado después en las fracturas que cortan la calcopirita, probablemente

debido a un exceso de azufre en la fase vapor que transportó el oro tras el depósito del Cu. La existencia y el papel de los fluidos metamórficos en la formación de la mineralización queda sin resolver, pero es probable que éstos existieran e interaccionaran con los fluidos magmáticos en algún estadio de la evolución de los fluidos.

Las inclusiones vítreas halladas en los fenocristales de cuarzo de la albitita de La Berrona demuestran claramente el origen magmático de esta roca. Los resultados de los análisis de LA-ICPMS muestran una composición albítica de SiO₂ (73.2±1.9 wt%), Na₂O (6.8±1.1 wt%), K₂O (0.1±0.1 wt%) y CaO (0.6±0.4 wt%) como elementos mayores. En concordancia con el comportamiento de los elementos traza en los sistemas hidrotermales, elementos como el Ba, Sr, V, Zr, Ni y P son compatibles con la mineralogía de la albitita, mientras que los elementos incompatibles como Cu, Pb, Zn, As y Mo entre otros permanecen en la fase fundida representada por las inclusiones vítreas silicatadas. La comparación con composiciones obtenidas en estudios experimentales así como los resultados de los isótopos radiogénicos sugieren que la roca se formó por fusión de la corteza, probablemente bajo condiciones ricas en agua y en presencia de F, los cuales desviaron el eutéctico del sistema hacia la componente albítica. Los fenocristales de cuarzo albergan también glóbulos de composición rica en óxidos de Fe-Ti-P (IOB, iron oxide blebs) que sugieren la existencia de una fase fundida de esta composición que fue segregada del fundido silicatado.

La mineralización de La Berrona es de origen hidrotermal con desarrollo de brechas y stockwork en la parte alta de la albitita y remplazamiento de magnetita-albita-actinolita de las rocas calizas encajantes y de la propia albitita. Las inclusiones fluidas analizadas en los fenocristales de cuarzo de la albitita así como en venas tempranas indican la existencia de fluidos de alta temperatura (Thom ~ 350 °C) y altos contenidos en Fe por lo que se pueden interpretar como formadores de la mineralización. La magnetita de la mineralización presenta bajo contenido en

Ti y P, por lo que posiblemente, estos fluidos no interaccionaron con la fase de óxidos de hierro segregada, rica en estos elementos.

La contribución más importante de esta tesis a la comunidad científica es quizás el hallazgo y estudio de inclusiones vítreas silicatadas en rocas albíticas asociadas a depósitos de magnetita. Este hallazgo sienta las bases para abrir una nueva línea de investigación que aúna la petrología de rocas ígneas ricas en sílice y albita y los estudios relacionados con yacimientos minerales de magnetita ($\pm\text{Cu}$ - $\pm\text{Au}$).

References

- Ábalos, B., Gil Ibarra, J. I., and Eguiluz, L., 1991, Cadomian subduction/collision and Variscan transpression in the Badajoz Cordoba shear belt, southwest Spain: *Tectonophysics*, v. 199, p. 51-72.
- Ábalos, B., and Díaz Cusí, J., 1995, Correlation between seismic anisotropy and major geological structures in SW Iberia: a case study on continental lithosphere deformation: *Tectonics*, v. 14, p. 1021-1040.
- Adshead, N. D., 1995, Geology, alteration and geochemistry of the Osborne Cu - Au deposit, Cloncurry district, NW Queensland, James Cook University, 382 p.
- Albarede, F., and Bottinga, Y., 1972, Kinetic disequilibrium in trace element partitioning between phenocrysts and host lava: *Geochemica et Cosmochemica Acta*, v. 36, p. 141-156.
- Aldiss, D. T., 1981, Plagiogranites from the ocean crust and ophiolites: *Nature*, v. 289, p. 577-578.
- Almarza, J., 1996, Petrología y geoquímica de los yacimientos de uranio del sureste de Badajoz, Universidad de Sevilla, 349 p.
- Anderson, A. T. J., 2003, Melt (glass ± crystals) inclusions, in Samson, I., Anderson, A., and Marshall, D., eds., *Fluid inclusions: Analysis and Interpretation*, 32: Ottawa, Mineralogical Association of Canada, p. 300.
- Apalategui, O., Contreras, F., Eguiluz, L., and Quesada, C., 1986-1987, Mapa geológico de España 1/50000, núm. 918 Santa Olalla de Cala in IGME, ed., Serie Magna.
- Apalategui, O., Barranco, E., Contreras, F., Delgado, M., and Roldan, F. J., 1990, Mapa Geológico Nacional de España. 1/50000, núm 916: Aroche. In IGME, ed., Serie Magna.
- Apraiz, A., Eguiluz, L., and Ábalos, B., 1993, Evolución metamórfica y anatexia en el núcleo de Lora del Río (Zona de Ossa Morena): *Revista de la Sociedad Geológica de España*, v. 6, p. 85-103.
- Apraiz, A., and Eguiluz, L., 1996, El núcleo metamórfico de Valuengo (Zona de Ossa Morena, Macizo Ibérico): petrografía, termobarometría y evolución geodinámica: *Revista de la Asociación Geológica de España*, v. 9, p. 29-49.
- Apraiz, A., 1998, Geología de los macizos de Lora del Río y Valuengo (Zona de Ossa Morena). Evolución tectonometamórfica y significado geodinámico, Universidad del País Vasco, 575 p.
- Apraiz, A., and Eguiluz, L., 2002, Hercinian tectono-thermal evolution associated with crustal extension and exhumation of the Lora del Río metamorphic core complex (Ossa Morena Zone, Iberian Massif, SW Spain): *International Journal Earth Sciences*, v. 91, p. 76-92.
- Arth, J. C., 1979, Trondhjemites, dacites, and related rocks, in Barker, F., ed., 123-162.

- Audétat, A., Günter, D., and Heinrich, C. A., 1998, Formation of a magmatic-hydrothermal ore deposit: Insights with LA-ICP-MS analysis of fluid inclusions: *Science*, v. 297, p. 2091-2094.
- Audétat, A., and Günter, D., 1999, Mobility and H₂O-loss from fluid inclusions in natural quartz crystals: *Contributions to Mineralogy and Petrology*, v. 137, p. 1-14.
- Audétat, A., and Günther, D., 1999, Mobility and H₂O loss from fluid inclusions in natural quartz crystals: *Contributions to Mineralogy and Petrology*, v. 137, p. 1-14.
- Audétat, A., Günter, D., and Heinrich, C. A., 2000, Magmatic-hydrothermal evolution in a fractionating granite: A microchemical study of the Sn-W-F mineralized Mole Granite (Australia): *Geochemica et Cosmochemica Acta*, v. 64, p. 3373-3393.
- Audétat, A., Pettke, T., Candela, P. A., Piccoli, P. M., and Heinrich, C. A., 2003, The magmatic-hydrothermal evolution of two barren granites: A melt and fluid inclusion study of the Rito del Medio and Canada Pinabete plutons in Northern New Mexico : *Geochemica et Cosmochemica Acta*, v. 67, p. 97-122.
- Audétat, A., 2008, The composition of magmatic-hydrothermal fluids in barren and mineralized intrusions: *Economic Geology*, v. 103, p. 877-908.
- Azer, M. K., Stern, R. J., and Kimura, J., 2010, Origin of a Late Neoproterozoic (605±13 Ma) intrusive carbonate-albitite complex in Southern Sinai, Egypt: *International Journal Earth Sciences*, v. 99, p. 245-267.
- Azor, A., González Lodeiro, F., and Simancas, J. F., 1993, Cadomian subduction/collision and Variscan transpression in the Badajoz-Córdoba shear belt, southwest Spain: a discussion on the age of the main tectonometamorphic events: *Tectonophysics*, v. 217, p. 342-346.
- Azor, A., González Lodeiro, F., and Simancas, J. F., 1994, Tectonic evolution of the boundary between the Central Iberian and Ossa Morena Zones (Variscan belt, southwest Spain): *Tectonics*, v. 13, p. 45-61.
- Azor, A., Expósito, I., González Lodeiro, F., Simancas, F., and Martínez Poyatos, D., 2004, Deformación y metamorfismo prevariscos: Los núcleos metamórficos de baja presión de Valuengo y Monesterio, *in* Vera, J. A., ed., *Geología de España: Madrid, Instituto Geológico y Minero de España*, p. 173-177.
- Azor, A., Expósito, I., González Lodeiro, F., Simancas, F., and Martínez Poyatos, D., 2004, Formaciones precámbricas (Zona de Ossa Morena), *in* Vera, J. A., ed., *Geología de España: Madrid, Instituto Geológico y Minero de España*, p. 166.
- Azor, A., Expósito, I., González Lodeiro, F., Simancas, F., and Martínez Poyatos, D., 2004, Propuesta de un modelo evolutivo para la Zona de Ossa Morena, *in* Vera, J. A., ed., *Geología de España: Madrid, Instituto Geológico y Minero de España*, p. 188-189.
- Bachiller, N., Quílez, E., Casquet, C., and Galindo, C., 1996, Albititas metasomáticas y venas de cuarzo en los leucogranitos de Burguilos del Cerro

- (España). Modelo de evolución hidrotermal basado en el estudio de inclusiones fluidas: *Geogaceta*, v. 20, p. 1504-1506.
- Bachiller, N., 1997, Geocronología Rb-Sr de los leucogranitos del complejo plutónico de Burguillos del Cerro (Badajoz): *Geogaceta*, v. 21, p. 29-30.
- Baker, T., 1996, The geology and genesis of the Eloise Cu-Au deposit, Cloncurry district, NW Queensland, Australia, James Cook University of North Queensland, 303 p.
- Baker, T., and Lang, J. R., 2001, Fluid inclusions characteristics of intrusion-related gold mineralization, Tombstone-Tungsten magmatic belt, Yukon Territory, Canada: *Mineralium Deposita*, v. 36.
- Bakker, R. J., 1999, Adaptation of the Bowers and Helgeson (1983) equation of state to the H₂O-CO₂-CH₄-N₂-NaCl system: *Chemical Geology*, v. 154, p. 225-236.
- Bakker, R. J., 2003, Package FLUIDS 1. Computer programs for analysis of fluid inclusion data and for modelling bulk fluid properties: *Chemical Geology*, v. 194, p. 3-23.
- Bandrés, A., Eguiluz, L., Gil Ibarguchi, J. I., and Palacios, T., 2002, Geodynamic evolution of a Cadomian arc region: the northern Ossa Morena Zone, Iberian Massif: *Tectonophysics*, v. 352, p. 105-120.
- Bandrés, A., Eguiluz, L., Pin, C., Paquette, J. L., Ordoñez, B., Le Fèvre, J., Ortega, L. A., and Gil Ibarguchi, J. I., 2004, The northern Ossa Morena Cadomian batholith (Iberian Massif): magmatic arc origin and early evolution: *International Journal Earth Sciences*, v. 93, p. 860-885.
- Barker, F., Arth, J. C., Peterman, Z. E., and Friedman, I., 1976, The 1.7 to 1.8 b.y. old trondhjemites of Southwestern Colorado and Northern New Mexico: Geochemistry and depths of genesis: *Bull. Geol. Soc. Am.*, v. 87, p. 189-198.
- Barker, F., 1979, Trondhjemite: Definition, environment and hypothesis of origin, *in* Barker, F., ed., *Trondhjemites, dacites and related rocks*, Elsevier, p. 1-12.
- Barton, M. D., and Johnson, D. A., 2000, Alternative brine sources for Fe oxide (-Cu-Au) systems: Implications for hydrothermal alteration and metals, *in* Porter, T. M., ed., *Hydrothermal iron oxide copper-gold and related deposits: a global perspective*: Adelaide, AMF, p. 43-60.
- Barton, M. D., and Johnson, D. A., 2004, Footprints of Fe-oxide (-Cu-Au) systems: SEG 2004, 2004, p. 112-116.
- Barton, M. D. a. J., D.A., 1996, Evaporitic-source model for igneous-related Fe oxide- (REE-Cu-Au-U) mineralization: *Geology*, v. 24, p. 259-262.
- Bellido, F., Díez-Montes, A., and Sánchez, T., 2010, Caracterización geoquímica y estudio comparativo de plagiogranitos de las Zonas Surportuguesa y Ossa-Morena (SO del Macizo Ibérico, España): *Estudios Geológicos*, v. 66.
- Beus, A. A., 1966, Geochemical analysis of the phenomena of high-temperature post-magmatic metasomatism and ore-formation in granitoids, *in* Vinogradov, A. P., ed., *Chemistry of the Earth's Crust, 1: Jerusalem, Israel Program for Scientific Translations*.

- Biddau, R., Cidu, R., and Frau, F., 2002, Rare earth elements in waters from the albitite-bearing granodiorites of Central Sardinia, Italy: *Chemical Geology*, v. 182, p. 1-14.
- Blatrix, P., and Burg, J. P., 1981, $^{40}\text{Ar}/^{39}\text{Ar}$ dates from Sierra Morena (Southern Spain): Variscan metamorphism and Cadomian orogeny: *Neues Jb. Mineral. Mh.*, p. 470-478.
- Boctor, N. Z., Poop, R. K., and Frantz, J. D., 1980, Mineral-solution equilibria-IV. Solubilities and the thermodynamic properties of Fe_2O_3 in the system $\text{Fe}_2\text{O}_3\text{-H}_2\text{-H}_2\text{O-HCl}$: *Geochemica et Cosmochemica Acta*, v. 44, p. 1509-1518.
- Bodnar, J. R., and Vityk, M. O., 1994, Interpretation of microthermometric data for $\text{H}_2\text{O-NaCl}$ fluid inclusions, *in* De Vivo, B., and Frezzoti, M. L., eds., *Fluid inclusions in minerals*, p. 117-130.
- Bodnar, R. J., 1995, Fluid inclusion evidence for a magmatic source of metals in porphyry copper deposits, *in* Thompson, J. H. F., ed., *Magmas, Fluids and Ore Deposits*, 23, Mineralogical Association of Canada, Short Course Series, p. 139-152.
- Boguslavskiy, I. S., Kalenov, A. D., and Egel, L. Y., 1966, Metasomatic albitite found for the first time in the MPR.: *Doklady Akad*, v. 168, p. 159-162.
- Boulvais, P., Ruffet, G., Cornichet, J., and Mermet, M., 2007, Cretaceous albitization and dequartzification of Hercynian peraluminous granite in the Salvezines Massif (French Pyrenees): *Lithos*, v. 93, p. 89-106.
- Bowers, T. S., and Helgeson, H. S., 1985, Calculation of the thermodynamic and geochemical consequences of nonideal mixing in the system $\text{H}_2\text{O-CO}_2\text{-NaCl}$ on phase relations in geological system: equation of state for $\text{H}_2\text{O-CO}_2\text{-NaCl}$ fluids at high pressures and temperatures: *Geochemica et Cosmochemica Acta*, v. 47, p. 1247-1275.
- Brown, P. E., and Hagemann, S. G., 1994, MacFlinCor: A computer program for fluid inclusion data reduction and manipulation, *in* de Vivo, B., and Frezzoti, M. L., eds., *Fluid inclusion in minerals: Methods and Applications*.
- Brun, J. P., and Burg, J. P., 1982, Combined thrusting and wrenching in the Ibero-Armorican arc: a corner effect during continental collision: *Earth Planetary Science Letters*, v. 61, p. 319-332.
- Burke, E. A. J., 2001, Raman microspectrometry of fluid inclusions: *Lithos*, v. 55, p. 139-158.
- Burnham, C. W., 1979, Magmas and Hydrothermal fluids, *in* Barnes, H.L., eds., *Geochemistry of hydrothermal Ore Deposits*, Wiley 71-36, New York.
- Burnham, C. W., and Nekvasil, H., 1986, Equilibrium properties of granite pegmatite magmas: *American Mineralogist*, v. 71, p. 239-263.
- Burnham, C. W., Ohmoto, H., 1980, Late-stage processes of felsic magmatism: *Mining geology special issue*, v. 8, p. 1-11.
- Burrows, D. R., and Spooner, E., 1989, Relationships between Archaean lode gold quartz vein deposits and igneous intrusions in the Timmins and Val d'Or areas, Abitibi Subprovince, Canada.: *Economic Geology Monograph*, v. 6, p. 424-444.

- Caballero, J. M., 1993, Las episienitas de la Sierra de Guadarrama: un caso singular de alteración hidrotermal de edad posthercínica, Universidad Complutense de Madrid, 313 p.
- Caballero, J. M., 1999, Modelización del proceso de episienitización (de cuarzificación-albitización): formulación cinética y transporte advectivo en medio continuo: *Estudios Geológicos*, v. 55, p. 9-26.
- Capdevila, R., Matte, P., and Paredes, J., 1971, La nature du Précambrien et ses relations avec le Paléozoïque dans la Sierra Morena Centrale (Sud de l'Espagne): *Comptes Rendues Academie des Sciences Paris*, v. D273, p. 1359-1362.
- Carbonell, R., Simancas, F., Juhlin, C., Pous, J. P., Perez Estaun, A., Gonzalez-Lodeiro, F., Muñoz, G., Heise, W., and Ayarza, P., 2004, Geophysical evidence of a mantle derived intrusion in SW Iberia: *Geophys. Res. Lett.*, v. 31.
- Carcangiu, G., Palomba, M., and Tamanini, M., 1997, REE-bearing minerals in the albitites of central Sardinia, Italy: *Mineralogical Magazine*, v. 61, p. 271-23.
- Carriedo, J., Tornos, F., Velasco, F., and Terrón, A., 2006, Mineralizaciones de magnetita asociadas a skarns y bandas de cizalla: La mina de Cala (Huelva): *Gogaceta*, v. 40, p. 235-238.
- Carriedo, J., and Tornos, F., 2009, Diversos orígenes para los depósitos de tipo magnetita- (Cu-Au) en la Zona de Ossa Morena: *Macla*, v. 11, p. 51-52.
- Carriedo, J., and Tornos, F., 2010, The Iron Oxide Copper-Gold Belt of the Ossa Morena Zone, Southwest Iberia: Implications for IOCG Genetic Models, *in* Porter, T. M., ed., *Hydrothermal Iron Oxide Copper-Gold & Related Deposits: A Global Perspective*, 3: Adelaide, PGC Publishing, p. 441-460.
- Carriedo, J., Tornos, F., and Tomé, C., 2010, Coexistence of different styles of the IOCG-like deposits in SW Iberia: *Proceedings of the 10th Biennial SGA Meeting Townsville, Australia*
- Carvalhosa, A., 1965, Contribuição para o conhecimento geológico da região entre Portel e Ficalho (Alentejo): *Memória dos Serviços Geológicos de Portugal*, v. 11, p. 130.
- Casquet, C., and Velasco, F., 1978, Contribución a la geología de los skarns cálcicos en torno a Santa Olalla de Cala (Huelva-Badajoz): *Estudios Geológicos*, v. 34, p. 399-405.
- Casquet, C., 1980, Fenómenos de endomorfismo, metamorfismo y metasomatismo en los mármoles de Rivera de Cala (Sierra Morena). Universidad Complutense de Madrid, p. 295.
- Casquet, C., and Tornos, F., 1991, Influence of depth and igneous geochemistry on ore development in skarns: The Hercinian Belt of the Iberian Peninsula Skarns, their petrology and metallogeny, *Augustithis*, Athens, 1991, p. 555-591.
- Casquet, C., Eguiluz, L., Galindo, C., Tornos, F., and Velasco, F., 1998, The Aguablanca Cu-Ni (PGE) intraplutonic ore deposit (Extremadura, Spain). Isotope (Sr, Nd, S) constraints on the source and evolution of magmas and sulphides: *Geogaceta*, v. 24, p. 71-74.

- Casquet, C., Galindo, C., Tornos, F., Velasco, F., and Canales, A., 2001, The Aguablanca Cu-Ni ore deposit (Extremadura, Spain), a case of synorogenic orthomagmatic mineralization: age and isotope composition of magmas (Sr, Nd) and ore(s): *Ore Geology Reviews*, v. 18, p. 237-250.
- Casquet, C., 2004, *Journal of Iberian Geology*, Special Issue: The Ossa Morena Zone (Iberian Massif): Geological findings at the turn of the 21st Century, 30: Madrid, Universidad Complutense.
- Castorina et al., F., Masi, U., Padalino, G., and Palomba, M., 2006, Constraints from geochemistry and Sr-Nd isotopes for the origin of albitite deposits from Central Sardinia (Italy): *Miner. Deposita*, v. 41, p. 323-338.
- Cathelineau, M., 1983, Potassic alteration in french hydrothermal U deposits: *Mineralium Deposita*, v. 18, p. 89-97.
- Cathelineau, M., 1987, U-Th-REE mobility during albitization and quartz dissolution in granitoids: evidence from southeast French Massif Central: *Bull Min*, v. 110, p. 249-259.
- Cathelineau, M., 1988, Accessory mineral alteration in peraluminous granites at the hydrothermal stage: a review: *Rend Soc Ital Mineral Petrol*, v. 43, p. 499-508.
- Clark, A. H., and Kontak, D. J., 2004, Fe-Ti-P Oxide melts generated through magma mixing in the Antauta Subvolcanic Center, Peru: implications for the origin of nelsonite and iron Oxide-dominated hydrothermal deposits: *Economic Geology*, v. 99, p. 377-395.
- Coleman, R. G., and Peterman, Z. E., 1975, Oceanic plagiogranite: *J. geophys. Res.*, v. 80, p. 1099-1108.
- Conrad, W. K., Nichols, I. A., and Wall, V. J., 1988, Water-saturated and undersaturated melting of metaluminous and peraluminous crustal compositions at 10 kb: evidence for the origin of silicic magmas in the Taupo Volcanic Zone, New Zealand, and other occurrences: *Journal of Petrology*, v. 29, p. 765- 803.
- Cook, N. D. J., and Ashley, P. M., 1992, Meta-evaporite sequence, exhalative chemical sediments and associated rocks in the Proterozoic Willyama Supergroup, South Australia: Implications for metallogenesis: *Precambrian Research*, v. 56, p. 211-226.
- Corriveau, L., 2007, Iron oxide copper-gold deposits: a Canadian perspective, *in* Goodfellow, W. D., ed., *Mineral deposits of Canada: a synthesis of major deposit-types, district metallogeny, the evolution of geological provinces, and exploration methods*, Special Publication no. 5: St. John's, NL, Canada, Geological Association of Canada, Mineral Deposits Division, p. 307-328.
- Coullaut, J. L., 1979, *Geología y metalogenia del criadero de San Guillermo Colmenar*, Jerez de los Caballeros, Badajoz: Curso Rosso de Luna, IGME, p. 1-20.
- Coullaut, J. L., Babiano, F., and Fernández, J., 1980, Mineralizaciones de hierro del Suroeste de España. Mina La Valera. : *Jornadas Sidero Metalúrgicas*, Huelva, 1980, p. 97-108.

- Coullaut, J. L., Fernández Carrasco, J., and Aguilar Tomás, M. J., 1981, Mapa y memoria explicativa de la Hoja 1:50000, N° 875 (Jerez de los Caballeros) del Mapa Geológico Nacional (MAGNA): Madrid, Instituto Geológico y Minero de España.
- Crawford, M. L., and Hollister, L. S., 1978, Metamorphic fluids: The evidence from fluid inclusions, *in* Walther, J. V., and Wood, B. J., eds., Fluid rock interaction during metamorphism, 5: New York, Springer-Verlag.
- Crespo Blanc, A., 1989, Evolución geotectónica del contacto entre la Zona de Ossa Morena y la Zona Sudportuguesa en las Sierras de Aracena y Aroche (Macizo Ibérico Meridional): un contacto mayor en la cadena hercínica europea, Universidad de Sevilla, 327 p.
- Cuervo, S., Tornos, F., Spiro, B., and Casquet, C., 1996, El origen de los fluidos hidrotermales en el Skarn férrico de Colmenar-Santa Bárbara (Zona de Ossa Morena): *Geogaceta*, v.20(7), p.1499-1500.
- Charoy, B., and Pollard, P. J., 1989, Albite-rich, silica-depleted metasomatic rocks at Emuford, Northeast Queensland; mineralogical, geochemical, and fluid inclusion constraints on hydrothermal evolution and tin mineralization: *Economic Geology*, v. 84, p. 1850-1874.
- Chaudhri, N., Kaur, P., Okrusch, M., and Schimrosczyk, A., 2003, Characterisation of the Dabla Granitoids, North Khetri Copper Belt, Rajasthan, India: Evidence of Bimodal Anorogenic Felsic Magmatism: *Gondwana Research*, v. 6, p. 879-895.
- Chauris, L., 1985, Premières données géochimiques sur les albitites metasomatiques des environs de Brest (Finistère, France): *Bull Soc Géol Fr*, v. 8, p. 885-889.
- Cheilletz, A., and Giuliani, G., 1982, Rôle de la déformation du granite dans la genèse des episyenites feldspathiques des massifs de Lovios-Geres (Galice) et des Zaer (Maroc Central): *Miner. Deposita*, v. 17, p. 387-400.
- Chen, H., Clark, A. H., and Kyser, T. K., 2010, The Marcona Magnetite Deposit, Ica, South-Central Peru: A Product of Hydrous, Iron Oxide-Rich Melts?: *Economic Geology*, v. 105, p. 1441-1456.
- Chou, I. C., and Eugster, H. P., 1977, Solubility of magnetite in supercritical chloride solutions: *American Journal of Science*, v. 277, p. 1296-1314.
- Dallmeyer, R. D., and Martínez García, E., 1990, Pre-Mesozoic Geology of Iberia: Berlin-Heidelberg-New York- Tokyo, Springer Verlag, p. 416.
- Dallmeyer, R. D., and Quesada, C., 1992, Cadomian vs. Variscan evolution of the Ossa-Morena zone (SW Iberia): field and $^{40}\text{Ar}/^{39}\text{Ar}$ mineral age constraints: *Tectonophysics*, v. 216, p. 339-364.
- Dallmeyer, R. D., Franke, W., and Weber, K., 1995, Pre-Permian geology of central and eastern Europe: Berlin, Springer-Verlag, 604 p.
- Danyushevsky, L. V., McNeil, A. W., and Sobolev, A. V., 2002, Experimental and petrological studies of melt inclusions in phenocrysts from mantle-derived

- magmas: an overview of techniques, advantages and complications: *Chemical Geology*, v. 183, p. 5-24.
- Davidson, P., 2004, A new methodology for the study of the magmatic-hydrothermal transition in felsic magmas: applications to barren and mineralised systems, University of Tasmania, 336 p.
- De Jong, G., and Williams, P. J., 1995, Giant metasomatic system formed during exhumation of mid crustal Proterozoic rocks in the vicinity of the Cloncurry fault, NW Queensland: *Australian Journal of Earth Sciences*, v. 42, p. 281-290.
- Diamond, L. W., 1990, Fluid inclusion evidence for P-V-T-X evolution of hydrothermal solutions in late-Alpine gold-quartz veins at Brusson, Val d'Ayas, northwest Italian Alps: *American Journal of Science*, v. 290, p. 912-958.
- Diamond, L. W., 1992, Stability of CO₂ clathrate hydrate + CO₂ liquid + CO₂ vapour + aqueous KCl-NaCl solutions: experimental determination and application to salinity estimates of fluid inclusions: *Geochemica et Cosmochemica Acta*, v. 56, p. 273.
- Diamond, L. W., 1994, Salinity of multivolatile fluid inclusions determined from clathrate hydrate stability: *Geochemica et Cosmochemica Acta*, v. 58, p. 19-41.
- Doetsch, J., 1967, La investigación de Magnetitas y los sondeos comprobatorios en el Suroeste de España: *Notas y comunicaciones del IGME*, v. 97, p. 41-106.
- Doetsch, J., 1973, Estado actual de la Investigación de Criaderos del Suroeste de España: *Boletín Geológico y Minero*, v. 84, p. 103-124.
- Domergue, C., 1987, Catalogue des mines et des fonderies antiques de la Péninsule Ibérique: *Publicaciones de la Casa de Velázquez, Serie Archéologie*, v. VIII.
- Driesner, T., and Heinrich, C. A., 2007, The system H₂O-NaCl. Part I: Correlation formulae for phase relations in temperature-pressure-composition space from 0 to 1000 °C, 0 to 5000 bar, and 0 to 1 X_{NaCl}: *Geochimica et Cosmochimica Acta*, v. 71, p. 4880-4901.
- Driesner, T., 2007, The system H₂O-NaCl. Part II: Correlations for molar volume, enthalpy, and isobaric heat capacity from 0 to 1000°C, 1 to 5000 bar, and 0 to 1 X_{NaCl}: *Geochimica et Cosmochimica Acta*, v. 71, p. 4902-4919.
- Drummond, M. S., Ragland, P. C., and Wesolowski, D., 1986, An example of trondhjemite genesis by means of alkali metasomatism: Rockford Granite, Alabama Appalachians: *Contributions to Mineralogy and Petrology*, v. 93, p. 98-113.
- Dupont, R., 1979, Cadre géologique et métallogénese des gisements de fer du sud de la province de Badajoz (Sierra Morena Occidentale-Espagne), *Institut Nationale Polytechnique de Lorraine*, 371 p.
- Dymek, R. F., and Owens, B. E., 2001, Petrogenesis of Apatite-Rich Rocks (Nelsonites and Oxide-ApatiteGabbro-norites) Associated with Massif Anorthosites: *Economic Geology*, v. 96, p. 797-815.
- Eguiluz, L., 1988, Petrogénesis de rocas ígneas y metamórficas en el Anticlinorio Burguillos-Monesterio, Macizo Ibérico Meridional., *Universidad del País Vasco*.

- Eguiluz, L., 1989, Lineación de estiramiento, estructuras C-S y sentido de movimiento en el granito del Castillo (Zona de Ossa Morena, España): *Studia Geologica Salmanticensia*, v. 4, p. 205-215.
- Eguiluz, L., Gil Ibarguchi, J. I., Ábalos, B., and Apraiz, A., 2000, Superposed Hercynian and Cadomian orogenic cycles in the Ossa-Morena zone and related areas of the Iberian Massif: *Geological Society of America Bulletin*, v. 112, p. 1398-1412.
- Elthon, D., 1991, Geochemical evidence for formation of the Bay of Islands ophiolite above a subduction zone: *Nature*, v. 354, p. 140-143.
- Etxebarria, M., Chalot-Prat, F., Apraiz, A., and Eguiluz, L., 2006, Birth of a volcanic passive margin in Cambrian time: Rift paleogeography of the Ossa-Morena Zone, SW Spain: *Precambrian Research*, v. 147, p. 366-386.
- Expósito, I., 2000, Evolución estructural de la mitad septentrional de la Zona de Ossa Morena y su relación con el límite Zona de Ossa Morena/Zona CentrIObérica, Universidad de Granada, 295 p.
- Expósito, I., Simancas, J. F., González Lodeiro, F., Bea, F., Montero, P., and Salman, K., 2003, Metamorphic and deformational imprint of Cambrian-Lower Ordovician rifting in the Ossa-Morena Zone (Iberian Massif, Spain): *Journal of Structural Geology*, v. 25, p. 2077-2087.
- Fernández Carrasco, J., Coullaut Saez de Sicilia, J. L., Aguilar Tomás, M. J., and Quesada, C., 1981, Mapa geológico de España 1/50000, núm. 875 Jerez de los Caballeros *in* IGME, ed., Serie Magna.
- Fernández-Suárez, J., Gutiérrez Alonso, G., Jenner, G. A., and Tubrett, M. N., 2000, New ideas on the Proterozoic-Early Paleozoic evolution of NW Iberia: insights from U-Pb detrital zircon age: *Precambrian Research*, v. 102, p. 185-206.
- Floyd, P. A., Yaliniz, M. K., and Goncuoglu, M. C., 1998, Geochemistry and petrogenesis of intrusive and extrusive ophiolitic plagiogranites, Central Anatolian Crystalline Complex, Turkey: *Lithos*, v. 42, p. 225-241.
- Fournier, R. O., 1999, Hydrothermal processes related to movement of fluid from plastic into brittle rock in the magmatic-epithermal environment: *Economic Geology*, v. 94, p. 1193-1211.
- Frantz, J. D., Poop, R. K., and Boctor, N. Z., 1980, Solubility constants of rock-forming minerals: *Carnegie Institution of Washington Year Book*, v. 79, p. 340-345.
- Frezzoti, M. L., 1992, Magmatic immiscibility) and fluid phase evolution in the Mount Genis granite (southeastern Sardinia, Italy): *Geochemica et Cosmochemica Acta*, v. 56, p. 21-23.
- Fricke, W., 1941, Die Geologie des Grenzgebietes zwischen nordöstlicher Sierra Morena und Extremadura, University of Berlin, 91 p.
- Fyfe, W. S., and Henley, R. W., 1973, Some thoughts on chemical transport processes, with particular reference to gold: *Mineral Science & Engineering*, v. 5, p. 295-303.

- Fyon, J. A., Crocket, J. H., and Schwartz, M. O., 1983, Application of stable isotope studies to gold metallogeny in Timmins-Porcupine Camp: Ontario Geological Survey, Toronto, Ontario, Canada, Oplen-File Report, v. 5464, p. 182.
- Gabaldón, V., Garrote, A., and Quesada, C., 1985, El Carbonífero inferior del norte de la Zona de Ossa Morena: C.R.X. Congress. Internationale Stratigraphie et Geologie du Carbonifere, Madrid, 1985, p. 173-186.
- Galindo, C., and Casquet, C., 2004, El magmatismo pre-varisco de la Zona de Ossa Morena, *in* Vera, J. A., ed., Geología de España: Madrid, Instituto Geológico y Minero de España, p. 190-194.
- Ghiorso, M. S., Carmichael, I. S. E., and Moret, L. K., 1979, Inverted high-temperature quartz. Unit cell parameters and properties of the inversion: Contributions to Mineralogy and Petrology, v. 68, p. 307-323.
- Giese, U., and Bühn, B., 1993, Early Paleozoic rifting and bimodal volcanism in the Ossa-Morena Zone of southwest Spain: Geol. Rudxh., v. 83, p. 143-160.
- Glyuk, D.S., Trufanova, L.G., and Bazarova, S.B., 1980, Phase relations in the granite H₂O-LiF system at 1000 kg f/cm²; Geochemistry International, v.17, p. 35-48.
- Goldfarb, R. J., Ayuso, R., Miller, M. L., Ebert, S. W., Marsh, E. E., Petsel, S. A., Miller, L. D., Bradley, D., Johnson, C., and McClelland, W., 2004, The Late Cretaceous Donlin Creek Gold Deposit, Southwestern Alaska: Controls on Epizonal Ore Formation: Economic Geology, v. 99, p. 643-671.
- Goldstein, R. H., and Reynolds, T. J., 1994, Systematics of fluid inclusions in diagenetic minerals: Society for Sedimentary Geology Short Course 31, 199 p.
- González Aguado, M. T., and Gumiel, P., 1984, El yacimiento de Sn de del Trasquilón (Cáceres): una mineralización asociada a una cúpula granítica: Boletín Geológico y Minero, v. 95, p. 354-373.
- Götze, J., Plötze M., Habermann, D., 2001, Origin, spectral characteristics and practical applications of the cathodoluminescence (CL) of quartz - a review: Mineralogy and Petrology, v. 71, p. 225-250.
- Groves, D. I., Goldfarb, R. J., Robert, F., and Hart, C. J. R., 2003, Gold deposits in metamorphic belts: overview of current understanding, outstanding problems, future research, and exploration significance: Economic Geology, v. 98, p. 1-29.
- Guillong, M., Latkoczy, C., Seo, J. H., Günter, D., and Heinrich, C. A., 2008a, Determination of sulfur in fluid inclusions by laser ablation ICP-MS: Journal of Analytical Atomic Spectrometry, v. 23, p. 1581-1589.
- Guillong, M., Meier, D. L., Allan, M. M., Heinrich, C. A., and Yardley, B. W. D., 2008b, SILLS: a Matlab-based program for the data reduction of Laser Ablation ICP-MS data of homogeneous materials and inclusions., *in* Sylvester, P., ed., Laser Ablation ICP-MS in the Earth Sciences: Current Practices and Outstanding Issues, Mineralogical Association of Canada.
- Günther, D., Frischknecht, R., Heinrich, C. A., and Kahlert, H. J., 1997, Capabilities of an argon fluoride 193 nm excimer laser for laser ablation inductively coupled

- plasma mass spectrometry microanalysis of geological materials: *Journal of Analytical Atomic Spectrometry*, v. 12, p. 939-944.
- Günther, D., Audétat, A., Frischknecht, R., and Heinrich, C. A., 1998, Quantitative analysis of major, minor and trace elements in fluid inclusions using laser ablation inductively coupled plasma mass spectrometry: *Journal of Analytical Atomic Spectrometry*, v. 13, p. 263-270.
- Gustafson, L. B., and Hunt, J. P., 1975, The porphyry copper deposit at El Salvador, Chile: *Economic Geology*, v. 70, p. 857-912.
- Gutiérrez Alonso, G., Fernández-Suárez, J., Jeffries, T. E., Jenner, G. A., Tubrett, M. N., Cox, R., and Jackson, S. E., 2003, Terrane accretion and dispersal in the northern Gondwana margin. An Early Paleozoic analogue of a long-lived active margin: *Tectonophysics*, v. 365, p. 221-232.
- Halter, W. E., Pettke, T., and Heinrich, C. A., 2002a, The origin of metal ratios in porphyry type ore deposits: *Science*, v. 296, p. 1844-1845.
- Halter, W. E., Pettke, T., Heinrich, C. A., and Rothen-Rutishauser, B., 2002b, Major to trace element analysis of melt inclusions by laser ablation ICP-MS: methods of quantification: *Chemical Geology*, v. 183, p. 63-86.
- Halter, W. E., Heinrich, C. A., and Pettke, T., 2004a, Laser-ablation ICP-MS analysis of silicate and sulfide melt inclusions in an andesitic complex II: evidence for magma mixing and magma chamber evolution: *Contributions to Mineralogy and Petrology*, v. 147, p. 397-412.
- Halter, W. E., Pettke, T., and Heinrich, C. A., 2004b, Laser-ablation ICP-MS analysis of silicate and sulfide melt inclusions in an andesitic complex I: analytical approach and data evaluation: *Contributions to Mineralogy and Petrology*, v. 137, p. 385-396.
- Harris, N., Inger, S., and Massey, J., 1993, The role of fluids in the formation of High Himalayan leucogranites, *in* Treloar, P. J., and Searle, M. P., eds., *Himalayan tectonics*, Special Publication, 74: London, Geological Society, p. 391-400.
- Hauri, E. H., Wang, J. E., Dixon, P. L., King, C., Mandeville, C. W., and Newman, S., 2002, SIMS investigations of volatiles in volcanic glasses, I: calibration, sensitivity and comparisons with FTIR: *Chemical Geology*, v. 183, p. 99-114.
- Hedenquist, J. W., and Lowenstern, J. B., 1994, The role of magmas in the formation of hydrothermal ore deposits: *Nature*, v. 370, p. 519-526.
- Hedenquist, J. W., Arribas, A., and Reynolds, T. J., 1998, Evolution of an intrusion-centered hydrothermal system: Far Southeast-Lepanto porphyry and epithermal Cu-Au deposits, Philippines: *Economic Geology*, v. 93, p. 373-404.
- Heinrich, C. A., Ryan, C. G., Mernagh, T. P., and Eadington, P. J., 1992, Segregation of ore metals between magmatic brine and vapor - a fluid inclusion study using pixel microanalysis: *Economic Geology*, v. 87, p. 1566-1583.
- Heinrich, C. A., Günther, D., Audétat, A., Ulrich, T., and Frischknecht, R., 1999, Metal fractionation between magmatic brine and vapor, determined by microanalysis of fluid inclusions: *Geology*, v. 27, p. 755-758.

- Heinrich, C. A., Pettke, T., Halter, W. E., Aigner-Torres, M., Audétat, A., Günter, D., Hattendorff, B., Bleiner, D., Guillong, M., and Horn, I., 2003, Quantitative multi-element analysis of minerals, fluid and melt inclusions by laser-ablation inductively-coupled mass spectrometry: *Geochimica et Cosmochimica Acta*, v. 67, p. 3473-3496.
- Heinrich, C. A., Driesner, T., Stefánsson, A., and Seward, T. M., 2004, Magmatic vapor contraction and the transport of gold from the porphyry environment to epithermal ore deposits: *Geology*, v. 32, p. 761-764.
- Heinrich, C. A., 2005, The physical and chemical evolution of low-salinity magmatic fluids at the porphyry to epithermal transition: a thermodynamic study: *Mineralium Deposita*, v. 39, p. 864-889.
- Heinrich, C. A., 2007, Fluid-fluid interactions in magmatic-hydrothermal ore formation, *Reviews in Mineralogy & Geochemistry*, 65, Mineralogical Society of America, p. 363-387.
- Henriquez, F., Naslund, H. R., Nyström, J. O., Vivallo, W., Aguirre, R., Dobbs, F. M., and Lledo, H., 2003, New field evidence bearing on the origin of the El Laco magnetite deposit, Northern Chile, a discussion: *Econ Geol*, v. 98, p. 1497-1500.
- Hezarkhani, A., Williams-Jones, A. E., and Gammons, C. H., 1999, Factors controlling copper solubility and chalcopyrite deposition in the Sungun porphyry copper deposit, Iran: *Mineralium Deposita*, v. 34, p. 770-783.
- Hitzman, M. W., Oreskes, N., and Einaudi, M. T., 1992, Geological characteristics and tectonic setting of proterozoic iron oxide (Cu-U-Au-REE) deposits: *Precambrian Research*, v. 58, p. 241-287.
- Hitzman, M. W., 2000, Iron oxide-Cu-Au deposits: what, where, when and why?, *in* Porter, T. M., ed., *Hydrothermal Iron-Oxide Copper-Gold and Related Deposits: A Global Perspective*, 1: Adelaide, PGC Publishing p. 9-25.
- Hodkiewicz, P., Groves, D., Davidson, G., Weinberg, R., and Hagemann, S., 2009, Influence of structural setting on sulphur isotopes in Archean orogenic gold deposits, Eastern Goldfields Province, Yilgarn, Western Australia: *Mineralium Deposita*, v. 44, p. 129-150.
- Holness, M. B., 2010, Decoding dihedral angles in melt-bearing and solidified rocks.: *Journal of the Virtual Explorer*, v. 35.
- Hurai, V., Simon, K., Wiechert, U., Hoefs, J., Konečný, P., Huraiová, M., Pironon, J., and Lipka, J., 1998, Immiscible separation of metalliferous Fe/Ti-oxide melts from fractionating alkali basalt: conditions and two-liquid elemental partitioning: *Contributions to Mineralogy and Petrology*, v. 133, p. 12-29.
- IGME, 1979, Investigación de Magnetita en el área de la Berrona: IGME, Ministerio de Industria - Dirección General de Minas, v. ref. 10608.
- IGME, 1994, Mapa Metalogenético de España escala 1/200000, hoja nº57-68, Cheles-Villafranca de los Barros, *in* IGME, ed.
- Iwamori, H., 1997, Heat sources and melting in subduction zones: *J. geophys. Res.*, v. 102, p. 14,803 - 14,820.

- Jacobs, G. K., and Kerrick, D. M., 1981, Devolatilization equilibria in H₂O-CO₂ and H₂O-CO₂-NaCl fluids: an experimental and thermodynamic evaluation at elevated pressures and temperatures: *American Mineralogist*, v. 66, p. 1135-1153.
- Julivert, M., Fontboté, J. M., Ribeiro, A., and Conde, L. N., 1974, Mapa Tectónico de la Península Ibérica y Baleares, escala 1:1.000.000, in Instituto Geológico y Minero de España, I., ed.
- Kehayov, R., Bogdanov, K., Fanger, L., VonQuadt, A., Pettke, T., and Heinrich, C. A., 2003, The fluid chemical evolution of the Elatsite porphyry Cu-Au-PGE deposit, Bulgaria, in Eliopoulos, D. G., ed., *Mineral Exploration and Sustainable Development*, 1173-1176: Millpress, Rotterdam.
- Koepke, J., Feig, S., Snow, J., and Freise, M., 2004, Petrogenesis of oceanic plagiogranites by partial melting of gabbros: an experimental study: *Contributions to Mineralogy and Petrology*, v. 146, p. 414-432.
- Kolker, A., 1982, Mineralogy and geochemistry of Fe-Ti oxide and apatite (nelsonite) deposits and evaluation of the liquid immiscibility hypothesis: *Economic Geology*, v. 77, p. 1146-1158.
- Kovalenko, N. I., 1978, The genesis of rare metal granitoids and related ore deposits., in Stempok, M., Burnol, L., and Tischendorf, G., eds., *Metallization associated with acid magmatism*, 3: *Czech Geol Surv*, p. 235-247.
- Kovalenko, V. I., and Kovalenko, N. I., 1984, Problems of the origin, ore-bearing and evolution of rare-metal granitoids: *Physics of The Earth and Planetary Interiors*, v. 35, p. 51-62.
- Kwak, T. A. P., 1986, Fluid inclusions in skarns (carbonate replacement deposits): *Journal of Metamorphic Geology*, v. 4, p. 363-384.
- Lagache, M., and Weisbrod, A., 1977, The system: two alkali feldspars KCl-NaCl-H₂O at moderate to high temperatures and low pressures: *Contributions to Mineralogy and Petrology*, v. 62, p. 77-101.
- Landtwing, M. R., and Pettke, T., 2005, Relationships between SEM-cathodoluminescence response and trace-element composition of hydrothermal vein quartz: *American Mineralogist*, v. 90, p. 122-131.
- Lang, J. R., and Baker, T., 2001, Intrusion-related gold systems: the present level of understanding: *Mineralium Deposita*, v. 36, p. 477-489.
- Lentz, D. R., 1999, Carbonatite genesis: a reexamination of the role of intrusion-related pneumatolytic skarn processes in limestone melting: *Geology*, v. 27, p. 335-338.
- Lerchbaumer, L., and Audétat, A., 2009, Partitioning of Cu between vapor and brine - an experimental study based on LA-ICP-MS analysis of synthetic fluid inclusions: Abstracts of the 19th annual V.M. Goldschmidt conference, *Geochemica et Cosmochimica Acta*, v. 73, p. A744.
- Lerchbaumer, L., and Audétat, A., 2011, Preferential partitioning of copper into the vapor phase, An artifact?: *Goldschmidt 2011, Prague (Czech Republic)*, 2011, p. 1302.

- Leroy, J., 1978, The Margnac and Fanay uranium deposits of the La Crouzille District (western Massif Central, France): geologic and fluid inclusion studies: *Economic Geology*, v. 73, p. 1611-1634.
- Li, Y., Audétat, A., Lerchbaumer, L., and Xiong, X. L., 2009, Rapid Na, Cu exchange between synthetic fluid inclusions and external aqueous solutions: evidence from LA-ICP-MS analysis: *Geofluids*, v. 9, p. 321-329.
- Liang, L., Zicheng, C., and Yangjie, L., 1995, Geochemical characteristics of the plagiogranites in the vicinity of Bingdaban, Central Tianshan: *Chinese Journal of Geochemistry*, v. 14, p. 246-248.
- Liebscher, A., and Heinrich, C. A., 2007, Fluid Fluid Interactions in the Earth's Lithosphere: *Reviews in Mineralogy and Geochemistry*, v. 65, p. 1-13.
- Liñán, E., and Quesada, C., 1990, Ossa-Morena Zone. Stratigraphy, Rift Phase (Cambrian), in Dallmeyer, R. D., and Martínez García, E., eds., *Pre-Mesozoic Geology of Iberia*: Berlín, Springer-Verlag, p. 259-266.
- Locutura, J., Tornos, F., Florido, P., and Baeza, L., 1990, Ossa-Morena Zone: Metallogeny, in Martínez, E., and Dallmeyer, R. D., eds., *Pre-Mesozoic Geology of Iberia*, Springer Verlag, p. 321-332.
- Lowell, J. D., and Gilbert, J. M., 1970, Lateral and vertical alteration-mineralization zoning in porphyry ore deposits: *Economic Geology*, v. 65, p. 373-407.
- Lowenstern, J. B., 1994, Dissolved volatile concentrations in an ore-forming magma: *Geology*, v. 22, p. 893-896.
- Lowenstern, J. B., 2003a, Studies of melt inclusions prove critical to understanding the behaviour of volatiles in volcanic systems., in De Vivo, B., and Bodnar, B., eds., *Melt inclusions in volcanic systems: Method, Applications and Problems*, 5: Amsterdam, Elsevier, p. 1-21.
- Lowenstern, J. B., 2003b, Melt inclusions come of age: Volatiles, Volcanoes, and Sorby's Legacy, in De Vivo, B., and Bodnar, B., eds., *Melt inclusions in Volcanic Systems: Methods, Applications and Problems*, 5: Amsterdam, Elsevier, p. 1-22.
- Lu, F., Anderson, A. T., Jr., and Davis, A. M., 1995, Diffusional gradients at the crystal/melt interface and their effect on the compositions of melt inclusions: *Journal of Geology*, v. 103, p. 591-597.
- Lunar, R., Briones, R., Piña, R., Capote, R., Ortega, L., Quesada, C., Gervilla, C., Tejero, R., Maldonado, C., Martínez, C., and Martínez, E., 2008, El yacimiento de Ni-Cu-(EPG) de Aguablanca (Macizo Ibérico): marco tectónico, mineralogía, geocronología y modelo metalogénico: Madrid.
- Mangas, J., and Arribas, A., 1987, Fluid inclusion study in different styles of tin deposits associated with the Hercynian granites of western Spain: *Chemical Geology*, v. 61, p. 193-208.
- Manning, D.A.C., 1980, An experimental study of the effects of fluorine on the crystallization of granitic melts, in Evans, A.M., ed., *Metallisation associated with acid magmatism*, 6.

- Manning, D. A. C., 1981, The effect of fluorine on liquidus phase relationships in the system Qz-Ab-Or with excess water at 1 kb: *Contributions to Mineralogy and Petrology*, v. 76, p. 206-215.
- Mark, G., 1998, Albitite formation by selective pervasive sodic alteration of tonalite plutons in the Cloncurry district, Queensland: *Australian Journal of Earth Sciences*, v. 45, p. 765-774.
- Mark, G., and Foster, D. R. W., 2000, Magmatic-hydrothermal albite-actinolite-apatite-rich rocks from the Cloncurry district, NW Queensland, Australia: *Lithos*, v. 51, p. 223-245.
- Markl, G., 2001, A new type of silicate liquid immiscibility in peralkaline nepheline syenites (lujavrites) of the Llimaussaq complex, South Greenland: *Contributions to Mineralogy and Petrology*, v. 141, p. 458-472.
- Martínez Poyatos, D., 1997, Estructura del borde meridional de la zona CentriOBérica y su relación con el contacto entre las zonas CentriOBérica y de Ossa Morena, Universidad de Granada, 222 p.
- Matte, P., 1986, Tectonics and plate tectonics model for the Variscan Belt of Europe: *Tectonophysics*, v. 126, p. 329-374.
- Matte, P., 2001, The Variscan collage and orogeny (480-290 Ma) and tectonic definition of the Armórica microplate: a review: *Terra Nova*, v. 13, p. 122-128.
- Matthai, S. K., Henley, R. W., and Heinrich, C. A., 1995, Gold precipitation by fluid mixing in bedding-parallel fractures near carbonaceous slates at the Cosmopolitan Howley gold deposit, northern Australia: *Economic Geology*, v. 90, p. 2123-2142.
- McCuaig, T. C., and Kerrich, R., 1998, P-T-t deformation-fluid characteristics of lode gold deposits: evidence from alteration systematics: *Ore Geology Reviews*, v. 12, p. 381-453.
- McLelland, J., Morrison, J., Selleck, B., Cunningham, B., Olson, C., and Schmidt, K., 2002, Hydrothermal alteration of late- to post-tectonic Lyon Mountain Granitic Gneiss, Adirondack Mountains, New York: Origin of quartz - sillimanite segregations, quartz - albite lithologies, and associated Kiruna-type low-Ti Fe-oxide deposits: *Journal of Metamorphic Geology*, v. 20, p. 175-190.
- Meinert, L. D., 1995, Compositional variation of igneous rocks associated with skarn deposits. Chemical evidence for a genetic connection between petrogenesis and mineralization, *in* Thompson, J. H. F., ed., *Magmas, fluids, and ore deposits*, 23, Mineralogical Association of Canada. Short Course Series, p. 401-418.
- Montero, P., Salman, K., Zinger, T., and Bea, F., 1999, Rb-Sr and single zircon grain $^{207}\text{Pb}/^{206}\text{Pb}$ chronology of the Monesterio granodiorite and related migmatites. Evidence of Late Cambrian melting event in the Ossa Morena Zone, Iberian Massif: *Estudios Geológicos*, v. 55, p. 3-8.
- Montero, P., Salman, K., Bea, F., Azor, A., Expósito, I., Lodeiro, F., Martínez Poyatos, D., and Simancas, J. F., 2000, New data on the geochronology of the

- Ossa Morena Zone, Iberian Massif Variscan: Proceedings of the Appalachian dynamics: The building of the Upper Paleozoic basement, Galicia, 2000.
- Munhá, J., Oliveira, J. T., Ribeiro, A., Oliveira, V., Quesada, C., and Kerrich, R., 1986, Beja-Acebuches ophiolite, characterization and geodynamic significance: *Maleo*, v. 2, p. 2-31.
- Murphy, J. B., and Nance, R. D., 1989, Model for the evolution of the Avalonian-Cadomian belt: *Geology*, v. 17, p. 735-738.
- Murphy, J. B., and Nance, R. D., 1991, Supercontinent model for the contrasting character of Late Proterozoic orogenic belts: *Geology*, v. 19, p. 469-472.
- Nadeau, O., William-Jones, A. E., and Stix, J., 2010, Sulfide magmas as a source of metals in arc related magmatic hydrothermal fluids: *Nature Geoscience*, v. 3, p. 501-505.
- Naslund, H. R., 1983, The effects of oxygen fugacity on liquid immiscibility in iron-bearing silicate melts: *American Journal of Science*, v. 283, p. 1034-1059.
- Naslund, H. R., Henriquez, F., Nyström, J. O., Vivallo, W., and Dobbs, F. M., 2002, Magmatic Iron Ores and Associated Mineralisation: Examples from the Chilean High Andes and Coastal Cordillera, *in* Porter, T. M., ed., *Hydrothermal Iron Oxide Copper-Gold & Related Deposits: A Global Perspective*, 2: Adelaide, Porter, T.M., p. 207-226.
- Naslund, H. R., Henríquez, F., Nyström, J. O., Aguirre, R., and Lledó, H., 2003a, El Lago, Chile: Evidence for the eruption of an immiscible Fe-O-S-P melt: *Geol.Soc.Amer.Abstr.with Progr.*, v. 34, p. 394.
- Naslund, H. R., Aguirre, R., and Lledó, H., 2004, Evidence for the formation of massive magnetite ores by liquid immiscibility: IAVCEI General Assembly, Pucón, Chile, 2004.
- Naumov, V. R., Solovova, I. P., Kovalenker, V. A., and Rusinov, V. L., 1993, Immiscibility in acidic magmas: evidence for melt inclusions in quartz phenocrysts of ignimbrites: *European Journal of Mineralogy*, v. 5, p. 937-941.
- Nielsen, R. L., Michael, P. J., and Sours-Page, R., 1998, Chemical and physical indicators of compromised melt inclusions: *Geochemica et Cosmochemica Acta*, v. 62, p. 831-839.
- Nesbitt, H. E., and Young, G. M., 1982, Early Paleozoic climates and plate motions inferred from major element chemistry of lutites: *Nature*, v. 299, p. 715-717.
- Nyström, J. O., and Henriquez, F., 1994, Magmatic features of iron ores of the Kiruna type in Chile and Sweden; ore textures and magnetite geochemistry: *Economic Geology*, v. 89, p. 820-839.
- Ochner, A., 1993a, U-Pb Geochronology of the Upper Proterozoic-Lower Paleozoic geodynamic evolution in the Ossa Morena Zone (SW Iberia): Constraints on the timing of the Cadomian Orogeny, Swiss Federal Institute of Technology Zurich, ETH, 249 p.
- Ohmoto, H., and Rye, R. O., 1979, Isotopes of Sulfur and Carbon, *in* Barnes, H. L., ed., *Geochemistry of hydrothermal ore deposits*: New York, John Wiley and Sons, p. 509-567.

- Oliveira, V., 1986, Prospecção de minérios metálicos a sul do Tejo: *Geociências-Revista da Univ. de Aveiro*, v. 1, p. 15-22.
- Oliver et al., N. H. S., Cleverley, J. S., Mark, G., Pollard, P. J., Fu, B., Marshall, L. J., Rubenach, M. J., Williams, P. J., and Baker, T., 2004, Modeling the Role of Sodic Alteration in the Genesis of Iron Oxide-Copper-Gold Deposits, Eastern Mount Isa Block, Australia: *Economic Geology*, v. 99, p. 1145-1176.
- Ordóñez-Casado, B., 1998, Geochronological studies of the Pre-Mesozoic basement of the Iberian Massif: the Ossa Morena Zone and the Allochthonous Complexes within the Central Iberian Zone, Swiss Federal Institute of Technology Zürich, ETH, 207 p.
- Ordóñez-Casado, B., Martin-Izard, A., and García Nieto, J., 2008, SHRIMP-zircon U-Pb dating of the Ni-Cu-PGE mineralized Aguablanca gabbro and Santa Olalla granodiorite: Confirmation of an Early Carboniferous metallogenic epoch in the Variscan Massif of the Iberian Peninsula: *Ore Geology Reviews*, v. 34, p. 343-353.
- Oreskes, N., and Einaudi, M. T., 1992, Origin of hydrothermal fluids at Olympic Dam; preliminary results from fluid inclusions and stable isotopes: *Economic Geology*, v. 87, p. 64-90.
- Orville, P. M., 1963, Alkali ion exchange between vapor and feldspar phases: *American Journal of Science*, v. 261, p. 201-237.
- Osman, M. Y., and Maekawa, H., 2007, Mineralogy and origin of Mlakawa albitite from Kurdistan region, northeastern Iraq: *Geosphere*, v. 3, p. 624-645.
- Palomba, M., 2001, Geological, mineralogical, geochemical features and genesis of the albitite deposits of Central Sardinia (Italy): *Rendiconti Seminario Facoltà Scienze Università Cagliari Supplemento*, v. 71, p. 35-57.
- Palomeras, I., Carbonell, R., Flecha, I., Simancas, F., Ayarza, P., Matas, D., Martínez Poyatos, D., Azor, A., González Lodeiro, F., and Pérez-Estaún, 2009, Nature of the lithosphere across the Variscan Orogen of SW Iberia: Dense wide-angle seismic reflection data: *Journal of Geophysical Research*, v. 114, p. B02302.
- Palomeras, I., Carbonell, R., Ayarza, P., Fernández, M., Simancas, J. F., Poyatos, D. M., González Lodeiro, F., and Pérez-Estaún, A., 2011, Geophysical model of the lithosphere across the Variscan Belt of SW-Iberia: Multidisciplinary assessment: *Tectonophysics*, v. 508, p. 42-51.
- Park, C. F. J., 1961, A magnetite "flow" in Northern Chile: *Economic Geology*, v. 56, p. 431-436.
- Patiño Douce, A. E., and Dana Johnston, A., 1991, Phase equilibria and melt productivity in the pelitic system: implications for the origin of peraluminous granitoids and aluminous granulites: *Contributions to Mineralogy and Petrology*, v. 1991, p. 202-218.
- Patiño Douce, A. E., and Beard, J. S., 1995, Dehydration-melting of Biotite Gneiss and Quartz Amphibolite from 3 to 15 kbar: *Journal of Petrology*, v. 36, p. 707-738.

- Patiño Douce, A. E., and Beard, J. S., 1996, Effects of pressure and H₂O content on the compositions of primary crustal melts: Geological society of America Special papers, v. 315, p. 11-21.
- Patiño Douce, A. E., 1997, Generation of metaluminous A-type granites by low-pressure melting of calc-alkaline granitoids: *Geology*, v. 25, p. 743-746.
- Patiño Douce, A. E., and Harris, N., 1998, Experimental Constraints on Himalayan Anatexis: *Journal of Petrology*, v. 39, p. 689-710.
- Patiño Douce, A. E., 1999, What do experiments tell us about the relative contributions of crust and mantle to the origin of granitic magmas?, in Castro, A., Fernández, C., and Vigneresse, J. L., eds., *Understanding granites: integrating new and classical techniques*, 158: London, Geological Society of London. Special publication, p. 55-75.
- Penniston-Dorland, S.C. 2001, Illumination of vein quartz textures in a porphyry copper ore deposit using scanned cathodoluminescence: Grasberg Igneous Complex, Irian Jaya, Indonesia: *American Mineralogist*, v. 86, 652-666.
- Pereira, M. F., Chichorro, M., and Williams, I. S., 2009, Variscan intra-orogenic extensional tectonics in the Ossa Morena Zone (Évora-Aracena-Lora del Río metamorphic belt, SW Iberian Massif): SHRIMP zircon U-Th-Pb geochronology: Geological Society, London, Special Publications, v. 327, p. 215-237.
- Perring, C. S., Pollard, P. J., and Nunn, A. J., 2001, Petrogenesis of the Squirrel Hills granite and associated magnetite-rich sill and vein complex: Lightning creek prospect, Cloncurry district, Northwest Queensland: *Precambrian Research*, v. 106, p. 213-238.
- Pettke, T., Diamond, L. W., and Kramers, J. D., 2000, Mesothermal gold lodes in the north-western Alps: A review of genetic constraints from radiogenic isotopes: *European Journal of Mineralogy*, v. 12, p. 213-230.
- Philpotts, A. R., 1967, Origin of certain iron-titanium oxide and apatite rocks: *Economic Geology*, v. 62, p. 303-315.
- Phillips, G. N., and Powell, R., 2010, Formation of gold deposits: a metamorphic devolatilization model: *Journal of Metamorphic Geology*, v. 28, p. 689-718.
- Pin, C., Liñán, E., Pascual, E., Donaire, T., and Valenzuela, A., 1999, Late Proterozoic crustal growth in Ossa Morena: Nd isotope and trace element evidence from the Sierra de Córdoba volcanics: XV Reunión de Geología del Oeste Peninsular (International Meeting on Cadomian Orogens), Badajoz, Spain, 1999, p. 215-218.
- Pin, C., Liñán, E., Pascual, E., Donaire, T., and Valenzuela, A., 2002, Late Neoproterozoic crustal growth in the European Variscides: Nd isotope and geochemical evidence from the Sierra de Córdoba Andesites (Ossa Morena Zone, Southern Spain): *Tectonophysics*, v. 352, p. 133-151.
- Piña, R., Lunar, R., Ortega, L., Gervilla, C., Alapieti, T., and Martínez, C., 2006, Petrology and geochemistry of mafic-ultramafic fragments from the Aguablanca (SW Spain) Ni-Cu ore breccia: Implications for the genesis of the deposit: *Economic Geology*, v. 101, p. 865-881.

- Pokrovski, G. S., Borisova, A. Y., and Harrichoury, J.-C., 2008, The effect of sulfur on vapor-liquid fractionation of metals in hydrothermal systems: *Earth and Planetary Science Letters*, v. 266, p. 345-362.
- Polito, P., Kyser, T., and Stanley, C., 2009, The Proterozoic, albitite-hosted, Valhalla uranium deposit, Queensland, Australia: a description of the alteration assemblage associated with uranium mineralisation in diamond drill hole V39: *Mineralium Deposita*, v. 44, p. 11-40.
- Pollard, P., 2006, An intrusion-related origin for Cu–Au mineralization in iron oxide–copper–gold (IOCG) provinces: *Mineralium Deposita*, v. 41, p. 179-187.
- Pollard, P. J., 1988, Mineralogical and geochemical features of rare metal granites: 5th International Symposium Tin/Tungsten Granites in Southeast Asia and the Western Pacific IGCP Project, Matsue (Japan), 1988, p. 131-133.
- Pollard, P. J., 2000, Evidence of a magmatic fluid and metal source for Fe-oxide Cu-Au mineralization, *in* Porter, T. M., ed., *Hydrothermal iron oxide copper-gold and related deposits: a global perspective*, 1: Adelaide, PGC, p. 27-41.
- Pollard, P. J., 2001, Sodic (–calcic) alteration in Fe-oxide–Cu–Au districts: an origin via unmixing of magmatic fluids: *Mineralium Deposita*, v. 36, p. 93-100.
- Porter, T. M., 2002, *Hydrothermal Iron Oxide Copper-Gold & Related Deposits: A Global Perspective*: Adelaide, PGC Publishing.
- Porter, T. M., 2010, *Hydrothermal Iron Oxide Copper-Gold and Related Deposits: A Global Perspective: Advances in the Understanding of IOCG Deposits*, 3 and 4: Adelaide, PGC Publishing, p. 600.
- Powell, R., Will, M. T., and Phillips, G. N., 1991, Metamorphism in Archaean greenstone belts; calculated fluid compositions and implications for gold mineralization: *Journal of Metamorphic Geology*, v. 9, p. 141-150.
- Quesada, C., 1990, Precambrian successions in SW Iberia: their relationship to "Cadomian" orogenic events, *in* D.R., L., Strachan, R. A., and Topley, C. G., eds., *The Cadomian Orogeny*, 51, Geological Society Special Publication, p. 353-362.
- Quesada, C., 1991, Geological constraints on the Paleozoic tectonic evolution of tectonostratigraphic terranes in the Iberian Massif: *Tectonophysics*, v. 185, p. 225-245.
- Quesada, C., Fonseca, P., Munhá, J., Oliveira, J. T., and Ribeiro, A., 1994, The Beja-Acebuches Ophiolite (Southern Iberia Variscan fold belt): Geological characterization and geodynamic significance: *Boletín Geológico y Minero*, v. 105, p. 3-49.
- Rapien, M. H., Bodnar, R. J., Szabó, C. S., Wood, C. P., and Sutton, S. R., 2003, Melt inclusion study of the embryonic porphyry copper system at White Island, New Zealand: *Society of Economic Geology*, v. Special Publication, 10, p. 98-120.
- Rapp, R. P., Watson, E. B., and Miller, C. F., 1991, Partial melting of amphibolite/eclogite and the origin of Archean trondhjemites and tonalites: *Precambrian Research*, v. 51, p. 1-25.

- Redmond, P. B., Einaudi, M. T., Inan, E. E., Landtwing, M., and Heinrich, C. A., 2004, Copper deposition by fluid cooling in intrusion-centered systems: new insights from the Bingham porphyry deposit, Utah: *Geology*, v. 32.
- Reynolds, T. J., and Beane, R. E., 1985, Evolution of hydrothermal fluid characteristics at the Santa Rita, New-Mexico, porphyry copper-deposit: *Economic Geology*, v. 80, p. 1328-1347.
- Ribeiro, A., Munhá, J., Fonseca, P., Araújo, A. A., Pedro, J. C., Mateus, A., Tassinari, C., Machado, G., and Jesús, A., 2010, Variscan ophiolite belts in the Ossa Morena Zone (Southwest Iberia): Geological characterization and geodynamic significance: *Gondwana Research*, v. 17, p. 408-421.
- Ridley, J. R., and Diamond, L. W., 2000, Fluid chemistry of orogenic lode gold deposits and implications for genetic models: *Society of Economic Geologists Reviews in Economic Geology*, v. 13, p. 141-162
- Robardet, M., and Gutiérrez-Marco, J. C., 1990, Ossa Morena Zone: Passive Margin Phase (Ordovician-Silurian-Devonian), *in* Dallmeyer, R. D., and Martínez García, E., eds., *Premesozoic Geology of Iberia*: Berlin, Springer-Verlag, p. 267-272.
- Roedder, E., 1951, Low - temperature liquid immiscibility in the system $K_2O - FeO - Al_2O_3 - SiO_2$: *American Journal of Science*, v. 35, p. 282-286.
- Roedder, E., 1984, Fluid inclusions: *Mineralogical Society American Reviews in Mineralogy*, 12, 644p.
- Romeo, I., Capote, R., Tejero, R., Lunar, R., and Quesada, C., 2006a, Magma emplacement in transpression: The Santa Olalla Igneous Complex (Ossa-Morena Zone, SW Iberia): *Journal of Structural Geology*, v. 28, p. 1821-1834.
- Romeo, I., Lunar, R., Capote, R., Quesada, C., Dunning, G. R., Pina, R., and Ortega, L., 2006b, U-Pb age constraints on Variscan magmatism and Ni-Cu-PGE metallogeny in the Ossa-Morena Zone (SW Iberia): *Journal of the Geological Society*, v. 163, p. 837-846.
- Ronacher, E., Richards, J. P., Reed, M. H., and Adams, P. D., 2004, Characteristics and evolution of the hydrothermal fluid in the North zone high-grade area, Porgera gold deposit, Papua New Guinea: *Economic Geology*, v. 99, p. 843.
- Rotherham, J. F., Blake, K. L., Cartwright, I., and Williams, P. J., 1998, Stable isotope evidence for the origin of the Starra Au-Cu deposit, Cloncurry district: *Economic Geology*, v. 93, p. 1435-1449.
- Ruiz, C., 1974, Génesis de los depósitos de hierro del Suroeste de la provincia de Badajoz, E.T.S.I.M 227 p.
- Rusk, B., and Reed, M., 2002, Scanning electron microscope-cathodoluminescence analysis of quartz reveals complex growth histories from the Butte porphyry copper deposit, Montana: *Geology*, v. 30, p. 727-730
- Rusk, B., 2009, Insights into hydrothermal processes from cathodoluminescence and trace elements in quartz: SGA 2009, Townsville, Australia, 2009.
- Rusk, B. G., Reed, M. H., Dilles, J. H., Klemm, L. M., and Heinrich, C. A., 2004, Compositions of magmatic hydrothermal fluids determined by LA-ICP-MS of

- fluid inclusions from the porphyry copper-molybdenum deposit at Butte, MT: *Chemical Geology*, v. 210, p. 173-199.
- Rusk, B. G., Reed, M. H., and Dilles, J. H., 2008, Fluid Inclusion Evidence for Magmatic-Hydrothermal Fluid Evolution in the Porphyry Copper-Molybdenum Deposit at Butte, Montana: *Economic Geology*, v. 103, p. 307-334.
- Sabet, A. H., Tsogoev, V. B., Sarin, L. P., Azazi, S. A., El Bedewi, M. A., and Ghobrial, G. A., 1976, Tin-tantalum deposit of Abu Dabab: *Annals Geol. Surv. Egypt*, v. 6, p. 93-117.
- Salman, K., 2002, Estudio petrológico, geoquímico y geocronológico de los granitoides del área Monesterio-Cala, Zona de Ossa Morena (Macizo Ibérico), Universidad de Granada, 232 p.
- Sanabria, R., Casquet, C., Tornos, F., and Galindo, C., 2005, Las mineralizaciones ferríferas del coto minero San Guillermo (Jerez de los Caballeros, Badajoz, España): *Geogaceta*, v.38, p.223-226.
- Sánchez-Carretero, R., Eguiluz, L., Pascual, E., and Carracedo, M., 1990, Ossa Morena Zone: Igneous rocks, *in* Dallmeyer, R. D., and Martínez García, E., eds., *Pre-Mesozoic Geology of Iberia*: Berlin, Springer-Verlag, p. 292-313.
- Sánchez-García, T., Bellido, F., and Quesada, C., 2003, Geodynamic setting and geochemical signatures of Cambrian-Ordovician rift-related igneous rocks (Ossa-Morena Zone, SW Iberia): *Tectonophysics*, v. 365, p. 233-255.
- Sánchez-García, T., Quesada, C., Bellido, F., Dunning, G. R., and González del Tánago, J., 2008, Two-step magma flooding of the upper crust during rifting: The Early Paleozoic of the Ossa Morena Zone (SW Iberia): *Tectonophysics*, v. 461, p. 72-90.
- Sánchez-García, T., Bellido, F., Pereira, M. F., Chichorro, M., Quesada, C., Pin, C., and Silva, J. B., 2010, Rift-related volcanism predating the birth of the Rheic Ocean (Ossa-Morena zone, SW Iberia): *Gondwana Research*, v. 17, p. 392-407.
- Sánchez Carretero, R., Eguiluz, L., Pascual, E., and Carracedo, M., 1990, Ossa Morena Zone: Igneous rocks, *in* Dallmeyer, R. D., and Martínez García, E., eds., *Pre-Mesozoic Geology of Iberia*: Berlin, Springer-Verlag, p. 292-313.
- Schäfer, H. J., 1990, Geochronological investigations in the Ossa Morena Zone, SW Spain, Swiss Federal Institute of Technology ETH, 153 p.
- Schmitz, C. and Burt, D. M., 1990, The Black Pearl Mine, Arizona: Wolframite veins and stockschider pegmatite related to an albitic stock, *in* Stein, H. J., and Hannah, J. L., eds., *Ore-bearing Granite Systems: Petrogenesis and Mineralizing Processes*, 246, Geological Society of America Special Paper, p. 221-232.
- Schütz, W., Ebner, J., and Meyer, K., 1987, Trondhjemites, tonalites and diorites in the South Portuguese Zone and their relations to the vulcanites and mineral deposits of the Iberian Pyrite Belt: *Geologische Rundschau*, v. 76, p. 201-212.
- Schwartz, M. O., 1992, Geochemical criteria for distinguishing magmatic and metasomatic albite-enrichment in granitoids – examples from the Ta-Li granite Yichun (China) and the Sn-W deposit Tikus (Indonesia): *Mineralium Deposita*, v. 27, p. 101-108.

- Seo, J. H., Guillong, M., and Heinrich, C. A., 2009, The role of sulfur in the formation of magmatic-hydrothermal copper-gold deposits: *Earth and Planetary Science Letters*, v. 282, p. 323-328.
- Severs, M. J., Azbej, T., Thomas, J. B., Mandeville, C. W., and Bodnar, R. J., 2007, Experimental determination of H₂O loss from melt inclusions during laboratory heating: Evidence from Raman spectroscopy: *Chemical Geology*, v. 237, p. 358-371.
- Seward, T. M., and Barnes, H. L., 1997, Metal transport by hydrothermal ore fluids, *in* Barnes, H.L. ed. *Geochemistry of Hydrothermal Ore Deposits*, Wiley, p. 173-235
- Shelley, D., and Bossière, G., 2000, A new model for the Hercynian Orogen of Gondwana France and Iberia: *Journal of Structural Geology*, v. 22, p. 757-776.
- Sherbini, O.A., and Quadi, T.M., 2004, Origin of the rare-metal-bearing peraluminous Albite Granite of the Umm Al Suquian Pluton, Asir Region, Kingdom of Saudi Arabia: *J. King Saud Univ*, v. 1, p. 41-59.
- Silva, J. B., Oliveira, J. T., and Ribeiro, A., 1990, Structural outline of the South Portuguese zone, *in* Martínez, E., and Dallmeyer, R. D., eds., *Premesozoic Geology of Iberia*: London, Springer Verlag.
- Sillitoe, R., 2003, Iron oxide-copper-gold deposits: an Andean view: *Mineralium Deposita*, v. 38, p. 787-812.
- Sillitoe, R. H., and Burrows, D. R., 2003, New field evidence bearing on the origin of the El Laco magnetite deposit, Northern Chile, a reply: *Economic Geology*, v. 98, p. 1501-1502.
- Simancas, J. F., Carbonell, R., González Lodeiro, F., Perez Estaun, A., Juhlin, C., Ayarza, P., Kashubin, A., Azor, A., Martínez Poyatos, D., Almodóvar, G. R., Pascual, E., Sáez, R., and Expósito, I., 2003, Crustal structure of the transpressional Variscan orogen of SW Iberia: SW Iberia deep seismic reflection profile (IBERSEIS): *Tectonics*, v. 22.
- Simancas, J. F., Expósito, I., Azor, A., Martínez Poyatos, D., and González Lodeiro, F., 2004, From the Cadomian orogenesis to the early Paleozoic Variscan rifting in Southwest Iberia: *Journal of Iberian Geology*, v. 30, p. 53-71.
- Simon, A. C., Pettke, T., Candela, P. A., Piccoli, P. M., and Heinrich, C. A., 2004, Magnetite solubility and iron transport in magmatic-hydrothermal environments: *Geochimica et Cosmochimica Acta*, v. 68, p. 4905-4914.
- Sisson, V. B., and Hollister, L. S., 1990, A fluid-inclusion study of metamorphosed pelitic and carbonate rocks, south-central Maine: *American Mineralogist*, v. 75, p. 59-70.
- Smithies, R. H., 2000, The Archaean tonalite-trondhjemite-granodiorite (TTG) series is not an analogue of Cenozoic adakite: *Earth and Planetary Science Letters*, v. 182, p. 115-125.
- Sobolev, A. V., and Shimizu, N., 1993, Ultra-depleted primary melt included in an olivine from the Mid-Atlantic Ridge: *Nature*, v. 363, p. 151-154.

- Sobolev, A. V., 1996, Melt inclusions in minerals as a source of principle petrological information: *Petrology*, v. 4, p. 209-220.
- Spencer, K.J., and Lindsley, D.H., 1981, A solution model for coexisting iron-titanium oxides: *American Mineralogist*, v. 66, p. 1189-1201
- Spiering, E. D., Rodriguez Pevida, L., Castelo, J. M., García Nieto, J., and Martínez, C., 2005, Aguablanca: a new nickel mine in a potential new Ni/Cu and IOCG belt of southern Spain and Portugal: Geological Society Nevada. Symposium 2005, 2005.
- Stampfli, G. M., von Raumer, J. F., and Borel, G. D., 2002, Paleozoic evolution of pre-Variscan terranes: From Gondwana to the Variscan collision, *in* Martínez Catalán, J. R., Hatcher, R. D., Arenas, R., and Díaz García, F., eds., *Variscan-Appalachian dynamics: The building of the late Paleozoic basement*, 364: Boulder, Colorado, Geological Society of America Special Paper, p. 263-280.
- Stapel, G., 1999, The nature of isostasy in West Iberia and its bearing on Mesozoic and Cenozoic regional tectonics, *Vrije Universiteit*, 148 p.
- Student, J. J., and Bodnar, R. J., 2004, Silicate melt inclusions in porphyry copper deposits: identification and homogenization behaviour: *Canadian Mineralogist*, v. 42, p. 1583-1599.
- Stüwe, K., 1998, Tectonic constraints on the timing relationships of metamorphism, fluid production and gold-bearing quartz vein emplacement: *Ore Geology Reviews*, v. 13, p. 219-228.
- Thomas, J. B., 2003, Melt inclusion geochemistry, Virginia Polytechnic Institute and State University, 96 p.
- Thomas, R., and Klemm, W., 1997, Microthermometric study of silicate melt inclusions in Variscan granites from SE Germany: volatile contents and entrapment conditions: *Journal of Petrology*, v. 38, p. 1753-1765.
- Thompson, J. H. F., and Newberry, R. J., 2000, Gold deposits related to reduced granitic intrusions, *Society of Economic Geologists, Review Series*, v.13, 377-397..
- Tornos, F., 1991, Las episienitas de la Sierra de Guadarrama, propuesta de clasificación petrográfica: *Boletín de la Sociedad Española de Mineralogía*, v. 14, p. 273-284.
- Tornos, F., Casquet, C., Galindo, C., Velasco, F., and Canales, A., 2001, A new style of Ni-Cu mineralisation related to magmatic breccia pipes in a transpressional magmatic arc, Aguablanca, Spain.: *Miner. Deposita*, v. 36, p. 700-706.
- Tornos, F., Casquet, C., Relvas, J., Barriga, F., and Sáez, R., 2002, Transpressional tectonics and ore deposit formation: The southwestern margin of the Iberian Variscan belt, *in* Blundell, D., Neubauer, F., and von Quadt, A., eds., *The timing and location of major ore deposits in an evolving orogen*, 206: London, Geological Society London Special Publication, p. 179-198.
- Tornos, F., Casquet, C., and Galindo, C., 2003, Hydrothermal iron oxide (- Cu - Au) mineralization in SW Iberia: Evidence for a multiple origin, *in* Eliopoulos,

- D. G., ed., Mineral exploration and sustainable development: Rotterdam, Millpress, p. 395-398.
- Tornos, F., and Chiaradia, M., 2004, Plumbotectonic Evolution of the Ossa Morena Zone, Iberian Peninsula: Tracing the Influence of Mantle-Crust Interaction in Ore-Forming Processes: *Economic Geology*, v. 99, p. 965-985.
- Tornos, F., Inverno, C. M. C., Casquet, C., Mateus, A., Ortiz, G., and Oliveira, V., 2004, The metallogenic evolution of the Ossa Morena Zone: *Journal of Iberian Geology*, v. 30, p. 146-181.
- Tornos, F., and Casquet, C., 2005, A new scenario for related IOCG and Ni-(Cu) mineralization: the relationship with giant mid-crustal mafic sills, Variscan Iberian Massif: *Terra Nova*, v. 17, p. 236-241.
- Tornos, F., 2011, Magnetite-Apatite and IOCG deposits formed by magmatic-hydrothermal evolution of complex calc-alkaline melts: Let's talk ore deposits: proceedings of the Eleventh Biennial SGA Meeting, Antofagasta, Chile, 2011.
- Tornos, F., Velasco, F., Morata, D., Barra, F., and Rojo, M., 2010, The Tropezón Cu-Mo-(Au) deposit, Northern Chile: the missing link between IOCG and porphyry copper systems?: *Mineralium Deposita*, v. 45, p. 313-321.
- Tornos, F., Velasco, F., Morata, D., Barra, F., and Rojo, M., 2011, The magmatic hydrothermal evolution of the El Laco deposit as tracked by melt inclusions and isotope data: Let's talk ore deposits: proceedings of the Eleventh Biennial SGA Meeting, Antofagasta, Chile, 2011.
- Ulrich, T., Günter, D., and Heinrich, C. A., 1999, Gold concentrations of magmatic brines and the metal budget of porphyry copper deposits: *Science*, v. 399, p. 676-679.
- Ulrich, T., Günter, D., and Heinrich, C. A., 2001, The evolution of a porphyry Cu-Au deposit, based on LA-ICP-MS analysis of fluid inclusions: Bajo de la Alumbrera, Argentina: *Economic Geology*, v. 97, p. 1888-1920.
- Ulrich, T., Günter, D., and Heinrich, C. A., 2002, The evolution of a porphyry Cu-Au deposit, based on LA-ICP-MS analysis of fluid inclusions: Bajo de la Alumbrera, Argentina: *Economic Geology*, v. 96.
- Vázquez, F., and Fernández Pompa, F., 1976, Contribución al conocimiento geológico del SW de España en relación con la prospección de magnetitas: *Memorias del Instituto Geológico y Minero de España*, v. 89, p. 130.
- Vázquez Guzmán, F., 1983, *Depósitos minerales de España*: Madrid, IGME, Instituto Geológico y Minero de España.
- Velasco, F., 1976, Mineralogía y metalogenia de los skarns de Santa Olalla (Huelva), *Universidad del País Vasco*, 290 p.
- Velasco, F., and Amigó, J. M., 1981, Mineralogy and origin of the skarn from Cala (Huelva, Spain): *Economic Geology*, p. 719-727.
- Vera, J. A., 2004, *Geología de España*: Madrid, Instituto Geológico y Minero de España.

- Visser, W., and Koster Van Groos, A. F., 1979a, Phase relations in the system K_2O - FeO - Al_2O_3 - SiO_2 at 1 atmosphere with special emphasis on low temperature liquid immiscibility: *American Journal of Science*, v. 279, p. 70-91.
- Visser, W., and Koster Van Groos, A. F., 1979b, The effect of pressure on liquid immiscibility in the system K_2O - FeO - Al_2O_3 - SiO_2 : *American Journal of Science*, v. 279, p. 1160-1175.
- Visser, W., and Koster Van Groos, A. F., 1979c, Effects of P_2O_5 and TiO_2 on liquid-liquid equilibria in the system K_2O - FeO - Al_2O_3 - SiO_2 : *American Journal of Science*, v. 279, p. 970-988.
- Wallace, P. J., Anderson, A. T., and Davis, A. M., 1995, Quantification of pre-eruptive evolved gas contents in silicic magmas: *Nature*, v. 377, p. 612-616.
- Watson, E. B., 1976, Two-liquid partition coefficients: experimental data and geochemical implications: *Contributions to Mineralogy and Petrology*, v. 56, p. 119-134.
- Watson, E. B., Sneeringer, M. A., and Ross, A., 1982, Diffusion of dissolved carbonate in magmas: experimental results and applications: *Earth and Planetary Science Letters*, v. 61, p. 346-358.
- Watson, T. L., and Taber, S., 1913, Geology of the titanium and apatite deposits of Virginia: *Virginia Geological Survey Bulletin*, v. 3a, p. 308.
- Webster, J., Thomas, R., Rhede, D., Foerster, H. J., and Seltmann, R., 1997, Melt inclusions in quartz from an evolved peraluminous pegmatite: geochemical evidence for strong tin enrichment in fluorine-rich and phosphorous-rich residual liquids: *Geochimica et Cosmochimica Acta*, v. 61, p. 2589-2604.
- Webster, J. D., and Thomas, R., 2006, Silicate melt inclusions in felsic plutons: A synthesis and review, *in* Webster, J., ed., *Melt Inclusions in Plutonic Rocks*, 36, MAC Short Course p. 165-188.
- Weihed, P., and Williams, P., 2005, Metallogeny of the northern Fennoscandian Shield: a set of papers on Cu-Au and VMS deposits of northern Sweden: *Mineralium Deposita*, v.40 p.347-350.
- Wilkinson, J. J., 1991, Volatile production during contact metamorphism: the role of organic matter in pelites: *Journal of Geological Society*, v. 148, p. 731-736.
- Williams-Jones, A. E., and Heinrich, C. A., 2005, 100th Anniversary special paper: Vapor transport of metals and the formation of magmatic-hydrothermal ore deposits: *Economic Geology*, v. 100, p. 1287-1312.
- Williams, P. J., 1994, Iron mobility during synmetamorphic alteration in the Selwyn Range area, NW Queensland: Implications for the origin of ironstone-hosted Au-Cu deposits: *Mineralium Deposita*, v. 29, p. 250-260.
- Williams, P. J., Barton, M. D., Johnson, D. A., Fontboté, J. M., de Haller, A., Mark, G., and Oliver et al., N. H. S., 2005, Iron Oxide Copper-Gold Deposits: Geology, Space-Time Distribution, and Possible Models of Origin: *Economic Geology*, v. 100th Anniversary Volume, p. 371-405.
- Winter, J. D., 2010, *An introduction to igneous and metamorphic petrology*, Prentice Hall.

- Wyllie, P. J., Wolf, M. B., and van der Laan, S. R., 1997, Conditions for formation of tonalites and trondhjemites: magmatic sources and products, *in* De Wit, L. D. A., ed., *Greenstone Belts*: Oxford, Oxford University Press, p. 256-266.
- Xu, K. Q., Zhu, J. C., and Xu, S. J., 1987, Geological environments and geochemical differences of W, Sn, Nb/Ta-bearing granites and their related mineral deposits in South China: 4th International Symposium IGCP Project 220, Guilin (China), 1987, p. 194-197.
- Zajacz, Z., Halter, W. E., Pettke, T., and Guillong, M., 2008, Determination of fluid/melt partition coefficients by LA-ICPMS analysis of co-existing fluid and silicate melt inclusions: Controls on element partitioning: *Geochimica et Cosmochimica Acta*, v. 72, p. 2169-2197.
- Zajacz, Z., Hanley, J. J., Heinrich, C. A., Halter, W. E., and Guillong, M., 2009, Diffusive reequilibration of quartz-hosted silicate melt and fluid inclusions: Are all metal concentrations unmodified?: ECROFI Meeting 20th, University of Granada, Spain, September 2009, 2009.
- Zajacz, Z., Seo, J. H., Candela, P. A., Piccoli, P. M., and Tossell, J. A., 2011, The solubility of copper in high-temperature magmatic vapors: a question for the significance of various chloride and sulfide complexes: *Geochimica et Cosmochimica Acta*, v. In Press, Accepted Manuscript.

Appendix IA: SEM-CL analysis of hydrothermal quartz: Case histories in magnetite – ($\pm\text{Cu}$ - $\pm\text{Au}$) deposits

Introduction

SEM-CL (Scanning Electron Microscope - Cathodoluminescence) is a useful technique for the observation of microtextures in minerals that are not visible through conventional petrographic microscopy (transmitted light, TL) or BSE (Backscattered electron) images. The CL has been used to study a wide variety of geologic environments such as sedimentary petrology, diagenetic processes, deformation of rocks, or evolution of hydrothermal systems. Furthermore, is a key technique for detailed geochronological studies since it reveals the zonation of zircon, apatite and other minerals

Recent studies on hydrothermal quartz have shown that the combination of SEM-CL images with other techniques, such as fluid inclusion analysis, is a useful technique for characterizing ore forming events (Rusk and Reed 2002; Landtwing and Pettke, 2005). Careful discrimination and characterization of different generations of quartz and its relationship with successive FIA (Goldstein and Reynolds, 1994) allow the reconstruction of the fluid evolution in a given system. In most cases, individual quartz crystals contain fluid inclusions trapped at different moments and from chemically different fluids.

The changes in CL response result from the intrinsic lattice defects such as translations, point defects, mineral inclusions, as well as extrinsic defects such as incorporations of trace elements (Götze et al 2001).

In this study we show some case histories of eight hydrothermal quartz samples, both hydrothermal quartz from veins and magmatic quartz from

magmatic phenocrysts. The images reveal textures of growth zoning, quartz-filled microfractures, truncation, concentric growth and splatter and cobweb-like textures, among others. These features represent independent processes in the complex history of quartz growth in response to fracturation, dilation, growth into open space or dissolution and recrystallization.

Geological setting and sampling

We have selected samples from a wide variety of environments, including three deposits in SW Spain (Cala, Sultana and La Berrona) and two magnetite (Cu-Au) deposits in Northern Chile (Silvita and Taltal). The studied samples from the Ossa Morena Zone include: (1) chalcopyrite (Au) -bearing quartz veins from the Sultana deposit and (2) quartz from miarolitic cavities in the Santa Olalla Plutonic Complex (see Chapter II); (3) skarn-related quartz and (4) shear zone-related quartz from the Cala mine, hosted by the Cala stock in the Santa Olalla Plutonic Complex (Velasco et al., 1979; Carriedo, (P.h.D in progr.), (5) quartz cementing magmatic-hydrothermal breccia, and (6) vein quartz of the La Berrona deposit (in the Valuengo area, see Chapter III). The samples from IOCG deposits in N Chile (Central Andes) include: (7) vuggy euhedral quartz coexisting with chalcopyrite and tourmaline supporting diorite fragments in the Silvita deposit and (8) vein and breccia quartz associated to chalcopyrite, pyrite and magnetite in the Taltal deposit (Tornos et al., 2010).

Methods

SEM-CL analyses were performed at the CIC (Centro de Instrumentación Científica, University of Granada) (Spain) under the supervision of Isabel Guerra. Doubly polished sections were coated with a film of carbon that was removed for the further fluid inclusion study. The images were taken in a SEM Leo 1430 VP

equipment with the following analytical conditions: 15 kV, 2nA e-probe and a beam current of 80mA. The work distance was 16 mm.

The gray scales of SEM-CL images have been grouped in a color scale level: CL-bright (light to gray), CL-gray (gray), CL-dull (gray to dark) and CL-dark (dark gray to black).

Quartz textures

Observed textures are grouped into six main categories: euhedral growth zoning of various intensities and parallel or perpendicular to c-axis, dark-luminescent patches, cobweb and splatter textures, corroded grains, truncated grains, late vein fillings and micro-cracks crosscutting earlier quartz. The first two are related to the precipitation of quartz into open spaces and the last four ones are interpreted as due to dissolution, recrystallization and fracturing processes after the precipitation of the quartz crystal (Rusk and Reed, 2002).

Sultana mine: euhedral growing over deformed cores

Contrasting CL shows that the vein infilling in the Sultana vein includes three distinct stages of quartz crystallization; (1): an early generation of quartz (Q1) comprises the bulk of the vein and corresponds to milky quartz in hand sample. Q1 is bright-luminescent with local euhedral growing into open spaces. It has superimposed dark-luminescent patches of grayer luminescence related quartz. Superimposed on this Q1 there is a second generation of quartz, characterized by the presence of clear and well-defined bands of bright and gray luminescence (Q2). The concentric growth of the Q2 points towards the center of the vein and is oriented parallel to c-axis of the crystals (Fig 1A). Sulfides are always associated to the late Q2 generation of quartz. A third generation of quartz (Q3) shows very dark-luminescence and occurs filling late fractures that crosscut both the first and the second generation of quartz. Mosaics of adjacent images

were used as a basis to map fluid inclusion assemblages and to establish a detailed correlation between each FIA and different quartz domains (Chapter II).

The Santa Olalla granite-hosted miarolitic cavities (2) are filled with bright to dull luminescent quartz showing a very clear growth zoning in an open space (Fig.1B). In this case, the euhedral zonation is perpendicular to the c axis of quartz. The combinations of the study of fluid inclusion assemblages with the CL images of the quartz suggest the circulation of similar fluids in the Sultana vein and those exsolved from the host Santa Olalla tonalite (see Chapter II).

Cala mine: dissolution and deformation processes in skarn- and shear zone – related quartz (see Appendix Ib)

The images of quartz within cavities in the prograde garnet-rich skarn in the Cala magnetite ($\pm\text{Cu}\pm\text{Au}$) mine (3) show a first generation of gray luminescent grains (Q1) with euhedral growths and local dissolution zones (corroded grains). There is a second generation of dark luminescent quartz developed along microfractures that crosscut Q1 (Fig.1C).

SEM-CL images of quartz associated with the shear zone-related mineralization (4) reveal complex textures with multiple superimposed stages of precipitation and recrystallization (Fig.1D). Images show grain truncations and splatter or cobweb textures that are a clear evidence of intense fracturation. The correlation with FIA is not straightforward due to the intense deformation. However, CL images reveal some gray luminescent “shadow zones” with poorly defined growth zoning that contain suitable FIA (see Appendix IB)

La Berrona deposit: early zoned quartz and further deformation processes.

In the La Berrona deposit there is an intense hydrothermal brecciation where fragments of albitite are supported by actinolite and magnetite with later quartz infilling (5). The SEM-CL images show an early gray to dull luminescent zoned (20

to 200 μm width) quartz. This early generation is clearly affected by a later fracturation shown by the existence of a dense network of micro-cracks and fractures healed by dark luminescent quartz (Fig. 1E). A-veins (6) hosted by the albitite and interpreted as formed in a still partly ductile rock show an important truncation of gray luminescent grains, a feature probably due to the absence of enough space for euhedral growing (Fig. 1F).

Silvita mine: late quartz growing in several stages

SEM-CL images from the Silvita mine (7) are probably the best examples of the superposition of hydrothermal processes as represented by a wide range of textures. In the sample shown in the Figure 1G there is an early concentric growth zone of a first generation of gray- bright luminescent quartz (Q1) perpendicular to the c-axis (pointing out of page). Afterwards, there was a process of dissolution, with precipitation of new bright luminescent quartz. Grain growing continued, and after several zones formed in the absence of deformation, some microfaults displaced quartz banding about ca. 200 μm . These fractures generated space now filled with dark luminescent quartz. The quartz continued growing until the precipitation of chalcopyrite, nowadays replaced by atacamite and cuprite.

Taltal deposit: Hydrothermally-altered igneous quartz textures

The samples of the Taltal magnetite-(Cu-Mo-Au) deposit (8) have a particular SEM-CL texture related with the hydrothermal alteration of the previous igneous quartz. Bright to gray luminescent quartz show corroded grain boundaries and was followed by the precipitation of dark quartz in the created cavities, suggesting an intermediate stage of quartz dissolution (Fig. 1H). In fact, the ore assemblage precipitated synchronously with this second generation of quartz. In some grains, there are embayed cores of bright luminescence quartz with euhedral gray overgrowths, being cores and rims optically continuous. This

texture could be caused by the precipitation of core quartz, followed by the dissolution and precipitation of euhedral quartz.

Discussion

The comparative study of the quartz textures by SEM-CL reveals complex stories of growing and fracturing that are not visible in conventional transmitted light microscopy. These textures give clues that are critical for the understanding of hydrothermal processes and ore formation. Euhedral growth zones of various intensities as well as concentric banding within individual grains are due to growth of quartz in an open space. The origin of CL in euhedral zones is not well known but may result from cyclic incorporation of trace elements during precipitation (Penniston, 2001, Landwing and Pettke, 2005). Embayed cores with euhedral overgrowths and mosaics of grains are due to the dissolution along fractures and grain boundaries. Cobweb and splatters, networks and microfaulting textures form in response to mechanical fracturation. Potential causes for dissolution textures of quartz in hydrothermal systems are fluctuations in pressure, temperature and fluid composition (Rusk and Reed, 2002). Some textures can be related with the ore precipitation stage such as in Sultana or the Cala deposits, probably developing open spaces that were critical for sulfide precipitation. The study of fluid inclusion assemblages in the different quartz domains detected by the SEM-CL definitely help to understand the evolution of fluids within the hydrothermal system.

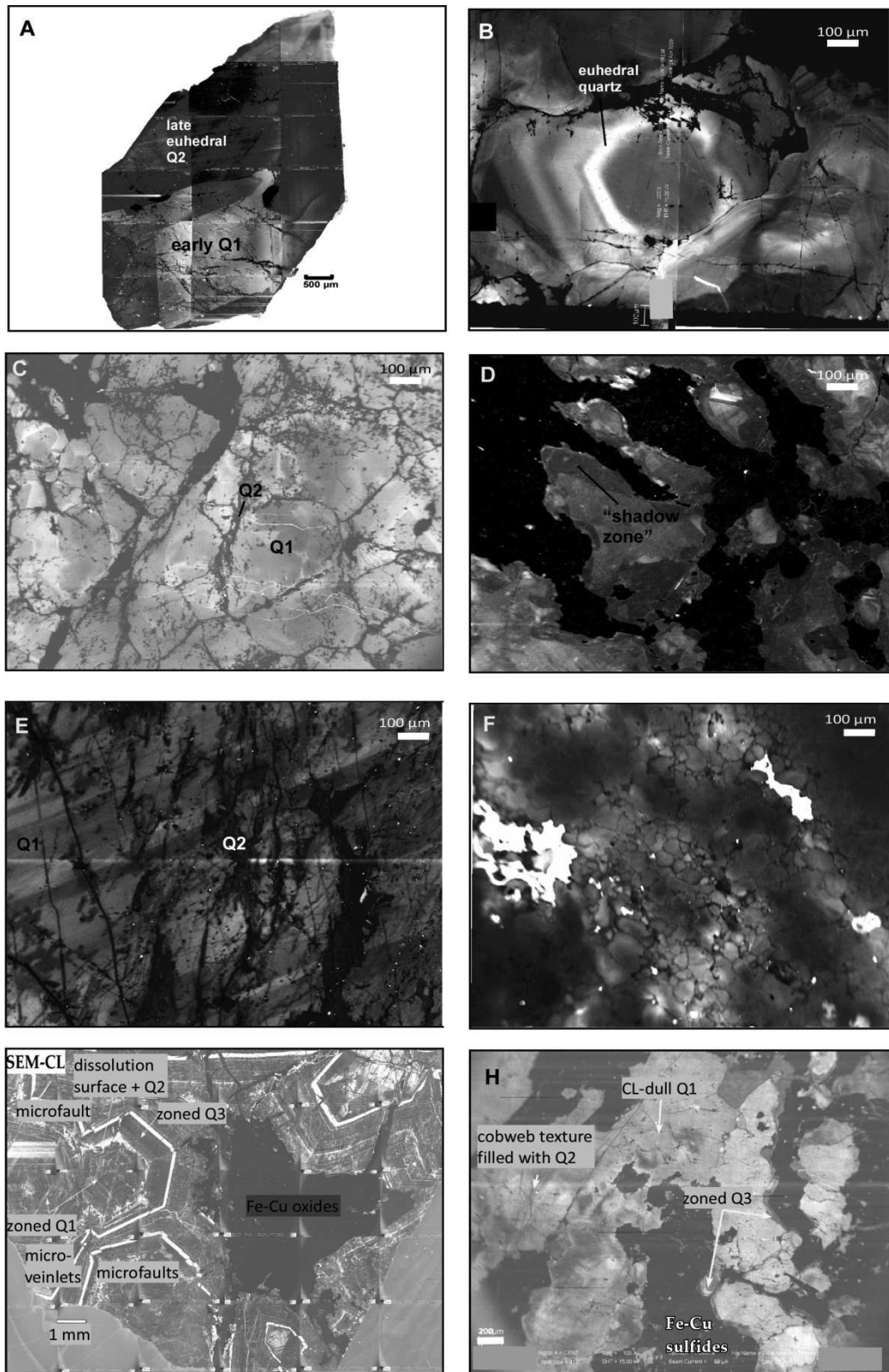


Figure 1. SEM-CL images of the seven studied areas. See the text for explanation

Conclusions

The SEM-CL technique has been successfully applied for the study of different mineralizations in the OMZ (SW Spain) and the Central Andes (N Chile). As we show in this study, this technique is critical for the thoughtful petrographic study that must precede any fluid inclusion study in order to obtain consistent and realistic results. In this study, SEM-CL images show numerous textures of quartz related to the history of the fluid evolution in five ore deposits that will help to better understand their formation.

Appendix IB: Preliminary characterization of the hydrothermal fluids related to the magnetite-copper deposit of Cala (Huelva, SW Spain)

Introduction

The Cala mine (SW Spain) has been one of the most important iron producers of Iberia during the 20th century. Estimated current reserves are 60 Mt @ 39% Fe and 0.2% Cu, but the deposit continues open at depth. The Cala orebody has been considered as a typical calcic skarn developed on Cambrian carbonatic rocks adjacent to an intrusion of monzogranite (Velasco and Amigó, 1981). However, recent studies (Tornos and Casquet, 2005; Carriedo et al., 2006, 2010) show that the deposit has a more complex evolution, showing some features typical of IOCG-like and shear-zone related deposits. Despite its good accessibility and the poor alteration of the original mineral assemblages, the detailed characterization of the circulating fluids in the Cala mine is difficult to constrain. This is due to the multi-stage deformation that has produced widespread reequilibration and decrepitation of most of the fluid inclusions in the suitable minerals such as quartz, calcite or garnet. This manuscript includes the information collected during a preliminary study that tried to characterize the hydrothermal fluids involved in the formation of the system, using the best preserved fluid inclusion assemblages in both the skarn and the shear zone-related magnetite zones. The study suggest that, as the papers above propose, the formation of the orebody is not exclusively related with a classical skarn, but to a complex polyphase hydrothermal system, possibly involving both magmatic and metamorphic fluids that were channelized in a pull apart structure within a large transpressive structure.

Geological setting

The Cala deposit is adjacent to a small ellipsoidal monzogranite stock (the Cala stock) which is part of the Santa Olalla Plutonic Complex (Fig.1). Both the orebody and the plutonic rocks are emplaced in a small pull apart extensional structure formed during the sinistral Variscan transpression (Tornos et al., 2002). The magmatic-hydrothermal evolution of the deposit is resumed in four main stages based on Carriedo (P.h.D. in prep.):

- a) Intrusion of small plugs of granodiorite synchronous with the formation of a prograde garnet-pyroxene rich calcic skarn on calc silicate hornfels and limestone, later replaced by a magnetite-actinolite rich skarn.
- b) Development of a sinistral ductile-brittle shear zone, which produced the replacement of the previous skarn and the host dolomite by a zoned alteration including ankerite-hematite, actinolite-magnetite and quartz-magnetite-ankerite-actinolite zones.
- c) Further intrusion of a, apparently barren, coarse grained granodiorite-monzogranite (Cala stock).
- d) Formation of quartz-ankerite Cu (Au) rich veins.
- e) Late thrusts with overthrusting of the Cala stock on the earlier mineralization.
- f) Extensional collapse and a late hydrothermal activity with formation of a quartz-chlorite-ankerite assemblage.

Fluid inclusion study

Suitable fluid inclusion assemblages have been found in the calcic skarn and in the shear zone-related mineralization. Petrographic relationships, microthermometric data and phase proportions of the fluid inclusions suggest that

these hydrothermal rocks formed in relationship with the circulation of fluids having different compositions.

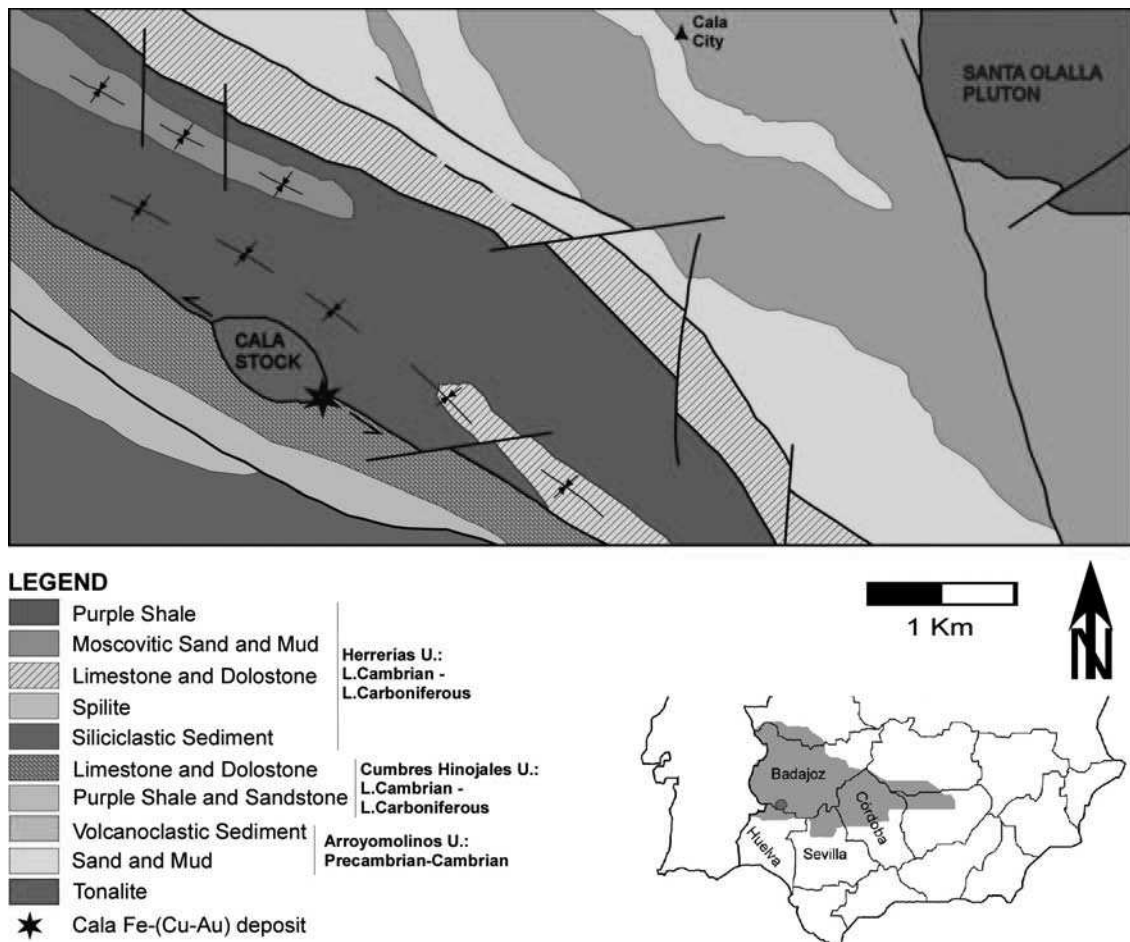


Figure 1. Geological map of the Cala mine in Huelva with the main lithologies in the area. Modified after Apalategui et al. (1987).

Fluid Inclusion Assemblages (FIA), Quartz Domains, Microthermometric and Raman Results

No fluid inclusions have been found in the prograde skarn. However, this garnet-rich skarn has abundant vugs filled with quartz, calcite, epidote, actinolite and magnetite. This assemblage is interpreted as precipitated from the exhausted fluids that formed the prograde skarn but at lower temperatures. Quartz and

epidote contain small two-phase fluid inclusions with 85-90% vol. liquid. SEM-CL images of quartz show a first generation of grains (Q1), sometimes with euhedral growths and local dissolution zones. There is a second generation of quartz (Q2) along microfractures and crosscutting Q1. Two types of fluid inclusion are distinguished within Q1. Type I, brine inclusions having 8-10 μm in size, 80-85% vol. liquid, and contain halite and other small daughter crystals like sylvite and hematite (Fig.2). Microthermometry reveals total homogenization temperatures between 370° and 400°C by dominant disappearance of the vapor phase. Salinities determined by final melting of halite range between 26 and 40 % NaCl eq. These inclusions coexist in the same FIA with vapor-rich inclusions. They have between 30 and 40 vol. % liquid, with a single vapor bubble. CO₂ is minor and has only been identified by laser-Raman spectroscopy. The homogenization temperatures are 341°-350 °C and salinities have not been calculated due to the absence of liquid CO₂. However, in a few inclusions, clathrate have been observed with melting temperatures over 0°C. A third type of unambiguously secondary fluid inclusion has been distinguished along the Q2. These inclusions are usually small and difficult to measure.

Cathodoluminescence (CL) images of the shear zone-related mineralization show complex textures with multiple superimposed stages of quartz precipitation-recrystallization. Re-equilibration has modified or destroyed most of the inclusions and, thus, is unlikely that primary fluid inclusions can be found. However, there are some “shadow zones” protected by magnetite and pyrite in which likely primary euhedral quartz has been preserved. These grains contain suitable FIA for microthermometric study (Fig. 2). The first group includes halite-saturated inclusions with a liquid (80-85% vol) and a vapor phase. Their size is small (1-9 μm), always having a halite crystal and another transparent phase, probably sylvite. The homogenization temperatures range between 500 and 580°C and estimated salinities are 35-40 wt % NaCl eq., estimated from the final melting of halite (Bodnar and Vityk, 1994). A second, more abundant, group of inclusions has

significant amounts of CO₂, with variable amounts of CH₄. They are also small and usually have the double CO₂ bubble. Total homogenization temperatures are more variable, ranging between 420° and 500°C. Almost all of them decrepitate over 500°C. Salinities have been calculated by clathrate disappearance and range between 4 and 19.3 wt % NaCl eq. The CH₄ phase has been identified by Raman spectroscopy and by microthermometry.

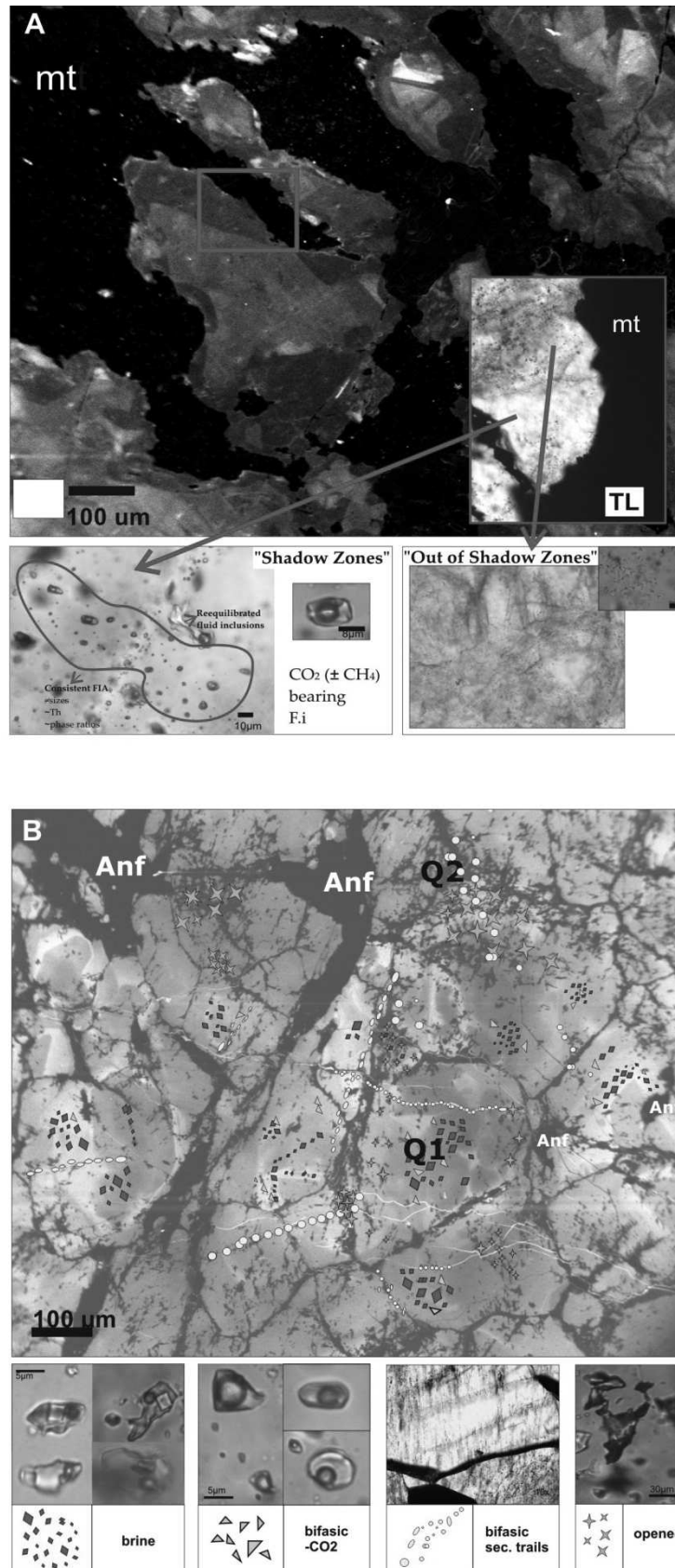


Figure 2. Fluid inclusion types in the shear zone related **(A)** and the skarn related mineralization **(B)** in the Cala mine

Discussion

The fluid inclusion data show that the superimposed hydrothermal events are related with the circulation of fluids of different origins.

The FIA of the skarn probably reflect exhausted aqueous magmatic brines. The small CO₂ contents could be derived from devolatilization of the carbonates during metasomatism (Crawford and Hollister, 1986; Wilkinson, 1991). The polysaline composition is typical of the prograde stages of skarns, where the fluid-rock interaction produced fluids enriched in Ca and Mg.

Fluids circulating through the shear zone were immiscible CO₂-CH₄ -rich aqueous brines. The most likely origin for such fluids is the metamorphic devolatilization/derivation from the underlying carbonate-pelite sequence of early Cambrian age. However, in these inclusions, post-entrapment and re-equilibration is usual with common leakage of fluid. Most of the fluid inclusions out of "shadow zones" show unambiguous evidences of post-trapping, with large variations in both density and salinity.

Conclusions

The magnetite-(Cu-Au) mineralization of the Cala mine shows a complex hydrothermal evolution, in response to several tectonic and magmatic pulses. This preliminary fluid inclusion study confirms that some of the ore is related with magmatic-related skarn processes, but most of the mineralization is associated with the circulation of immiscible CO₂-rich brines of likely metamorphic derivation.

Appendices II (tables in the excel file):

IIA. Hand samples

The letters SU, BE and CA and following numbers indicate the name of the site (SU: Sultana, BE: La Berrona) and the number of each sample respectively. Samples collected by Jorge Carriedo and Fernando Tornos are preceded by the letter J and F respectively.

All the collected hand samples have a brief description (column *Description*) of the mineralogy and lithology of the rock.

The abbreviations used in the table are:

Qtz: quartz

ab: albite

py: pyrite

cpy: chalcopyrite

sph: sphalerite

act: actinolite

d.p.: double polished thick section

p.: polished section

t.s.: normal thick section

Other samples collected along the first field campaigns in deposits that have finally not incorporated in the last version of this thesis are not included in the tables (e.g. Colmenar, El Soldado, etc.).

IIB. Microthermometric data of fluid and melt inclusion assemblages

Microthermometry of fluid inclusions

The microthermometric procedure is explained in the method-section in the thesis. The salinity of fluid inclusions was expressed in wt-% NaCl equivalent and was determined from final melting of ice (Bodnar y Vityk, 1994), final melting of clathrate or final melting of halite (Bodnar and Vityk, 1994) depending on the phases present within the inclusion.

The *cycling technique* for measuring fluid inclusions is used in small inclusions (<8 μm) in which the phase changes are very difficult to observe or in all inclusions in which final melting of the last crystal either of ice or of clathrate (when CO_2 is present) cannot be seen. These two measurements are critical, as they are used for the calculation of the salinity of the fluid. The technique consists of bracketing the temperature after several cooling-heating runs as it is shown in the next example taken from Goldstein and Reynolds (1994):

1. Freeze the inclusion and warm it rapidly to a temperature below the hypothesized T_m ice.
2. Warm slowly until the bubble looks in any way different than it did in step 1.
3. Immediately lower the temperature and watch in the bubble became more deformed or smaller than before. Then, hypothesize that ice was still present at the highest temperature achieved in the run and begin to warm again.
4. Warm the inclusion to a higher temperature (0.1, 0.5 or 1°C depending on the desired resolution) than that reached in step 2 and then reduce again the temperature (as in the step 3).

5. If the observation of bubble change determined in 3 is repeated, repeat step 4 to an even higher temperature. Continue repeating this procedure until next step behavior is observed.
6. If during cooling, the bubble does not appear to change by shrinkage or deformation, the ice probably melted within the temperature interval just preceding the highest temperature achieved in step 4.

The cycling technique can also be used for the determination of the homogenization temperature of the bubble when it is not clear when it disappeared. For example, if the inclusion is heated from 25° to 320°C, the bubble gradually shrinks and in proceeding to 330°C becomes more difficult to perceive so the observer considers that the bubble has disappeared because it cannot longer be seen. At this instant, the observer should heat the inclusion to a temperature at which the bubble had just been clearly visible (320°C). In this case the bubble is indeed once again visible at 320°C, which suggest that undercooling was not required to generate the vapor bubble, meaning that the bubble was still present but simply not visible to the observer at 330 °C. The inclusion is then heated to a higher temperature (325°C) and then cool back to the temperature at which the observer could before clearly see the bubble. If the bubble is still present, the inclusion had not been homogenized at 325 °C so continue rising the temperature (i.e. 330°C) and heating until at 320°C the bubble does not appear, so the inclusion had been homogenized between 325° and 330°C.

Abbreviations and symbols

Chip:	Fluid inclusion waver
Size (microns):	Maximum dimension size of fluid inclusion
Tmcla:	Final melting temperature of clathrates
Tmice:	Final ice melting temperature
TL+V→ L:	Homogenization temperature to the liquid phase

TL+V → V:	Homogenization temperature to the vapor phase
TmCO₂:	Melting point temperature of CO ₂
ThCO₂:	Homogenization temperature of CO ₂ (L→V)
TNaCl:	Melting temperature of halite
TKCl:	Melting temperature of silvite
NaCl wt-% eq.:	Apparent salinity
Thtot:	Final homogenization temperature
NaCl % eq.:	Salinity in NaCl equivalent percentage
LA-ICPMS Nr:	Number of the LA-ICPMS analysis for each fluid inclusion
Laser Nr:	Number of the LA-ICPMS project
****:	Quality of the LA-ICPMS signal from * to ****
X:	Ignored LA-ICPMS signal
Raman Nr:	Number of the Raman analysis for each fluid inclusion

Microthermometry of melt inclusions

In order to avoid as much as possible the decrepitation and diffusion processes in the microthermometry runs of silicate melt inclusions, we followed the heating run procedure used by Student and Bodnar (2004):

1. Heat the sample at 30°C/min from the room temperature to 500°C
2. Heat the sample at a rate of 10 °C/min until first melting was observed
3. At this point, a heating rate of 1 – 2 °C/min was used until homogenization was achieved as indicated by either the complete dissolution of the last visible crystal or vapor bubble.

IIC. LA-ICPMS data of fluid and melt inclusions

The LA-ICPMS procedure and settings for both fluid and melt inclusions are given in the method sections of this thesis. All the sample wavers were cleaned

with acetone and with warm aqua regia (3/4 HCl concentrate and 1/4 HNO₃ concentrate) in order to eliminate the surface contamination. In addition, the samples were hand-polished with diamond compound on both sides of the wavers. The LA-ICPMS chamber was also carefully cleaned with washing liquid to avoid any contamination of previous analyses (Jun Hung Seo, pers. comm., 2010). The deconvolution of the LA-ICPMS signals was made with the SILLS computer program (Guillong et al., 2008; ETH ZURICH). For fluid inclusions, Na, K, Mn, Zn, Cs and Pb were selected for the contribution of the host mineral correction.

Limit of detection (LOD): For any element i the limit of detection is the lowest significant intensity at 99% confidence level. The LOD is dependent on the optimization of the instrument parameters and the number of measurements of each element in the signal interval. In the LA-ICPMS tables included in this thesis, the upper LOD is given as <LOD in fluid inclusion assemblages were the value of the corresponding element was below the limit of detection in all the fluid inclusions. Some authors (i.e. Ulrich et al., 2001) plot the upper limit of detection in the LA-ICPMS elemental concentration plots but the real meaning of this value is obscure as it is not based on the observation of clear signals. In the Figures x and x of the Chapters II and III respectively, only the values in which the observation of clear and distinguishable signals is possible are shown in order to avoid misleading in the interpretation.

IID. Raman spectroscopy analyses of fluid inclusions

The molar fractions of gas species present in fluid inclusions were calculated using the Placzek's polarizability theory derived formula (Burke, 2001; Dubessy et al., 1989):

$$X_a = [A_a / (\sigma_a \epsilon_a)] / \sum [A_i / (\sigma_i \epsilon_a)]$$

Where X_a , A_a and σ_a are the molar fraction, the peak area and the Raman cross-section for species a ; A_i and σ_i are the appropriate values for all species present in any given fluid inclusion. The Raman cross-sections (σ) are taken from the Table 2 in Burke (2001) as follows: $\sigma_{\text{CO}_2} = 2.5$, $\sigma_{\text{CH}_4} = 7.5$ and $\sigma_{\text{N}_2} = 1$. The instrumental efficiency (ϵ_a) is taken as unity in the components.

Special care was taken trying to measure fluid inclusions that were far from the LA-ICPMS pits in order to avoid any modification of gas speciation (Lambrecht et al., 2008).